Liqiu Wang
Editor

Advances in Transport Phenomena 2009

Springer

Liqiu Wang (Ed.)

Advances in Transport Phenomena 2009

Liqiu Wang (Ed.)

Advances in Transport Phenomena 2009

Springer

Prof. Liqiu Wang
Department of Mechanical Engineering
The University of Hong Kong
Pokfulam Road
Hong Kong
E-mail: lqwang@hku.hk

ISBN 978-3-642-02689-8 e-ISBN 978-3-642-02690-4

DOI 10.1007/978-3-642-02690-4

Advances in Transport Phenomena ISSN 1868-8853

Library of Congress Control Number: 2009937145

Typeset & *Cover Design:* Scientific Publishing Services Pvt. Ltd., Chennai, India.

Printed in acid-free paper

9 8 7 6 5 4 3 2 1

springer.com

Preface

The term *transport phenomena* is used to describe processes in which mass, momentum, energy and entropy move about in matter. *Advances in Transport Phenomena* provide state-of-the-art expositions of major advances by theoretical, numerical and experimental studies from a molecular, microscopic, mesoscopic, macroscopic or megascopic point of view across the spectrum of transport phenomena, from scientific enquiries to practical applications. The annual review series intends to fill the information gap between regularly published journals and university-level textbooks by providing in-depth review articles over a broader scope than in journals. The authoritative articles, contributed by internationally-leading scientists and practitioners, establish the state of the art, disseminate the latest research discoveries, serve as a central source of reference for fundamentals and applications of transport phenomena, and provide potential textbooks to senior undergraduate and graduate students.

The series covers mass transfer, fluid mechanics, heat transfer and thermodynamics. The 2009 volume contains the four articles on biomedical, environmental and nanoscale transports. The editorial board expresses its appreciation to the contributing authors and reviewers who have maintained the standard associated with *Advances in Transport Phenomena*. We also would like to acknowledge the efforts of the staff at Springer who have made the professional and attractive presentation of the volume.

Serial Editorial Board

Contents

List of Contributors

Numbers in parenthesis indicate the pages on which the authors' contribution begins.

Chen, H.S.
Institute of Particle Science & Engineering, University of Leeds, Leeds LS2 9JT, UK (135)

Ding, Y.L.
Institute of Particle Science & Engineering, University of Leeds, Leeds LS2 9JT, UK (135)

Finlay, W.H.
Department of Mechanical Engineering, University of Alberta, Edmonton, Alberta, T6G 2G8, Canada (1)

Frizon, F.
Commissariat à l'Énergie Atomique (CEA), Nuclear Energy Division, Waste Treatment and Conditioning Research Department, 30207 Bagnols-sur-Cèze, France (31)

Gin, S.
Commissariat à l'Énergie Atomique (CEA), Nuclear Energy Division, Waste Treatment and Conditioning Research Department, 30207 Bagnols-sur-Cèze, France (31)

Golshahi, L.
Department of Mechanical Engineering, University of Alberta, Edmonton, Alberta, T6G 2G8, Canada (1)

Jegou, C.
Commissariat à l'Énergie Atomique (CEA), Nuclear Energy Division, Waste Treatment and Conditioning Research Department, 30207 Bagnols-sur-Cèze, France (31)

Quintard, M.
Institut de Mécanique des Fluides, C.N.R.S., Toulouse, France (179)

Wang, L.Q.
Department of Mechanical Engineering, the University of Hong Kong, Pokfulam Road, Hong Kong, P.R. China (179)

Recent Advances in Understanding Gas and Aerosol Transport in the Lungs: Application to Predictions of Regional Deposition

Laleh Golshahi and W.H. Finlay*

Abstract. Recent developments in understanding the physical processes responsible for gas and aerosol transport in the alveolar region of the lung are reviewed. Predicting regional deposition in the lungs is important both for environmental exposure and respiratory drug delivery. There is a strong connection between transport and deposition in the lung; thus, a large number of experiments, theoretical developments and computational studies on gas and aerosol transport, both in animals and with human subjects, have been developed so far to enhance our understandings of possible adverse effects of toxic particulate matter inhalation and determining therapeutic strategies for inhalation drug delivery (i.e. aerosol administration). Due to the intrinsic limitations of accurate measurement of detailed regional deposition in the lung, mathematical models have been favored extensively for prediction of regional deposition. The goal of the present article is to review recent advances in model development for predicting the regional deposition in the lung with a focus on the lung parenchyma. These advances build on recent model predictions considering the complex structure, time-varying, and cyclic process of alveolar expansion and contraction. Since validation of the developed mathematical models has improved with the advent of an experimental technique known as aerosol bolus dispersion, the latter subject has been linked to the review of the subject.

Keywords: Acinus, aerosol bolus dispersion, intrapulmonary mixing, lung, lumen, pulmonary mechanics, regional deposition, simulation, transport mechanisms.

Introduction

Deposition models quantitatively describe the behavior of the particles in the airways by combining the lung geometry with the fluid dynamics of the airways.

Laleh Golshahi · W.H. Finlay
Department of Mechanical Engineering, University of Alberta, Edmonton, Alberta, T6G 2G8
warren.finlay@ualberta.ca

* Corresponding author.

L.Q. Wang (Ed.): Advances in Transport Phenomena 2009, ADVTRANS 1, pp. 1–30.
springerlink.com

Characterizing the dispersion, transport, and predictive understanding of regional deposition (i.e. where and how much inhaled particles deposits within respiratory tract) of therapeutic aerosols, is beneficial in improving the design of aerosol delivery devices (e.g. nebulizers, dry powder inhalers and pressurized metered dose inhalers) and drug dosage calculations. In addition, an association between exposure to environmental aerosols and respiratory mortality level has been illuminated by cohort toxicological studies [1]. Thus, to minimize the malignancy of unwanted environmental aerosol exposure, it is important that a predictive model of regional deposition in the human airways be available for epidemiologists and toxicologists.

The anatomy of the lung (including the bifurcating structure of the tracheobronchial airways, and expanding and contracting alveoli) affects the fluid dynamics of the gas flow inside the airways, and over the last century, many studies have focused on the fluid dynamics of the gas flow inside the airways. In this communication, reviewing the fluid dynamics of the flow and gas transport mechanisms in the lung will be limited to a brief description that is needed for a more extensive following discussion of aerosol dispersion. More details of fluid flow in the lung can be found in previous reviews on the topic [2-6]. Here we instead focus on aerosol dispersion and mixing (including the non imaging technique of bolus dispersion), supplementing another recent review whose focus was on extrathoracic and total respiratory tract deposition [7].

1 Gas Transport in the Respiratory Tract

1.1 Bulk Convection, Longitudinal Mixing, Diffusion and Dispersion

The lung transports oxygen-enriched air from the mouth and nose to the alveolar region through the conducting airways and delivers oxygen to blood cells by passing it through alveolar membranes. Similarly, waste carbon dioxide is taken away from those cells. This transport is caused by a combination of convective, or bulk gas transport, and mixing [5]. Diaphragm and intercostal muscles (i.e. the muscles between ribs) contract and expand the chest cavity and cause pressure gradients along the airways. Convective or bulk gas transport is a result of this pressure gradient [8]. During bulk flow, all gas species move at the mean velocity of the air stream regardless of the concentration of the individual species in the mixture. The direction of the convective flow depends on the sign of the pressure difference [2]. The convective flow accelerates and decelerates rapidly when the breathing rate is high and in such cases inertia is considered as an important transport phenomenon. Convective flow is called unsteady at such high breathing rates, whereas, air flow can be considered quasi-steady when the breathing rate is low and inertia is negligible in those cases [2]. If the flow is quasi-steady, the Reynolds number (Re) is generally the pertinent parameter for determining whether the flow is laminar or turbulent (see [9] or Table 1 in [5] for the details of airway geometry and Reynolds numbers). The Reynolds number is of the form

$$\mathrm{Re} = \frac{ud}{\nu} \tag{1}$$

Both longitudinal velocity (u) and airway diameter (d) decrease toward higher generations in tracheobronchial tree, therefore, the maximum Reynolds number is expected in the trachea [5].

The second major gas transport phenomena, so called longitudinal mixing, is defined as the relative motion of one gas species (e.g. oxygen) with respect to another gas species in the direction of flow [5]. Mixing can be caused by diffusion processes or by dispersion processes. The latter depends on local velocity patterns. Airway geometry determines the relative importance of these two mixing processes (diffusion versus dispersion) [5]. A concentration gradient of a specific molecular species across the front that is separating inspired air from resident gas is the driving force for molecular diffusion (diffusive transport) [8]. The Schmidt number (Sc) ($Sc = \frac{\nu}{D}$), which is the ratio of viscous to mass diffusivity, is an important parameter in this regard, where its large value indicates weak mass diffusion [2]. Molecular diffusion always occurs (due to random thermal oscillation of the molecule), as long as the molecules in a mixture experience a temperature above absolute zero [2]. However, this transport phenomenon mostly exists in distal airways, where the total cross sections are large [5]. In proximal airways, the axial velocity profile has the principal influence on mixing. Friction near airway walls retards the translation of molecules in that region so that centrally located fresh molecules are translated at greater than average speed and can penetrate into residual air. This type of mixing is called *longitudinal dispersion* or *steady streaming* and in order to understand and predict this type of mixing, velocity profiles in airways need to be determined since longitudinal dispersion depends on the difference in speed between gas molecules at different radial positions [5]. Since a turbulent velocity profile is blunter than a laminar one, laminar dispersion is generally more extensive than turbulent dispersion.

So called augmented dispersion [10] arises in the respiratory system in the form of circulation patterns (that may happen in a lateral or radial plane) due to secondary flows in a way to limit longitudinal dispersion due to continuous gas molecule interchange at different radial positions, which consequently diminish the dispersive effect of the axial velocity profile [5]. Secondary flow refers to counter rotating vortices mirrored about the plane of symmetry in curved tubes, arising from centrifugal effects (Dean instability) [10]. Zhao and Lieber have conducted multiple experiments, using a two velocity component laser doppler anemometer, both for steady inspiratory and expiratory flow followed by mathematical modeling, and have demonstrated that secondary flow patterns are present in lung bifurcation geometries [11-13].

Streamlines of air also converge as they pass through the glottal constriction in the larynx and the axial velocity is accelerated in a way that a jet of gas detached from the surrounding airway walls is formed immediately downstream of the glottal constriction. The slope of the velocity profile (shear rate) is large in the

boundary between this jet and the surrounding wall so that turbulent velocity fluctuations are generated. The circulating flows in the longitudinal direction can form "dead zones" in which a gas species is temporarily trapped, which adds to the nonuniformity of axial transport rates and enhances dispersion [5].

Another mixing mechanism is the so called *convective exchange*, which is a drift in species for oscillating flows and is a non-diffusional transport mechanism that helps to explain the normal respiratory exchange of gases, aerosols and successful ventilation with very low tidal volumes (high frequency ventilation) [14]. This phenomenon is related to differences between velocity profiles during inspiration and expiration. Schroter *et al.* measured velocity profiles for steady one-way flow through models of a single bifurcation [15]. Inspiratory flow velocity profiles are asymmetric and the velocity peak swings to the inner wall of the daughter branches in the plane of the bifurcation, while perpendicular to the plane of the bifurcation the velocity profile is blunter and quite symmetric, with some peaking of velocity near anterior and posterior tube walls [5] (see Fig. 6 in [5]). Subsequent studies have confirmed these flow patterns and a complete review of flow visualization in bifurcations can be found in [6]. It has been found that expiration velocity profiles are generally more uniform (flatter) than inspiratory profiles [15]. This difference in flow profiles implies that fluid particles carried forward during inspiration will not return to their initial lung depth after expiration and a net longitudinal displacement of the fluid particles will be observed (see Fig. 2 in [16]). Fluid particles near the center of the tube experience a net distal movement while a net proximal movement occurs for particles near the tube wall [14,16]. This net cyclic flow process is called convective exchange [16]. The "convective-exchange" mechanism can be used to explain a result that has been observed in human studies in which radioactive particles have reached and deposited in alveoli after several breaths even when tidal volumes much smaller than anatomical dead space were inhaled [16,17].

The velocity profiles in multiple airway branching are more complicated since the exiting profile from a daughter branch is the entering profile to its progeny [5]. An enhancement of the convective exchange effect would be expected for multiple bifurcations and a cumulative net deformation greater than the effect of a single bifurcation is expected [14]. Scherer *et al.* have performed experiments with bronchial airway models for both single and multiple planar bifurcations in series [16]. The flows were fluid mechanically similar to those of air during normal breathing in approximately generations 7-15. The pertinent nondimensional convected distance ($L\pi R^2/V_T$) was considered as a parameter to determine the efficiency of the exchange mechanism of moving fluid particles longitudinally. L is the distance that tracer particles are convected forward per cycle over the first five flow cycles, and R is the tube radius. Physically ($L\pi R^2/V_T$) is the ratio of the net volume the tracer was swept along the tube divided by the fluid volume that goes through the bifurcation. Plotting $L\pi R^2/V_T$ versus Reynolds number of the flow within different lung generations shows an increase in the efficiency of the convective exchange mechanism in the upper airways compared to the lower airways

for laminar flow (see Fig. 7 in [16]). $L\pi R^2/V_T$ is measured to be an order of magnitude higher for multi-branched (MB) compared with single branched (SB) geometries at similar values of Reynolds number and frequency number $\alpha = R\sqrt{\omega/\upsilon}$ (see Fig. 7 in [16]). This increase in exchange efficiency has been noted as an important feature of bronchial design and may be due to the greater relative uniformity of the expiratory velocity profiles in the multi-branched case compared to single branched [16]. A possible reason for the direct relation between the strength of the convective exchange mechanism and Reynolds number has been suggested as resulting from the increased strength of fluid swirling in upper airways at high Reynolds number, which increases the uniformity (flatness) of the expiratory profile compared with the inspiratory profile i.e. greater relative differences between inspiratory and expiratory velocity profiles increase the efficiency of the convective exchange mechanism [16].

Scherer *et al*. have defined a Peclet number characteristic of the convective exchange process (Pe^{CE}) [16]. In order to determine the relative importance of the convective-exchange mechanism relative to molecular diffusion one must realize that the distance a gas molecule or aerosol particle is displaced over an oscillatory cycle of time duration *1/f* in the multi-branched geometry is *L*, while over the same cycle time, molecular diffusion (with coefficient of diffusion D_{mol}) will mix respiratory gases over a length of the order of magnitude equal to $L_D \approx \sqrt{2D_{mol}/f}$. The ratio of L/L_D is suggested as a parameter to determine the relative importance of convective exchange compared to molecular diffusion i.e.

$$Pe^{CE} = L/L_D = L/(\sqrt{2D_{mol}/f}) \tag{2}$$

Calculation of Pe^{CE} over different Wiebel generations has shown that $Pe^{CE}>1$ over all the upper and central conducting airways (Wiebel generations 1-12), indicating that the convective exchange mechanism is an important mode of mass transfer along the central airways [16]. For aerosol particles of 0.5 μm in diameter or larger, calculations of Pe^{CE} give values greater than one throughout much of the respiratory tract during normal breathing (tidal volume 500, 15 breaths/min). This suggests that the convective exchange mechanism is an important transport phenomenon for aerosols in the respiratory tract. However, for gases in the lower conducting airways and in the respiratory zone $Pe^{CE}<<1$, and the main mode of mass transfer for gases in those regions is molecular diffusion [16].

1.2 Cardiogenic Gas Mixing

In concert with other parameters affecting velocity profiles in airways, cardiac pulsations cause ‘cardiogenic mixing’, which may have important effects on velocity patterns in the conducting airways [18]. Small oscillations of respiratory flow occurring at the same frequency as the heartbeat are routinely observed during both inspiration and expiration, but are most obvious during post-expiratory

pauses where the base flow is more flat [19]. It has been demonstrated that gas mixing in the airways is affected by the cardiogenic pulsations, which can be considered as an increase in effective diffusion coefficient by a factor of five [20]. It is thought that cardiogenic oscillations are transmitted from the contracting heart through the lung parenchyma and are an important gas mixing mechanism in conducting airways [20-32]. In a study of tracheal insufflation of O_2 (TRIO) using a catheter placed 1 cm above the main carina on anesthetic dogs, it was shown that cardiogenic oscillations (CO) increase gas mixing approximately four fold and this value was independent of the insufflation flow rate (0.2- 10 l/min) [21]. The contribution of CO during constant-flow ventilation (CFV) on eleven dogs has been studied and it was shown that with cardiac arrest, alveolar ventilation decreased an average of 37% and defibrillation resulted in a return of alveolar ventilation to 81% of the prearrest value [22].

Because there have been no direct measurements of acinar gas mixing caused by cardiac activity, it is unknown whether cardiogenic oscillations also enhance gas mixing in the acini [33]. Analyzing expired gases at the mouth showed that cardiogenic oscillations contribute only about 4% to alveolar gas mixing during tidal ventilation [27]. Other studies have also confirmed that the effect of cardiogenic oscillations in the alveolar region is probably minimal [22,28,30,31]. Potentially, an increase in effective diffusivity due to cardiogenic mixing could displace the diffusion front toward the proximal airways (mouthward), thus decreasing dead space (V_D). The gas in the conducting airways constitutes the dead space (V_D), which is considered as a volume of air up to a location where a large change in gas concentration takes place [34]. This would improve mixing between inspired and alveolar gas. To date, controversy exists concerning the influence of cardiac activity on gas mixing [33]. Bidani *et al*. believed that pulsatility of pulmonary capillary blood flow increases gas exchange [35], whereas others suggested that the cardiac effects on gas mixing are caused by direct action of the heart on the lung parenchyma [24,27,32,36].

2 Aerosol Transport in the Respiratory Tract

Due to the importance of determining the fate of inhaled aerosols in different fields of study such as industrial hygiene, drug delivery, and aerosol bolus dispersion (i.e. a physiological test of the lungs that is used in early diagnosis of pulmonary diseases), a large number of both experimental and theoretical studies have been devoted to this subject over many years. In this review we focus on anatomically specific models of systems (physiological-physical) and not on anatomically nonspecific models, according to the model classification in a review by Paiva and Engel (1987) [37].

2.1 Trumpet Model-1D Transport Equation

One of the first models developed for aerosol transport and deposition in the lung is based on the work of Taulbee and Yu [38], in which a one-dimensional

transport equation (trumpet model) thoroughly discussed in the early 1970s [39,40], is used to describe gas transport and mixing in the human lung with a term added to account for aerosol deposition. Weibel's model [41] has commonly been used as the geometrical boundaries for such a transport equation.

Axial distance is the only spatial coordinate in these one-dimensional models; therefore, it is not possible to distinguish the radial concentration gradient of particles across the cross section of the duct in such models. This limitation has been justified considering the molecular diffusion coefficients of gases, and consequently the trumpet model has been successfully used to predict gas transport in the lung [37]. However, even submicron particles (e. g. 0.01 μm in diameter) have a Brownian diffusivity that is several orders of magnitude smaller than the molecular coefficient of any gases and this fact violates the assumption of instantaneous radial diffusion for aerosols [42]. In spite of this limitation in diffusivity of the aerosols, the models that assume instantaneous radial diffusion for aerosols are successful in predicting experimental observations [43]. Darquenne and Paiva have suggested an explanation for this paradoxical observation [42]. They have considered a one-dimensional transport equation as follows:

$$\frac{\partial C}{\partial t} = D\frac{s}{S}\frac{\partial^2 C}{\partial x^2} + \frac{1}{S}\frac{\partial (sD)}{\partial x}\frac{\partial C}{\partial x} - \frac{\dot{Q}}{S}\frac{\partial C}{\partial x} - \frac{L}{S} \tag{3}$$

where D is the effective diffusion coefficient, s is the total airway cross section, S is the alveoli plus airway cross section, x is the axial coordinate, $\dot{Q}$ is the flow rate [equal to $S \times$ mean axial velocity in airways (u)]. Equation 3 has been used to compare particle concentration (C) as a function of time (t) and position along the lung path (x) in three available lung models called A, B, and C [42]. The effective diffusion coefficient D in Eq. 3 considers Brownian diffusion and convective mixing that are involved in particle transport during a respiratory cycle from the fresh air into the resident air. The coefficient for Brownian diffusion (molecular diffusion coefficient) is:

$$D_B = \frac{ckT}{3\pi\mu d_p} \tag{4}$$

where c is the Cunningham slip correction factor that corrects the drag force for the decreased air resistance when the particles' diameter d_p is on the same order of magnitude as the mean free path of the gas molecule, k is Boltzmann's constant, T is the temperature ($^\circ$K), and μ is the dynamic viscosity of air. The effective diffusion coefficient D, is the sum of Brownian diffusion coefficient D_B and the apparent diffusion coefficient by dispersion (D_a).

Convective exchange was discussed above when discussing gas exchange mechanisms, and in the context of aerosol transport it is the bulk process that transfers particles from the tidal air to the residual air. The following equation has been suggested by Scherer *et al*. [44] for convective mixing

$$D_a = \gamma u d \tag{5}$$

where D_a is the apparent diffusion coefficient, γ is a coefficient and equals 1.08 for inspiration and 0.37 for expiration, and d is airway diameter. Despite being specifically developed for gases, many researchers extend Eq.5 to particles. Because of the higher diffusivity attributed to the particles with use of Eq.5, it is expected that the particles will penetrate to the deeper airways, so that deposition in proximal airways will be underestimated while for the lower airways the deposition may be overestimated [45]. Numerical studies have been conducted to duplicate the experiments of Scherer *et al.* [44] to quantify particle dispersion and the value of γ was found equal to 7 and 26 for inhalation [46] and exhalation [47], respectively [45]. Conversely, experiments of Schulz *et al.* [48] on dogs have shown that a single D_a can be used to characterize convective mixing both for inert gases and particles in the first lung generations.

While other researchers have suggested different equations for apparent diffusion, the equation of Scherer is most common. Yu [49] and Taulbee and Yu [38] have proposed the following equation for D_a, in which aerosol dispersion is considered to be generated due to airway asymmetry:

$$D_a = \frac{\sigma^2}{2} ul \tag{6}$$

where ℓ is the average airway length and σ is the SD of an airway generation. From Weibel's data, σ varies from 0.5 to 0.8. Ultman [5] suggested D_a in the following form and considered that convective mixing happens due to nonuniformities in the axial velocity profiles in the airway:

$$D_a = 0.167 ul \tag{7}$$

The aerosol deposition rate in the lung is expressed as L in the mass transport equation (Eq. 3) and is defined as follows:

$$L = L_i + L_s + L_d \tag{8}$$

Where L_i, L_s and L_d are deposition due to impaction, sedimentation and diffusion, respectively. Darquenne and Paiva have used the equations of Taulbee and Yu [38] for the deposition terms in respiratory system [42].

Two assumptions are embedded in Eq.3: instantaneous radial diffusion of the aerosols, and symmetry of airway branching [42]. For laminar flow in a duct with circular cross section, Taylor [50,51] has demonstrated that the following condition needs to be satisfied to be able to use a one-dimensional equation of transport:

$$D_B >> \frac{ur^2}{4l} \tag{9}$$

where r is the airway radius.

Darquenne *et al.* have used the following reasons for arguing the insuitability of a one-dimensional equation to describe aerosol transport. First, Eq. 9 is never

satisfied for the case of particles in the lung; therefore, a one-dimensional equation may not be realistic. Second, radial transport induced by turbulence or laminar secondary flows are present in the process of convective mixing in the proximal airways where the Reynolds' number is high; thus Eq. 5 does not apply for convective mixing. Finally, the one-dimensional equation is restricted to a symmetrical structure [42], where the spatial coordinate in the transport equation (Eq. 3) is with respect to a reference point (e.g. the entry of the model) such that in an actual (asymmetric) lung, regions that are equally distant from the entry of the model may have very different functional properties (e.g. some alveolar sacs in which the velocity is near zero are at the same distance from the model entry as other airways with a convective velocity much larger than zero). Despite these issues, Darquenne *et al.* compared three different structural models with the recent experiments of Heyder *et al.* [52] and demonstrated that neither the model structure nor the consideration of an asymmetrical multibranch structure results in significant differences in the prediction of aerosol transport and deposition in the lung [42]. This implies that total deposition is a very insensitive index. As a result of this observation, Darquenne *et al.* have suggested that it may not be crucial to consider acinar asymmetry, which simplifies modeling of aerosol transport, significantly. However, it should be considered that this conclusion is based on calculations performed with approximated D_a.

2.2 Two and Three Dimensional Models of the Alveolated Region of the Lung

As mentioned above, one dimensional models have been suggested as physically unrealistic because of assumptions that include symmetry, uniformity of particulate velocity and concentration over the cross section of the airways, and radial diffusion being represented by a single effective diffusion constant. These limitations can be overcome by two dimensional [53-56] and two dimensional axisymmetric models [57-60]. However, total surface area of the alveoli may not be expressed precisely in such two dimensional models. Therefore, as a result of the lower area, total deposition in such models is likely to be underestimated (whereas 1D simulations underestimate the penetration of the aerosols in the alveoli and overestimate deposition) [56, 61]. Another limitation of two-dimensional models has been suggested to be their limitation in examining the effect of gravity if it is present outside the plane of the 2D model and this limitation should be considered since the deposition of larger particles (>0.5 μm in diameter) has been found to be sensitive to the orientation of alveoli with respect to gravity [56,61]. Three-dimensional models of the alveolated region have been studied [56,61-65] and because their validation relies on aerosol bolus dispersion experiments, their details will be presented here after an introduction to aerosol bolus dispersion. However, it is worth noting that higher total deposition of small particles have been estimated by Darquenne *et al.* when using 3D- instead of 2D-particle motion [56].

2.3 Aerosol Bolus Dispersion Experiments and Models

If convective mechanisms were absent, inhaled particles should only be present in the tidal air and the residual air should be particle free. However, several studies have demonstrated that inhaled particles are transported from tidal to residual air [66-69].

An experimental approach, called bolus dispersion, has been suggested by Heyder *et al*. [70], to examine the extent and possible importance of convective mixing in peripheral airways. This method consists of inspiration of an aerosol bolus (i.e. aerosol particles are not distributed throughout the entire breath but are instead confined to a small bolus within the inspired air) at different levels of inspired volume (penetration volume), V_p, followed by the measurement of the expired aerosol concentration. An aerosol bolus is defined as a volume of gas, which contains particles, that is surrounded by particle-free air. Aerosol boluses are attractive as a tracer for convective mixing because their volumetric axial dispersion can be easily measured as they pass through defined segments of the respiratory system [70]. Monodisperse aerosol particles 0.5-1 μm in diameter are used as tracers in this method for studying convective gas transport because such particles behave as a "nondiffusive gas" [66].

The inspired and expired aerosol bolus is characterized by means of its mode and half-width on a plot of concentration vs. volume [70]. The expired curves present a bell shape and are characterized by their mode (M) and half-width (H). The mode has been defined as the volume at which the maximum aerosol concentration occurs. Half-width is defined as the width of the bolus (in cm^3) measured between the two points of one-half the maximum concentration. Another controlled variable in such experiments is the location or volumetric penetration of the bolus in the inspired breath. Volumetric penetration (V_p) has been defined as the volume of air inhaled from the mode of the aerosol bolus to the end of inhalation. It can be considered as the volume of air that follows the mode of the bolus into the lungs. For 17 healthy male subjects Heyder *et al*. found the following correlations relating H_{ex} (half-width expiration) to V_p at the higher lung volume (88% total lung capacity i.e. TLC) and the lower end-inspiratory lung volume (62% TLC), respectively:

$$H_{ex} = 156\ cm^3 + 0.514\ V_p \tag{10}$$

$$H_{ex} = 179\ cm^3 + 0.539\ V_p \tag{11}$$

A group of researchers [71] have characterized their aerosol bolus dispersion experimental data using a different set of four indices, as follows. The first is Aerosol Dispersion (ΔH), also called half-width change between the inspired and expired bolus, which is defined as follows:

$$\Delta H = \sqrt{H_{ex}^2 - H_{in}^2} \tag{12}$$

Second is modal shift ($MS=M_{in}-M_{ex}$), i.e., the volumetric difference between the position of the mode of the inspired bolus and that of the expired bolus. Particle deposition and the expired volume needed to recover 50% of the inspired particles (REC_{50}) are the remaining two indices that have been used for characterizing the ventilation in the lung. REC_{50} reflects both the extent of particle deposition and modal shift; hence, if more deposition occurs, more exhaled volume will be necessary for recovery of 50% of the inspired particles and thereby REC_{50} will increase due to increased deposition [71]. On the other hand a modal shift toward lower values of V_p (i.e. penetration volume) that causes the bolus to be exhaled earlier will decrease REC_{50}.

Lung ventilation distribution changes with lung disease [72,73] and is different in smokers [74]. Aerosol bolus dispersion measurement has been suggested as a simple and noninvasive method to supplement conventional methods used in lung diagnosis, considering reference values for ventilation distribution in healthy subjects [75]. The number concentration in the respired air is monitored continuously as a function of the respired air volume in aerosol bolus dispersion and data are collected by an online, open flow apparatus, which combines aerosol photometry and pneumotachography [76]. The diagnostic capability of this method has been tested in several studies to date: in patients with cystic fibrosis [71], papain-induced peripheral lung injury in excised animal lungs [77], changes in lung ventilation distribution due to ozone exposure [78], in obliterative bronchiolitis after lung transplant [79], and as a mean for aerosol-derived airway morphometry (ADAM) in healthy subjects [80], asthmatic children [81], and in patients with lung emphysema [82]. The aforementioned studies have suggested that the extent of bolus dispersion is related to the severity of airway obstruction.

The dependence of aerosol bolus dispersion in the human lung on the lung volume, bolus volume, and gender has also been studied by Brown *et al*. [83]. Measuring the difference in volume variance between exhaled and inhaled boluses (σ_v^2) showed a significant effect of gender, with σ_v^2 greater in males than in females. Bolus volume has also shown a significant effect on the measured values of σ_v^2 [83]. The potential effect of age on aerosol dispersion has been tested by Schulz *et al*. who have studied aerosol bolus dispersion in the respiratory tract of children [84]. There was no noticeable correlation of bolus dispersion with age, body height or lung function parameters, and, except for boluses penetrating very deep into the lung, dispersion was weakly related to lung volume. It was concluded that, per se, there is no correlation between airway size and bolus dispersion. More recently, Schulz *et al*. have indicated that lung size influences bolus dispersion measurements and have suggested a normalization procedure for lung volume before interpreting the aerosol dispersion data [85].

2.3.1 Validation of Mathematical Dispersion Models with Aerosol Bolus Dispersion Experimental Data

Bolus dispersion data have been used to test the predictive ability of mathematical models. The results of the bolus dispersion study by Heyder *et al*. have been compared with three theoretical models by Darquenne *et al*. [42] and several conclusions have been inferred from that analysis, which have applications for further

model developments. They found that use of an asymmetrical acinus model did not change the half-width (H), which is in contradiction with what has been observed previously in intra-acinar gas simulations where the expiratory concentration profiles were found to be highly sensitive to acinar asymmetry [37]. It has been speculated that this discrepancy is due to the fact that for gases, the Peclet number (which indicates the relative importance of transport by convection to diffusion), is near one at the level of the respiratory bronchioles, whereas for aerosols the Peclet number of one occurs only within the alveoli. Therefore, the asymmetry in airways which affects the velocity profile does not play a significant role in aerosol dispersion [42]. In addition, the study of Darquenne *et al*. suggested that expired aerosol concentrations are insensitive to ventilation nonuniformities. This could simplify aerosol dispersion modeling even further [42]. Lastly, the simulations are highly sensitive to axial dispersion (i.e. variation of D_a).

Better agreement has been found between the numerical calculations of Darquenne *et al*. [42] and the experimental data of Anderson *et al*. who have suggested that aerosol bolus dispersion data can be used as an effective tool for early detection of obstructive lung diseases such as cystic fibrosis [71] . However, Darquenne *et al*. have suggested that the good agreement between simulations and experiments may be coincidental [42]. One of the reasons for this argument is that the value of apparent diffusion coefficient (D_a) that has been applied to the simulations may not be valid in the alveolar zone, and the work of Tsuda *et al*. [59] have emphasized that the presence of the alveoli profoundly affects aerosol transport. Tsuda *et al*. have indicated that assuming a uniform radial profile results in overestimation of the local deposition rate. They found that deposition rate in an alveolated duct was always smaller than that in an equivalent straight tube of the same volume. A highly nonuniform deposition pattern, with higher deposition near the alveolar entrance ring, has been observed in the numerical work of Tsuda *et al.* [59] as well as experimental observations in animals [86].

2.4 Models Considering Motion and Structure of the Alveolar Region

It is worth further examining aerosol transport and deposition in an alveolus, which has been summarized by Haber *et al*. [64] Until lately, a simple Poiseuille flow has been assumed inside the lumen and it has been widely accepted that gravitational deposition of fine particles (i.e. 0.5-2.5 μm in diameter that are likely penetrating into the gas exchange region of the lung [87]) can be reasonably predicted inside the lumen, ignoring the complexity of the flow that exists inside the alveoli. The simplified models of Fuch [88] and Pich [89] that were developed for a horizontal, long, straight, pipe were later modified by Wang [90] and Heyder [91], who focused on the cases of particle motion inside inclined pipes, and the case of randomly oriented pipes, respectively.

Recently, modifications have been implemented on aforementioned “classic models” of an acinus, considering that the alveolated structure of acinar ducts is likely playing a major role in the acinar fluid mechanics [92,93]; and

consequently, in the transport of fine particles [59,60]. The experimental study of Tsuda *et al*. has indicated that the structure of the conduit, and particularly the ratio of alveolar to central duct volume (V_a/V_d) has a significant effect on axial dispersion in alveolated ducts [93]. Both theoretical and experimental studies showed that the effective diffusivity or dispersion coefficient (D) (measured by combined mass spectrometry and application of a generalized Fick's law) in alveolated channels was profoundly smaller than the molecular diffusivity of the tracer gas for small Peclet numbers (Pe), while for large Peclet, D was appreciably greater than the Taylor [50]-Aris [94] result for flow enhanced dispersion in straight tube non-alveolated parallel plates [92,93]. Verbanck and Paiva also predicted D to be smaller than D_B (Eq. 4) in the limit of small Pe ($Pe<<1$) and argued that this reduction is strongly dependent on the ratio of alveolar to central duct volume [95]. This phenomenon is explained by Tsuda *et al*. [93] by considering that in the alveolated channel, lateral diffusion guides tracer molecules toward the dead end pockets (alveoli) and once they enter an alveolus they will have a prolonged residence time. There is limited axial dispersion of tracer in the alveolus; thus, the overall rate of axial dispersion is reduced compared to purely molecular diffusion [93]. The residence time of a tracer in the alveolus and the size of the alveolar opening both alter the rate of the explained dispersion reduction, so that increasing the ratio of alveolar to central duct volume (V_a/V_d) for a fixed opening decreases the axial dispersion.

Combined effects of irreversibility of alveolar flow (convective mixing) and a stretched and folded pattern of streamlines have been suggested as the mechanisms that lead to a sudden increase in lung mixing [96]. Convective mixing in the context of aerosol dispersion has a similar meaning to what has been explained previously for the gas and refers to the irreversible transfer of particles between inhaled and resident air. Such transfer is speculated to be a result of several factors such as velocity patterns, airway and alveolar geometries, asymmetries between inspiratory and expiratory flow, nonhomogeneous ventilation of the lungs, and cardiogenic mixing [96]. Complex stretched and folded patterns of streamlines have been first observed during experiments at very low Reynolds number (to exclude inertial effects) in a rat lung filled with white silicone oil and ventilated with blue silicon oil for several tidal breaths [97].

Breathing is a dynamic process and other factors related to the dynamic process of breathing such as alveolar expansion (rhythmical motion of the alveolar walls) should be considered. Time-dependent low Reynolds number flows in cyclically expanding and contracting alveolated duct structure have been modeled [65, 97-102]. It has been demonstrated that the fluid path lines in the acinus are highly complex. Such complex flow patterns result in chaotic trajectories and are in contradiction to past investigated flow patterns in rigid wall acinus models that resulted in periodic fluid path lines repeated with every breathing cycle [56,59,60]. These findings suggest that neglecting alveolar expansion and contraction may cause underestimation of fine aerosol deposition inside the alveolus [64].

Haber *et al*., have performed a mechanistic analysis to clarify the physics of gravitational sedimentation coupled with particle convection in the chaotic, complex alveolar flow in rhythmically expanding and contracting alveoli, which

is fundamentally different from steady, Poiseuille flow applied in many previous studies [64]. The model was a simplified alveolar duct model including a rigid axisymmetric duct surrounded by toroidal pockets that opened to a central thoroughfare [64]. The simulations were done for flow rates in the range of 10^{-6}-10^{-1} cm^3/s and the particles were 1-10 μm in diameter. The flow field in the acinus has been characterized numerically and trajectories of micrometer sized particles for which gravitational settlings are important were studied [60]. At lower flow rates, gravity dominated deposition and the deposition process in alveolated duct was far more complex that the nonalveolated duct. Gravitational deposition in alveolated ducts was shown to be strongly dependent on the combined effects of the curvature of gas streamline and the duct orientation relative to gravity [60]. The most interesting finding was that for the medium range of flow rates in that study, inertial impaction also played a significant role in deposition simultaneously with gravitational settling, and particle inertia suppressed deposition substantially compared with the case of gravity alone. This finding was in contradiction to the assumption that the effects of these two transport phenomena are additive [64]. Consequently, due to the gravity-inertia interaction, a higher number of particles can reach the deeper zone in the lung periphery than the number predicted by the classic straight pipe model. At higher flow rates, inertial impaction has even been observed at the acinar level because of the curved nature of the streamlines. The deposition rate has been underestimated by considering straight pipe models at these high flow rates.

One of the findings of Haber *et al.* [64] is that alveolar flow can be approximated as a creeping (inertialess) flow, because the Reynolds number of airflow in the acinus is generally much smaller than unity. This finding led Haber *et al.* to conclude that another parameter more appropriate than the Reynolds number must be introduced to characterize the inertialess alveolar flow. The previously proposed parameter of λ [64,98,100] and γ (the reciprocal of λ) which is defined as follows was suggested for characterizing the alveolar flow

$$\gamma \approx \frac{8Q_D}{Q_A}\left(\frac{R_0}{R_D}\right)^3 \tag{13}$$

where Q_D is the instantaneous volumetric ductal flow passing by the alveolus, Q_A is the instantaneous volumetric flow entering the alveolus, R_0 is the mean radius of the alveolus, and R_D is the mean radius of the acinar duct adjacent to the alveolus. Since both Q_A and Q_D are proportional to tidal volume and breathing frequency, the latter two parameters cancel out, which leaves γ solely a function of acinar tree geometry (see Appendix B in [64]).

It has been demonstrated that the alveolar flow pattern and specifically the presence of alveolar recirculation depends strongly on the value of γ that characterizes the relative strength of the axial ductal flow and the lateral alveolar entering and exiting flow. The results showed that for larger γ, corresponding to flow conditions in more proximal acinar generations, there was more chance of alveolar

recirculation flow and a larger alveolar area covered with recirculation. The presence/absence of the recirculation region determines the behavior of fine sized particles in the alveolus. The value of γ is large where ductal flow dominates the alveolar lateral flow, (e.g. in respiratory bronchioles), and a large recirculation inside the alveolus is induced by the strong ductal shear flow passing by the alveolar opening. This alveolar recirculation flow increases the number of particles entering the alveolus mouth and moving inside the alveolus and those particles move quickly to the alveolus wall, where they finally deposit. This process is most likely at γ values below 100 [64].

The combined effect of γ and particle size has also been considered. When γ is very large (>1000), deposition of submicron particles (e.g 0.5 μm) is most probable during early inspiration near the proximal side of the alveolar rim (see Fig 7 in [64]). When γ is small (e.g. γ<10), the uniform deposition of submicron particles at the bottom of the alveolus during a few breathing cycles throughout both the inspiration and the expiration periods has been predicted. These findings suggest that the detailed alveolar flow pattern, in addition to the direction and magnitude of the gravitational force, are needed to predict submicron particles deposition, whereas, for the larger particles (1 μm<d_p< 2.5 μm) the alveolar flow patterns do not significantly influence their deposition. It has also been indicated that submicron particle entrapment within the alveolus increases with increase of breathing frequency by several times with respect to normal breathing rate and there is a high probability that those entrapped particles deposit on alveolar walls [103].

Recently, a rhythmically expanding and contracting hemisphere has been modeled by a three-dimensional analytical model considering time-dependent changes of the air velocity field within the hemispherical alveolus (used in both the continuity and momentum equations) as a superposition of uniform velocity, v_{uni}, and radial velocity, v_{rad}, as follows [63]:

$$v = v_{rad}\frac{s}{s+t} + v_{uni}\frac{t}{s+t} \tag{14}$$

where v is defined as the air velocity at a point inside the alveolus, t and s are the distances of that point from the wall and the orifice (i.e. the entrance ring of hemisphere), respectively. Uniform velocity, v_{uni}, has been considered perpendicular to the 'alveolar orifice', pointed into and out of the alveolus during inhalation and exhalation, respectively, and its absolute value has been calculated as the ratio of the flow rate at the orifice to the time dependent cross section of the orifice. The radial component has been considered toward the wall during inhalation and toward the center of hemisphere during exhalation (see Fig.3 in [63]). The absolute value of radial component has been determined with the application of the continuity and mass conservation equations, considering the breathing parameters and the resulting maximum and minimum diameters, assuming that its value at the alveolus wall is equal to the velocity of the wall. Trajectories of the particles in the flow were calculated numerically including simultaneous deposition by inertial impaction, gravitational sedimentation, Brownian diffusion, and interception.

Alveolar deposition is obtained by multiplying entrance probabilities by the calculated deposition and the number of alveoli. Despite, the benefit of this model for simplifying the calculation of the flow field in the most peripherally located alveoli close to the alveolar sacs, the assumption of a uniform flow field in this model makes it unacceptable for more centrally located respiratory airways (i.e. those which are not fully alveolated).

Tsuda *et al*. also considered diffusional deposition in the absence of gravity for submicron particles and they found that aerosol deposition in alveolated ducts was highly uneven, with higher deposition density near the alveolar entrance. The local deposition was strongly affected by the curved streamlines that were formed due to the shape of the wall [59]. In summary, a main finding of these initial studies considering alveolated ducts is the coupling of the curved gas streamlines in the central channel of the acinus (due to the presence of side-walled alveoli) with gravity, which may enhance the guiding of the particles toward the entrance of the alveolus and cause deposition there. It is worth noting that the deposition rates in the study of Tsuda *et al*. have been related to two dimensionless parameters: Sherwood number (*Sh*), which can be thought of as the dimensionless ratio of a diffusional time scale to a deposition time scale, and Graetz number (*Gz*), which can be considered as the dimensionless ratio of a convectional time scale to the diffusional timescale [59,104].

Similar alveolated duct computer models solving a convection-diffusion equation both in one-dimension [42] and multi-dimensions (2D and 3D) have presented similar findings. They have demonstrated heterogeneous deposition in the acinar region, with more deposition along the alveolar walls and higher deposition density near the alveolar entrance ring. Particle trajectories depend on the particle size and the local flow field [56].

Since acinar airway bifurcations may have an effect on flow structure and consequently on local deposition, Darquenne *et al*. have extended the work of Tsuda *et al*. for the diffusional range by considering a branching structure instead of a single duct. The branching structure instead of a single duct leads to a difference in the particle distribution at the inlet of the daughter branches at each bifurcation [56]. Darquenne *et al*. have computed the flow pattern in the alveolated duct and they have indicated that most of the fluid elements travel in the central channel and only a small portion of the flow enters the alveoli and recirculates slowly inside them. Tsuda *et al*. have shown that the formation of recirculation zones inside the alveoli for very low Reynolds number (Re=0.01) depends on the alveolar wall shape but Darquenne *et al*. have noticed that the recirculation zones are always present for the Reynolds numbers of 0.06-0.004 considered in their study. To examine the effect of a bifurcation in the alveolar zone of the human lung, two three-dimensional models of aerosol transport and deposition were used to simulate particle trajectories in generations 18-22 of the lung in different orientations with respect to gravity [61]. The results reveal the importance of modeling the bifurcation due to the relative contribution of aerodynamic drag and gravitational sedimentation within the bifurcation zone and indicate that deposition would typically be overestimated in a model without the bifurcation compared to the one with bifurcation.

Physiological impacts of such localized deposition patterns within the alveolus e.g. the preferential deposition of submicron particles near the entrance rings of the alveoli when γ is large, may result in damage to the respiratory system. This is because some components, such as stress fibers and smooth muscle, which are important role players for maintaining the structure and dynamics of the lung parenchyma, are located at the alveolar entrance rings [64].

2.5 Semi-empirical Models Including Recent Understandings of Transport in Acinus

Although numerical and computational (CFD) models enhance our understanding of airflow patterns and deposition of particles, they may be too computationally intensive for analysis of the flow in many bifurcations, breathing cycles, and overall dispersion [7]. Instead, semi-empirical models incorporating dispersion have been developed by Wexler and Park both for single [105] and multiple breath [106] aerosol transport and deposition.

In those models it has been assumed that the major cause of aerosol dispersion is the difference between inhalation and exhalation profile, as presented by Scherer and Haselton [16], combined with secondary motion intensity as a function of lung depth characterized by local geometry and flow characteristics. Free parameters in this model, which considers both convective flow in the lumen and mixing at bifurcations, are adjusted to match the dispersion measurements (e.g. standard deviation, mode shift (MS), and skewness) of Brand et al. [75]. Quasi-steady flow was suggested in most of the lung regions because Womersley number (α) and flow amplitude decreases rapidly after the first seven generations [3, 107]. Local axial transport of particles as a function of radial position, *r*, has been defined by the following profile whose bluntness depends on the variable *n*:

$$v(r,z,t) = \left(\frac{n+2}{n}\right).\frac{Q(t)}{A(z)}.\left[1-\left(\frac{r}{R}\right)^{n}\right] \tag{15}$$

The local lumen radius is *R*, *Q(t)* is the volume flow rate and *A(z)* is the lumen cross sectional area at the lung depth, *Z*. In Eq.15 the value of n=2 represents the parabolic profile which is the characteristic of well developed laminar flow, while n>2 represents average transport profiles that are blunter than parabolic and n<2 characterizes sharper transport profiles.

The volumetric lung depth of the aerosol bolus as a function of radial position could be calculated by integrating *A(z)* over *z*, considering the velocity profile that is given in Eq.15. The volumetric lung depth after inhalation and during exhalation are given in Eqs. 16,17 , respectively, as follows:

$$V_{in}^{proximal}(r) = \frac{n_{in}+2}{n_{in}}.TV.\left[1-\left(\frac{r}{R}\right)^{n_{in}}\right] \tag{16}$$

$$V_{ex}(r) = V_{in}(r) - \frac{n_{ex}+2}{n_{ex}}.EV.\left[1-\left(\frac{r}{R}\right)^{n_{ex}}\right] \tag{17}$$

Where *TV* is the inhaled (tidal) volume, *EV*=*Qt* is the exhaled volume, *t* is time during the exhalation, and n_{in} and n_{ex} are the exponents that have been defined for describing the average effective inspiratory and expiratory particle transport profiles, respectively.

A narrow bolus volume of 20 ml upon inhalation has been considered to be consistent with the experiments of Brand *et al.*[75]. After calculation of $V_{in}^{proximal}$ in Eq.16 V_{in}^{distal} has been calculated by the addition of 20 ml to the volumetric position of the proximal edge $V_{in}^{proximal}$. To consider for the deposition in extrathoracic region, the equation of Cheng has been used for oral airway deposition in adults as a function of Stokes number (similar for inspiration and expiration) [108]. In addition, empirical equations that have been developed to predict particle loss in the tracheobronchial and pulmonary region due to three mechanisms of impaction [109,110], diffusion [111] and sedimentation [89] have been applied for the prediction of deposition in each generation.

In order to consider enhanced deposition due to secondary flow, the cumulative mixing intensity (CMI_i) (which adds in the secondary motions that particles experience during exhalation), is calculated as the integral of local mixing intensity (LMI_i) (which itself is expressed as the product of local effective volume (LEV_i) and the Reynolds number), from its deepest volumetric lung depth to the mouth (see Eq. 11 in [105]). This is because two factors, LEV_i and the Dean number, at a given volumetric lung depth, influence the magnitude of the secondary motion, significantly. The local effective volume is defined as the volume occupied by the quadruple vortices (due to secondary flows) at each generation and is given as follows:

$$LEV_i = N_i \frac{\pi}{4} d_i^3 \tag{18}$$

where N_i is the number of branches and d_i is the average lumen diameter at generation *i*. The eddies swirl in *LEV* at each bifurcation during exhalation and their magnitude is characterized via the Dean number, which is a dimensionless number for characterizing secondary flow in curved channels and is defined as follows at each generation *i*:

$$De_i = \left(\frac{u_i d_i}{\upsilon}\right)\left(\frac{L_i}{2R_{c,i}}\right)^{0.5} = \mathrm{Re}_i\left(\frac{L_i}{2R_{c,i}}\right)^{0.5} \tag{19}$$

where u_i is local flow velocity, L_i is the airway length, $R_{c,i}$ is the airway radius of curvature, and υ is the kinematic viscosity of the fluid. Dean number is proportional to *Re*, thus, local mixing intensity can be characterized as the product of local effective volume and Reynolds.

A function (See Eq. 13 in [105]) that contains the sum of the differences between all the bolus descriptors (i.e. STD, MS, and skewness) that have been measured by Brand *et al.*[75], and the predicted results using Wexler *et al.*'s equations at eight mean penetration volumes (20-800 ml) has been minimized by adjusting the three model parameters (n_{in}, n_{ex}, and S). S is a scaling factor that is represented in the parameter CMI_i (cumulative mixing intensity) and can be identified by considering the measured range of mixing intensities at each lung depth. By following this procedure Wexler *et al.* suggested n_{in}=1.7, and n_{ex}=5 for the particle transport exponents and S=0.01 for the scaling factor of CMI_i.

The inspiratory particle transport profile with n_{in}=1.7 is slightly sharper than a laminar velocity profile, which indicates that during inhalation the secondary motions are weak, and the streaming is large (larger than for a parabolic profile: n=2). In addition, the effective expiratory particle transport profile is found to be different from plug flow (where n_{ex}=∞); thus, the assumption of complete radial mixing over the lumen, assumed in some previous bolus dispersion models, is incorrect [112,113]. As a result of this difference between inspiratory and expiratory profile the bolus is stretched and its tip reaches a volumetric depth more than twice the inhaled volume. This suggests that particles can penetrate deeper to distal volumes in the lung than the inhaled volume would suggest.

Acknowledging the fact that on a single breath inhaled particles rarely travel to the pulmonary region, subsequent breaths should be considered to estimate aerosol dispersion and deposition in the lung. Wexler *et al.* have developed a semi-empirical model for simulating aerosol transport and deposition for multiple-breaths [106]. Simulations showed that the rate of concentration increase of the retained particles decreases with each breaths and the concentration is in an approximately steady-state condition after 8 breaths [106]. They found only a slight increase in the pulmonary deposition of ultrafine and 1-10 μm particles during multi-breaths compared to the deposition during single breath because a large fraction of those particles deposit during early breaths and only a few of them remain in the retained air. In contrast, multi-breath pulmonary deposition of fine particles (0.1-1 μm) is about two times higher than that of single breath simulation. This can be explained by recalling that the deposition of fine particles due to the combination of the three deposition mechanisms is the lowest (being in the transitional range), so that retained fractions at the end of exhalation are significantly higher (14-32%) and these high fractions of retained particles should be considered by multi-breaths models [114].

2.6 Hygroscopic (Unstable) Aerosols

In the context of aerosol dispersion, it is worth mentioning that hygroscopic (unstable) aerosols may undergo growth and evaporation on their path through the lung. The physicochemical characteristics of a hygroscopic particle, such as its size, shape, density, and composition may change significantly as a result of water vapor evaporation or condensation [115]. Due to such time dependent changes, many models available for predicting stable (nonhygroscopic) particles cannot be used directly. An alternative approach has been suggested whereby available hygroscopic models [116-118] are used to track the size and density change of a bolus of hygroscopic particles through the nasal pathways [115,119] and different generations of an ideal symmetric lung geometry, so that stable particle deposition models can be applied considering the size of the bolus calculated within each generation.

However, it has been pointed out that the possible effect of the particles on the fluid surrounding the particles should be considered [120-124]. Thus, the heat and mass transfer equations should be treated as two-way coupled in a sense that the water vapor content and the temperature of the continuous fluid can change due to hygroscopic growth and shrinkage of the particles and this in turn affects the rate of heat and mass transfer from the droplet surface [118]. A one-dimensional hygroscopic model for coupling heat and mass has been presented by Finlay *et al.* [123] and recently an experimental study [125] using temperature measurements as a mean for validation of the theory showed that the plug flow model, developed by Finlay *et al.* [123], accurately predicts hygroscopic changes.

In addition it is worth noting that Longest and Xi [126] found that relative humidity conditions above 100% are possible in the upper respiratory tract during inhalation of warm or hot saturated airstream, where for instance for the case of inhalation of warm saturated air at 3 ^{o}C above body temperature, 200 and 400 nm particles in diameter, may grow to above 3 μm near the trachea inlet [126].

It should be considered that the majority of the discussed models are developed for symmetric and ideal lung geometry. However, a model for hygroscopic particle deposition applied both for symmetric and asymmetric lung geometries showed that for lung deposition (tracheobronchial and pulmonary region), the deposition data obtained by application of the symmetric geometries are reasonable and are recommended when computation time is an issue [127].

Finally, for the evaporation of a multi-component aerosol in the upper respiratory airways semi-empirical correlations have been developed that are capable of identifying different compounds for a range of volatilities [128]. The variation of the gas phase specific heat affects the evaporation of the multi-component aerosols significantly, and further studies are warranted in this area.

2.7 Diseased Lungs

Recently, the area of modeling regional deposition in diseased lungs has received more attention based on knowledge obtained from imaging, the data of which

reveals less homogenous deposition patterns in diseased lungs compared to the healthy ones [129,130]. Regional deposition in diseased lungs depends on the distribution of disease, which can be quite different from subject to subject [131]. In addition to intersubject variability, intrasubject variability in an individual (change of disease distribution with time at different stages of disease) should also be considered. Indeed, the geometry of the lung is subject-dependent, and it is not easy to provide a detailed three-dimensional geometry of diseased lungs, so that modeling deposition in diseased lungs at a precise level is challenging.

There have been several attempts to model deposition in diseased lungs, based on increased airway resistance due to possible obstruction in airways [132-137]. Among others, Weibel's symmetric lung morphology was used by Brown and Bennett [136], who altered airway diameter in each generation based on measured lung volume, assuming that deviations in regional ventilation of CF patients from values measured for healthy subjects were a result of regional resistance due to the effect of disease on lumen reduction. Two findings of clinical studies have served as the basis for the model of Brown and Bennett; first, pulmonary impairment begins in the small airways and progresses proximally, and second, the apex is more severely affected than the base of the lung [129,138]. Their model suggested enhanced particle deposition in large airways of apical regions and to a lesser extent in the basal lung in the tracheobronchial region of the CF lung, whereas, in the pulmonary region, increased deposition in basal regions was noticed while there was decreased or absent deposition in the apical lung; conversely, particle deposition in the TB airways of healthy subjects was directly related to the level of ventilation [129].

Both breathing patterns and airway morphology are different in asthmatic patients compared to healthy subjects; thus, a quantitative assessment of the data available on pulmonary function tests (PFT), breathing parameters, and airway resistance has been utilized to adjust a one-dimensional Eulerian deposition model for asthmatic subjects [137]. The results suggest an increase in deposition using asthmatic airway diameters relative to the healthy case for the range of tested parameters, which has been considered a large increase compared to the intersubject variability of the healthy case. Computational fluid and particle dynamics techniques also suggest increased deposition due to airway constrictions [139].

To simplify the modeling, a symmetric morphology and homogeneous ventilation have been considered by Robinson *et al.*, among others. This assumption has been justified based on several studies that have suggested good predictions from such a symmetrical model [42,43]. The suitability of simplified symmetric lung models for sufficiently accurate prediction of particle deposition is not conclusive and some researchers consider the effect of morphology of the lung on ventilation distribution [140-142], and intersubject variability by the application of stochastic models [143,144] for estimating particle deposition in the lung. In addition, it has been suggested that the asymmetric flow splitting and the complex geometry of the asymmetrical tracheobronchial model lead to a heterogeneous particle deposition with hot spots of deposition mainly at carinal ridges [145]. Recently, Hofmann *et al.*, have also indicated the importance of variability and asymmetry of the branching airways on enhancing the effect of flow irreversibility and the

resulting dispersion of the inhaled aerosol bolus, with the application of a semi-empirical stochastic model [146].

Despite all the uncertainties in determining realistic lung morphologies, regional deposition can be partially optimized by controlling the size of inhaled particles and the inhalation pattern. An *in vivo* study using a single-breath regional deposition technique, in which the concentration profile during inhalation and exhalation of non-radioactive, monodisperse test particles was measured at different inhalation flow rates, suggests that maximum peripheral deposition (about 60%) occurs when 2-3 μm particles are inhaled with airflow rates of 250-500 cm^3/sec [147]. Controlled, slow breathing pattern (<200 cm^3/sec) has been suggested to decrease intersubject variability in total lung deposition for a given dose between healthy subjects and CF patients with impaired lung function and airway obstruction [148].

3 Summary

Recent research has improved our understanding of gas and aerosol transport in lung and this understanding has allowed improvements in models for predicting the behaviour of aerosols in the lung. While correlations can be used to successfully predict extrathoracic and total lung deposition [7], localized regional deposition within the lung requires detailed understanding of the fluid motion that has only recently begun to be well understood, particularly in terms of its effects on dispersion of aerosol boluses. While considerable progress has been made recently in this regard, as has been discussed herein, the complexity of the lung geometry and its variation between individuals, between disease states, and with age allows room for much future research.

References

1. Oberdorster, G.: Pulmonary effects of inhaled ultrafine particles. International Archives of Occupational and Environmental Health 74, 1–8 (2001)
2. Chang, H.K.: Convection, diffusion and their interaction in the bronchial tree. Advances in Experimental Medicine and Biology 227, 39–52 (1988)
3. Grotberg, J.B.: Respiratory Fluid Mechanics and Transport Processes. Annual Review of Biomedical Engineering 3, 421–457 (2001)
4. Grotberg, J.B.: Pulmonary flow and transport phenomena. Annual Review of Fluid Mechanics 26, 529–571 (1994)
5. Ultman, J.S.: Gas transport in the conducting airways. In: Engel, L.A., Paiva, M. (eds.) Gas Mixing and Distribution in the Lung. Lung Biology in Health and Disease Series, vol. 25, pp. 63–136. M. Dekker, New York (1985)
6. Pedley, T.J.: Pulmonary fluid dynamics. Annual Review of Fluid Mechanics 9, 229–274 (1977)
7. Finlay, W.H., Martin, A.R.: Recent advances in predictive understanding of respiratory tract deposition. Journal of Aerosol Medicine 21, 1–17 (2008)

8. Heyder, J., Balnchard, J.D., Feldman, H.A., Brain, J.D.: Convective mixing in human respiratory tract: estimated with aerosol boli. Journal of Applied Physiology 64, 1273–1278 (1988)
9. Finlay, W.H.: The Mechanics of Inhaled Pharmaceutical Aerosols: An Introduction. Academic Press, London (2001)
10. Fresconi, F.E., Prasad, A.K.: Convective dispersion during steady flow in the conducting airways of the human lung. Journal of Biomechanical Engineering 130, 011015, 1–9 (2008)
11. Zhao, Y., Lieber, B.B.: Steady inspiratory flow in a model symmetric bifurcation. Transactions of the ASME 116, 488–496 (1994)
12. Zhao, Y., Lieber, B.B.: Steady expiratory flow in a model symmetric bifurcation. Transactions of the ASME 116, 318–323 (1994)
13. Zhao, Y., Brunskill, C.T., Lieber, B.B.: Inspiratory and expiratory steady flow analysis in a model symmetrically bifurcating airway. Transactions of the ASME 119, 52–58 (1997)
14. Scherer, P.W., Haselton, F.R.: Bronchial bifurcations and respiratory mass transport. Science 208, 69–71 (1980)
15. Schroter, R.C., Sudlow, M.F.: Flow patterns in models of the human bronchial airways. Respiration Physiology 7, 341–355 (1969)
16. Scherer, P.W., Haselton, F.R.: Convective exchange in oscillatory flow through bronchial-tree models. Journal of Applied Physiology 53, 1023–1033 (1982)
17. Thomson, M.L., Short, M.D.: Mucociliary function in health, chronic obstructive airway disease, and asbestosis. Journal of Applied Physiology 26, 535–539 (1969)
18. Horsfield, K., Davies, A., Mills, C., Cumming, G.: Effect of flow oscillations on the stationary concentration front in a hollow cast of the airways. Lung 157, 103–111 (1980)
19. West, J.B., Hugh-Jones, P.: Pulsatile gas flow in bronchi caused by the heart beat. Journal of Applied Physiology 16, 697–702 (1961)
20. Fukuchi, Y., Roussos, C.S., Macklem, P.T., Engel, L.A.: Convection, diffusion and cardiogenic mixing of inspired gas in the lung: an experimental approach. Respiratory Physiology 26, 77–90 (1976)
21. Burwen, D.R., Watson, J., Brown, R., Josa, M., Slutsky, A.S.: Effect of cardiogenic oscillations on gas mixing during tracheal insufflation of oxygen. Journal of Applied Physiology 60, 965–971 (1986)
22. Cybulsky, I.J., Abel, J.G., Menon, A.S., Salerno, T.A., Lichtenstein, S.V., Slutsky, A.S.: Contribution of cardiogenic oscillations to gas exchange in constant-flow ventilation. Journal of Applied Physiology 63, 564–570 (1987)
23. Engel, L.A.: Gas mixing within the acinus of the lung. Journal of Applied Physiology 54, 609–618 (1983)
24. Engel, L.A., Menkes, H., Wood, L.D.H., Utz, G., Joubert, J., Macklem, P.T.: Gas mixing during breath holding studied by intrapulmonary gas sampling. Journal of Applied Physiology 35(1), 9–17 (1973)
25. Engel, L.A., Wood, L.D.H., Utz, G., Macklem, P.T.: Gas mixing during inspiration. Journal of Applied Physiology 35, 18–24 (1973)
26. Fukuchi, Y., Cosio, M., Kelly, S., Engel, L.A.: Influence of pericardial fluid on cardiogenic gas mixing in the lung. Journal of Applied Physiology 42, 5–12 (1977)
27. Horsfield, K., Gabe, I., Mills, C., Buckman, M., Cumming, G.: Effect of heart rate and stroke volume on gas mixing in dog lung. Journal of Applied Physiology 53, 1603–1607 (1982)

28. Ingenito, E., Kamm, R.D., Watson, J.W., Slutsky, A.S.: A model of constant flow ventilation in a dog lung. Journal of Applied Physiology 64, 2150–2159 (1985)
29. Sikand, R.S., Magnussen, H., Scheid, P., Piiper, J.: Convective and diffusive gas mixing in human lungs: experiments and model analysis. Journal of Applied Physiology 40, 362–371 (1976)
30. Slutsky, A.S.: Gas mixing by cardiogenic oscillations: a theoretical quantitative analysis. Journal of Applied Physiology 51, 1287–1293 (1981)
31. Slutsky, A.S., Khoo, M.C.K., Brown, R.: Simulation of gas transport due to cardiogenic oscillations. Journal of Applied Physiology 58, 1331–1339 (1985)
32. Wei, J.H., Hoffman, E.A., Ritman, E.L., Wood, E.H.: Cardiogenic motion of right lung parenchyma in anesthetized intact dogs. Journal of Applied Physiology 58, 384–391 (1985)
33. Mackenzie, C.F., Skacel, M., Barnas, G.M., Brampton, W.J., Alana, C.A.: Effects of cardiac oscillations and lung volume on acinar gas mixing during apnea. Journal of Applied Physiology 68, 2013–2018 (1990)
34. Fowler, W.S.: Lung function studies. II. The respiratory dead space. The American Journal of Physiology 154, 405–416 (1948)
35. Bidani, A., Flumerfelt, R.W., Crandall, E.D.: Analysis of the effects of pulsatile capillary blood flow and volume on gas exchange. Respiration Physiology 35, 27–42 (1978)
36. Hauge, A., Nicolaysen, G.: Pulmonary O_2 transfer during pulsatile and non- pulsatile perfusion (Abstract). Acta Physiologica Scandinavica 109, 325–332 (1980)
37. Paiva, M., Engel, L.A.: Theoretical studies of gas mixing and ventilation distribution in the lung. Physiological Reviews 67, 750–796 (1987)
38. Taulbee, D.B., Yu, C.P.: A theory of aerosol deposition in the human respiratory tract. Journal of Applied Physiology 38, 77–85 (1975)
39. Paiva, M.: Computation of the boundary conditions for diffusion in the human lung. Computers and biomedical research 5, 585–595 (1972)
40. Scherer, P.W., Shendalman, L.H., Greene, N.M.: Simultaneous diffusion and convection in single breath lung washout. Bulletin of mathematical biophysics 34, 393–412 (1972)
41. Weibel, E.R.: Morphology of the lung. Academic Press, London (1963)
42. Darquenne, C., Paiva, M.: One-dimensional simulation of aerosol transport and deposition in the human lung. Journal of applied Physiology 77, 2889–2898 (1994)
43. Yu, C.P., Diu, C.K.: A comparative study of aerosol deposition in different lung models. American Industrial Hygiene Association Journal 43, 54–65 (1982)
44. Scherer, P.W., Shendalman, L.H., Greene, N.M., Bouhuys, A.: Measurement of axial diffusivities in a model of the bronchial airways. Journal of applied Physiology 38, 719–723 (1975)
45. Asgharian, B., Price, O.T.: Deposition of ultrafine (NANO) particles in the human lung. Inhalation Toxicology 19, 1045–1054 (2007)
46. Lee, J.W., Lee, D.Y., Kim, W.S.: Dispersion of an aerosol bolus in a double bifurcation. Journal of Aerosol Science 31, 491–505 (2000)
47. Lee, D.Y., Lee, J.W.: Dispersion during exhalation of aerosol bolus in a double bifurcation. Journal of Aerosol Science 32, 805–815 (2001)
48. Schulz, H., Heilmann, P., Hillebrecht, A., Gebhart, J., Meyer, M., Piiper, J., Heyder, J.: Convective ad diffusive gas transport in canine intrapulmonary airways. Journal of Applied Physiology 72, 1557–1562 (1992)

49. Yu, C.P.: On equation of gas transport in the lung. Respiration Physiology 23, 257–266 (1975)
50. Taylor, G.I.: Dispersion of soluble matter in solvent flowing slowly through a tube. Proceedings of the Royal Society of London Series A 219, 186–203 (1953)
51. Taylor, G.I.: Conditions under which dispersion of a solute in a stream of solvent can be used to measure molecular diffusion. Proceedings of the Royal Society of London Series A 225, 473–477 (1954)
52. Heyder, J., Gebhart, J., Rudolf, G., Schiller, C.F., Stalhofen, W.: Deposition of particles in the human respiratory tract in the size range 0.005-15 micron. Journal of Aerosol Science 17, 811–825 (1986)
53. Darquenne, C.: A realistic two-dimensional model of aerosol transport and deposition in the alveolar zone of the human lung. Journal of Aerosol Science 32, 1161–1174 (2001)
54. Darquenne, C.: Heterogeneity of aerosol deposition in a two-dimensional model of human alveolated ducts. Journal of Aerosol Science 33, 1261–1278 (2002)
55. Darquenne, C., Prisk, G.K.: Effect of gravitational sedimentation on simulated aerosol dispersion in the human acinus. Journal of Aerosol Science 34, 405–418 (2003)
56. Darquenne, C., Paiva, M.: Two- and three-dimensional simulations of aerosol transport and deposition in alveolar zone of human lung. Journal of applied Physiology 80, 1401–1414 (1996)
57. Henry, F., Butler, J., Tsuda, A.: Kinematically irreversible acinar flow: A departure from classical dispersive aerosol transport theories. Journal of Applied Physiology 92, 835–845 (2002)
58. Lee, D., Lee, J.: Characteristics of particle transport in an expanding or contracting alveolated tube. Journal of Aerosol Science 34, 1193–1215 (2003)
59. Tsuda, A., Butler, J.P., Fredberg, J.J.: Effects of alveolated duct structure on aerosol kinetics I. Diffusional deposition in the absence of gravity. Journal of Applied Physiology 76, 2497–2509 (1994)
60. Tsuda, A., Butler, J.P., Fredberg, J.J.: Effects of alveolated duct structure on aerosol kinetics. II. Gravitational sedimentation and inertial impaction. Journal of Applied Physiology 76, 2410–2516 (1994)
61. Harrington, L., Prisk, G.K., Darquenne, C.: Importance of the bifurcation zone and branch orientation in simulated aerosol deposition in the alveolar zone of the human lung. Journal of Aerosol Science 37, 37–62 (2006)
62. Haber, S., Tsuda, A.: The effect of flow generated by a rhythmically expanding pulmonary acinus on aerosol dynamics. Journal of Aerosol Science 29, 309–322 (1998)
63. Balashazy, I., Hofmann, W., Farkas, A., Madas, B.G.: Three-dimensional model for aerosol transport and deposition in expanding and contracting alveoli. Inhalation Toxicology 20, 611–621 (2008)
64. Haber, S., Yitzhak, D., Tsuda, A.: Gravitational deposition in a rhythmically expanding and contracting alveolus. Journal of Applied Physiology 95, 657–671 (2003)
65. Haber, S., Butler, J.P., Brenner, H., Emanuel, I., Tsuda, A.: Shear flow over a self-similar expanding pulmonary alveolus during rhythmical breathing. Journal of Fluid Mechanics 405, 243–268 (2000)
66. Altshuler, B., Palmes, E.D., Yarmus, L., Nelson, N.: Intrapulmonary mixing of gases studied with aerosols. Journal of Applied Physiology 14, 321–327 (1959)
67. Heyder, J., Davies, C.N.: The breathing of half micron aerosols. III. Dispersion of particles in the respiratory tract. Journal of Aerosol Science 2, 437–452 (1971)

68. Muir, D.C.F.: Distribution of aerosol particles in expired air. Journal of Applied Physiology 23, 210–214 (1967)
69. Taulbee, D.B., Yu, C.P., Heyder, J.: Aerosol transport in the human lung from analysis of single breaths. Journal of Applied Physiology 44, 803–812 (1978)
70. Heyder, J., Blanchard, J.D., Feldman, H.A., Brain, J.D.: Convective mixing in human respiratory tract: estimates with aerosol boli. Journal of applied physiology 64, 1273–1278 (1988)
71. Anderson, P.J., Blanchard, J.D., Brain, J.D., Feldman, H.A., McNamara, J.J., Heyder, J.J.: Effect of cystic fibrosis on inhaled aerosol boluses. The American Review of Respiratory Disease 140, 1317–1324 (1989)
72. Hughes, J.M.B., Amis, T.C.: Regional ventilation distribution. In: Engel, L.A., Paiva, M. (eds.) Gas Mixing and Distribution in the Lung. Lung Biology in Health and Disease Series, vol. 25, pp. 177–220. M. Dekker, New York (1995)
73. Woolcock, A.J., Vincent, N.J., Macklem, P.T.: Frequency dependence of compliance as a test for obstruction in the small airways. The Journal of Clinical Investigation 48, 1097–1106 (1969)
74. Banerjee, M., Evans, J.N., Jaeger, M.J.: Uneven ventilation in smokers. Respiration Physiology 27, 277–291 (1976)
75. Brand, P., Rieger, C., Schulz, H., Beinert, T., Heyder, J.: Aerosol bolus dispersion in healthy subjects. The European Respiratory Journal 10, 460–467 (1997)
76. Gebhart, J., Heigwer, G., Heyder, J., Roth, C., Stahlhofen, W.: The use of light-scattering photometry in aerosol medicine. Journal of Aerosol Medicine 1, 89–112 (1988)
77. Rosenthal, F.S.: Aerosol deposition and dispersion characterize lung injury in a canine model of emphysema. Journal of Applied Physiology 78, 1585–1595 (1995)
78. Keefe, M.J., Bennett, W.D., Dewitt, P., Seal, E., Strong, A., Gerrity, T.: The effect of ozone exposure on the dispersion of inhaled aerosol boluses in healthy human subjects. The American Review of Respiratory Disease 144, 23–30 (1991)
79. Brand, P., App, E.M., Meyer, T.: Aerosol bolus dispersion in patients with bronchiolitis obliterans after heart-lung and double-lung transplantation. Journal of Aerosol Medicine 11, 41–53 (1998)
80. Brand, P., Rieger, C., Beinert, T., Heyder, J.: Aerosol derived airway morphometry in healthy subjects. European Respiratory Journal 8, 1639–1646 (1995)
81. Schulz, H., Schulz, A., Brand, P., Tuch, T., von Mutius, E., Erdl, R., Reinhardt, D., Heyder, J.: Aerosol bolus dispersion and effective airway diameters in mildly asthmatic children. European Respiratory Journal 8, 566–573 (1995)
82. Lehnigk, B., Schleiss, M., Brand, P., Heyder, J., Magnussen, H., Jorres, R.A.: Aerosol-derived airway morphometry (ADAM) in patients with lung emphysema diagnosed by computed tomography-reproducibility, diagnostic information, and modeling. European Journal of Medical Research 12, 74–83 (2007)
83. Brown, J.S., Gerrity, T.R., Bennett, W.D., Kim, C.S., House, D.E.: Dispersion of aerosol boluses in the human lung: dependence on lung volume, bolus volume, and gender. Journal of Applied Physiology 79, 1787–1795 (1995)
84. Schulz, A., Tuch, T., Brand, P., Schulz, H., Erdl, R., von Mutius, E., Reinhardt, D., Heyder, J.: Aerosol bolus dispersion in the respiratory tract of children. Experimental Lung Research 20, 119–130 (1994)
85. Schulz, H., Eder, G., Heyder, J.: Lung volume is a determinant of aerosol bolus dispersion. Journal of Aerosol Medicine 16, 255–262 (2003)

86. Zeltner, T.B., Sweeney, T.D., Skornik, W.A., Feldman, H.A., Brain, J.D.: Retention and clearance of 0.9 micron particles inhaled by hamsters during rest or exercise. Journal of Applied Physiology 70, 1137–1145 (1991)
87. Brain, J.D., Valberg, P.A.: Deposition of aerosol in the respiratory tract. The American Review of the Respiratory Disease 120, 1325–1373 (1979)
88. Fuch, N.A.: The mechanics of aerosols. Pergamon Press, Oxford (1964)
89. Pich, J.: Theory of gravitational deposition of particles from laminar flows in channels. Journal of Aerosol Science 3, 351–361 (1972)
90. Wang, C.S.: Gravitational deposition of particles from laminar flows in inclined channels. Journal of Aerosol Science 6, 191–204 (1975)
91. Heyder, J.: Gravitational deposition of aerosol particles within a system of randomly oriented tubes. Journal of Aerosol Science 6, 133–137 (1975)
92. Federspiel, W.J., Fredberg, J.J.: Axial dispersion in respiratory bronchioles and alveolar ducts. Journal of Applied Physiology 64, 2614–2621 (1988)
93. Tsuda, A., Federspiel, W.J., Grant Jr., P.A., Fredberg, J.J.: Axial dispersion of inert species in alveolated channels. Chemical Engineering Science 46, 1419–1426 (1991)
94. Aris, R.: On the dispersion of a solute in a fluid flowing through a tube. Proceedings of the Royal Society of London Series A 235, 67–77 (1956)
95. Verbanck, S., Paiva, M.: Effective axial diffusion in an expansile alveolar duct model. Respiratory Physiology 73, 273–278 (1988)
96. Darquenne, C., Prisk, G.K.: Effect of small flow reversals on aerosol mixing in the alveolar region of the human lung. Journal of Applied Physiology 97, 2083–2089 (2004)
97. Butler, J.P., Tsuda, A.: Effect of convective stretching and folding on aerosol mixing deep in the lung, assessed by approximate entropy. Journal of Applied Physiology 83, 800–809 (1997)
98. Henry, F.S., Butler, J.P., Tsuda, A.: Kinematically irreversible acinar flow: a departure from classical dispersive aerosol transport theories. Journal of Applied Physiology 92, 835–845 (2002)
99. Tippe, A., Tsuda, A.: Recirculating flow in an expanding alveolar model: experimental evidence of flow-induced mixing of aerosols in the pulmonary acinus. Journal of Aerosol Science 31, 979–986 (2000)
100. Tsuda, A., Henry, F.S., Butler, J.P.: Chaotic mixing of alveolated duct flow in rhythmically expanding pulmonary acinus. Journal of Applied Physiology 79, 1055–1063 (1995)
101. Tsuda, A., Otani, Y., Butler, J.P.: Acinar flow irreversibility caused by perturbations in reversible alveolar wall motion. Journal of Applied Physiology 86, 977–984 (1999)
102. Tsuda, A., Rogers, R.A., Hydon, P.E., Butler, J.P.: Chaotic mixing deep in the lung. Proceedings of the National Academy of Sciences of the United States of America 99, 10173–10178 (2002)
103. Balik, G., Reis, A.H., Aydin, M., Miguel, A.F.: Behavior of submicrometer particles in periodic alveolar airflows. European Journal of Applied Physiology 102, 677–683 (2008)
104. Rohsenow, W.M., Choi, H.: Heat, Mass, and Momentum Transfer, pp. 385, 441. Prentice-Hall, Englewood Cliffs (1961)
105. Park, S.S., Wexler, A.S.: Particle deposition in the pulmonary region of the human lung: A semi-empirical model of single breath transport and deposition. Journal of Aerosol Science 38, 228–245 (2007)

106. Park, S.S., Wexler, A.S.: Particle deposition in the pulmonary region of the human lung: Multiple breath aerosol transport and deposition. Journal of Aerosol Science 38, 509–519 (2007)
107. Ramuzat, A., Reithmuller, M.L.: PIV investigations of oscillating flows within a 3D lung multiple bifurcation model. In: 11th International Symposium on Applications of Laser Techniques to Fluid Flows, paper 19-1 (2002)
108. Cheng, Y.S.: Aerosol deposition in the extrathoracic region. Journal of Aerosol Science and Technology 37, 659–671 (2003)
109. Kim, C.S., Iglesias, A.J., Garcia, L.: Deposition of inhaled particles in bifurcating airway models: I. Inspiratory deposition. Journal of Aerosol Medicine 2, 1–14 (1989)
110. Kim, C.S., Iglesias, A.J., Garcia, L.: Deposition of inhaled particles in bifurcating airway models: I. Expiratory deposition. Journal of Aerosol Medicine 2, 15–27 (1989)
111. Ingham, D.B.: Diffusion of aerosols from a stream flowing through a cylindrical tube. Journal of Aerosol Science 6, 125–132 (1975)
112. Sarangapani, R., Wexler, A.S.: Modeling aerosol bolus dispersion in human airways. Journal of Aerosol Science 30, 1345–1362 (1999)
113. Sarangapani, R., Wexler, A.S.: The role of dispersion in particle deposition in human airways. Toxicological Sciences 54, 229–236 (2000)
114. Park, S.S., Wexler, A.S.: Size-dependent deposition of particles in the human lung at steady-state breathing. Journal of Aerosol Science 39, 266–276 (2008)
115. Schroeter, J.D., Musante, C.J., Hwang, D., Burton, R., Guilmette, R., Martonen, T.B.: Hygroscopic growth and deposition of inhaled secondary cigarette smoke in human nasal pathways. Journal of Aerosol Science and Technology 34, 137–143 (2001)
116. Persons, D.D., Hess, G.D., Muller, W.J., Scherer, P.W.: Airway deposition of hygroscopic hetrodispersed aerosols: results of a computer calculation. Journal of Applied Physiology 63, 1195 (1987)
117. Ferron, G.A., Kreyling, W.G., Haider, B.: Inhalation of salt aerosol particles-II. Growth and deposition in the human respiratory tract. Journal of Aerosol Science 19, 611–631 (1988)
118. Stapleton, K.W., Finlay, W.H., Zuberbuhler, P.: An in vitro method for determining regional dosages delivered by jet nebulizers. Journal of Aerosol Medicine 7, 325–344 (1994)
119. Kaufman, J.W., Scherer, P.W., Yang, C.G.: Predicted combustion product deposition in the human airway. Toxicology 115, 123–128 (1996)
120. Ferron, G.A., Oberdorster, G., Henneberg, R.: Estimation of the deposition of aerosolized drugs in the human respiratory tract due to hygroscopic growth. Journal of Aerosol Medicine 2, 271–282 (1989)
121. Eisner, A.D., Graham, R.C., Martonen, T.B.: Coupled mass and energy transport phenomena in aerosol/vapor-laden-gases-I. Theory of the hygroscopic aerosol effects on temperature and relative humidity patterns of inspired air. Journal of Aerosol Science 21, 833–848 (1990)
122. Graham, R.C., Eisner, A.D.: Coupled mass and energy transport phenomena in aerosol/vapor-laden gases-II. Computer modeling of water vapor/droplet interaction and entrainment. Journal of Aerosol Science 21, 849–858 (1990)
123. Finlay, W.H., Stapleton, K.W.: The effect on regional lung deposition of coupled heat and mass transfer between hygroscopic droplets and their surrounding phase. Journal of Aerosol Science 26, 655–670 (1995)

124. Broday, D.M., Georgopoulos, P.G.: Growth and deposition of hygroscopic particulate matter in the human lungs. Journal of Aerosol Science and Technology 34, 144–159 (2001)
125. Saleh, R., Shihadeh, A.: Hygroscopic growth and evaporation in an aerosol with boundary heat and mass transfer. Journal of Aerosol Science 38, 1–16 (2007)
126. Longest, P.W., Xi, J.: Condensational growth may contribute to the enhanced deposition of cigarette smoke particles in the upper respiratory tract. Journal of Aerosol Science and Technology 42, 579–602 (2008)
127. Asgharian, B.: A model of deposition of hygroscopic particles in the human lung. Journal of Aerosol Science and Technology 38, 938–947 (2004)
128. Longest, P.W., Kleinstreuer, C.: Computational models for simulating multicomponent aerosol evaporation in the upper respiratory airways. Journal of Aerosol Science and Technology 39, 124–138 (2005)
129. Brown, J.S., Zeman, K.L., Bennett, W.D.: Regional deposition of coarse particles and ventilation distribution in patients with cystic fibrosis. Journal of Aerosol Medicine 14, 443–454 (2001)
130. Kastelik, J.A., Wright, G.A., Aziz, I., Davies, M., Avery, G.R., Paddon, A.J., Howey, S., Morice, A.H.: A widely available method for the assessment of aerosol delivery in cystic fibrosis. Pulmonary Pharmacology and Therapeutics 15, 513–519 (2002)
131. Kaza, V., Katz, M.F., Cumming, S., Frost, A.E., Safdar, Z.: Correlation of chest radiograph pattern with genotype, age, and gender in adult cystic fibrosis a single center study. Chest 132, 569–574 (2007)
132. Goldberg, I.S., Lourenco, R.V.: Deposition of aerosols in pulmonary disease. Archives of Internal Medicine 131, 88–91 (1973)
133. Svartengren, M., Anderson, M., Bylin, G., Philipson, K., Camner, P.: Regional deposition of 3.6-micron particles in subjects with mild to moderately severe asthma. Journal of Aerosol Medicine 3, 197–207 (1991)
134. Martonen, T., Katz, I., Cress, W.: Aerosol deposition as a function of airway disease: cystic fibrosis. Pharmaceutical research 12, 96–102 (1995)
135. Segal, R.A., Martonen, T.B., Kim, C.S., Shearer, M.: Computer simulations of particle deposition in the lungs of chronic obstructive pulmonary disease patients. Inhalation Toxicology 14, 705–720 (2002)
136. Brown, J.S., Bennett, W.D.: Deposition of coarse particles in cystic fibrosis: model predictions versus experimental results. Journal of Aerosol Medicine 17, 239–248 (2004)
137. Robinson, R.J., Doolittle, R.L., Diflorio, J.N.: Use of asthmatic pulmonary function test data to predict lung deposition. Journal of Aerosol Medicine 20, 141–162 (2007)
138. Anderson, P.O., Sicker-Walker, R.H., Strominger, D.B., McAlister, W.H., Hill, R.L., Markham, J.: Quantitative assessment of regional ventilation and perfusion in children with cystic fibrosis. Radiology 111, 151–155 (1974)
139. Farkas, A., Balashazy, I., Szocs, K.: Characterization of regional and local deposition of inhaled aerosol drugs in the respiratory system by computational fluid and particle dynamics methods. Journal of Aerosol Medicine 19, 329–343 (2006)
140. Asgharian, B., Price, O.: Airflow distribution in the human lung and its influence on particle deposition. Inhalation Toxicology 18, 795–801 (2006)
141. Asgharian, B., Price, O.T., Hofmann, W.: Prediction of particle deposition in the human lung using realistic models of lung ventilation. Journal of Aerosol Science 37, 1209–1221 (2006)

142. Asgharian, B., Price, O., Oberdorster, G.: A modeling study of the effect of gravity on airflow distribution and particle deposition in the lung. Inhalation Toxicology 18, 473–481 (2006)
143. Goo, J., Kim, C.S.: Theoretical analysis of particle deposition in human lungs considering stochastic variations of airway morphology. Journal of Aerosol Science 34, 585–602 (2003)
144. Hofmann, W., Asgharian, B., Winkler-Heil, R.: Modeling intersubject variability of particle deposition in human lungs. Journal of Aerosol Science 33, 219–235 (2002)
145. Farkas, A., Balashazy, I.: Quantification of particle deposition in asymmetrical tracheobronchial model geometry. Computers in Biology and Medicine 38, 508–518 (2008)
146. Hofmann, W., Pawlak, E., Sturm, R.: Semi-empirical stochastic model of aerosol bolus dispersion in the human lung. Inhalation Toxicology 20, 1059–1073 (2008)
147. Brand, P., Meyer, T., Haussermann, S., Schulte, M., Scheuch, G., Bernhard, T., Sommerauer, B., Weber, N., Griese, M.: Optimum peripheral drug deposition in patients with cystic fibrosis. Journal of Aerosol Medicine 18, 45–54 (2005)
148. Brand, P., Friemel, I., Meyer, T., Schulz, H., Heyder, J., Haussinger, K.: Total deposition of therapeutic particles during spontaneous and controlled inhalations. Journal of Pharmaceutical Sciences 89, 724–731 (2000)

Mass Transfer Phenomena in Nuclear Waste Packages

F. Frizon*, S. Gin, and C. Jegou

Abstract. As part of an integrated management approach to the wasteforms arising from medical, industrial or research activities implementing radioactive materials, several countries throughout the world are considering geological disposal of long-lived intermediate- and high-level waste. An essential prerequisite is to develop a suitable waste disposition route in which waste conditioning is one of the key aspect. Conditioning is not only imposed by scientific necessities, such as the half-lives of the radioactive isotopes concerned and by their activity levels; it is also influenced by the specific approaches and developments in each country, such as the decision to reprocess the spent fuel from pressurized water reactors or to opt instead for direct disposal. Nevertheless, three mineral materials are found at the core of the strategies developed throughout the world: ceramics, comprising the fuel rods themselves, which can be destined for direct disposal with or without prior interim storage; nuclear glasses, used to condition solutions rich in minor actinides, fission products and activation products after fuel reprocessing, i.e. high-level waste; and cement materials, mainly secondary process waste, i.e. low- and intermediate-level waste. These three categories of nuclear waste conditioning materials are examined in this chapter with respect to mass transfer phenomena liable to occur in a deep geological repository. The fundamental mass transfer phenomena involved differ considerably depending on the physical and chemical properties of the materials, on the specific constraints raised by their presence in waste packages, and on the repository operating conditions — especially in a water-saturated geological environment. This section describes the principal transport phenomena involved according to the environmental conditions for each material. This systematic approach highlights the scientific issues associated with each material and identifies their particular features as the seat of mass transfer; each material is a subject of experimental investigation or specific modeling activities.

1 Introduction

Radioactive waste is produced in many countries by industrial activities including nuclear electricity production, defense programs, or medical and industrial

F. Frizon · S. Gin · C. Jegou
Commissariat à l'Énergie Atomique (CEA), Nuclear Energy Division,
Waste Treatment and Conditioning Research Department, 30207 Bagnols-sur-Cèze, France
fabien.frizon@cea.fr

* Corresponding author.

L.Q. Wang (Ed.): Advances in Transport Phenomena 2009, ADVTRANS 1, pp. 31–133.
springerlink.com

applications of radioisotopes. Rational management of radioactive wasteforms is dictated by their specific characteristics: their radiological activity, which determines the required level of protection, and their radioactive half-life, which determines the time period during which this protection must be maintained. The main objective of interim storage and disposal facilities is to isolate the waste from the biosphere until the residual activity becomes harmless for mankind and the environment. The proposed disposal concepts correspond to the waste categories considered:

- *Very low-level waste* arises mainly from dismantling nuclear facilities and will be produced in increasing quantities over the coming decades; it is destined for surface facilities.
- *Short-lived low- and intermediate-level waste* comes from the nuclear industry, research laboratories, and hospitals, and accounts for about 90% of the waste produced in France. With a half-life of less than 30 years, its activity will be comparable to the natural background radioactivity level after a few hundred years. This waste is placed in surface or subsurface interim storage facilities until its radioactivity decays to negligible levels.
- *Long-lived intermediate-level waste* represents 4% of the total activity and 9% of the waste production, while *high-level waste* contains 95% of the radioactivity but accounts for less than 1% of the total waste volume. These waste categories arise mainly from nuclear power production and from reprocessing of the spent fuel used to produce electricity. Waste containing radioactive materials with the longest half-lives must be immobilized for nearly a million years.

Long-lived intermediate- and high-level waste contains three types of radioelements: actinides, fission products, and activation products.

- Actinides are elements with atomic numbers of 89 and above. Uranium and actinium, for example, exist in nature whereas elements with higher atomic numbers than uranium are created by neutron captures that did not result in fission reactions.
- Fission products are created by the fission of heavy nuclei or by the decay of fission fragments, and include a wide range of chemical species.
- Activation products are formed mainly by neutron bombardment of the metals and alloys found in fuel assembly structural components.

Two spent fuel management strategies, which are not mutually exclusive, are considered in various countries. The first calls for direct disposal of spent fuel assemblies[1] after removal from the reactor, with or without a prior interim surface storage period. The second consists in reprocessing the fuel to separate reusable elements and to condition the remaining ultimate waste for disposal. The fuel rods are cut up and dissolved in nitric acid. Uranium and plutonium are chemically

[1] A nuclear fuel subassembly consists of a bundle of fuel rods, each comprising a Zircaloy cladding tube containing uranium oxide (UO_2) or mixed uranium and plutonium oxide ($(U\text{-}Pu)O_2$) fuel pellets.

extracted from this solution to fabricate fresh fuel. The solutions produced by reprocessing contain minor actinides together with fission and activation products; they are calcined and vitrified as primary waste packages. The structural components of the spent fuel subassemblies (containing mainly activation products) and the sludge produced by coprecipitation processes are immobilized in cement matrices as low- and intermediate-level waste.

Irrespective of the management strategies under consideration for spent fuel, long-lived intermediate- and high-level waste management will last for thousands of years. One proposed management route — which has already been adopted in some countries — is disposal in a deep geological formation. In this concept the waste is isolated from terrestrial surface phenomena and human activity over a time period consistent with their radiological half-life. It is based on the multiple-barrier principle to ensure slow release and minimal transfer of radionuclides to the biosphere. There are three principal types of barriers:

- The waste package, i.e. the waste itself, together with the material used to immobilize it, and the outer container. The container will remain leaktight for a certain period of time, after which the containment materials limit radionuclide release.
- The engineered barrier, whose structural materials maintain the package cohesion for a certain time and, to some extent, retain any radionuclides that might be released.
- A favorable site, i.e. a geological barrier between the repository and the biosphere, selected for its specific features, such as remoteness from any zones of strong seismic activity, or for strong retention in the event of radionuclide dispersal. Various types of geological host formations are being investigated throughout the world, including granite, volcanic tuff, salt, or clay.

From the moment of its construction and for a very long time thereafter, the repository will be subjected to many factors controlling both its evolution and the waste package environment. These factors can be classified into different phenomenological categories:

- Mechanical phenomena. The excavation of underground repository structures entails instantaneous changes in the natural mechanical stress patterns of the site. Its mechanical behavior then evolves during the repository operating phase and subsequently, after closure, under the effects of hydraulic processes such as desaturation and resaturation of the site, as well as chemical processes and thermal loading.
- Thermal phenomena. The installation of vitrified waste packages, spent fuel packages and, to a lesser extent, relatively non-exothermic cement-encapsulated waste packages, will progressively lead to a temperature rise within the repository and in the surrounding geological environment. Since the thermal power diminishes over time, this temperature rise is a transient phenomenon: after reaching a maximum the temperature will gradually decrease to the

ambient geothermal level. The peak temperatures should be reached between within a few decades or centuries, depending on the nature of the waste.

- Hydraulic phenomena. Excavating the repository results in a drop in the groundwater pressures during the operational phase. If the structures are ventilated by air that is not water-saturated, desaturation of the surrounding environment will also occur. Resaturation of the repository will begin after closure, and will be influenced especially by gas production arising from metal corrosion, the activity of microorganisms, and radiolysis. Water will come into contact with the high-level waste packages several thousands years after closure of the repository.
- Chemical phenomena. The arrival of exogenous materials and fluids will modify the chemical equilibria in the immediate vicinity of the repository: chemical degradation of concrete, aqueous corrosion of vitrified waste packages, dissolution of the spent fuel oxide matrix, etc. The environmental conditions responsible for the chemical modifications will vary over time, from the initial excavations to the restoration of ambient geological conditions; for example, the redox conditions will be oxidizing during the operational phase, but will become highly reductive within a decade after closure.
- Radiological phenomena related to radioactive decay as well as to radiation-induced perturbations.

Some of these factors can of course be coupled, and possible feedback effects among them cannot be disregarded. Moreover, the characteristic durations of these phenomena may depend on the particular concept selected. For example, some conditioning matrices such as glass are intrinsically highly durable: the repository conditions must therefore provide an environment ensuring the slowest possible chemical degradation of these matrices. Similarly, the mechanical durability of cement materials, for example, is highly dependent on their formulation and implementation. The work described in this document was performed with reference to the French disposal concept as applied, for the purposes of this study, to the region around the Bure underground laboratory in northern France.

Moreover, the environmental conditions of the repository containing the waste packages may vary significantly over time: water saturation, temperature, oxidation-reduction, etc. In the context of a deep geological repository, interactions between groundwater and the materials will be the principal cause of material degradation. The transport processes discussed here are therefore organized according to the presence or absence of water in contact with the waste package and material exchanges between the waste package and the external environment. Transport phenomena are first described for an unsaturated system in moist atmosphere in an open or closed system representative of the interim storage, operating or reversible disposal phases, then for a water-saturated system representative of the final state after closure and resaturation of the geological site (Figure 1).

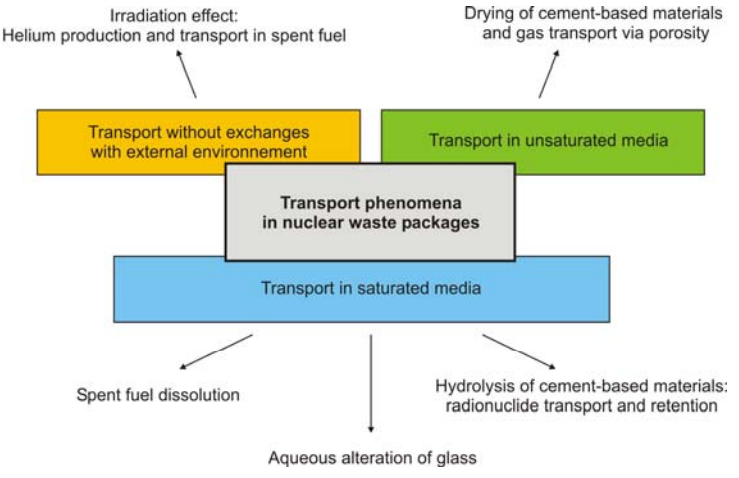

Fig. 1 Overview of transport phenomena and typological criteria discussed in this document

For each of the transport processes identified it is important to understand and model the phenomena and mechanisms involved in order to predict the long-term behavior of the packages under repository conditions. The very long-term evolution of conditioning material performance can be predicted confidently only on the basis of a validated phenomenology and clearly understood mechanisms. This understanding is founded on experimental investigation of simplified systems to determine and rank the parameters responsible for these mechanisms. This approach is, of course, supplemented by developing models — for which phenomenological modeling is an indispensable step toward validation and further investigation.

2 Fundamental Concepts of Waste Conditioning Matrices

The first part of this document reviews the fundamental physical and chemical properties of the materials, an indispensable prerequisite to understanding the issues of mass transfer in the context a geological repository:

- the chemical and mineralogical characteristics controlling their reactivity in contact with the environment, and therefore their inherent thermodynamic evolution;
- the nature and intensity of the radiation to which the materials are subjected by self-irradiation, which depends on the radionuclides loaded in the matrix;
- the microstructure, porosity and possible cracking of the materials, which determine whether or not preferential transport pathways are available.

The data described in section 2 are used to analyze the specific issues of mass transfer in these three materials (sections 3 and 4).

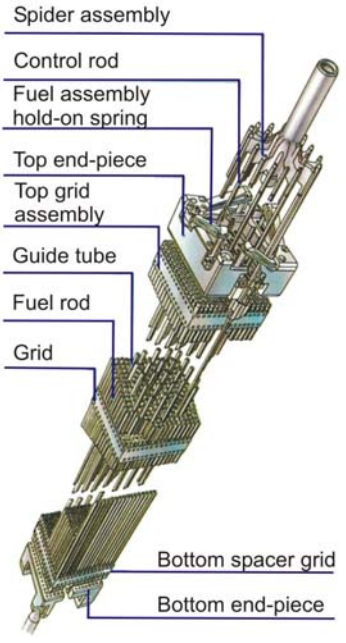

Fig. 2 Fuel assembly and control cluster

2.1 Spent Fuel

A nuclear fuel assembly for a pressurized water reactor (PWR) comprises 264 fuel rods (forming a 17×17 square array with 289 positions) maintained by 8 grids secured to 24 guide tubes; each rod has an outside diameter of 9.5 mm and is about 4 m high (Figure 2) [1]. Each sealed rod is pressurized with helium (to more than 25 bars at room temperature) and consists of a zirconium alloy cladding tube 580 µm thick containing a stack of 265 uranium oxide (UO_2) or mixed $(U,Pu)O_2$ oxide (MOX) fuel pellets. Each pellet is fabricated by sintering uranium oxide or mixed oxide powder to obtain grains with a mean diameter of 8 µm cohesively bonded together at the grain boundaries. MOX fuel is further characterized by the presence of plutonium-enriched zones known as Pu-rich aggregates from 5 to 30 µm in diameter, uniformly dispersed within the pellet. The fissile material content is less than 5% ^{235}U for uranium fuel, but can exceed 5% plutonium for MOX fuel.

The fuel rod undergoes numerous transformations during its residence time in the reactor. On removal from the reactor it continues to be subjected to numerous physical instabilities (irradiation arising from the decay of actinides and fission products, defects affecting diffusion processes), mechanical stresses, and chemical concentration gradients, etc. It is characterized in particular by very significant structural heterogeneity and by a quantity of fission products that is highly dependent on the type fuel and on the irradiation conditions. Its condition after irradiation, as described below, represents the initial spent fuel condition prior to transport and possible interim storage or disposal, and determines its long-term evolution [2-4].

2.1.1 Chemical Composition of a Spent Fuel Pellet on Removal from the Reactor

The chemical composition of nuclear fuel is modified under irradiation by the formation of fission products (FP). Except for a limited number of ternary fission reactions, each fission generates two new atoms. The occurrence probability of each FP is described by a curve with two peaks (Figure 3); the fission of each ^{235}U atom forms two atoms with mass numbers ranging from 85 to 105 and from 130 to 140, respectively. Other isotopes of U and Pu are produced by neutron capture as well as additional actinides by radioactive decay. The elements found in spent fuel cover a broad spectrum of the periodic table, and can be classified according to their chemical form in the fuel rod:

- elements capable of entering solution: solids that are soluble in the fluorine lattice of the $(U,Pu)O_2$ ceramic matrix such as actinides (representing the largest mass fraction in spent fuel), lanthanides (La, Ce, Pr, Nd, etc.), and other elements having soluble oxides (Zr, Nb, Sr);
- elements forming oxide precipitates: Rb, Cs, Ba, Zr, Nb, Mo, Te;
- fission products forming metallic precipitates: Mo, Tc, Ru, Rh, Pd, Ag, Cd, In, Sn, Sb, Te;
- fission gases (Kr, Xe, He), helium formed by alpha decay, and volatile FP in the reactor (I, Br, Rb, Cs, Te).

Despite these transformations, the oxygen potential or redox potential of spent fuel, generally designated by the O/M ratio, does not change significantly under irradiation. Regardless of the burnup it tends to follow the Mo/MoO_2 ratio. Molybdenum is abundant and largely unoxidized on removal from the reactor, exerting a buffering effect against any risk of rapid evolution; molybdenum can thus be found simultaneously in metal and oxide form.

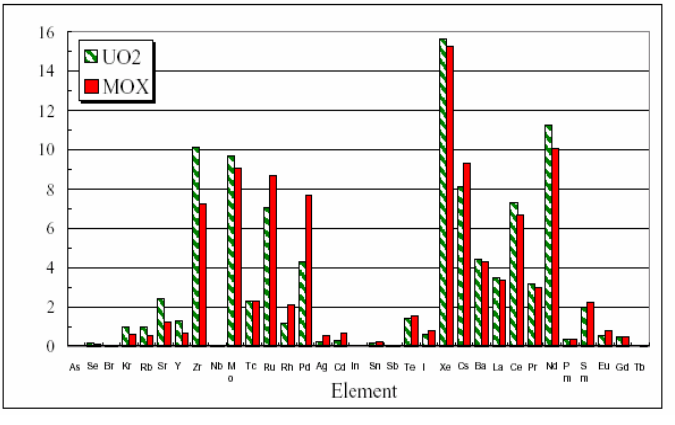

Fig. 3 Mass distribution of elements (except oxygen) in UOX and MOX fuel on removal from the reactor

2.1.2 Physical Condition of a Spent Fuel Pellet on Removal from the Reactor

The temperature gradient within the fuel pellet results in high stresses due to differential expansion of the fuel along its radius. The stress loading causes radial cracking of the pellet during heating and subsequent cooling. Circumferential cracks may also occur at high power levels. Irrespective of the burnup, the spent fuel pellet on removal from the reactor can be assumed to be fragmented into about fifteen pieces on average (Figure 4).

The swelling observed under irradiation is related to the occurrence of defects and fission products that affect the crystal lattice parameter (FP soluble in UO_2 and crystal defects due to irradiation) or form solid or gaseous secondary phases (in the case of insoluble fission products). The overall result is a burnup-dependent macroscopic increase in the fuel volume; under standard PWR conditions this swelling is about 0.6 to 0.7 vol% at 10 $GWd \cdot t_U^{-1}$. The main contributor to the overall volume increase is gas expansion due to the formation of fission products (xenon and krypton) that are thermodynamically insoluble in the UO_2 matrix and tend to coalesce in the form of unobservable nanometric bubbles inside the grains (intragranular bubbles). At high temperatures in the pellet central zone, intragranular bubbles can become mobile and migrate to the grain boundaries. The gas volume expansion is thus attributable to two factors: grain swelling due to the intragranular bubble population, and intergranular volume expansion due to the bubble population at the grain boundaries.

Areas significantly modified by irradiation in the reactor are observed in the pellet at microstructural scale. They include:

- the grain boundaries, in which metallic precipitates and fission gas bubbles accumulate. Although during irradiation the grain boundaries withstand very high stress levels due to the irradiation temperature, they become embrittled in the process. At the burnup levels and irradiation temperatures considered here, fractographs of spent PWR fuel pellets on removal from the reactor reveal mainly intergranular failures except in the central zone, whereas fresh fuel is subject to transgranular failures.

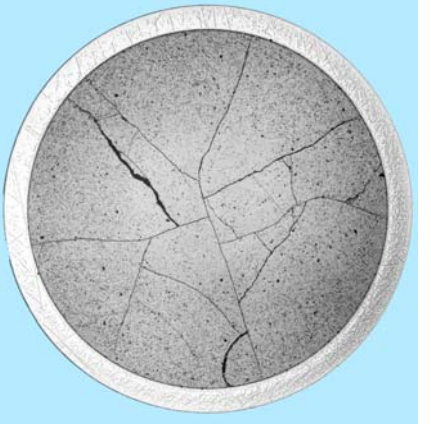

Fig. 4 Radial macrograph of a spent fuel pellet showing radial cracks

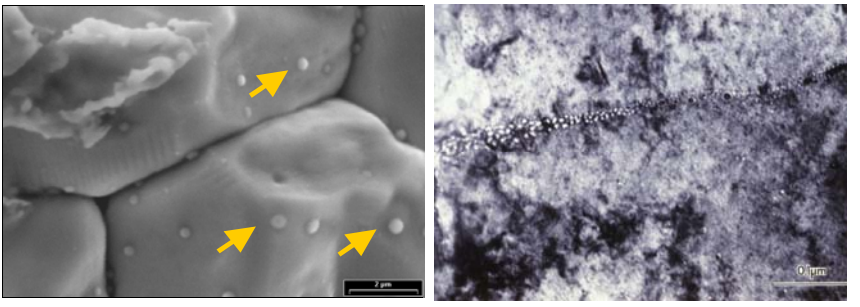

Fig. 5 SEM and TEM micrographs of grain boundaries after irradiation

- restructured zones around the pellet rim in UOX fuel with a burnup exceeding 40 $GWd{\cdot}t^{-1}$ and in the large Pu-rich aggregates (exceeding 10 to 20 µm) in the outer region of MOX fuel pellets.

Plutonium production in UOX fuel is significantly higher around the rim than in the remainder of the pellet because of the higher probability of capture of some neutrons by ^{238}U, whose absorption cross section exhibits strong resonance in the epithermal range, hence a significantly higher local burnup. The presence of a very large quantity of gas and fission products not at thermodynamic equilibrium and the major damage arising from the enormous fission density lead to microstructural transformations. The grain size — initially between 5 and 10 µm — becomes submicronic and numerous micrometric pores appear, resulting in high (10–30%) porosity in this region (Figure 6).

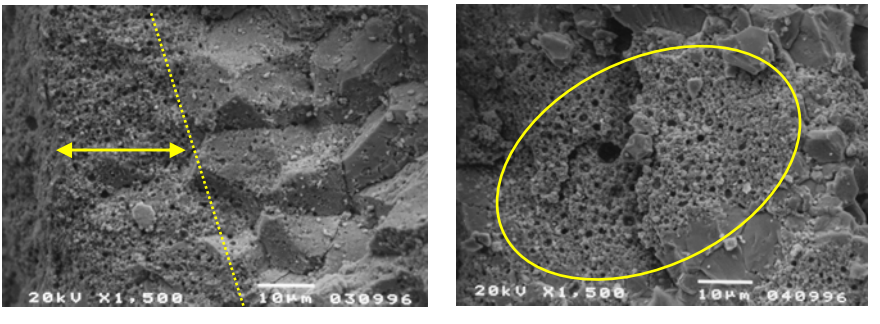

Fig. 6 Micrographs of restructured zones around the rim of a UOX fuel pellet (left) and in a plutonium-rich aggregate in a MOX fuel pellet (right)

2.1.3 Preliminary Remarks Concerning Transfer Phenomena in Spent Fuel

Two source terms are routinely considered when assessing the long-term performance of spent UOX and MOX fuel packages in contact with water:

- The *instant release inventory* concerns the fraction of the total radionuclide inventory that is not retained in the spent UO_2 or $(U,Pu)O_2$ fuel matrix and will

be released instantaneously when water comes into contact with the package. In a geological repository the release is expected to occur after corrosion of the container and resaturation of the site (standard scenario), whereas in interim storage it will occur immediately following immersion of a fuel assembly containing a failed rod (incident scenario). This source term depends on the fuel evolution prior to water ingress. The spent fuel pellet will be altered mainly by radioactive decay after the fuel has been removed from the reactor. This is accompanied by changes in the chemical inventory, the accumulation of irradiation damage, and the production of significant quantities of helium through alpha decay. Together, these factors are likely to result in intrinsic transformations in the fuel pellet. This evolution implies diffusion processes within the ceramic material that are thermally activated or related to self-irradiation, which must be accurately quantified and evaluated. For example, the helium behavior will depend to a large extent on its diffusion properties, which in turn depend on the package temperature over time, on the matrix damage level (defect concentration), and on alpha self-irradiation lasting thousands of years, which can result in further atomic mobility. The fundamental issue is therefore the evolution of the gas: Will it be trapped in the UO_2 grains? Will the solubility limit be reached quickly to the point of forming bubbles in the ceramic? Can it migrate to the grain boundaries and then into the free volumes, or form bubbles at the grain boundaries? These possible outcomes — which could jeopardize the mechanical stability of spent fuel through failure of the grain boundaries or grains, resulting in a significant increase in surface area prior to water ingress in a geological repository — must be taken into account over geological repository time scales and have been widely investigated in recent years.

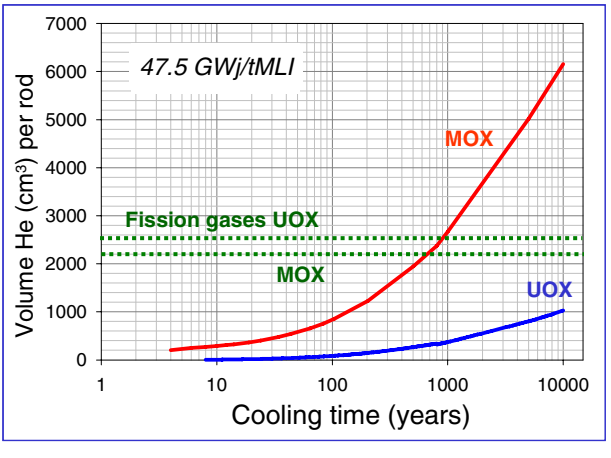

Fig. 7 Quantity of helium produced versus time in UOX and MOX fuel rods

- *Radionuclide release from the UO_2 matrix*. This source term will depend on the chemical stability of the matrix itself and requires knowledge of the type of mechanisms governing alteration in water to enable long-term predictions. The UO_2 stability will depend largely on the system redox conditions, which can be influenced by the fuel self-irradiation field and by water radiolysis. Although uranium is sparingly soluble (approx. 10^{-9} mol·L^{-1}) under reducing conditions similar to those encountered in a geological repository (in European concepts), its solubility can increase significantly at the UO_2/water interface because of the α radiation field that will predominate over the very long term. Water radiolysis — which produces oxidizing and reductive species, including radicals ($OH^{\bullet}$, $O_2^{\bullet-}$, $HO_2^{\bullet}$, e^-_{aq}, $H^{\bullet}$) and molecular species at concentrations that depend on the type of radiation (α or β-γ) and the dose deposited in the water — can establish oxidizing conditions at the UO_2/water interface (redox imbalance with the environment) and thus enhance the dissolution of the fuel matrix in a disposal site. The onset of oxidizing conditions is generally unfavorable since in that case the UO_2 fuel matrix is altered by an oxidizing dissolution mechanism (U(IV) is oxidized to U(VI)) as described in Figure 8 [5]. Matrix dissolution depends also to a large degree on the chemical composition of the water; the presence of chemical species that form uranium complexes, such as carbonates, enhances the oxidation of uranium to U(VI) in solution.

Diffusion processes at the reaction interface must be taken into account, and coupling between chemistry and transport is an essential factor. In the case of local alpha irradiation (to a depth of 40 µm) at the UO_2 matrix/water interface, interactions between species generated by water radiolysis and the UO_2 surface will largely depend on the nature and half-life of these species, on the chemical kinetics of the redox or complex formation reactions, and on the properties of diffusion into the homogeneous solution.

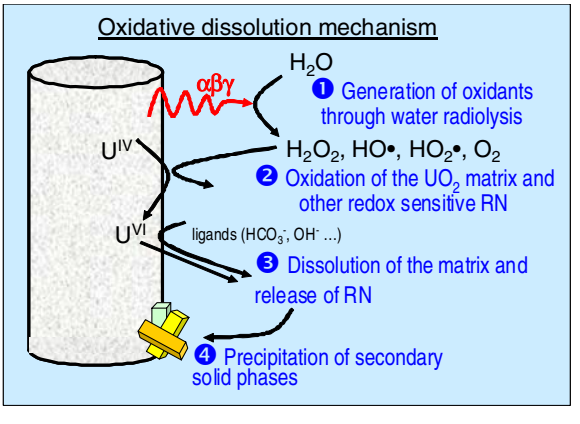

Fig. 8 Oxidizing dissolution of the spent UO_2 fuel matrix in contact with water

2.2 Glass

2.2.1 Introduction

Borosilicate glass structures are remarkably capable of incorporating chemical elements as cations, while ensuring good chemical durability and strong irradiation resistance. These materials have been used for more than thirty years at industrial scale to immobilize radionuclides arising from spent fuel treatment. All the countries in which these containment materials are produced (France, England, the United States, Russia) or in which they are currently stored after fuel reprocessing in a different country (Germany, Switzerland, Belgium, Japan, the Netherlands) are considering disposal of the packages in a deep geological formation. This is currently the benchmark solution to ensure long-term safety.

2.2.2 Chemical Composition and Structure

2.2.2.1 General Aspects

Because glass[2] is an amorphous material, it can accommodate a very large number of elements, mainly cations, with highly variable stoichiometry as in the case of fission product solutions of variable compositions.

The glass constituent elements are generally taken from three categories: network formers, network modifiers and intermediate elements based on criteria that include the coordination number, the binding forces, or their electronegativity with respect to oxygen.

- *Network-forming cations* (B, Si, Ge, P, tetracoordinate Al) form partially covalent bonds with oxygen atoms, constituting a polymer network; they are sufficient to form a glass by themselves: silicon, for example, in silicate glasses consisting of SiO_4 tetrahedra. In this case, each tetrahedron shares at least one O atom with another tetrahedron.
- *Network-modifying cations* (Sc, La, Y, Ga, In, Mg, Li, Ba, Ca, Sr, Na, Cd, K, Rb, Hg, Cs, etc.) cannot form a glass by themselves, but are inserted in the network. They break the polymer chains, leading to depolymerization of the network (creation of nonbridging oxygen atoms). They are generally alkalis or alkaline earths. Their ionic radii and coordination numbers are larger than for the network-forming ions. They are linked to oxygen atoms by ionic bonds. Note that alkali cations and alkaline earths can also play a charge compensating role in the glass structure, for example to compensate B or Al in four-fold coordination.
- *Intermediate elements* (Al, Zr, Ti, Be, Th, Fe,…) can be either network formers or network modifiers depending on the glass chemical composition. This is the case for Al in particular.

[2] The term “glass” is applicable to compounds capable, after melting, of forming a noncrystalline solid that conserves the structural disorder of a liquid, in a thermodynamically metastable “vitreous” state.

2.2.2.2 Glass Properties

The chemical composition of nuclear glass is above all specified according to the nature and composition variability of the fission product (FP) solutions. Moreover, the technological requirements of glass fabrication (viscosity of the glass melt) and the fundamental material qualities (homogeneity, thermal stability and crystallization, chemical durability) also affect the proportions of some constituents. For all these reasons, FP containment glasses are characterized by composition ranges.

Most countries in which fission product solutions are vitrified have selected borosilicate glasses. From the origin of research on the immobilization of civilian or military waste, however, as an alternative to the borosilicate matrices known in the industry for their chemical and thermal resistance, phosphate matrices were considered because of the following advantages: the glass precursor could be incorporated in liquid form (phosphoric acid), the melting temperature is relatively low, and higher waste loading proportions are possible [6]. Unfortunately, this type of glass has major drawbacks. It is impracticable to manufacture an industrial metal melting pot capable of resisting corrosion by such a mixture for an acceptable time [6-8]. In addition, the resulting glass is generally subject to significant devitrification, a phenomenon that sharply diminishes its chemical durability [9].

In France most borosilicate glass is produced at La Hague for the containment of minor actinides and fission products separated after reprocessing of spent light-water reactor fuel. We provide data only for the corresponding "R7T7" glass. Vitrified R7T7 waste packages are produced in the R7 vitrification unit (UP2-800 reprocessing plant) and the T7 vitrification unit (UP3 plant).

Basic data on R7T7 glass packages:

- About 13 000 vitrified waste packages have been produced at the end of 2008.
- Mean values[3] per package at the moment of production
  - Glass mass: 397.5 kg
  - Density: 2.75 $g \cdot cm^{-3}$
  - α activity: 214 TBq
  - $\beta\gamma$ activity: 15 640 TBq
  - $\beta\gamma$ dose rate (at 1 meter): 76.8 $Gy \cdot h^{-1}$
  - Neutron dose rate (at 1 meter): 0.042 $mGy \cdot h^{-1}$
  - Thermal power: 1883 W

The guaranteed chemical composition for glass produced in the R7 and T7 vitrification facilities is indicated in Table 1.

Most laboratory studies have been carried out on SON68 glass, the inactive equivalent of the benchmark glass in which radionuclides are simulated either by stable isotopes of the same element or by a stable element having the same chemical behavior in the glass.

[3] Mean values based on production up to December 1999.

Table 1 Composition range specified by AREVA NC for glass produced in the R7 and T7 vitrification facilities

Oxide	Nominal composition (wt%)	Specified interval (wt%)	
		min	max
SiO_2	45.1	42.4	51.7
B_2O_3	13.9	12.4	16.5
Al_2O_3	4.9	3.6	6.6
Na_2O	9.8	8.1	11.0
CaO	4.0	3.5	4.8
Fe_2O_3	2.9	-	<4.5
NiO	0.4	-	<0.5
Cr_2O_3	0.5	-	<0.6
P_2O_5	0.3	-	<1.0
Li_2O	2.0	1.6	2.4
ZnO	2.5	2.2	2.8
(FP + Zr + actinide) oxides + suspended fines	12.8	4.2	18.5
Actinide oxides	0.9	-	-
$SiO_2+B_2O_3+Al_2O_3$	-	>60	-

2.2.2.3 Glass Structure

Although glass is a well known and widely used material both in nature and in industry, its structure remains paradoxically poorly known [10]. The main reason for this is the lack of medium- and long-range symmetry and order, and the difficulty of implementing spectroscopic investigation techniques at short range (a few Å). The virtually infinite variety of glass chemical compositions is another factor adding to this complexity.

Although a silicate oxide glass has no medium- or long-range crystalline periodicity, there are strong short-range similarities between glass and crystal. The tetrahedral configuration of network formers is very similar in both cases.

Crystalline silica (quartz) is organized in tetrahedra comprising a central silicon ion surrounded by four oxygen ions at the vertices; the $(SiO_4)^{4-}$ tetrahedra are interconnected by shared vertices — i.e. "bridging" oxygen ions — ensuring electrical neutrality. Silicate glasses comprise the same $(SiO_4)^{4-}$ tetrahedra, except that they are not all interconnected ("nonbridging" oxygen ions). The structure forms a disordered network that includes vacancies capable of accommodating the sodium ions (Na^+) of a sodium silicate glass.

At microscopic scale, the disorder allows the incorporation of many chemical elements that would be incompatible with the strict order of a crystal structure.

2.2.2.4 Atomic Structure of the Cross-Linked R7T7 Glass Network

Research began in the early 1990s with the primary objective of acquiring basic atomic-scale knowledge of the organization of glass, and in particular of R7T7

glass. These studies were undertaken with an approach combining atomistic modeling and experimentation [11-20]. It is currently impossible to model the actual nuclear glass because of the chemical and physical complexity of the matrix, considering the number of constituent elements; these studies were therefore carried out on model glasses, most of which were representative the of complex nuclear glass. The model glasses contained 4, 5, or 6 oxides based on the major elements of the cross-linked R7T7 glass network.

To identify the short- and medium-range structural organization of these model glasses, the structural characteristics established by molecular dynamics were compared with the short- and medium-range environment determined experimentally by fine-structure spectroscopy (wide-angle scattering, X-ray absorption spectroscopy EXAFS and XANES, NMR, etc). This approach yielded a representative model capable of explicitly describing the cross-linked network of R7T7-type glass.

At atomic scale [16] this type of glass comprises mainly a disordered network formed by basic patterns including [SiO_4], [AlO_4] and [BO_4] tetrahedra, [BO_3] triangles, [ZrO_6] hexahedra, and containing the major network formers (Si, Al, B) (Figure 9).

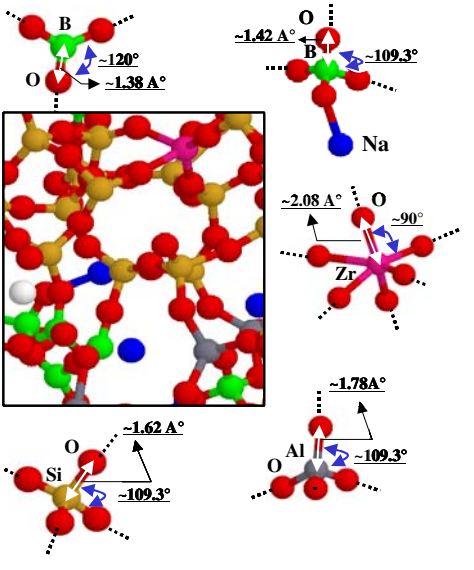

Fig. 9 Basic patterns constituting the glass models studied. This figure also indicates the angles and interatomic distances of each pattern

The sequence of patterns is based mainly on 5-, 6- and 7-member rings (Figure 10).

The alkali and alkaline earth metals have two roles in this network: either as charge compensators (Na_{cc}) necessary to ensure the stability of some patterns [BO_4], [AlO_4], and [ZrO_6], or as network modifiers (Na_m) that depolymerize the network by creating nonbridging oxygens (O_{nb}).

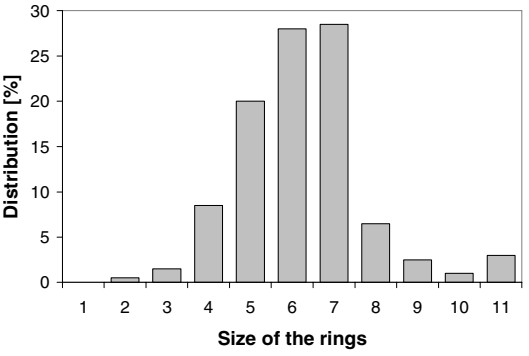

Fig. 10 Ring distribution in the 6-oxide glass

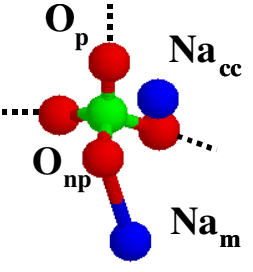

Fig. 11 Role of sodium atoms around a tetracoordinate boron atom

The degree of glass polymerization is important. For example for glass 6Ox the vast majority of network formers are connected by their vertices. Only about 6% of the oxygens are nonbridging, and most of them are situated on SiO_4 tetrahedra.

2.2.3 Preliminary Remarks Concerning Transport Phenomena in Glass

Glass performance in a geological repository is generally assessed by assuming that the glass is homogeneous and that the dissolution of radionuclides is limited by glass matrix alteration. The presence of crystals or unmelted phases in small quantities is not a serious problem if these products are sparingly soluble. Radionuclide release from the glass by diffusion and volatility during the repository thermal phase (a few hundred years) , like self-irradiation effects on the glass structure,' can also be disregarded on the basis of sound arguments'.

The models developed to evaluate the source term of nuclear waste glass in a geological repository are generally configured by experiments on inactive glass samples; dedicated tests on active glass specimens are then carried out for validation purposes. The source term can thus estimated from the calculated mass of altered glass, M, given by the following equation :''

$$M = \iint r(t,S)dSdt \tag{1}$$

where S is the reactive surface area, r the glass dissolution rate, and t the time.

At macroscopic scale, glass alteration by water can be considered as a surface reaction. Considering the fact that nuclear glass blocks are fractured by mechanical stresses during cooling, the surface area that must be taken into account is significantly greater than the geometric surface area of the block. The presence of fractures and cracks in the glass block entails coupling between chemistry and transport at various scales. After detailing the glass aqueous alteration mechanisms we will discuss how mass transfer between the glass and solution is affected by specific chemical reactions at the interfaces and how existing models describe the glass alteration kinetics with allowance for microscopic processes.

2.3 Cement

2.3.1 Physical Chemistry of Cement Materials

Cement-based materials are widely used in the nuclear industry for conditioning and disposal of low- and intermediate-level radioactive waste. They are produced by a setting reaction between anhydrous cement, aggregates, and water. A distinction is generally made between:

- pure paste, consisting only of cement and water,
- mortar, containing sand (aggregates smaller than 6.3 mm),
- concrete, including sand as well as larger aggregates. Concrete can be also reinforced by short metal fibers or rebars to increase its tensile strength.

Except in pathological cases such as an alkali-aggregate reaction, the properties of the aggregates are not subject to significant variation over time. The chemical evolution of cement materials is thus mainly controlled by that of the cement paste itself.

Cement paste is produced by hydration of anhydrous phases reacting on contact with water to form hydrated minerals by a dissolution/precipitation mechanism. A few hours after mixing, the material sets, i.e. in a few moments it changes from a suspension to a solid. Hydration then continues during a phase known as hardening. The mechanical properties vary rapidly during the first few hours after mixing, and then slowly improve over several months. Unlike the other inorganic materials such as plaster, cement maintains its cohesive structure after hardening even when exposed to water.

The most widely used composition, Portland cement, is a mixture of five main components: tricalcium silicate, dicalcium silicate, tricalcium aluminate, and tetracalcium aluminoferrite, forming clinker, an artificial rock obtained by calcining a clay-limestone mixture at 1450°C [21], and gypsum, as an additive (less than 5%).

When the materials are mixed these anhydrous phases react, are surrounded by water and form various hydrates, mainly calcium silicate hydrates, C-S-H, which account for 70% of the hydrates formed, calcium hydroxide or Portlandite, $Ca(OH)_2$ representing about 20% of the hydrates, and calcium aluminate and sulfoaluminate hydrates, ettringite $[Ca_2Al(OH)_6]_2Ca_2(SO_4)_3$, $25H_2O$ and calcium monosulfoaluminate hydrate (AFM) $[Ca_2Al(OH)_6]_2$, SO_4, $6H_2O$ representing about 10% of the hydrates.

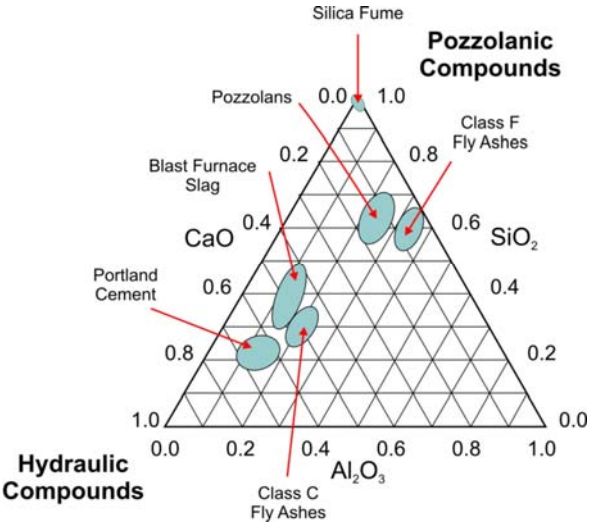

Fig. 12 $CaO\text{-}SiO_2\text{-}Al_2O_3$ ternary diagram identifying the inorganic compounds generally added to Portland cement

Various minerals can be added to Portland cement to obtain specific properties when the clinker is ground (Figure 12). This document discusses two types of standardized cement designated CEM I (ordinary Portland cement) and CEM V (composite blast furnace slag - fly ash cement) according to European standard EN 197-1. In addition to the chemical nature of the cement, the fundamental parameter used to characterize cement paste is the water/cement mass ratio, w/c, indicating the proportions of constituents in the mixture.

The resulting hardened cement paste is a heterogeneous material, consisting of a porous solid, a liquid phase, and a gas phase contained in the pores. The solid skeleton consists of hydrated minerals and possibly residual anhydrous cement. The interstitial solution, whose composition varies as the material ages, is highly basic (pH > 12.5).

2.3.2 Microstructure and Porosity of Cement Materials

Hydration results in the creation of pores within the hardened cement paste. Although other categories of pores are sometimes taken into consideration, e.g. hollow shell pores [22], the literature generally discriminates between two main types: capillary pores, and gel pores [23]. As the pore sizes are continuously distributed in cement pastes, the distinction between these categories is based on their phenomenological origin rather than a strict size differentiation.

The volumes initially filled with water that remain in the hardened cement paste as interconnected channels or as cavities interconnected only by C-S-H pores are known as capillary pores. Their characteristic dimensions range from 2 nm to 5 µm. The capillary porosity depends to a considerable extent on the initial w/c ratio, on the fineness of the anhydrous cement and the quantity of hydrated cement,

i.e. on the age of the material and the chemical composition of the initial anhydrides. The capillary porosity varies over time as hydrates precipitate in the volumes initially occupied by water, which of course diminishes the total porosity. Because of this mechanism, the porosity in cement materials is topologically complex.

Calcium silicate hydrates are the main constituents of hydrated cement paste, and are mainly responsible for the material cohesion and microstructure. Several models have been proposed to describe the microstructure of C-S-H gels [24, 25], which are generally described as colloidal, amorphous or slightly crystallized materials organized in a layered structure with pores typically 0.5 to 10 nm in size. As the resulting porosity is closely related to the C-S-H structure, it is practically independent of the w/c ratio [26] but varies according to the chemical nature of the anhydrous cement. A distinction is usually made between two types of C-S-H with low or high porosity (i.e. high or low density, respectively) in cement materials [27]. High-porosity external C-S-H is formed during the initial instants of hydration of the cement paste and fills the pore space with no spatial constraint. Subsequently, due to geometric constraints, internal C-S-H develops with a more compact morphology toward the interior of the anhydride grains [28].

Cement materials are thus multiphase porous media consisting of a porous solid skeleton (an assemblage of specific mineral phases) at metastable equilibrium with a liquid phase (an ionic solution) and a gas phase that may contain air, water vapor, etc. When the external environment can induce thermodynamic modifications in the residual anhydrous phases or in the hydrated constituent phases of the material, these reactions occur at the material/environment interfaces, i.e. both on the outer surface and on the surfaces developed by pores in the matrix, capillary pores, and micropores. The diffusion of liquids or gases through cement materials depends on whether or not the capillary porosity is connected only by micropores.

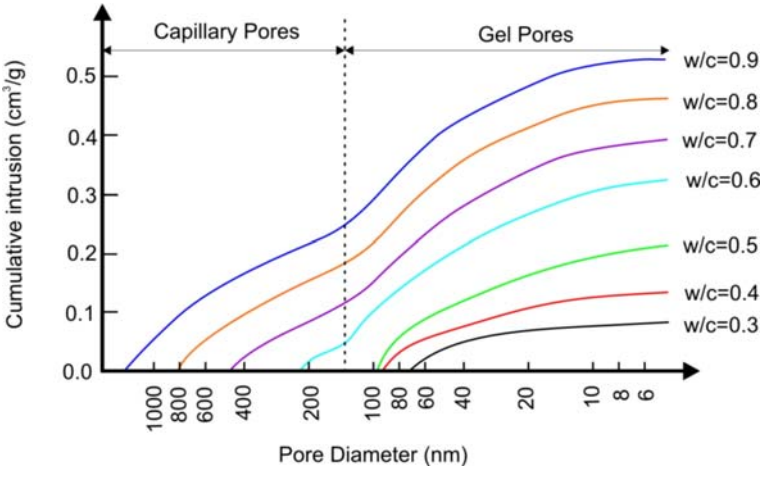

Fig. 13 Influence of water/cement ratio on the porosity distribution of CEM I cement pastes after curing for 28 days (adapted from[29])

2.3.3 Preliminary Remarks Concerning Transport Phenomena in Cement Materials

In the context of a deep geological repository, cement materials are notably used both as an encapsulation matrix for low- and intermediate-level waste and as constituent materials for waste containers. For each of these purposes the environmental context, the performance requirements, and of course the essential transport phenomena differ considerably.

The two essential periods in the lifetime of a geological repository — i.e. the phase of operation and reversibility during which the cement materials are exposed to moist but unsaturated atmospheric conditions, and the phase after closure during which water eventually comes into contact with the waste packages — represent very different environmental contexts for cement-encapsulated waste packages or concrete containers. The major transport phenomena involved are thus considerably different.

When cement materials are at equilibrium with a moist but unsaturated external environment, the material porosity can be partially desaturated, providing a pathway for gas to permeate or diffuse within the material. The gas may react with the mineral assemblage of the material and thereby modify its future properties — especially its durability — or it may be inert, in which case the material is simply a membrane through which the gas can pass (§ 3.3).

When the geological repository becomes water-saturated, gas transport diminishes and is superseded by ion transport; the material is then subject to two phenomena: alteration through interactions between the groundwater solution and the material, and radionuclide release from the cement material into the surrounding environment. In order to maintain context as general as possible, aqueous alteration is discussed here mainly through a description of hydrolysis in pure water, which is the underlying mechanism of all the other alteration phenomena observed in saturated media (§ 4.1.3). This phenomenon modifies the mineral assemblage constituting the material and therefore its properties. At the same time, water is also a vector for the diffusion of radionuclide ions initially contained in the encapsulation matrix or coming into contact with the concrete container. These elements diffuse into the surrounding environment through the porous network of the cement material. Depending on the chemical nature of each element, it may be retained to some extent on one or more hydrated cement mineral phases (§ 4.2.2).

Irrespective of the type of transport involved, these phenomena occur mainly in the porosity of the cement materials, which depends on their formulation. The results discussed here mainly concern cement pastes with relatively simple and controlled chemical properties.

3 Transfer Phenomena Related to the Evolution of the Dry Waste Package

3.1 Introduction

The initial stage of geological repository site management concerns the operating period, during which waste packages are placed in the underground structures. If

the repository site was initially water-saturated, local desaturation of the host rock occurs during this phase, principally as a result of ventilation. Unsaturated atmospheric conditions are maintained throughout the operating and reversible storage periods, and even after closure of the site if the host geological formation is situated above the aquifer. In this context, the waste packages are not exposed to water as long as the repository site does not become saturated by groundwater. Two main types of mass transfer can occur:

- through transport in a closed system, i.e. with no mass transfer to the surrounding environment.
- through transport in an unsaturated open system, i.e. mainly gas transport through unsaturated percolating porosity in porous materials.

Mass transfer can occur in closed systems as a result of irradiation: for example, displacement cascades in the glass, or helium production and transport under α irradiation. The example discussed here concerns the behavior of helium produced in the matrix; its diffusion properties have been widely investigated in recent years.

The porous cement materials used as outer containers for low- and intermediate-level waste are subject to the second type of mass transfer under unsaturated conditions. Gas can be produced by corrosion, by microbial activity, or by self-irradiation of some encapsulation matrices. Depending on the relative humidity of the surrounding environment, the intrinsic porosity of these materials can be at least partially unsaturated. The gas can then be released outside the container by diffusion or permeation.

3.2 Helium Behavior in Spent Fuel

After irradiation in the reactor, UOX or MOX fuel contains the major actinides, uranium and plutonium, together with minor actinides, the most abundant of which are isotopes of neptunium, americium and curium. Most of these isotopes are radioactive and disintegrate by alpha decay, emitting a helium-4 atom with each disintegration. Their half-lives range from about ten to a few million years; helium is therefore generated within the spent fuel over an extremely long time period. Helium does not constitute a radiological hazard, but its accumulation could affect the long-term behavior of spent fuel in a closed system, i.e. inside the sealed fuel rods without any contact with air or groundwater. The fundamental issue concerns helium mobility in spent fuel: will the helium generated after irradiation remain occluded in the crystal lattice, will it form small intragranular bubbles, or can it migrate to the grain boundaries or even to the free volumes in the fuel rod?

3.2.1 Purely Thermal Diffusion

Published results show that helium diffusion from the grains to the grain boundaries is a complex mechanism involving several steps. The components of this diffusion process have been investigated by various methods using isotopes ^{3}He and ^{4}He. Several studies of helium mobility were carried out by Nuclear Reaction Analysis (NRA) of the $^{3}He(d,p)^{4}He$ reaction [30-34]. This technique

determines the diffusion coefficients in a reference material without self-irradiation phenomena.

The analysis samples were generally polished ^{235}U-depleted UO_2 disks 8 mm in diameter and of variable thickness depending on the experimental strategy. They were implanted with energy levels ranging from 0.5 MeV to 2.9 MeV and at different fluence values, about 10^{13}, 2×10^{15}, 5×10^{15}, 1×10^{16} and 3×10^{16} $He^{+} \cdot cm^{-2}$. These fluence values correspond to the helium concentration generated in fuel at different time intervals during interim storage and after disposal. For example, fluence values of 5×10^{15} and 3×10^{16} $He^{+} \cdot cm^{-2}$ correspond respectively to UOX fuel with a burnup of 60 $GWd \cdot t^{-1}_{iHM}$ after 300 years and to MOX fuel after less than 800 years. These experiments and the results obtained are detailed in [30-34].

Two experimental approaches were implemented recently to characterize helium mobility in uranium dioxide by NRA, and are described below. The first consisted in estimating the impact of annealing on the helium concentration profile by nuclear reaction analysis of the energy of the protons arising from the reaction. The second strategy consisted in characterizing the helium mobility using three different approaches to the nuclear reaction (release during the annealing sequence, concentration profiles, He concentration mapping at the scale of an individual grain).

3.2.1.1 First Approach: Impact of Annealing on the Helium Concentration Profile by Analysis of the Energy of the Nuclear Reaction Protons.

The $^{3}He(d,p)^{4}He$ nuclear reaction has a maximum cross section for 450 keV deuterons. During the analysis, the incident deuteron beam energy was diminished from 1500 to 1000 keV in variable steps of 100 to 20 keV. The protons produced by the this reaction had an energy of about 13.5 MeV and were collected by a detector comprising three superimposed silicon wafers placed on the deuteron beam centerline.

The number of protons N_p received by the detector can then be expressed as a function of the incident deuteron energy E_d:

$$N_p(E_d) = N_d(E_d)\Omega \int_0^{\infty} \frac{d\sigma_{dH}}{d\Omega}(E_d - g(x))\rho(x)dx \qquad (2)$$

where:

- N_d: number of deuterons of energy E_d
- Ω: solid angle of proton detector
- $\frac{d\sigma_{dH}}{d\Omega}$: differential cross section of the reaction in the test configuration
- $g(x)$: deuteron deceleration in the material
- $E_d - g(x)$: deuteron energy of interaction at depth x
- $\rho(x)$: concentration profile, presumably Gaussian, of helium-3.

The analysis method consisted in determining the number of protons detected versus the incident deuteron energy for a fixed charge. Two methods were used, yielding comparable diffusion coefficients:

- mathematical processing based on refining the curve by convoluting the helium-3 profile with the cross section [35];
- simulation of an implantation profile and backscattered proton spectra in the experimental configuration, using SIMNRA [36]. In this case the material was described as multiple layers of homogeneous concentration. The layer concentrations were then adjusted so the simulated proton energy spectrum corresponded to the experimental spectrum.

This method was applied to samples implanted to depths of about 6 µm, at which the spatial resolution was about 500 nm. This strategy assumes a number of hypotheses concerning the shape of the concentration profiles. In this case Gaussian distributions were assumed for the profiles recorded before and after annealing.

The samples were annealed either in neutral atmosphere with a stream of N_2 + 1% H_2 in a tube furnace with provisions for online measurement of the oxygen partial pressure, or in reducing atmosphere (Ar + 10% H_2). Atomic diffusion was assumed to be the only mechanism liable to modify the concentration profile during annealing. Fick's second equation provided an analytical solution to the problem:

$$\rho(x) = \frac{C_0}{\sqrt{2\pi\sigma}} \exp\left(-\frac{(x - x_0)^2}{2\sigma^2}\right) \quad (3)$$

where C_0 is the concentration initially implanted in the sample, x_0 the implantation depth and σ the distribution variance. C_0 and σ are the two degrees of freedom.

The diffusion coefficients were calculated from the spreading of the experimental profiles, assumed Gaussian, according to the following relation:

$$\sigma^2 = \sigma_0^2 + 2\,D\,t \quad (4)$$

where σ and σ_0 represent the distribution variance before and after annealing (m), t the heat treatment duration (s), and D the thermal diffusion coefficient ($m^2 \cdot s^{-1}$).

3.2.1.2 Second Approach: Investigation of Helium Mobility by Coupling Three Complementary Nuclear Reaction Techniques: Release, Concentration Profiles by Detection of α Particles, He concentration mapping.

The second strategy consisted in characterizing helium mobility using the $^3He(d,p)^4He$ nuclear reaction in three different ways [37]: measurement of the helium release fraction during vacuum annealing sequences, characterization of the concentration profiles before and after each annealing sequence, and microbeam analysis of the ^3He distributions near the sample surface at the scale of an individual grain.

The concentration profiles were characterized by analyzing the energy spectra of the α particles arising from the nuclear reaction. An electronic coincidence

detection system for protons and α particles [38] was necessary to eliminate the background produced mainly by interactions between the deuterons and the material. Although the detection of α particles is more sensitive to surface effects than the preceding method because the working distance is less than about 2 µm, it provides higher resolution at the implantation depth (about 100 nm). The data (two space scales, one time scale) were analyzed using a three-dimensional model specifically developed with the Cast3M finite element solver.

3.2.1.3 Few Experimental Results

Figure 14 shows the homogeneous quantities with the diffusion coefficients obtained at temperatures ranging from 700°C to 1200°C. Roudil [30] determined the activation energy from experiments by assuming that atomic diffusion is the principal mechanism during annealing and that the diffusion coefficient follows an Arrhenius law:

$$D = D_0 \exp^{-\frac{E_a}{KT}} \tag{5}$$

where:

- D is the diffusion coefficient ($m^2 \cdot s^{-1}$)
- D_0 is the pre-exponential factor ($m^2 \cdot s^{-1}$)
- E_a is the activation energy (eV)
- K is the Boltzmann constant ($eV \cdot K^{-1}$)
- T is the temperature (K).

The thermal diffusion coefficients vary by half an order of magnitude depending on the implantation fluence. This difference at the highest concentration (about 1 at%) was attributed to exceeding the solubility limit and to a helium trapping mechanism during annealing in particular. The activation energy was about 2 $eV \cdot at^{-1}$, and the thermal diffusion coefficients were:

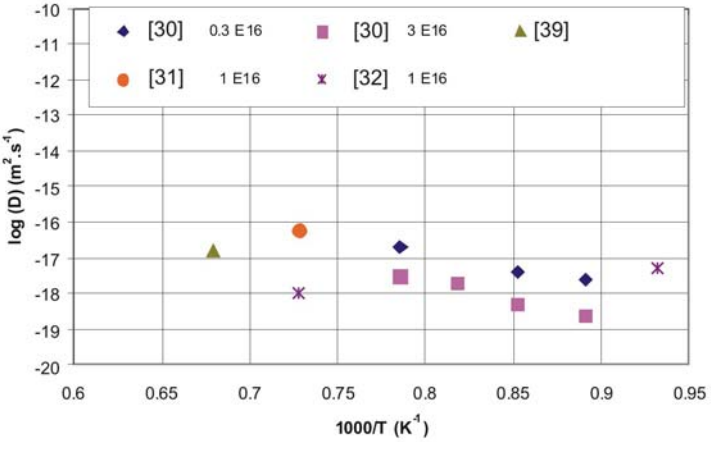

Fig. 14 Thermal diffusion coefficients and activation energy

- $D = 8\times10^{-9} \exp^{-\frac{2(\pm0.1)}{KT}}$ ($m^2 \cdot s^{-1}$) for a fluence below 1×10^{16} He·cm^{-2}
- $D = 4\times10^{-10} \exp^{-\frac{2.1(\pm0.1)}{KT}}$ ($m^2 \cdot s^{-1}$) for a fluence above 3.0×10^{16} He·cm^{-2}

This activation energy is comparable to values reported in the literature obtained by pressurized helium gas infusion [39] or by implantation and thermal desorption [40]. Extrapolating these results to temperatures below 500°C shows that in the absence of α self-irradiation, thermal diffusion of helium will not occur in the time and temperature range characterizing a repository or an interim storage facility.

Nevertheless, after helium implantation and annealing, the profiles were modified as the Gaussian distribution was enlarged nearer the surface. This phenomenon was more pronounced at shallow implantation depths and when the fluence did not exceed 1.0×10^{16}. Broadening occurred in the region of implantation-induced defects and at low concentrations could indicate an acceleration of the diffusion process via vacancy defects. At higher concentrations helium mobility arises from both diffusion and helium trapping. There is thus no true purely atomic diffusion coefficient, making comparisons difficult among authors. Microbeam characterization of samples implanted at shallow depths revealed the major influence of the grain boundaries in helium release.

Increased apparent atomic or overall diffusion in the polycrystalline material has also been reported in various studies of actinide-doped samples (i.e. subjected to alpha self-irradiation) [41, 42]. This phenomenon is nevertheless thermally activated (above 800–900 K) and the increase in helium mobility with respect to undoped UO_2 appears to be limited. Although this component could contribute to increasing the helium fraction released over time, it appears that most of helium produced in spent fuel will inevitably remain occluded in the grains.

These results indicate that irradiation defects and self-irradiation contribute to the macroscopic solubility and mobility of helium. Helium mobility in UO_2 without fission products is accelerated near the grain boundaries by crystal defects above about 700°C. The fact that this is practically the same temperature as the mobility of uranium vacancy defects is probably not a mere coincidence, although it is not known with certainty whether the helium atom follows the uranium vacancy or instead migrates more readily in the crystal lattice after defect annealing. The thermal component of diffusion is thus minimal at the temperatures relevant to the back end of the fuel cycle, and cannot lead to significant helium release in a situation representative of the transport, long-term interim storage, or disposal in a repository of spent fuel assemblies.

3.2.2 Athermal Diffusion

Athermal diffusion occurs at low temperatures and has been identified in materials subjected to irradiation. In UO_2 the mechanism is comparable to that produced by fission reactions under irradiation [43] giving the following expression for the diffusion coefficient, D^*:

$$D^* = A^* \cdot F^* \tag{6}$$

where:

- A^*: Proportionality constant specific to each element (m^5)
- F^*: α activity ($Bq \cdot m^{-3}$)

The proportionality coefficient A can be expected to be lower than found by Matzke for fissions in the reactor (about 10^{-39} m^5) because it implicitly includes the number of decay defects (1500 to 1700 for the recoil nucleus), which is much lower than in the case of a fission reaction.

The approaches described in [44] estimated from athermal diffusion of FP or U give a proportionality coefficient, A, of between 10^{-43} and 10^{-40} m^5. From this hypotheses, a diffusion coefficient can be proposed according to the alpha activity concentration of the fuel:

$$D^* (m^2 \cdot s^{-1}) = 2.0 \times 10^{-41} (m^5) \cdot A (Bq \cdot m^{-3}) \quad (7)$$

Over periods exceeding 100 years, when the alpha activity in spent fuel begins to decrease, the following expression can be proposed for PWR fuel [45]:

$$D^* (m^2 \cdot s^{-1}) = 3.8 \times 10^{-24} t^{-0.77} (\text{year}) \quad (8)$$

For UOX fuel with a burnup of 60 $GWd \cdot t^{-1}_{iHM}$ the helium diffusion coefficient should thus be less than 10^{-25} $m^2 \cdot s^{-1}$ (for an alpha activity of about 10^{15} $Bq \cdot m^{-3}$). In order to demonstrate the existence of this diffusion component at a laboratory time scale the aging effect of alpha radiation must be accelerated by doping the sample with short-lived actinides to increasing the instantaneous dose. Another possibility is to analyze very ancient samples (natural analogs).

The existence of an athermal diffusion mechanism has been demonstrated in $^{238}PuO_2$ samples some thirty years old, but is difficult to quantify because of their initial characteristics, especially the high initial porosity of the sample pellets. The helium analysis results appear to confirm that the proportionality coefficient on the instantaneous activity (A) is less than 10^{-40} m^5. Considering the alpha activity of spent fuel, this component will not have a significant impact on the fraction released during the period in which evolution occurs in a closed system.

3.2.3 Helium Mobility and Behavior in Spent Fuel and Natural Analogs

Based on the measured release kinetics, a large fraction (more than 50%) of the helium appears to be bound to vacancy defects annealed between 1000 and 1300 K; this is consistent both with the findings of atomistic modeling studies and with the activation energy of diffusion, approximately 2 $eV \cdot at^{-1}$.

Studies of natural analogs have confirmed that these results obtained at high temperatures (> 800 K) can be extrapolated over very long time periods with no apparent effect of the instantaneous dose rate, which is high in the case of simulations with actinide-doped samples. They have also revealed the early formation of nanometric bubbles that are emptied only when they reach a sufficient size and concentration (through high-temperature coalescence in this case). Although the oldest natural uranium oxides contain bubbles with higher helium concentrations, no trapping has been observed at the grain boundaries.

This is also the case for experiments with UO_2 pellets at temperatures ranging up to 1300°C.

Studies of fuel irradiated in the reactor, necessarily simpler than for fuel containing no fission products, showed that no more than a small fraction of the helium could be released from the fuel at temperatures below 500°C at low hydrostatic pressure: i.e. gas located at the grain boundaries or in intergranular bubbles following irradiation. Conversely, no significant helium release has been detected to date in a pressurized fuel rod within this temperature range.

Although there is a general convergence of the various approaches on the trapping and diffusion acceleration roles of irradiation defects, some unresolved issues remain. Further investigation would be necessaryin the following areas to predict possible changes in the fuel, especially in the zones that sustained the greatest alpha damage, in which the helium concentration will quickly reach the solubility limit:

- The solubility limit itself, or the bubble precipitation limit, versus the helium concentration and temperature.
- Modifications in the helium behavior and release kinetics in contact with fission gas bubbles in spent fuel.
- Exploration and validation of the proposed mechanisms according to the damage level due to alpha decay in the range from 1 to 20 or 30 dpa (e.g. simulation of $(U,Pu)O_2$ aggregates). Between damage induced by alpha doping for a few years or decades and the hundred or more dpa obtained over millions of years, it remains difficult to extrapolate from an "operational model" of helium behavior.
- Possible helium locations in the crystal lattice and especially interactions between helium and different types of vacancy defects.
- Mechanical strength of spent fuel — or at least fuel simulated by implantation — in contact with intra- and intergranular gas bubbles. The impact of intergranular bubbles on the mechanical strength of the fuel remains an unknown factor.
- The effect of irradiation in the reactor on helium mobility in the fuel. A few irradiation experiments have been carried out with heavy ions simulating the effect of fission products or alpha damage (electronic defects or heavy nucleus recoil defects). Following these initial experiments, which produced results apparently in contradiction with the helium release sometimes observed in the reactor and in doped fuel, the issue should be investigated in greater detail by taking into account the damage temperature and the dose accumulation kinetics.

3.3 Hydrogen Transfer in Cement Materials

The unsaturated conditions considered here are relevant to the evolution of cement materials under atmospheric conditions and to the determination of the specific hydrogen transfer properties of container materials in interim storage or reversible disposal.

3.3.1 Desiccation – Dehydration

Desiccation and drying of cement material designate the elimination of free water as a result of moisture imbalance: “drying” refers to water elimination when the material is placed in air with a relative humidity below its own internal relative humidity, whereas “self-desiccation” refers to a decrease in the moisture content of the material under endogenous conditions. “Dehydration” designates the release of constituent water (i.e. water chemically bound in hydrates) as a result of a temperature rise.

In the case of relatively impermeable materials such as cement, the weight loss during drying results mainly from moisture transfer in liquid form [46]. Water elimination has several consequences:

- Drying makes it more difficult for aggressive ionic agents to penetrate into cement materials by diffusion via the interstitial liquid.
- As the material dries, negative capillary pressure occurs in the pores creating tensile stresses that result in material shrinkage, and can lead to cracking and diminished mechanical strength.
- As the material dries, its porosity is less occupied by the interstitial solution and can constitute a pathway for percolating gas transfer. This pathway can allow penetration of aggressive gases, but can also allow gas release without deteriorating the material. These two issues are addressed below.

3.3.2 Atmospheric Carbonation

In unsaturated media, weathering by carbon dioxide is one of the main phenomena limiting the durability of cement materials. Degradation due to the reactivity of CO_2 in alkaline media occurs by neutralization of the cement hydrates by the acid formed by the dissolved gas.

The phenomenology thus involves both gas transfer and reactivity in the aqueous phase. It consists in the diffusion of atmospheric carbon dioxide in the concrete pores and in its dissolution on contact with the basic interstitial solution of the cement paste according to the following reaction:

$$CO_2 + 2OH^- \leftrightarrow CO_3^{2-} + H_2O \quad (9)$$

This dissolution entails progressive neutralization of the bases contained in the cement interstitial solution and leads to dissolution of the cement hydrates — especially those that buffer the pH at the highest values such as Portlandite ($Ca(OH)_2$). When it has been entirely consumed, or when it is no longer accessible [47, 48], carbonation then significantly affects the calcium silicate hydrates (C-S-H). The degradation of the cement mineral assemblage and the drop in the pH, which can reach 9 at the final stages of carbonation, can result in depassivation and corrosion of any steel rebars in the concrete.

Moreover, calcium carbonate ($CaCO_3$) microcrystals formed from the hydrates can partially obstruct the concrete pores if their molar volume exceeds that of the hydrated phases. This results in decreased porosity and a drop in the material permeability with respect to aggressive gaseous or ionic agents [49-51]. Filling of the pores is particularly prominent in the case of carbonation of CEM I-based

materials. Furthermore, structural water released locally during the carbonation reaction increases the *in situ* pore saturation [51] and thus helps to protect the material against the penetration of aggressive gaseous elements.

These phenomena impact the durability of cement materials widely used in civil engineering structures; they have been largely studied and several models have been proposed. However, as these issues are not specific to the use of cement materials for nuclear waste packages, the reader is invited to refer to the literature, for example [51]. In this document, as long as hydrogen transfer is concern, the carbonation impact will be taken into account only as a porosity modifier.

3.3.3 Hydrogen Transfer in Cement Materials

The long-term management of intermediate-level radioactive waste (ILW), either in a reversible deep geological repository or in temporary near-surface storage, will be accompanied by the production of gas generated by metal corrosion, by the activity of microorganisms, or by radiolysis. As several waste management concepts are still being considered, the amount of gas that would be released is uncertain. Most of the waste packages envisaged involve cement-based materials either as concrete containers or as primary encapsulating grout. As already noted, cement-based materials can be considered as multiphase porous media composed of a solid phase (a porous skeleton) in metastable chemical equilibrium with a liquid phase (pore water) and a gaseous phase (air, water vapor). Depending on whether the context is a closed environmental system and on the context of use (reversible or post-closure phase), these porous materials may or may not be water saturated, offering a path for gas transfer through the porosity.

Four basic modes of gas transfer can be considered in porous media: Knudsen diffusion, molecular diffusion, surface diffusion, and viscous flow. Three of these phenomena are related to concentration or partial pressure gradients (molecular diffusion, Knudsen diffusion, and surface diffusion), whereas one is related to the total pressure gradient (viscous or bulk flow). It is therefore possible to evaluate the transfer properties of cement paste, which is the main porous component in concrete, under a concentration gradient and a total pressure gradient corresponding respectively to a low and a high gas production rate. For each gas transfer mode, the gaseous flows through the hardened cement paste can be related to their formulation parameters, mainly the water-to-cement ratio and the nature of the cement used, and therefore to their pore structure.

3.3.3.1 Pore Structure of Cement Pastes

The porosity accessible to water, determined by drying at 60°C, is indicated for the three candidate materials in Table 2.

Table 2 Porosity accessible to water of the cement paste

Nature of cement	Water/cement ratio	Porosity accessible to water (%)
CEM I	0.35	27%
CEM I	0.45	34%
CEM V	0.45	35%

Unsurprisingly, whatever the type of cement, the higher the w/c ratio the greater the total porosity [52]. Moreover, at a given w/c ratio, the porosity of CEM V-based materials is greater than for CEM I-based materials [52]. These points are also clearly illustrated by the cumulative intruded pore volumes obtained by Mercury Intrusion Porosimetry (MIP) (Figure 15).

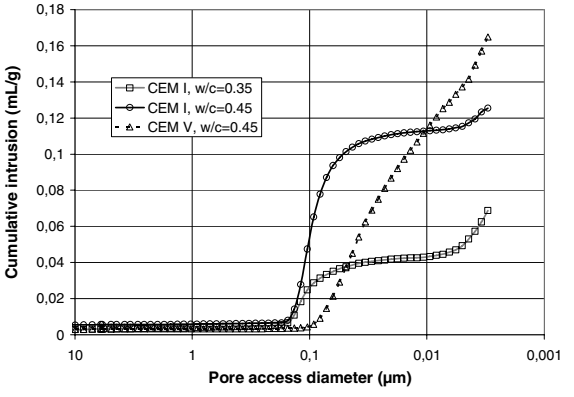

Fig. 15 CEM I (w/c = 0.35 and 0.45) and CEM V (w/c = 0.45) cement paste cumulative intruded pore volumes obtained by MIP

According to this plot, the threshold diameter — the minimum diameter of pores forming a continuous network through the cement paste [53] — varies with the type of cement and the w/c ratio. For the cement pastes considered here the threshold diameter increases slightly with the increasing water/cement ratio, but appears to depend to a greater extent on the nature of the cement paste: it is much larger for CEM I-based materials (about 150 nm for both pastes) than for CEM V-based materials (92 nm). This corroborates the idea that the capillary porosity is less continuous in mature CEM V cement pastes than in CEM I cement pastes [21]. Moreover, several researchers have found that the durability of cement paste is more sensitive to the threshold diameter than to the total porosity [54, 55].

3.3.3.2 Gas Diffusion through Cement Paste

The overall gas movement arising from concentration or partial pressure gradients, referred to here as diffusion, is assumed to result from a combination of molecular and Knudsen diffusion. The total flow of species i for a binary mixture of gas species i and j can then be written [56]:

$$J_i = J_{D,i} + J_{K,i} = -D_i \nabla c_i \tag{10}$$

where D_i is the combined molecular-Knudsen diffusion coefficient of species *i* in the porous medium, $J_{D,i}$ the diffusive molecular flow of gas *i* for a binary mixture and $J_{K,i}$ the diffusive Knudsen flow. The diffusion coefficients plotted in the following figures are the combined molecular-Knudsen diffusion coefficient of hydrogen in the cement paste samples.

3.3.3.2.1 Impact of w/c Ratio and Cement Type on Hydrogen Diffusion and Its Relation to Cement Paste Microstructure. The diffusion coefficients measured on CEM I cement pastes with w/c ratios of 0.35 and 0.45 and on CEM V (w/c = 0.45) are plotted in Figure 16 versus the degree of water saturation of the cement paste samples. The average diffusion coefficients obtained from at least three different measurements are also reported, joined by solid lines. The data near 100% water saturation (about 10^{-13} m^2/s) are based on hydrogen analysis corresponding to the chromatograph resolution limit (0.01%), and close to the ionic diffusion coefficient in cement-based materials.

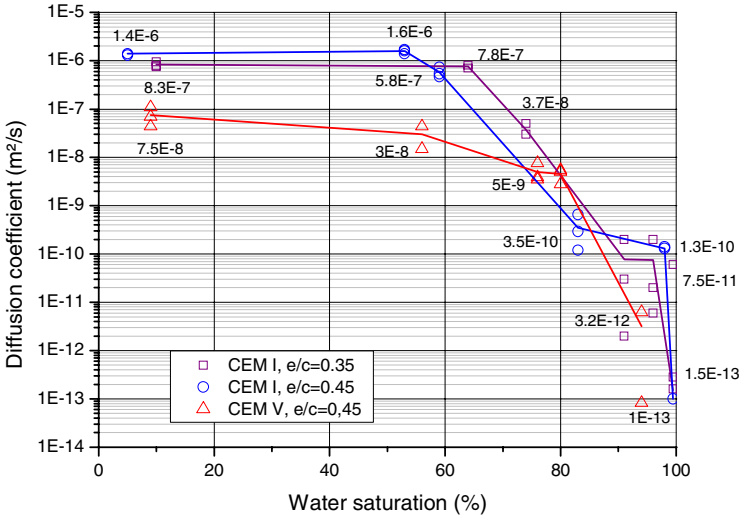

Fig. 16 Hydrogen diffusion coefficients versus water saturation for CEM I (w/c = 0.35 and 0.45) and CEM V (w/c = 0.45) cement paste samples (adapted from [57])

3.3.3.2.2 Comparison of CEM I Materials. Despite their different total porosities (Table 2), the overall behavior of both CEM I cement pastes is very similar: the diffusion coefficients are stable at about 10^{-6} m^2/s from 0% to 60% water saturation; the slope then rises until 82% water saturation, reaching a plateau at 10^{-10} m^2/s for 93% water saturation. Despite the greater uncertainty of the data near 100% water saturation, the diffusion coefficients appear to drop to about $10^{-13} m^2/s$, a value near that of the diffusion coefficients of ionic species in cement-based material pore solution [58].

The desaturation of smaller C-S-H pores, corresponding to the values at a low degree of water saturation and generally representing about 50% of the total porosity, does not lead to increased hydrogen diffusivity in the hardened cement pastes. This can be explained either by the very extensive porous network already available to gas diffusion at this desaturation state or by the small size and highly disorganized aspect of high-density C-S-H, which hinders their capacity for gas diffusion.

3.3.3.2.3 Comparison of CEM I and CEM V Materials. Despite their similar total porosities (Table 2), the overall behavior differs from one hardened cement paste to another. For up to 60% water saturation, each material has stable diffusion coefficients of about 10^{-6} m^2/s for CEM I-based paste and 5×10^{-8} m^2/s for CEM V-based paste. For the CEM I material, the plateau is followed by a decline to 10^{-10} m^2/s at 98% water saturation. From this point a small increase in water saturation leads to a very sharp drop in the diffusion coefficient. For CEM V material, the decrease in hydrogen diffusivity is slower and leads to a diffusion coefficient equal to 4.5×10^{-9} m^2/s at 80% water saturation. From this point the curve slopes rapidly down to about 3×10^{-12} m^2/s at 96% water saturation.

Regardless of the material, the diffusion coefficient curves do not vary significantly from the dry state up to 50% water saturation, suggesting that small C-S-H pores, much more present in CEM V systems than in CEM I-based materials [26], do not contribute significantly to hydrogen gas transfer. The differences between the two hardened cement pastes are thus related to the differences existing in the low density C-S-H pores and the capillary pore network.

3.3.3.3 Gas Permeation through Cement Paste

The permeability of a porous material characterizes the extent to which it can be traversed by a fluid with a pressure gradient. In the case of gas arising from corrosion or radiolysis, the fluid is inert with respect to the material. The term "intrinsic permeability" is used when the permeability does not depend on the nature of the fluid. For incompressible fluids the permeability coefficient k [m^2] is defined by the Darcy relation:

$$q = -\frac{k}{\mu} A \frac{dP}{dx} \tag{11}$$

where q is the volume flow rate of the fluid, with a dynamic viscosity μ, flowing through a material dx thick with a cross-sectional area A [m^2] subjected to a gradient dP.

In the case of compressible fluids such as gases the Darcy relation is not directly applicable and fluid compressibility must be taken into account. The effective gas permeability k_g was calculated with Darcy's law as modified by the Hagen-Poiseuille relation:

$$k_g = \frac{2Q_{P2}LP_2\mu}{S(P_1^2 - P_2^2)} \tag{12}$$

where k_g is the effective gas permeability (m^2), Q_{P2} is the flow rate measured at pressure P_2 (m^3·s^{-1}), L is the specimen length (m), μ is the dynamic gas viscosity (Pa·s), S is the specimen cross sectional area (m^2), P_1 is the absolute injection gas pressure (Pa) and P_2 is the exit gas pressure (Pa).

3.3.3.3.1 Impact of Water/Cement Ratio and Water Content on Nitrogen Permeability and Its Relation to the Cement Paste Microstructure. It is well known that the gas permeability properties of cement-based materials are

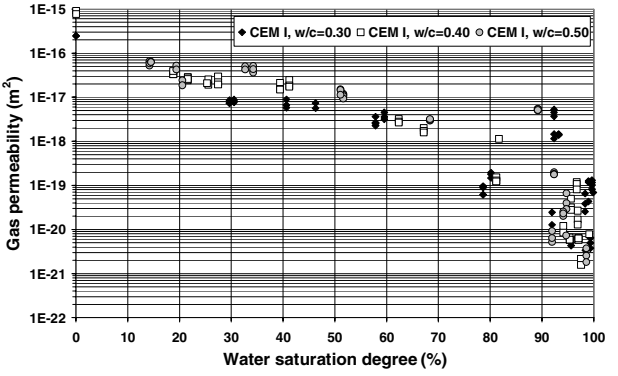

Fig. 17 Effective gas permeability for CEM I pastes (w/c = 0.30, 0.40 and 0.50) versus the average internal moisture content (water saturation)

extremely sensitive to various factors and above all to the internal moisture content, microstructural properties and potentially to the mechanical damage state (cracking state) of the materials [59, 60]. It is thus essential, when comparing the gas convective transfer capability of such materials, to compare them at known water saturation values. Figure 17 provides an example of the variation of the gas (N_2) permeability of hardened CEM I cement pastes at various w/c ratios (0.30, 0.40 and 0.50), characterized by average water porosities of 23, 30 and 35%, respectively. Overall, between a few percent and approximately 100% water saturation, the permeability decreases by about five orders of magnitude (10^{-16} to 10^{-21} m^2). Another remarkable result is that despite the variability and dispersion of the permeability values, the hierarchy between less and more porous materials — i.e. materials with lower and higher permeability — is well respected. Therefore, 0.50 w/c CEM I pastes are more permeable than 0.30 w/c pastes, and 0.40 w/c pastes exhibit intermediate behavior. Another noteworthy aspect is that the greater the water saturation, the higher the dispersion. This result is related to the difficulty of gas migration when the internal moisture content increases in the porous network.

Figure 18 provides further data on the effect of the cement paste microstructure. This figure shows the gas permeability variation versus the water saturation for various series of CEM I and CEM V pastes with different specific areas, designated *sa* (in cm^2/g) in this graph.

Figure 18 shows that the permeability of CEM V pastes varies on average between 10^{-15} m^2 and 10^{-20} m^2 for the water saturation domain considered, whereas CEM I pastes are about one order of magnitude less permeable than CEM V pastes. Although CEM V materials are characterized by globally smaller pore accesses, their total porosity is greater (refer to section 3.3.3.1). The effect of the finer pore distribution of CEM V pastes is therefore offset by a larger pore volume accessible to gas transfer. The total porosity thus appears to have a significant role in convective gas transfer in such porous media. Microstructural discrepancies are not great enough to have a significant effect on the permeation regime.

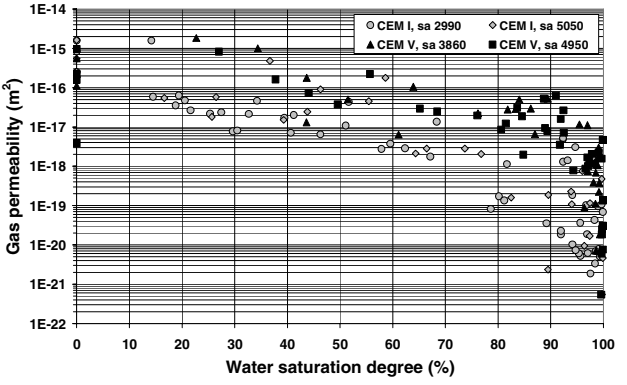

Fig. 18 Effective gas permeability in CEM I and CEM V pastes (w/c = 0.30, 0.40 and 0.50) characterized by various specific surface areas (*sa*, in cm^2/g) versus internal average moisture content (water saturation)

However, the discrepancy between CEM I and CEM V materials in terms of convective transfer is more significant when considering the permeability measured at high water saturation. For CEM I pastes the gas permeability slowly decreases between 10% and 80% water saturation, confirming the key role of water saturation. Above 80% saturation the permeability decreases even more significantly. The gas permeability variation of CEM I materials is smooth and progressive, even if a threshold is observed near 70–80% water saturation. For the CEM V materials, the change occurs more suddenly and at higher water saturation (80–90%). This phenomenon is believed to reflect the influence of cement paste microstructure on gas transfer [57].

Conversely, the dispersion of permeability values is greater between 80% and approximately 100% water saturation: at high water saturation, gas migration in the porous medium is very difficult as the capillaries are filled with water. Gas outflows are thus extremely irregular. Moreover, due to the gas injection pressure itself, gas can be transferred along unstable preferential pathways in which water can be temporarily displaced. Theoretically, gas migration by convection in water-saturated porous media is not possible. It must be assumed that the samples are not fully water-saturated and that there are sufficient passages for gas transfer. It can be assumed that near saturation the porous medium has reached a critical state (percolation threshold) involving random gas transfer.

3.3.3.3.2 Gas Permeability: From Hardened Cement Paste to Concrete Material. Figure 19 compares experimental gas permeability measurements on hardened CEM I pastes at various w/c ratios with two concrete samples. Concrete data were obtained from the French AFREM working group in the late 1990s [61].

The pastes and concretes exhibit relatively similar behavior. Except for the property differences relative to the pore network (lower porosity, connectivity,

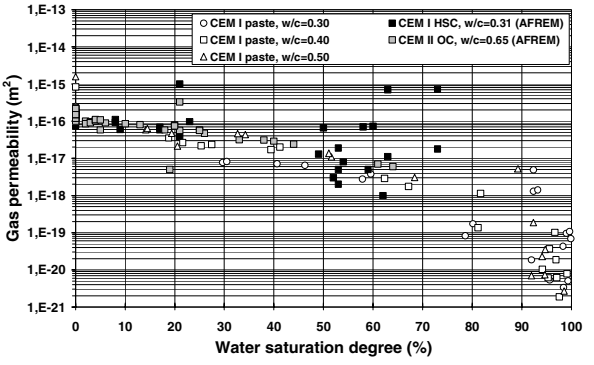

Fig. 19 Effective gas permeability of CEM I pastes (w/c = 0.30, 0.40 and 0.50), a high-strength CEM I concrete (w/c = 0.31) and ordinary CEM II concrete (w/c = 0.62) [61] with average internal moisture content (water saturation)

effect of aggregates) the two types of materials differ only slightly. Previous authors [62] have already reported that the addition of aggregates to a hydrated paste did not automatically lead to decreased permeability. Large aggregates appear to enhance convective gas transfer capability in concrete. On the other hand, the presence of microcracks and the higher porosity in a few specific domains such as the transition zones around the aggregates also appear to contribute to the higher gas permeability of concrete.

The experimental investigation of gas diffusion and permeation through the cement paste porosity shows that the gas transfer capability of the material depends on two interdependent factors: the water saturation state and the pore structure. Gas diffusion through hardened cement pastes depends to a large extent on the water saturation of the material. The diffusion coefficients range from 10^{-13} m^2/s for nearly saturated samples to 10^{-6} m^2/s for dry CEM I pastes and 8×10^{-8} m^2/s for dry CEM V hardened cement pastes. These limits depend more on the pore size distribution than on the total porosity of the materials. Depending on their size, each pore family exhibits different gas diffusion properties: the larger pores in hardened cement paste (mainly capillary pores) are of major importance in gas diffusion, whereas desaturation of the smaller pores does not lead to increased hydrogen diffusivity in the material. A more porous material with a smaller pore distribution, mainly in the microporous range, will thus present lower gas transfer capability at all saturation levels, even in nearly dry materials.

Concerning gas permeation, it is well known that cement-based material properties are extremely sensitive to the internal moisture content. Effective permeability values range from 10^{-21} m^2 for nearly saturated samples to 10^{-15} m^2/s for dry hardened cement pastes. Despite the variability and dispersion of the permeability, the hierarchy between less and more porous materials leads to lower and higher permeability total porosity. In these particular porous media, the total porosity seems to play a significant role in convective gas transfer.

Microstructural discrepancies are probably not sufficient to significantly influence the permeation regime when comparing CEM I and CEM V materials. However, the introduction of sand and aggregates in hydrated pastes, i.e. formulation of mortars and concretes, changes the pore distribution and affects their permeability, which is less sensitive to the pore distribution than gas diffusion. Models of these transfer phenomena, which are specific to nuclear waste management, are not yet been available, but will probably be developed in the coming years.

4 Transfer Phenomena Related to the Package Evolution in Contact with Water: Physicochemical Changes and Radioelement Transfer

If the geological disposal is located in a previously water-saturated geological environment, the hydraulic head will gradually be restored. The transient resaturation period concerning both the constructions and the surrounding rock formation is a complex phenomenon that depends not only on the permeability of the media involved (geological environment, repository materials, etc.) but also thermal or physical and chemical processes involving the waste itself, such as gas production due to metal corrosion, microbiological activity or radiolysis. The mean resaturation time cannot be estimated simply, and is directly dependent on the concepts selected and implemented in the repository. In any event, water will eventually come into contact with the waste package, and therefore with the materials. The overall system in which mass transfers occur can be then be considered a water-saturated open system. Two major interdependent phenomena will be examined in this context:

- aqueous alteration of the waste package materials,
- solubilization and transport of radionuclides released by leaching.

The phenomenology of degradation by water is discussed here for spent fuel, nuclear waste glass, and cement materials. This itemized approach is a rational way to address transport processes beginning with a material of homogeneous composition and initial microstructure at mesoscopic scale, and leading to a material in which the characteristic pore dimensions cover several orders of magnitude and which initially comprises a complex assemblage of mineral phases. By virtue of their intermediate position in terms of phenomenological complexity, but also thanks to extensive research on characterization and modeling carried out in this area[4], nuclear waste glass provides an opportunity for a detailed discussion of the issues arising from aqueous leaching of materials. The glass surface is altered by several chemical processes at rates that depend on many parameters

[4] In many countries that produce or receive nuclear waste glasses (France, England, the United States, Germany, Switzerland, Belgium, Japan, the Netherlands) these materials are used to condition a large fraction of the initial radiotoxicity spectrum, and have therefore been the subject of very detailed research for many years.

including the temperature, the groundwater composition, the nature of the surrounding solid materials, and the processes affecting the transport of dissolved species. The aqueous alteration of nuclear waste glass must therefore be investigated mainly through an approach coupling chemistry and transport phenomena. Coupling occurs at different scales: at atomic scale when water penetrates into the glass structure; at mesoscopic scale as the gel forms; at microscopic scale for the reactions between the glass and the surrounding solids; and at macroscopic scale if changes are taken into account that affect the repository vault. The system complexity further increases if the glass is assumed to be fractured: leaching then also depends on the behavior of the internal crack network.[5]

In addition to aqueous leaching phenomena, water is also a transfer vector for radionuclide ions in the materials. The objective is to specify and quantify the underlying mechanisms of radioelement retention, as well as to describe radionuclide transport. Of the three types of materials considered in this document, cement materials are subject to the widest range of retention phenomena. As they are also intrinsically porous media, radioelements that are not retained can migrate in response to a concentration gradient.[6]

4.1 Aqueous Alteration of Waste Package Materials

4.1.1 Aqueous Leaching of Spent Fuel and Oxidizing Dissolution of UO_2

The reactivity of a polycrystalline UO_2 surface under alpha irradiation in contact with water has been widely investigated experimentally in recent years [63-70], motivated by the prospect of direct disposal of spent fuel in a deep geological repository. In this regard it is worth remembering that over the long term, alpha radiolysis of water — which produces oxidizing and reductive species, radicals ($HO^{\bullet}$, $O_2^{\bullet -}$, $HO_2^{\bullet}$, e^-_{aq}, $H^{\bullet}$) or molecules (H_2O_2, etc.) — can lead to the onset of oxidizing conditions at the UO_2/water interface (redox disequilibrium with the environment) and accelerate the dissolution of the spent fuel UO_2 matrix under repository conditions [71-73]. The effects of alpha irradiation have been studied through two experimental approaches in recent years by leaching with chemical or electrochemical monitoring:

- external irradiation of a UO_2/water interface by a He^{2+} particle beam (3.3×10^{10} $\alpha \cdot cm^{-2} \cdot s^{-1}$ and 3.3×10^{11} $\alpha \cdot cm^{-2} \cdot s^{-1}$) generated by a cyclotron [64, 65] or using alpha sources [74];

[5] Although this topic concerns nuclear glass, we have found it interesting under certain conditions to use data for simplified glass compositions, natural (basaltic or obsidian) glasses, or archaeological (Roman or medieval) glasses, particularly when investigated as natural analogs.

[6] To simplify this document for the reader, the retention phenomena occurring in the waste package constituent materials are discussed separately from the description of aqueous alteration phenomena.

- UO_2 matrices doped with alpha-emitters ($^{238/239}Pu$, ^{233}U) to reproduce the evolution of alpha activity in spent fuel in a nuclear waste repository [63, 66-70].

Combined transport and radiolysis models [75, 76] have been developed in an attempt to reproduce experimental data and determine the oxidation/dissolution of UO_2 under α radiolysis of water. Our objective here is to describe the basis of a model coupling chemistry and transport, and to determine the extent to which it can reproduce experimental data on uranium release in solution and on the production of hydrogen peroxide by water radiolysis. Computed findings are compared here with experimental data for external irradiation by helium nuclei of a UO_2/water interface (pure aerated or deaerated water) [64, 65].

4.1.1.1 Description of the Radiolytic-Transport Model

The variation of the concentrations of the species generated by water radiolysis is described by equation (13), in which (a) represents a second-order reaction, (b) is a first-order reaction term, (c) is the contribution of radiolytic species and (d) is the diffusion term.

$$\frac{\partial C_i}{\partial t} = \underbrace{\sum_{j,k} n_{jki} M_{jki} \left[C_j\right]\left[C_k\right]}_{(a)} + \underbrace{\sum_{j} n_{ji} M_{ji} \left[C_j\right]}_{(b)} + \underbrace{K G_i \dot{D}(t)}_{(c)} + \underbrace{D \frac{\partial^2 C_i}{\partial x^2}}_{(d)} \qquad (13)$$

C_i is the concentration of species i (mol·L^{-1}), n_{jki} and M_{jki} depend respectively on the stoichiometric coefficients and the kinetic constants (k in dm^3·mol^{-1}·s^{-1}) of the reactions, K is the radiolytic conversion factor between G_i and $\dot{D}(t)$ equal to 1.036427×10^{-7} if the dose rate is expressed in Gy·h^{-1}, G_i corresponds to primary radiolytic yield of species i (molecules·100 eV^{-1}), $\dot{D}(t)$ is the dose rate (Gy·h^{-1}) and D is the diffusion coefficient (cm^2·s^{-1}).

The first three terms in the right member of eq. (13) provide a mathematical description of the reactions constituting the general water radiolysis model developed by Christensen [77] (Table 3).

Table 3 Reaction mechanism and rate constants for pure water radiolysis

Reactions	Rate constant (dm^3.·mol^{-1}.·s^{-1})
$OH^{\cdot}+H_2=H_2O+H^{\cdot}$	3.4×10^7
$OH^{\cdot}+H_2O_2=H_2O+HO_2^{\cdot}$	2.7×10^7
$OH^{\cdot}+O_2^{\cdot-}=OH^-+O_2$	1.0×10^{10}
$OH^{\cdot}+HO_2^{\cdot}=H_2O+O_2$	7.1×10^9
$OH^{\cdot}+OH^{\cdot}=H_2O_2$	5.5×10^9
$OH^{\cdot}+OH^{\cdot}=H_2O+O^{\cdot-}$	1.2×10^{10}
$OH^{\cdot}+HO_2^{\cdot}=HO_2^{\cdot}+OH^-$	7.5×10^9

Table 3 (*continued*)

Reactions	Rate constant ($dm^3.mol^{-1}.s^{-1}$)
$OH^- + H^- = H_2O$	7.0×10^9
$OH^- + e^- = OH^- + H_2O$	3.1×10^{10}
$OH^- + O^{\cdot -} = HO_2^-$	1.8×10^{10}
$O^{\cdot -} + H_2O = OH^- + OH^-$	1.7×10^6
$e^- + O_2 = O_2^{\cdot -} + H_2O$	1.9×10^{10}
$e^- + H_2O_2 = OH^- + OH^- + H_2O$	1.1×10^{10}
$e^- + O_2^{\cdot -} = HO_2^- + OH^-$	1.3×10^{10}
$e^- + H^+ = H^- + H_2O$	2.3×10^{10}
$e^- + H_2O = H^- + OH^- + H_2O$	1.9×10^1
$e^- + HO_2^- = O^{\cdot -} + OH^- + H_2O$	3.5×10^9
$e^- + e^- = H_2 + 2OH^-$	5.5×10^9
$e^- + HO_2^- = HO_2^- + H_2O$	2.0×10^{10}
$e^- + H^- = H_2 + OH^-$	2.5×10^{10}
$H^- + HO_2^- = H_2O_2$	2.0×10^{10}
$H^- + H_2O_2 = H_2O + OH^-$	9.0×10^7
$H^- + OH^- = e^-$	2.2×10^7
$H^- + O_2 = HO_2^-$	2.1×10^{10}
$H^- + O_2^{\cdot -} = HO_2^-$	2.0×10^{10}
$H^- + H^- = H_2$	7.8×10^9
$HO_2^- + O_2^- = O_2 + HO_2^-$	9.6×10^7
$HO_2^- + HO_2^- = H_2O_2 + O_2$	8.4×10^5
$HO_2^- = H^+ + O_2^{\cdot -}$	8.0×10^5
$H^+ + O_2^- = HO_2^-$	5.0×10^{10}
$H^+ + HO_2^- = H_2O_2$	2.0×10^{10}
$H_2O_2 = H^+ + HO_2^-$	3.56×10^{-2}
$H^+ + OH^- = H_2O$	1.43×10^{11}
$H_2O = H^+ + OH^-$	2.6×10^{-5}
$O_2^- + O_2^- = O_2 + HO_2^- - H^+$	1.8×10^9

This set of reactions was also used by Kelm and Bonhert [78] and the uranium file is given in Table 4.

Table 4 Reaction mechanism and rate constants for uranium dioxide oxidation

Reactions	Rate constant ($dm^3.\cdot mol^{-1}.\cdot s^{-1}$)
$UO_2+OH^{\cdot} = UO_3H$	4.0×10^{8}
$UO_2+H_2O_2 = UO_3H+OH^{\cdot}$	2.0×10^{-2}
$UO_2+HO_2^{\cdot} = UO_3H+H_2O_2-H_2O$	2.0×10^{8}
$UO_2+O_2^{-} = UO_3H+HO_2^{-}-H_2O$	2.0×10^{8}
$UO_2+O_2 = UO_3H+HO_2^{\cdot}-H_2O$	1.0×10^{-4}
$UO_3H+UO_3H = UO_3+UO_2+H_2O$	3.0
$UO_3H+OH^{\cdot} = UO_3+H_2O$	8.0×10^{8}
$UO_3H+e^{-} = UO_2+OH^{-}+H_2O$	5.0×10^{8}
$UO_3H+H_2O_2 = UO_3+H_2O+OH^{\cdot}$	2.0×10^{-2}
$UO_3H+O_2^{-} = UO_3+HO_2^{-}$	2.0×10^{8}
$UO_3H+O_2^{-} = UO_2+OH^{-}+O_2$	4.0×10^{8}
$UO_3H+HO_2^{\cdot} = UO_3+H_2O_2$	4.0×10^{8}
$UO_3+e^{-} = UO_3H+OH^{-}-H_2O$	5.0×10^{7}
$UO_3+O_2^{-} = UO_3^{-}+O_2$	4.0×10^{6}
$UO_3^{-}+H_2O = UO_3H+OH^{-}$	1.0×10^{1}
$UO_3H+H = UO_2+H_2O$	4.5×10^{6}
$UO_3+H = UO_3H$	4.5×10^{5}
$UO_3+HO_2^{\cdot} = UO_3H+O_2$	4.0×10^{6}
$UO_3H+O_2 = UO_3+HO_2$	1.0×10^{-4}

Moreover, the alpha primary radiolytic yields used for the simulation are given in Table 5.

Table 5 Primary radiolytic yields for alpha irradiation of neutral water used in the model

Radiolytic species	G_α (molecules·100 eV^{-1})
$OH^{\cdot}$	0.24
e^{-}_{aq}	0.06
H	0.21
H_2	1.3
H_2O_2	0.985
H^{+}	0.06
OH^{-}	0
$HO_2^{\cdot}$	0.22
$-H_2O$	2.71

Chemsimul [79] was used to compute the first three terms of equation (14):

$$\frac{\partial C_i}{\partial t} = \sum_{j,k} n_{jki} M_{jki} \left[C_j\right]\left[C_k\right] + \sum_{j} n_{ji} M_{ji} \left[C_j\right] + KG_i \dot{D}(t) \tag{14}$$

Basically, Chemsimul is able to assemble the Ordinary Differential Equation (ODE) system from all the individual pieces in the reaction system. ODE systems in chemical kinetics are nonlinear and often autonomous. LSODA solver from the Hindmarsh ODEPACK collection is used to solve the systems in Chemsimul [79].

The last term (d) of equation (13) represents diffusion given by Fick's second law. Coupling between the radiolysis and transport models is achieved by a finite difference method and the diffusion equation is solved using an implicit scheme:

$$C_i^n = (1+2\lambda)C_i^{n+1} - \lambda\left(C_{i+1}^{n+1} + C_{i-1}^{n+1}\right) \tag{15}$$

where $\lambda = D\dfrac{\Delta t}{\Delta x^2}$.

D is the diffusion coefficient ($m^2 \cdot s^{-1}$), Δt is the time step (s), Δx represents the layer size (m), i the space index and n the time index.

The finite difference method (implicit scheme) always ends by solving a linear equation system given by:

$$[A] \cdot x = B \tag{16}$$

[A] represents a symmetric and tridiagonal matrix, x is the solution vector and B is the vector resulting from the boundary conditions.

One of the algorithms used to solve a linear system is the Gauss method. The aim of this method is to replace the matrix [A] by the product of two triangular matrices ([L] and [U]) having the same solution. The calculation procedure (coupling, boundaries conditions and initial conditions) is discussed below.

A similar approach has been implemented in a model named TraRaMo, which considers also explicitly the diffusion but is based on another kinetic code namely Macksima-Chemist [75].

4.1.1.2 Calculation Procedure

Initially the system is divided into an arbitrary number of layers (the number N depends on the system geometry and the computing time) and Chemsimul is used as a module in each layer. The first 40 micrometers are submitted to alpha radiation and beyond this distance the solution is composed of deionized water. To account for the system heterogeneity, a single layer of the UO_2 system is assumed to react as if uranium were in solution in a thin layer of water adjacent to the fuel (Figure 20). The alpha dose rate profile or Bragg curve can be taken into account to model the energy loss in water either for an alpha-doped pellet or for external irradiation.

The calculation proceeds iteratively. After supplying the input data (chemical reactions, diffusion coefficient (D), layer thickness (Δx), time step (Δt), dose rate, etc.), a Chemsimul file is created in each water layer. In all the calculations, $D = 10^{-5}$ $cm^2 \cdot s^{-1}$ for all the radiolytic species, $\Delta x = 10$ µm and $\Delta t = 0.05$ s. In the first layer (Figure 20), the input Chemsimul file is composed of the complete radiolytic scheme (Tables 4 and 5), i.e. the reactions between radiolytic species and uranium are taken into account. In the following three layers submitted to alpha irradiation (alpha dose rate profile or summation of Bragg curves, Figure 20), the kinetic scheme describing the alpha water radiolysis (Table 3) is

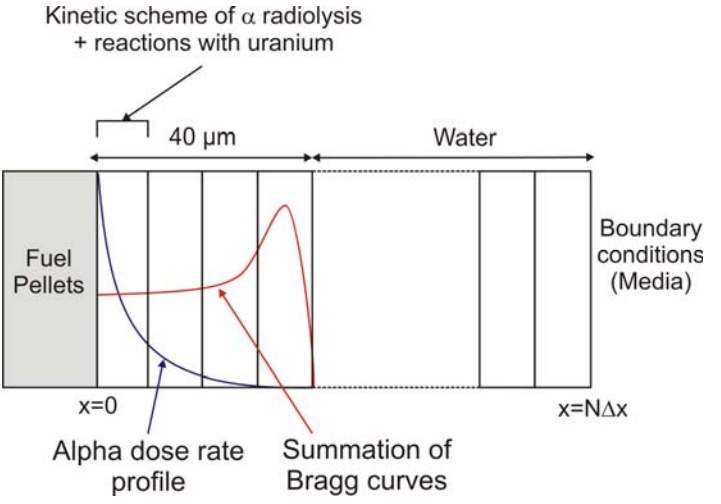

Fig. 20 Description of the system used for the calculation

used in the Chemsimul file. Finally, in all the other cells, the Table 3 is also used as kinetic scheme but the dose rate is zero (the range of alpha particles in water is approximately 40 µm).

The computation procedure is as follows: first a Chemsimul run is performed for each space increment. Then, from the concentration calculated by the Chemsimul kinetic code, the diffusion of species between the layers takes place by using a finite difference method. This coupling is done during the same time step:

$$\Delta t = \frac{\Delta x^2}{2D} \tag{17}$$

Equation (17) shows that the time step is a function of the layer thickness and the species diffusion coefficient. Consequently, according to the penetration length of the alpha emitters (approximately 40 µm) and the diffusion coefficient value, the time step is expected to be very short.

The boundary and initial conditions depend on the experimental conditions (aerated or deaerated media, Ar/H_2, pH, etc.) and are listed below:

- Initial conditions ($t = 0$)
  - $[UO_2] = 5 \times 10^{-4}$ mol·L^{-1}, in the first layer (Figure 20)
  - $[H^+]$ and $[OH^-] = 10^{-7}$ mol·L^{-1} (pH = 7),
  - $[O_2] = 2.5 \times 10^{-4}$ mol·L^{-1} and $[H_2] = 3.95 \times 10^{-10}$ mol·L^{-1} in aerated media,
  - $[O_2] = 1.23 \times 10^{-10}$ mol·L^{-1} and $[H_2] = 3.95 \times 10^{-10}$ mol·L^{-1} in deaerated media,
  - The concentration of all other radiolytic species is equal to 0.

- Boundary conditions
  - $[UO_2]= 5 \times 10^{-4}$ mol·L^{-1}, in the first layer for $x = 0$ (Figure 20) and = 0 for $x = N \cdot \Delta x$
  - Neumann boundary conditions are applied to all the other species.

$$\frac{\partial C_i}{\partial x}(0,t) = \frac{\partial C_i}{\partial x}(N \cdot \Delta x, t) = 0 \tag{18}$$

It is important to note that since the calculation proceeds in an iterative way, the concentrations resulting from diffusion at time t are used as initial conditions for the radiolysis calculations of the following time step $t + \Delta t$.

4.1.1.3 Limitations. Chemsimul [79] describes the kinetics of a set of chemical reactions in homogeneous media, whereas the system in question is heterogeneous and even includes an interface. Moreover, it is commercial software which mathematically limits the coupling with the diffusion equation because the Chemsimul run is first performed in each compartment and then diffusion takes place during the same time step.

Obviously, the calculation time increases as the layer thickness decreases. A tradeoff must therefore be found between the thickness and the number of layers. The relation between the calculation time and the main (numerical) parameters is shown in Table 6.

Table 6 Calculation time as a function of the time step and the number of layers

Δx (μm)	Δt (s)	Number of layers in 40 μm	Number of iterations for 1 h of leaching	Number of Chemsimul calculations carried out in the 40 μm layer	Calculation time to model 1 hour of leaching
1	5×10^{-4}	40	7200000	2.88×10^{8}	250 days
5	1.25×10^{-2}	8	288000	2304000	48.00 hours
10	0.05	4	72000	288000	6.00 hours
20	0.2	2	18000	36000	45 min

Moreover, the thickness of the water layer must be chosen with the same order of magnitude as the diffusion length of the radiolysis species [80]. Due to the calculation time, it is only possible to simulate one hour of leaching experiments. This type of model is thus suitable for data from short leaching experiments such as external irradiation lasting 1 hour.

The chemical reactions and kinetic constants concerning the effect of radiolytically generated species on dissolution of the UO_2 matrix do not appear to be very solidly established. Some heterogeneous reaction constants have been obtained by analogy with well-known kinetic constants for homogeneous metal ion reactions in water [81]. Furthermore, these constants used for the general scheme of radiolysis have then varied over time as the research progresses. For

example, for the $UO_2+H_2O_2 = UO_3H+OH^-$ reaction an experimental kinetic constant of 0.1 $dm^3 \cdot mol^{-1} \cdot s^{-1}$ was obtained in a nitric environment [81]. A value of 0.2 $dm^3 \cdot mol^{-1} \cdot s^{-1}$ was assumed by Christensen in 1994 for his radiolysis model [82] but was changed to 0.02 $dm^3 \cdot mol^{-1} \cdot s^{-1}$ a few years later [77].

Precipitation phenomena at the UO_2 surface are not taken into account in the model. An initial dissolved UO_2 concentration is specified in the first layer, which assumes that the surface is continuously renewed.

The primary radiolytic yields corresponding to alpha radiation are still not well known (especially at high flux) and can lead to calculation errors: the primary yields depend on the type of radiation (the effect of linear energy transfer), the dose rate and the water characteristics (deionization, impurities). At high LET values (alpha particles and ions) a very large number of clusters occurs over a short distance, cluster overlapping becomes a problem with very rapid recombination of radiation-generated radicals.

Finally, both molecules and radicals are assumed to diffuse with the same diffusion coefficient. If different diffusion coefficients are applied the calculation time step will not be the same for all species and the boundary conditions between each layer would have to be modified accordingly.

4.1.1.4 Comparison with Published Data

4.1.1.4.1 Aerated Conditions. The calculations were compared with some experimental results for external irradiation by helium nuclei of a UO_2/water interface already published in the literature [64, 65]. In this configuration, the alpha dose profile is well described by the summation of Bragg curves (Figure20) and an increase of the uranium release versus time is observed under alpha irradiation (Figure 21).

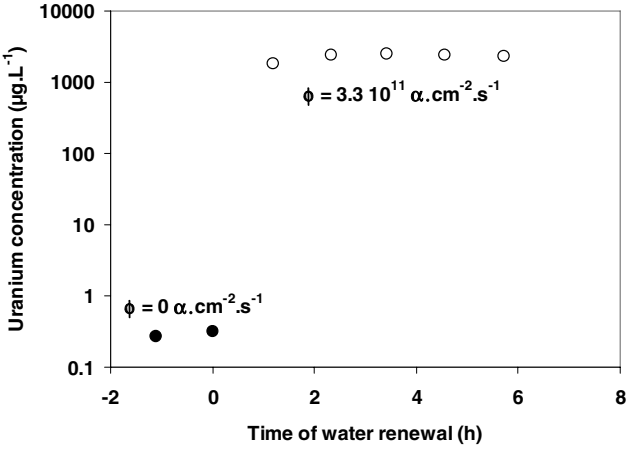

Fig. 21 Uranium release versus time (number of cycles) under alpha irradiation at a flux of 3.3×10^{11} $\alpha \cdot cm^{-2} \cdot s^{-1}$ in aerated media [65]

Figure 22 presents the calculation for 200 layers 10 µm thick irradiated for one hour in aerated media. Note the slight consumption of oxygen (O_2) and OH radicals at the interface, then a maximum concentration at the level of the Bragg curve. The $OH^{\bullet}$ radical concentration in solution decreases strongly to reach a steady state whereas the O_2 concentration remains equal to 2.5×10^{-4} mol·L^{-1} (aerated media). Hydrogen peroxide is also consumed at the UO_2 surface and its concentration is highest in the fourth layer (40 µm from the interface). The

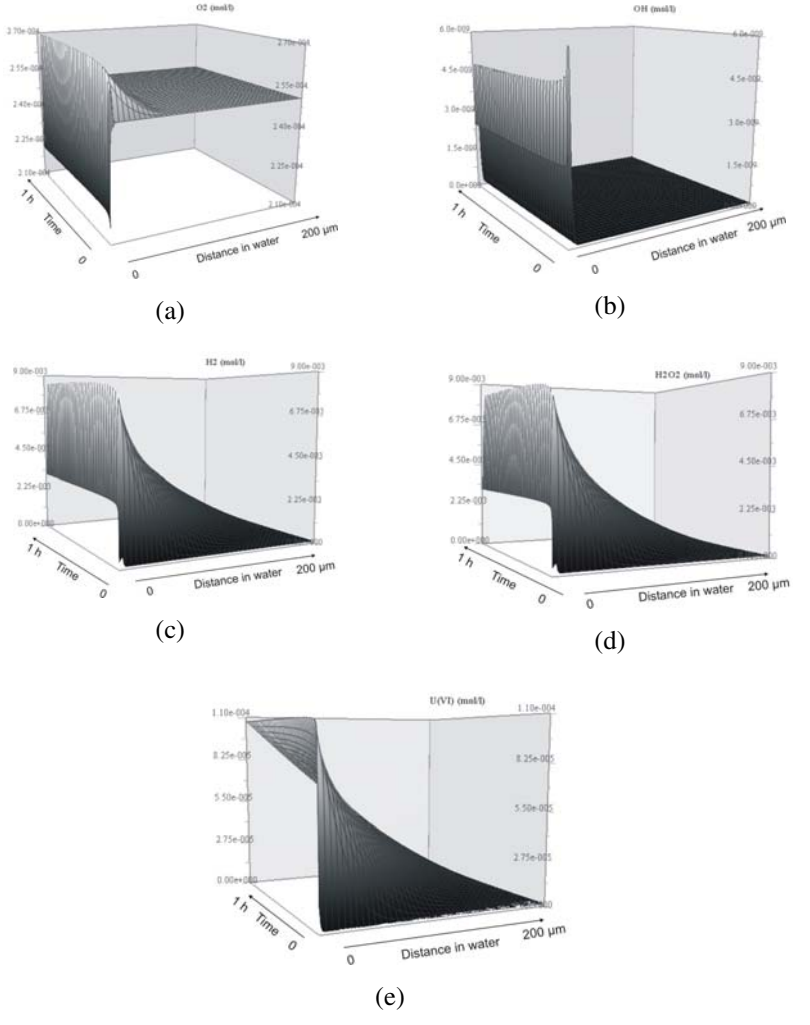

Fig. 22 Evolution of O_2 (a), $OH^{\cdot}$ (b), H_2O_2 (c), H_2 (d) and U(VI) (e) in the solution (Number of layers = 200, Experimental time = 1.00 h00). In aerated conditions, the boundary conditions are $[O_2]_{dissolved} = 2.5 \times 10^{-4}$ mol·L^{-1}mol.l^{-1} and $[H_2]_{dissolved} = 3.95 \times 10^{-10}$ mol·L^{-1}mol.l^{-1}. As the layer thickness is always 10 µm, the four local dose rates are: $D_{\alpha 1}=1.64 \times 10^{8}$ Gy.·h^{-1}, $D_{\alpha 2}=1.91 \times 10^{8}$ Gy.·h^{-1}, $D_{\alpha 3}=2.49 \times 10^{8}$ Gy.·h^{-1}, $D_{\alpha 4}=3.43 \times 10^{8}$ Gy.·h^{-1}

maximum H_2O_2 concentration is about 9×10^{-3} mol·L^{-1} near the interface and reaches 1.2×10^{-4} mol·L^{-1} in solution, which is approximately one order of magnitude below the experimental value [64, 65]. The consumption of oxidants in the first layer converts UO_2 to hexavalent uranium, which diffuses into solution. The U(VI) concentration 2 mm from the interface is about 3×10^{-6} mol·L^{-1}, corresponding to 720 $\mu g_U \cdot L^{-1}$ of uranium released in solution, while experimentally uranium in solution is 3 times higher (2280 ± 230 $\mu g_U \cdot L^{-1}$) (Figure 21). Finally, hydrogen (H_2) is produced in large amounts at the UO_2/water interface compared with its solubility in water (9×10^{-3} mol·L^{-1} vs 3.95×10^{-10} mol·L^{-1}). This production is essentially due to a radiolytic process and is probably related to the presence of hydrogen bubbles observed experimentally at the interface [64].

Calculations were also carried out at lower flux (3.3×10^{10} $\alpha \cdot cm^{-2} \cdot s^{-1}$) in aerated media. The four alpha dose rates at the first layers are one order of magnitude lower than in the case of high flux; the calculated hydrogen peroxide concentration is 1.8×10^{-5} mol·L^{-1} in solution and for U(VI) the concentration is 2.8×10^{-7} mol·L^{-1}, which corresponds to 67 $\mu g_U \cdot L^{-1}$. As in the case of high flux, the factor of 3 between the calculated and experimental results is maintained since experimentally U(VI) = 210 $\mu g_U \cdot L^{-1} \pm 20$ $\mu g_U \cdot L^{-1}$ and $[H_2O_2] = 4.8 \times 10^{-4}$ mol·L^{-1} [64]. The comparison between the experimental results and the calculation is given in Table 7.

Table 7 Comparison of calculated and experimental uranium and hydrogen peroxide concentrations

Media	Flux (α.cm^{-2}.s^{-1})	$[U]_{measured}$ (μg.L^{-1})	$[H_2O_2]_{measured}$ (mol·L^{-1})	$[U]_{calculated}$ (μg.L^{-1})	$[H_2O_2]_{calculated}$ (mol·L^{-1})
Aerated	3.3 10^{11}	2280	3.5 10^{-3}	714	1.2 10^{-4}
Aerated	3.3 10^{10}	210	4.8 10^{-4}	67	1.8 10^{-5}
Deaerated	3.3 10^{11}	595	3.0 10^{-4}	238	1.0 10^{-4}

4.1.1.4.2 Deaerated Conditions and Influence of Hydrogen. The model was also compared with experiments performed in deaerated media [83]. Experimentally, concentrations of 3×10^{-4} mol·L^{-1} for H_2O_2 and 2.5×10^{-6} mol·L^{-1} for U(VI) were measured in solution under an alpha ion flux of 3.3×10^{11} $\alpha \cdot cm^{-2} \cdot s^{-1}$, which is slightly lower than in aerated media. The calculation accounts for this slight decrease since concentrations of 10^{-4} mol·L^{-1} for H_2O_2 and 10^{-6} mol·L^{-1} for U(VI) were calculated at a distance of 2 mm from the interface, (Figures 23b and 23c respectively). From the calculation, a large amount of oxygen is produced at the UO_2/water interface (Figure23a) and a high hydrogen peroxide concentration is generated by radiolysis. The very high flux generates a strong alpha dose rate in the first forty micrometers, which creates approximately the same conditions in aerated or deaerated media. The calculation more closely fits the experimental results in deaerated media than in aerated media (Table 7).

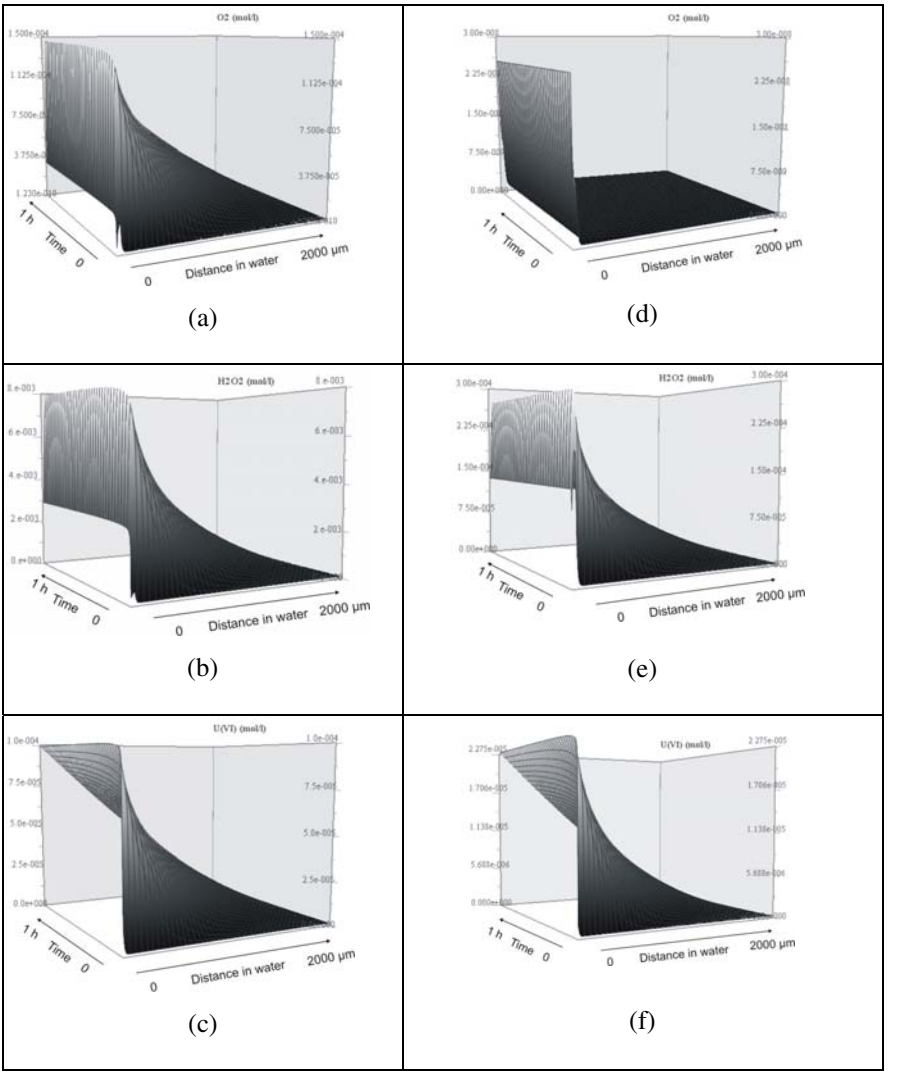

Fig. 23 Evolution of O_2 (a), H_2O_2 (b), U(VI) (c), in the solution, in deaerated conditions, and of O_2 (d), H_2O_2 (e), U(VI) (f) in dissolved hydrogen media. Number of layers = 200, Experimental time = 1.00 h00 and the four local dose rates are: $D_{\alpha 1}=1.64 \times 10^8$ Gy.·h^{-1}, $D_{\alpha 2}=1.91 \times 10^8$ Gy.·h^{-1}, $D_{\alpha 3}=2.49 \times 10^8$ Gy.·h^{-1}, $D_{\alpha 4}=3.43 \times 10^8$ Gy.·h^{-1}

Finally, calculations were performed with a large hydrogen concentration in deaerated media and at high flux to check the inhibition of matrix oxidation/dissolution as reported in the literature [84]. For all irradiated UO_2 materials (spent fuel or alpha-doped pellets), there seems to be a certain concentration of dissolved hydrogen above which it is difficult to measure oxidative dissolution rates. But these experimental results are valid only for weak

flux systems. Taking into account the high flux produced by external irradiation experiments, the generated concentrations of oxidant species are higher and must have an effect on primary radiolytic yields. To study the system response, a large amount of hydrogen was introduced to avoid any limitation due to H_2 consumption.

The calculation shows that the oxygen is completely consumed with a concentration of about 10^{-11} mol·L^{-1} (Figure 23d). Likewise, the $OH^{\bullet}$ radical concentration drastically decreases at the interface and is completely consumed in solution. The only reaction of H_2 is with $OH^{\bullet}$ radicals. The $H^{\bullet}$ atom produced from this reaction reacts with an O_2 molecule to form $HO_2^{\bullet}$. This hydroperoxyl radical reacts with itself to produce H_2O_2. As the result, the concentration of hydrogen peroxide remains relatively high at about 5×10^{-6} mol·L^{-1} in solution (Figure 23e) despite the high hydrogen concentration. This concentration is nevertheless 30 times lower than in deaerated media and consequently entails a relatively high concentration (1.9×10^{-7} mol·L^{-1}) of U(VI) in solution (Figure 23f). Although dissolved hydrogen has been added to the system, this does not prevent oxidation of the UO_2 matrix to UO_3. This result is in contradiction with the experimental results obtained on spent fuel or on alpha-doped pellets [84]. Indeed, experimentally, very low concentrations of oxygen, hydrogen peroxide and uranium were measured in solution. The model of the radiolysis phenomena for high LET radiation and in particular for high flux from models in homogeneous phase is partly responsible for the results obtained [85]. Increasing the flux is equivalent to increasing the recombination kinetics of the radicals in favor of the molecular species and thus artificially increasing the oxidant molecular species yield. This increase in the molecular yields leads to an increase in the H_2O_2 concentrations over time without triggering the hydrogen inhibiting mechanism. This inhibiting mechanism in the present model is based on a chain reaction requiring radicals and will probably have to be reexamined in comparison with published results, particularly for systems involving solid/solution interfaces.

Some experiments with dissolved hydrogen in solution are also necessary to quantify its real impact on oxidative dissolution at this high flux level.

In sum, several combined transport and radiolysis models were developed to predict the oxidation/dissolution of UO_2 under α radiolysis of water. The UO_2/water interface is divided into an arbitrary number of layers. The Chemsimul kinetic code is used for radiolysis calculations in each layer and the modeling of transport between the layers is based on Fick's law. The calculation proceeds iteratively, and an alpha dose rate profile is taken into account as input data. To limit the calculation time, which depends on the computing power and the duration of the leaching experiment described, a tradeoff between the thickness and the number of cells has to be found. At present, simulations of leaching experiments lasting several days cannot be carried out due to the very long calculation time. However, the calculation has been compared with experimental results obtained under irradiation at high flux levels of a UO_2/water interface subjected to a beam of He^{2+} particles generated by a cyclotron. Owing to computer time limitations, calculations are carried out for 200 layers, each 10 µm thick, to simulate 1-hour experiments. In the experimental geometry (monoenergetic linear alpha beam), the alpha dose rate profile is well described by a summation of

Bragg curves. The comparison relates to experiments performed in aerated and deaerated media at high flux of 3.3×10^{10} $\alpha \cdot cm^{-2} \cdot s^{-1}$ and 3.3×10^{11} $\alpha \cdot cm^{-2} \cdot s^{-1}$. The calculated uranium content in solution is 3 times lower than the experimental value and the hydrogen peroxide concentration is 10 times lower in aerated media. In deaerated media, however, the comparison is quite good.

Finally, a calculation was carried out with a large imposed dissolved hydrogen concentration in solution to check the inhibition of matrix dissolution. The release of uranium in solution is relatively high despite the hydrogen concentration in solution because of the primary formation of hydrogen peroxide. This is probably due to a lack of knowledge concerning the inhibiting mechanism under alpha radiolysis (influence of the surface under alpha irradiation, hydrogen activation, validity of primary radiolytic yield in presence of H_2, etc.) which is not taken into account in this type of calculations.

4.1.2 Aqueous Alteration of Glass

4.1.2.1 Introduction

Glass alteration by water is dominated by four mechanisms: water diffusion in the structure resulting in ion exchange and preferential dissolution of network-modifying alkali metals; hydrolysis of the hydrated silicate network; silica condensation resulting in the formation of a gel; and precipitation of secondary phases [86, 87]. All four types of reactions generally occur simultaneously. Depending on the reaction progress, however, each in turn can control the overall glass dissolution kinetics. The relative importance of each mechanism in the glass dissolution process generally depends to a large extent on the glass composition and on the leaching conditions (temperature, pH, solution composition, renewal rate, etc.).

Figure 24, for example, shows the morphology of a nuclear glass sample leached for several weeks at 90°C in a dilute medium. At the top of the image the

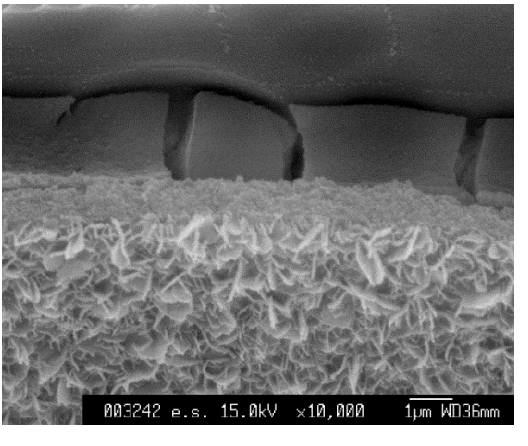

Fig. 24 Scanning electron micrograph of the alteration film formed on SON68 glass after 38 days at S/V = 0.06 cm^{-1}, T = 90°C, pH 9 [88]

glass is clearly visible, probably hydrated in the outer region, together with the gel formed by hydrolysis and condensation reactions affecting mainly silicon, and crystallized secondary phases (smectites) at the solution interface. The gel formed under these conditions does not retain much silicon (most of which dissolves) and is therefore highly porous, accounting for the shrinkage pattern due to drying.

The key transport phenomena for assessing the long-term behavior of nuclear glass are observed mainly with regard to the diffusion of water in the solid and of reactive species (water and solvated cations) in the gel. The following section briefly describes the chemical reactions before turning to the more specific effects related to transport phenomena.

4.1.2.2 Initial Stages of Alteration Dominated by Ion Exchange

The first effects of water on the glass lead to preferential dissolution of network-modifying alkali ions [89-91]. Leaching or selective dissolution of network-modifying cations, driven by the chemical potential gradient of the species involved, was first attributed to simple ion exchange reactions (often known as interdiffusion) between charged hydrogen species and alkali ions from the glass [92] or even between molecular water and alkali metal cations [93, 94].

The nature of the diffusing reactive hydrogen species has not been satisfactorily determined to date, probably because several such species are involved because of the importance of the glass chemical composition [95]. The difficulty is compounded by the relatively variable H/Na ratios measured in the leached glass layers (Table 8).

Table 8 H/Na ratios reported in leached glass layers. An H/Na ratio of 1, 2 or 3 implies an exchange between an alkali ion and a proton, a water molecule, or a hydronium ion, respectively

Reference	Glass	H/Na
[96]	SiO_2, Na_2O, CaO	2.9 ± 0.3
[97]	SiO_2, Na_2O	1.75
[98]	SiO_2, Na_2O	2.0 ± 0.3 or 3.2 ± 0.4 depending on the Na concentration
[94]	SiO_2, Na_2O, CaO	~ 2 near the surface, ~ 1 near the alteration front
[99]	SON68	2.6 ± 0.3 (measured H/Σ*alk*)

In borosilicate and aluminosilicate glasses, water diffusion in the glass network of course leads to preferential release of network-modifying alkali ions, but also to a local structural reorganization. Geneste et al. [95] showed by *ab initio* molecular dynamics simulations that the substitution of protons for charge-compensating Na atoms bound to BO_4 tetrahedra directly alters the covalent glass structure because the proton cannot exert a charge-compensating role in these glasses. This breaks a covalent bond and causes the boron coordination number to change from IV to III.

$$B^{IV}\text{-O-SiNa} + H_3O^+ \rightarrow B^{III} + \equiv \text{Si-OH} + H_2O + Na^+ \quad (19)$$

Ion exchange thus results in local structure reorganization. Diffusion processes — especially in borosilicate glass — therefore cannot be described by simple exchange reactions. Bunker [100] even suggested that sodium is leached rather by hydrolysis in this case, since ion exchange is accompanied by rupture of Al-O or B-O bonds. It would thus be preferable to speak of "reactive interdiffusion" when describing the first stages of nuclear glass alteration [87, 101][7]. The resulting amorphous layer involves complex reactive interdiffusion mechanisms concerning water in one direction and solvated ions in the other direction. They involve not only the initial glass structure (forming the hydrated glass layer) but also mechanisms by which the least soluble elements such as silicon are reorganized and recondensed (the gel). Frugier et al. [87] suggest the term "passivating reactive interphase" (PRI) to focus on its properties irrespective of any controversy regarding its small-scale structure.

4.1.2.3 Hydrolysis

Hydrolysis of the bridging bonds of the glass network (Si-O-Si, Si-O-Al, Si-O-Zr, Si-O-B, etc.) is attributed to the nucleophilic properties of water, and is thus activated at basic pH. In the case of the bond between two silicon tetrahedra the reaction is expressed as follows:

$$\equiv \text{Si-O-Si} \equiv + OH^- \leftrightarrow \equiv \text{Si-OH} + \equiv \text{Si-O}^- \quad (20)$$

$$\equiv \text{Si-O}^- + H_2O \leftrightarrow \equiv \text{Si-OH} + OH^- \quad (21)$$

For silicate minerals and glasses — including nuclear glasses — the material dissolution rate is limited by the rate of hydrolysis of the Si-O bonds [105]. Theoretical calculations of the activation energy of $Si\text{-}O_{bridging}$ bond rupture versus the degree of connectivity (Q^n) suggest that the dissolution of silicate glass and minerals is controlled by hydrolysis of Q^1Si or Q^2Si [106]. The net hydrolysis of Si-O bonds is related to the bond strength (influenced by the neighboring cation) [107, 108] and the volume density of sites subjected to hydrolysis (influenced by interdiffusion [87]). As the interdiffusion kinetics are inversely proportional to the square root of time, they are always more rapid than the hydrolysis kinetics during the initial instants. The hydrolysis kinetics of bridgning bonds are therefore always applicable to a dealkalinized layer and never directly to the underlying pristine glass. This layer very quickly reaches a steady-state thickness of a few nanometers in neutral or slightly basic conditions [87] (refer to figure in section 4.2.2.1.4).

The dissolution rate limited by the hydrolysis reaction (forward rate) is sensitive to two parameters: the temperature and the pH. The temperature dependence follows an Arrhenius law with an activation energy generally ranging

[7] Ion exchange can also be described as the hydrolysis of alkali metal oxides, insofar as the dissolution of a single (hydr)oxide occurs through an exchange reaction that breaks a cation-oxygen bond, which is then replaced by a proton-oxygen bond [102]. This viewpoint as adopted especially by Oelkers [103] allows these reactions to be generalized to the alkaline earths (e.g. Ca, Mg), which are also preferentially released but at lower rates than the alkali metals under certain conditions (e.g. at acid pH) [104].

from 70 to 90 kJ·mol^{-1}. As predicted [106] there does not appear to be any relation between the activation energy corresponding to solid dissolution and the connectivity of the silicate network.

The pH dependence of the rate for nuclear borosilicate glass follows a curve with a minimum at near-neutral pH and $[H^+]^n$ power laws with n coefficients of about −0.3 in basic media and +0.4 in acidic media [109]. These coefficients vary only slightly with the glass composition.

4.1.2.4 Formation of the Passivating Reactive Interphase by Interdiffusion

The passivating reactive interphase (PRI) exists regardless of the alteration conditions but is very thin in the case of strong hydrolysis kinetics. When the rate of hydrolysis diminishes or even ceases, this thickness can increase significantly and the formation mechanism becomes a major phenomenon of glass alteration.

When a fraction of the silicon is removed from the passivating reactive interphase, the latter reorganizes more readily as a gel. The passivating properties of the gels vary with the size of the removed silicon fraction [110]. Thick depleted gels are therefore more readily observed than more passivating reactive interphases that are only a few nanometers thick. It has been clearly established that the gel structure differs from the pristine glass, especially because of silica condensation reactions [110-115]. The formation of gels at the glass/solution interface is one of the essential leaching characteristics of both nuclear and natural silicate glass. The dynamics of gel formation are highly complex [116]. Some gels have been shown to be capable of reorganizing, until closure of their porosity, as demonstrated experimentally and simulated numerically [117].

The hydrolysis rate is observed to diminish when the concentrations of PRI constituents — especially silicon — increase in solution. Until recently, two opposing approaches dominated in the literature to account for such a rate drop, one based on the chemical affinity expressed with respect to the initial glass, and the other on the passivating effect of the alteration gel [118, 119]. The efforts undertaken notably in the framework of the European GLAMOR Program [120] have since contributed to the convergence of these two approaches (for more details see [87, 121]).

The metastability of the gels theoretically allows them to crystallize, and in fact it has been established that the precipitation of secondary crystalline phases is one of the reasons for the persistence of a residual alteration rate for nuclear glass [122-124]. In a geological repository environment the main crystalline phases likely to form are phyllosilicates, hydrated calcium silicates, and zeolites. The precipitation of phyllosilicates appears to be controlled by thermodynamic equilibria (relatively independent of kinetic effects), and is therefore dependent on the temperature, the pH, and the concentrations of constituent elements in solution, and the latter can become the limiting parameter. Zeolite precipitation, however, is subject to the much more significant kinetic effects of nucleation and growth [125]. Irrespective of the type of borosilicate, the resumption of alteration can occur in alkaline conditions: in that cas it appears to be related to massive precipitation of crystallized zeolite secondary phases [126, 127]. The above-mentioned phases are not specific to nuclear glasses, and also occur when natural glass is leached [128-130].

4.1.3 Mass Transfer in the Glass

4.1.3.1 Chemistry/Transport Coupling at Atomic and Mesoscopic Scale

Water diffusion in the glass is directly dependent on topological criteria such as ring size in the structure [131]. Bunker showed that the diffusivity diminishes exponentially when the cavities become smaller than the hydrodynamic diameter of a water molecule (0.27 nm). In the case of silica, Bakos [132] used ab initio methods to calculates a barrier of ~0.8 eV for water molecule diffusion through 6-member rings; the barrier rises sharply to 1.8 eV when the ring size drops to 5. Given chemical complexity of nuclear glasses, the diffusion coefficients or activation energies involved can only be determined empirically by monitoring the release of alkali ions in solution or the element concentration profiles in the hydrated glass. The concentration curves of species diffusing in solution or in the solid are fitted using various models (Table 9). A detailed review of these models is available in [133].

Table 9 Main hypotheses of models used to fit the diffusion coefficients

Hypotheses			Model
→ Stationary initial interface	-	–	→ Fick's law
→ Mobile interface	→ $D_H = D_{Na}$	→ Steady state	→ Boksay
		→ Time-dependent	→ Boksay
	→ $D_H \neq D_{Na}$	→ Steady state	→ Doremus
		→ + structural factor	→ Lanford

Fick's simple model and Boksay's model constitute the basis for models of ion exchange in the glass. In the case of one-dimensional diffusion in a semi-infinite solid ($x' > 0$), Fick's second law is expressed as follows:

$$\frac{\partial C}{\partial t} = \frac{\partial}{\partial x'}\left(D \frac{\partial C}{\partial x'} \right) \tag{22}$$

where C is the concentration of diffusing species, t the time, x' the diffusion thickness, and D the diffusion coefficient.

Assuming D is constant and meets the boundary condition $C = C_0$ for $x' = 0$ and $t > 0$ and the initial condition $C = 0$ for $x' > 0$ and $t = 0$, the normalized concentration of diffusing species (H or Na) can be expressed versus time and depth [134]:

$$\frac{C}{C_0} = erfc \frac{x'}{2\sqrt{D_H t}} \tag{23}$$

This model does not allow for constant shrinkage of the fluid-solid interface during dissolution. It can only be applied during the initial stages of leaching, when the diffusion rate is very high, or when dissolution becomes very slow.

Boksay's model [135, 136] takes into account the shifting interface (dissolution) by changing the variable: $x = x' - at$ where x is the diffusion thickness, x' the total altered glass thickness, and a the shrinkage rate. If a is constant, Fick's law is expressed as follows:

$$\frac{\partial C}{\partial t} = \frac{\partial}{\partial x}\left(D\frac{\partial C}{\partial x}\right) + a\left(\frac{\partial C}{\partial x}\right) \tag{24}$$

Assuming steady-state conditions, i.e. $\frac{\partial C}{\partial t} = 0$, assuming D_H and D_{Na} are constant and equal, and allowing for the following boundary conditions:

- for hydrogen, $x = 0 \rightarrow C_H = 1$; $x = \infty \rightarrow C_H = 0$; $\frac{\partial C_H}{\partial x} = 0$
- for sodium, $x = 0 \rightarrow C_{Na} = 0$; $x = \infty \rightarrow C_{Na} = 1$; $\frac{\partial C_{Na}}{\partial x} = 0$

where C_H and C_{Na} are the normalized hydrogen and sodium concentrations compared with the bulk water, then double integration yields the following solutions:

$$C_H = \exp\frac{-ax}{D} \tag{25}$$

$$C_{Na} = 1 - \exp\frac{-ax}{D} \tag{26}$$

This model thus gives exponential concentration profiles for diffusing species in the solid, whereas the observed shape is generally sigmoidal.

The diffusion/exchange mechanism depends in fact on several parameters related to the glass structure and solution chemistry, and these models have therefore been further refined. For example:

- The Doremus model [91] allows for mobility depending on the diffusing species
- The Lanford model [96] incorporates a structural factor to allow for greater ionic mobility near the interface with the bulk water.

4.1.3.1.1 Effect of the Glass Composition. The ion exchange equilibrium depends on the exchange site and electronic charge distribution [131, 137], but the protonation site reactivity differs according to the nature of the site. For silanol groups there is very little exchange above pH 12, but complete exchange below pH 8. In simple alkali silicate glass, all the network-modifying cations are compensated by nonbridging oxygen atoms. In alkali borosilicate and aluminosilicate glass, however, the network-modifying cations can also be charge compensators at BO_4^- and AlO_4^- sites in addition to nonbridging oxygen [93]. Moreover, protonation of Al-O-Si and B-O-Si bonds catalyzes their hydrolysis

because it is difficult to exchange network-modifying cations at AlO_4^- and BO_4^- sites without attacking the covalent bonds between network formers [131, 137]. This explains behavior such as the simultaneous release of boron (a network former) and sodium or lithium (mobile elements) in solution in the case of borosilicate glasses [138, 101] in which the Na/(Al + B^{IV}) ratio is near 1:1 [139].

The site reactivity differences also account for the variations in the apparent diffusion coefficients measured by analysis of the elements released into solution, for glasses of different composition. Moreover, the higher the alkali content of the glass, the higher the diffusion coefficient.

Diffusion coefficients can be difficult to compare due to differences in the glass compositions, leaching conditions, and measurement techniques, but can a few orders of magnitude can be indicated for neutral or basic pH (Table 10).

Table 10 Order of magnitude of diffusion coefficients for different glass compositions

Glass	D ($m^2 \cdot s^{-1}$)	Temperature (°C)	pH	Reference
Si-Na	10^{-17}–10^{-15}	60–100	DW	[90]
	10^{-15}	30	4.9	[97]
Si-Na-Ca	10^{-18}	90	DW	[96]
	10^{-20}–10^{-17}	60-100	DW	[90]
Medieval potassium stained glass windows	10^{-17}–10^{-18}	Ambient	-	[140]
Medieval sodium stained glass windows	10^{-20}	Ambient	-	[140]
Roman archaeological glass	10^{-22}	15	Seawater	[141]
	10^{-16}	100	DW	
Si-Na-Al	10^{-18}–10^{-19}	70	DW	[93]
	10^{-16}	25	DW	[142, 143]
Alkali borosilicate glass	10^{-17}–10^{-18}	90	9.5	[144]
SON68	10^{-21}–10^{-22}	90	7–10	[99]
	10^{-21}–10^{-24}	30–90	7–10	[101]
Obsidian	10^{-22}	22	DW	[145]

DW: Deionized water.

4.1.3.1.2 Effect of Temperature. The temperature dependence of the ion exchange rate (r) or the diffusion coefficient (D) generally follows an Arrhenius law from which the activation energy (E_a) of the process can be determined:

$$\ln(r) = \ln(A_r) - \frac{E_{a,r}}{RT} \tag{27}$$

$$\ln(D) = \ln(A_D) - \frac{E_{a,D}}{RT} \tag{28}$$

where A_r, A_D are pre-exponential terms, $E_{a,r}$ and $E_{a,D}$ represent the activation energy ($J \cdot mol^{-1}$), R is the ideal gas constant ($R = 8.314\ J \cdot mol^{-1} \cdot K^{-1}$) and T is the temperature (K). Various published values are indicated in Table 11.

Table 11 Activation energy of ion exchange rate for different glass compositions

Glass composition (wt%)	pH	Ea ($kJ \cdot mol^{-1}$)	Reference	From
33.7 Na_2O, 66.3 SiO_2	8	33.6	[146]	r
8.1 Al_2O_3, 34.3 Na_2O, 57.7 SiO_2	8	38.4	[146]	r
15.6 Al_2O_3, 35.1 Na_2O, 49.3 SiO_2	8	43.2	[146]	r
22.7 Al_2O_3, 34.9 Na_2O, 42.4 SiO_2	8	48.5	[146]	r
14 Na_2O, 10 B_2O_3, 76 SiO_2	9.5 (90°C)	74.5	[144]	D
14 Na_2O, 10 B_2O_3, 73 SiO_2, 3 CaO	9.5 (90°C)	86.2	[144]	D
14 Na_2O, 10 B_2O_3, 68 SiO_2, 3 CaO, 5 ZnO	9.5 (90°C)	89.5	[144]	D
14 Na_2O, 10 B_2O_3, 59 SiO_2, 3 CaO, 5 ZnO, 9 Fe_2O_3	9.5 (90°C)	84.1	[144]	D
14 Na_2O, 10 B_2O_3, 57 SiO_2, 3 CaO, 5 ZnO, 9 Fe_2O_3, 2 ZrO_2	9.5 (90°C)	84.9	[144]	D
Nuclear glass PNL-3008				
15.4 Na_2O, 11.2 B_2O_3, 43.5 SiO_2, 2.9 CaO, 5.2 ZnO, 12.1 Fe_2O_3, 4.8 TiO_2, 2.4 NiO, 0.5 Cr_2O_3	9.5 (90°C)	84.9	[144]	D
Nuclear glass PNL-7668				
14.2 Na_2O, 8.98 B_2O_3, 42.3 SiO_2, 2.2 CaO, 3.27 ZnO, 9.16 Fe_2O_3, 1.76 ZrO2, 2.96 TiO_2, 1.85 MoO_3, 0.19 NiO, 0.43 Cr_2O_3, 4.11 La_2O_3, 1.40 Nd_2O_3, 1.06 Cs_2O_3, 5.90 other	9.5 (90°C)	83.2	[144]	D
SON68 glass	8 (90°C)	36.7	[101]	r
SON68 glass	8 (90°C)	86.3	[101]	D
Obsidian (natural samples and experiments in pure water)	-	80	[145]	D
Obsidian	Pure water	81-90	[147]	D

Two issues are worth commenting. First, a distinction must be made between the activation energy of the diffusion rate (r) and that of the diffusion coefficient (D), which are linked by the following relation:

$$r = 2\rho\sqrt{\frac{D}{\pi t}} \tag{29}$$

Beyond the fit of the experimental data points, which can vary depending on whether a linear (r) or parabolic (D) law is used, the difference between (27) and (28) amounts to a factor of 2 on the activation energy. Chave et al. [101]

determined an activation energy of 86.3 kJ·mol^{-1} for SON68 glass based on the diffusion coefficients, and 36.7 kJ·mol^{-1} based on the diffusion kinetics. McGrail et al. [146] calculated this value from the following formula:

$$E_a = E_b + E_s \tag{30}$$

where E_b is the binding energy of a sodium atom site at a nonbridging site and E_s the elastic strain energy related to the distortion of the glass network to move a sodium atom away from its equilibrium position.

Second, these values are higher than for a pure diffusion process in a liquid (~20 kJ·mol^{-1}) due to the complex interactions between water and protons, and the different nature of the Na bonds in the network (Na can be a network modifier or a charge compensator). For example, data reported by [146] show that Na release becomes more difficult when the aluminum content increases in the glass as network-modifying sodium bonds become charge compensating.

4.1.3.1.3 pH Effect. Bunker [131] showed that the equilibrium constant of the ion exchange reaction depends on the H^+ concentration: the importance of ion exchange diminishes as the pH increases. This dependence highlights the importance of site reactivity in this phenomenon, since it varies with the pH.

Chave et al. [101] determined a relation for the pH-dependence of the diffusion coefficient (D) for SON68 glass at 50°C for pH values between 8 and 10:

$$D\ (\mathrm{m^2 \cdot s^{-1}}) = 2.29 \times 10^{-25}\ [\mathrm{OH^-}]^{-0.35 \pm 0.03} \tag{31}$$

The diffusion coefficient decreases by a factor of 4 as the pH increases from 8 to 10.

4.1.3.1.4 Effect of the Solution Chemical Composition. The results for the influence of the ionic strength and solution chemistry on ion exchange are contradictory, probably because of the complexity of the effects arising from these parameters. The expression for the equilibrium constant of the ion exchange reaction is also dependent on the Na^+ concentration; if the concentration in solution is high (for example in NaCl solution), it can inhibit the exchange reaction [92, 94, 131, 148, 149]. The ions in solution can also compete with the protons. This effect was considered for minerals such as feldspars ($KAlSi_3O_8$) [150]. McGrail et al. [151] and Pederson et al. [152] also showed that the rates of ion exchange with alkali silicate glass were significantly lower in solutions saturated with NaCl than in pure water, although the rates were identical at the pH of the isoelectric point (pH_{pI} = 2.3). The difference is much less pronounced for alkali aluminosilicate glass, where the surface electrical potentials are lower because their isoelectric point is higher (pH_{pI} = 4.1–4.4) and nearer the experimental pH (pH = 6). For [152] the ionic strength affects the surface electric charge and the hydrogen concentration near the surface according to the following relation:

$$\left[\mathrm{H}^+_{surface}\right] = \left[\mathrm{H}^+_{solution}\right] \exp\left(-\frac{e\Psi_0}{kT}\right) \tag{32}$$

where e is the standard charge unit, Ψ_0 is the surface electrical potential, k is the Boltzmann constant, and T is the temperature. Ψ_0 is dependent on the nature of the solid surface, the pH, the electrolyte concentration, and the temperature. The surface is negatively charged when $pH > pH_{pI}$. The surface potential becomes increasingly negative in the presence of NaCl, which diminishes the H^+ concentration near the surface, and can slow down ion exchange. However, Chave and al. [101] did not report any significant difference according to the ionic strength. The diffusion coefficients of SON68 glass are very similar under otherwise identical leaching conditions for ionic strength values of < 0.005 M and 0.27 M. Similar findings were reported by [128]. Although the high initial concentrations in solution result in relatively significant analytical uncertainties, no slowdown was observed for the Na release in NaCl solutions (< 0.01 M) for basaltic glasses.

These contradictory conclusions raise the issue of the process limiting the rate of ion exchange. The answer may lie in the work by McGrail et al. [146], who carried out experiments on sodium aluminosilicate glass in solutions in which D_2O was substituted for H_2O. The sodium release was 30% slower in D_2O than in H_2O, although the hydrolysis rate was unchanged. This difference cannot be attributed to the diffusion of water or H_3O^+ ions as the limiting step of ion exchange because the molar mass differences would involve differences of only 5 and 7%, respectively. The rate of ion exchange appears instead to be limited by the rupture of the O-H (or O-D) bond in the water molecule or H_3O^+ ion, as differences in the vibration frequency can lead to a discrepancy of about 29% between D_2O and H_2O. These data confirm the reactivity of diffusion.

4.1.3.2 Competition between Ion Exchange and Hydrolysis

During the initial instants of leaching, interdiffusion is the overriding mechanism (theoretically infinite at t_0) until the rate of progression of the interdiffusion front becomes equal to the that of the dissolution front (steady state). Hence:

$$r_0 \approx \frac{D}{e} \tag{33}$$

where r_0 is the initial dissolution rate, D the diffusion coefficient, and e the diffusion thickness [136]. The diffusion thickness is then constant and can be determined from Fick's second law:

$$e = 2\sqrt{\frac{Dt}{\pi}} \tag{34}$$

The time necessary to reach steady-state conditions, $\tau \geq t$ is written:

$$\tau \geq \frac{D\pi}{4V_0^2} \tag{35}$$

The nomogram (Figure 25) can be used to estimate the time necessary to reach steady-state conditions depending on the diffusion coefficient and the initial glass

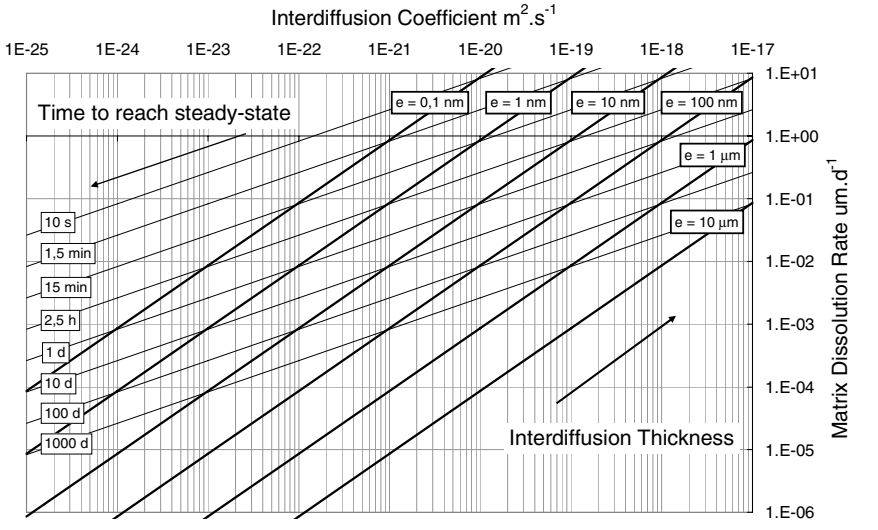

Fig. 25 Orders of magnitude of the time necessary to reach steady-state conditions and of the altered glass thickness versus the reactive diffusion coefficient and matrix dissolution rate (Boksay's model). Example: glass with a dissolution rate of 10^{-2} µm·d^{-1} and a reactive dissolution coefficient of 10^{-21} m^2·s^{-1} will reach steady-state conditions in less than 10 days and the interdiffusion thickness will be 10 nanometers

alteration rate. For SON68 glass, for example, steady-state conditions occur within less than 10 s and the interdiffusion thickness is 0.1 nm for an initial rate of 1 µm·d^{-1} and a diffusion coefficient of 10^{-22} m^2·s^{-1}, i.e. under conditions corresponding to leaching in pure water at 90°C. For basaltic glasses the selective dissolution step is also very brief: 5 days for experiments in pure water at 60°C and S/V = 0.1–0.2 cm^{-1} [153, 154], less than 4 days for experiments in pure water at 90°C and S/V = 0.1 cm^{-1} [155].

Moreover, if it is assumed that the activation energy corresponding to the diffusion coefficient is slightly higher than that of dissolution, then steady-state conditions between the two mechanisms are reached sooner as the temperature rises.

4.1.4 Examples of Coupled Chemistry/Transport Phenomena

4.1.4.1 Passivating Role of the Gel

Many models based on thermodynamic approaches have been proposed in the literature to simulate glass dissolution kinetics [156-159]. However, some authors [121, 126, 160-162] have identified inadequacies in these models near equilibrium, and suggest that the release of glass constituent elements into solution is inhibited by the gel. A discrepancy of one to three orders of magnitude is observed between the rates predicted by these models and the experimentally

measured values, indicating that the rate drop cannot be attributed to solution saturation alone [160]. In addition, [162] compared the equilibrium constant K determined from the free energy of formation of a simple 3-oxide glass measured by calorimetry [161] with the ionic product of the Q activities measured after one year of leaching at high reaction progress (with a high glass-surface-area-to-solution-volume ratio) when the rates had diminished practically to zero. He observed that the [1−exp(−A/RT)] term was equal to 0.75, indicating that the rate drop cannot be explained only by simple thermodynamic considerations.

Moreover, alteration was observed to resume when the sample was placed in ultrapure water, although the maximum rate was lower by a factor of 300 than the initial pristine glass alteration rate of 7×10^{-3} $g \cdot m^{-2} \cdot d^{-1}$ measured in pure water. A few days after solution renewal, the rate was identical with the value measured during first stage of alteration. This experiment reveals the passivating effect of the gel, comparable to rust formed by corrosion of iron, which forms a diffusion barrier [163].

Gin's conclusions appear to contradict results previously reported in the literature [164]. However, the gel examined by Chick was formed in static mode but in a very dilute medium (S/V 0.01 cm^{-1}) corresponding to conditions near the initial rate. It is therefore unsurprising that the gel is nonpassivating in this medium. The data generally show that the passivating gel properties cannot be dissociated from the leaching conditions [165].

Recent results demonstrating the impact of the gel structural transformations on the diminishing alteration rate were obtained by coupling several experimental techniques (gas adsorption isotherm, X-ray and neutron scattering, mass spectroscopy, and electron microscopy) and numerical simulations at mesoscopic scale by a Monte-Carlo method [108]. Five glass compositions were investigated: $(61\text{-}x)SiO_2 \cdot xZrO_2 \cdot 17B_2O_3 \cdot 18Na_2O \cdot 4CaO$, where x ranged from 0 to 8 mol% (these glass compositions are hereafter designated xZr). Substituting zirconia for a fraction of the silica made it possible to characterize the influence of insoluble oxides on the alteration kinetics and on the morphology of the altered layer. Leaching experiments were carried out at 90°C with a solution buffered to pH 6.9 ± 0.1. Two types of experiments were carried out to measure the initial dissolution rate and to characterize alteration under silica saturation conditions. The initial dissolution rate, controlled by hydrolysis of the silicate network, dropped very significantly as the zirconia content increased in the glass (from 37 to 0.091 $g \cdot m^{-2} \cdot d^{-1}$) with only a relatively slight reduction in the silicon concentration at saturation. The dissolved boron fraction is plotted versus time for the test glasses in Figure 26.

A major drop in the alteration rate was observed after increasing time intervals and at increasingly high levels for the glass samples containing 0, 1, and 2% ZrO_2. Conversely, alteration continued after saturation of the solution with respect to silica, and was practically complete for the glasses with 4, 6 and 8% ZrO_2. The results show that substituting zirconium for silica considerably slows the glass dissolution kinetics, but ultimately leads to a much greater degree of alteration. To account for these results the morphology of the alteration film was characterized by various techniques and simulated by a Monte Carlo method to obtain

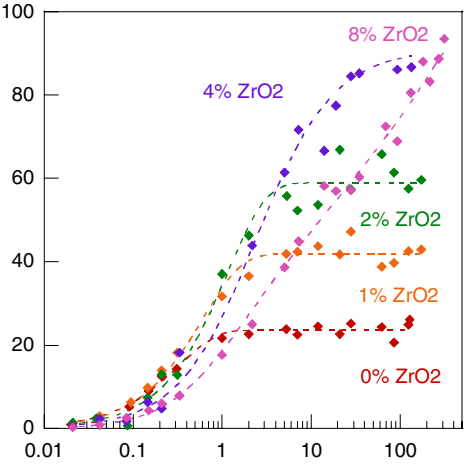

Fig. 26 Glass alteration kinetics. Dissolved boron fraction versus time for glass samples 0Zr, 1Zr, 2Zr, 4Zr and 8Zr. The kinetics for sample 6Zr (not shown) were comparable to those of 8Zr, but more rapid. Dashed lines are visual guidelines (from [108])

topological data on the evolution of the porous network, especially with regard to open or closed porosity.

The gel morphology after different leaching times was systematically investigated by SAXS. The evolution of the X-ray scattering curves indicates a structural reorganization of the gel during leaching (Figure 27). The initially filamentary structures became increasingly branched and the pore size increased. The reorganization was sufficient in glass 0Zr at the longest leaching time to reach the "Porod regime" in which scattering is controlled by the smooth surface of the pores. The measured surface area diminished with time, indicating that the gel continued to undergo structural reorganization well after the rate drop. The restructuring occurred much more slowly in the other glasses, for which the SAXS specific surface area cannot be determined, since the pores were neither large nor smooth enough to reach the q^{-4} Porod regime (Figure 27b).

Neutron scattering with index matching was also used to characterize the gels. This powerful technique clearly proves that the restructuring of the gel layer leads to the closure of the pores in the glass without zirconia, wheras this transformation is inhibited in the 4% ZrO_2 glass.

Finally, Figure 28a is a TEM image of sample 0Zr after leaching, showing a gel cross section 100 nm thick obtained by focused ion beam thinning. The total gel thickness is 3 to 4 micrometers. Its porosity is revealed by the granularity of the image. The pore sizes range from 2 to 10 nm. A nonporous gel region 150 nm thick is clearly visible near the outer edge (Figure 28b). The presence of this dense layer accounts for the pore closure demonstrated by the three experiments described above.

A Monte Carlo simulation model of multi-element glass alteration was developed to interpret these results [166]. Note that in this model the network-forming cations (Si, B) are randomly distributed at the nodes of a diamond lattice, the cations at coordination number 6 (Zr) are placed inside a cage of six SiO_4 tetrahedra, and the alkali or alkaline earth ions at interstitial positions either as

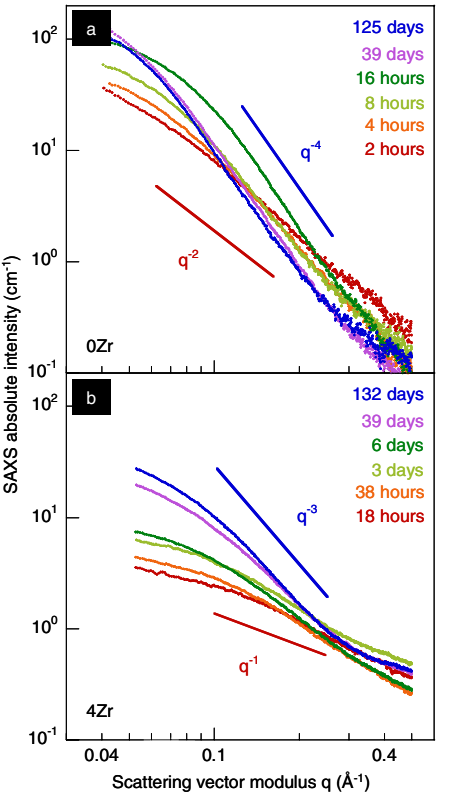

Fig. 27 Small angle X-ray scattering. Scattered intensity versus scattering vector modulus (q) after different alteration times for samples 0Zr (a) and 4Zr (b). The variations approximating q^{-1} or q^{-2} observed for short durations are characteristic of scattering by linear or ramified structure, respectively. The q^{-4} behavior observed for glass 0Zr for the longest durations indicates scattering by smooth pores of sufficient size (from [108])

charge compensators (B(IV), Zr(VI)) or as network modifiers generating nonbridging oxygen atoms. Leaching kinetics are characterized by dissolution probabilities that depend on the nature of the cation and its environment. The probability that partially soluble elements (Si) will recondense on the surface is proportional to their concentration in solution. The model generates a porous structure by the release of soluble and partially soluble elements. When silicon reaches its saturation concentration in solution the porous structure reorganizes, driven by the dynamics of dissolution and recondensation of silicate species. In the absence of any oxides less soluble than silica, this structural reorganization leads to increased pore size and smoothness that is consistent with X-ray scattering experiments (Fig. 23). Densification of the outer gel layers is also observed together with pore closure and significant shrinkage. The morphology arising from this process is shown in Figure 28c. It displays the same characteristics as the electron microscope image: the presence of closed porosity and a densified outer gel layer. This structural change prevents the release of soluble elements and inhibits further alteration. This model quantitatively reproduces the effect of the concentration of soluble elements (boron and alkali ions) on the alteration kinetics. The addition of oxides less soluble than silica slows the leaching kinetics, but also hinders the gel structural reorganization. As a

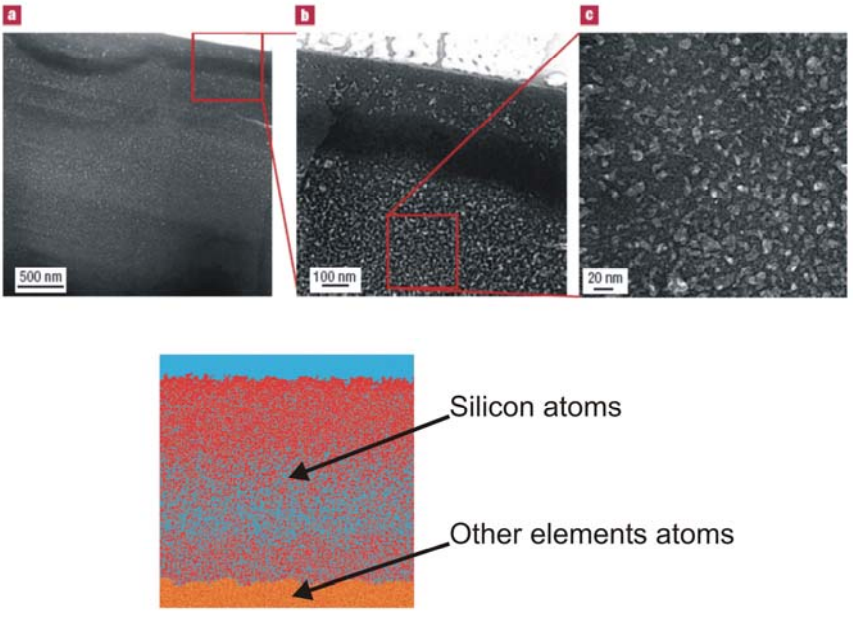

Fig. 28 Morphology of the gel layer. a) transmission electron microscope view of sample 0Zr at the end of alteration; the gel (top) is slightly lighter than the pristine glass (bottom); b) detail of the dark band corresponding to the densified zone of the outer gel layers; c) longitudinal cross section of the gel by Monte Carlo simulation of alteration of glass with the same composition (from[108])

result the pores remain small and rough; densification and shrinkage are no longer observed. The porosity closes only intermittently, resulting in continued alteration. The presence of very insoluble elements thus paradoxically leads to a greater degree of alteration that is consistent with the experimental results shown in Fig. 22.

A cause-effect relationship has thus been established between the altered layer morphology and the leaching kinetics in borosilicate glass. Substituting an insoluble oxide (zirconia in this case) for a significant fraction of silica prevents the gel structural reorganization and, by inhibiting the pore closure mechanism, leads to greater alteration. The large drop in the leach rate observed for some glass compositions is due to pore closure by gel densification, which transforms the glass from a state in which dissolution is controlled mainly by hydrolysis to a state in which it is controlled by the accessibility of the reaction interface to water. This mechanism explains how the alteration film constitutes a diffusion barrier with apparent diffusion coefficients generally very near the values found in solids.

4.1.4.2 Multi-scale Coupling

Frugier et al. [87] have developed a new nuclear glass alteration model (GRAAL) allowing for coupling between chemistry and transport at microscopic scale. This model provides a simplified but explicit description of the residual rate mechanisms that represents an improvement over previous models [138, 167,

168]. In the GRAAL model the transient rate drop phase is simulated in a simple manner in order to focus on the residual rate regime, considered essential under geological repository conditions [169]. Only the "passivating reactive interphase" (PRI) is formally described; the less passivating gels are not. The key mechanisms taken into account in the GRAAL model are summarized below and shown graphically in Figure 29:

- Exchange and hydrolysis reactions involving the mobile glass constituents (alkalis, boron, etc.) rapidly occur during the initial instants.
- Slower hydrolysis, especially of silicon, results in the existence of an initial glass dissolution rate.
- The difference between these two kinetics results in the creation of an amorphous layer at the glass/solution interface regardless of the alteration conditions. The PRI layer is gradually reorganized by hydrolysis and condensation mechanisms.
- The PRI dissolves as long as the solution is not saturated with respect to its constituent elements (Si, Zr, Al, Ca, etc.). Renewal of a pure water solution sustains the dissolution process.
- The PRI constitutes a barrier against the transport of water toward the glass and of solvated glass ions into solution. The existence of this transport-inhibiting effect rapidly causes this layer to control glass alteration.
- Some glass constituent elements precipitate as crystallized secondary phases. The precipitation of these crystallized phases on the external surface or in solution can sustain glass alteration.

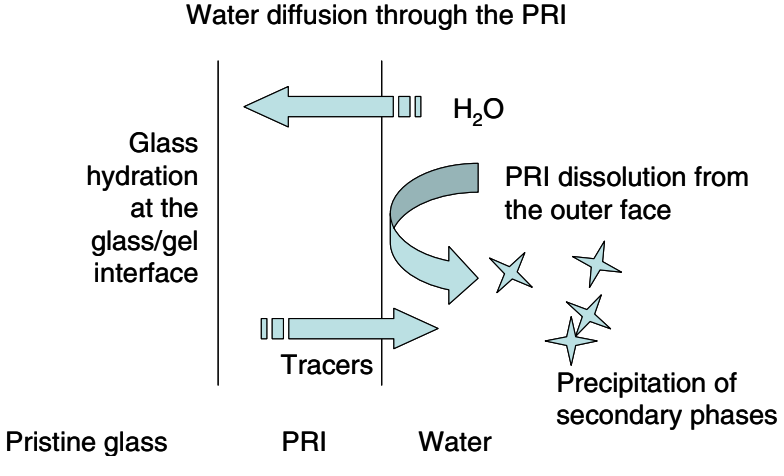

Fig. 29 Simplified diagram of the predominant mechanisms of glass alteration taken into account in the GRAAL model

The PRI is assumed to form mainly by water diffusion in the glass, hydrolysis of the most soluble glass elements and reorganization of the silicate network.

Moreover, hydrolysis of the B-O-Si bonds is theoretically limited by kinetics expressed as a rate, r_{hydr}. With the following notations:

- $e(t)$ [µm] the gel thickness at time t
- $E(t)$ [µm] the total dissolved gel thickness at time t
- $D_{w,gel}$ [$m^2 \cdot s^{-1}$] the water diffusion coefficient in the PRI

This gives equation 36, in which the water diffusion profile in the PRI is assumed linear in the interval [$E(t)$, $E(t)+e(t)$]:

$$\frac{de}{dt} = \frac{r_{hydr}}{1 + \frac{e\, r_{hydr}}{D_{w,gel}}} - \frac{dE}{dt} \tag{36}$$

The PRI is then assumed to dissolve following a first-order law based on silica:

$$\frac{dE}{dt} = r_{disso}\left(1 - \frac{C_{Si}(t)}{C_{sat}}\right) \tag{37}$$

where r_{disso} [$m \cdot s^{-1}$] is the gel dissolution rate in pure water, $C_{Si}(t)$ [$kg \cdot m^{-3}$] the silicon concentration in the aqueous solution at time t, C_{sat} [$kg \cdot m^{-3}$] the silicon concentration at saturation in equilibrium relation between gel and aqueous solution.[8]

These equations could be implemented in a geochemical code to describe the complete system including secondary phase precipitation and aqueous species transport. A simple version of the model has been developed, in which secondary phase precipitation concerns only silicon by a sink term; it is assumed that only a single phase is formed. The GRAAL model in this version meets two fundamental requirements:

- accurately describe the chemistry with allowance for at least the major glass constituent elements as well as those supplied by the surrounding medium likely to have a significant impact on the glass alteration kinetics;
- describe glass alteration in such a way as to allow coupled chemistry-transport calculations at the scale of a repository vault. The proposed glass model must therefore be easily interfaceable with modules describing the other nearfield materials.

Describing not only (1) the solution chemistry but also ion transport (2) in solution and (3) in the glass alteration film by means of a single model at each point in space and time is an extremely complex task. The existing models describe only on or two of these aspects simultaneously. Models based on Monte Carlo methods are designed to study morphological changes in the passivating reactive interphase, but the chemistry and transport of ions in solution are only taken into account in a very simplified manner [166, 170]. Analytical models describe the surface layer but without allowance for chemistry and transport in solution provided by geochemical codes [138, 167]. Geochemical models are suitable for a detailed description of chemistry and transport in solution, but

[8] The effect of silicon speciation is not described here.

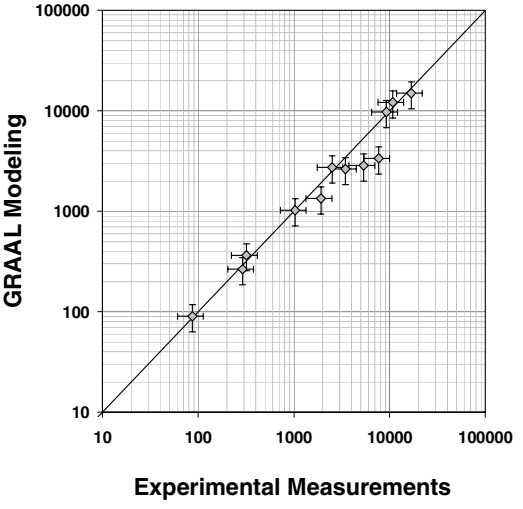

Fig. 30 Altered glass mass calculated by the model compared with experimentally measured values. Calculations were performed at the last sampling interval of each experiment

generally do not take any account of reactive diffusion phenomena at the interfaces [171, 172] — not because the latter are denied by their users [138, 139, 171], but simply because they are not formally taken into account: it is extremely complex to take all three mechanisms rigorously into account in a model for which the parameters are independent, limited in number, and measurable.

Nevertheless, these three key mechanisms and their coupling determine the glass alteration kinetics. GRAAL describes a simple and effective manner of coupling transport phenomena at different scales (items 1 and 2) with the evolution of the chemical composition in solution (item 3). This approach not only ensures that none of these mechanisms is neglected, but also allows for changes in their relative importance as a function of time, of the degree of confinement (high or low glass-surface-area-to-solution-volume ratio), and of the solution renewal rate.

The model has been implemented using the CHESS/HYTEC calculation code (versions 3.5 & 3.6) developed by the *École Nationale Supérieure des Mines de Paris* and uses the CTDP database [173]. Although the model uses a simple formalism with a limited number of parameters, it satisfactorily accounts for the element concentrations in solution. It describes variations of more than three orders of magnitude in the altered glass quantities correctly describing the effects of the three main parameters: time, the S/V ratio, and the Q/S ratio.

4.1.4.3 Preponderance of the Various Alteration Drivers

Figure 31 and Figure 32 show the ranges in which the various alteration drivers predominate over time depending on the experimental conditions. Figure 31 indicates the altered glass thickness values attributed to the diffusion mechanism, to the onset of saturation in the initially pure solution in contact with the glass (S/V), and to the effect of solution renewal (Q/S). The sum of these contributions

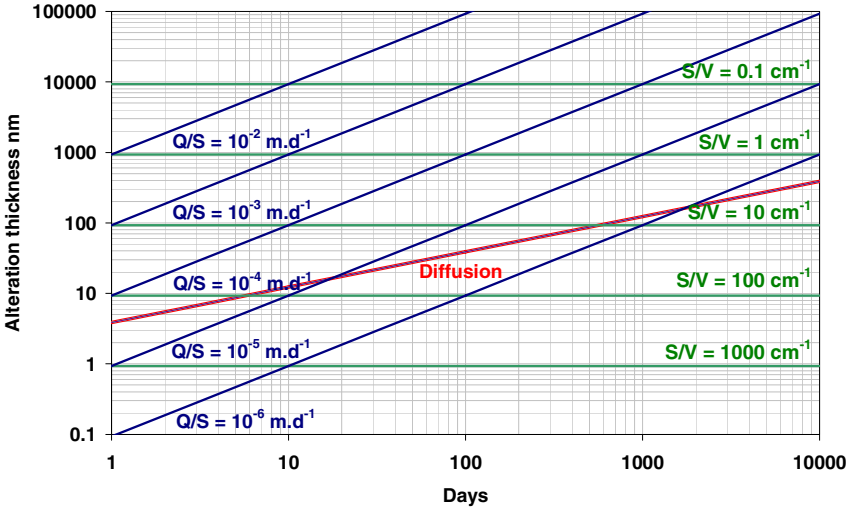

Fig. 31 Ranking of alteration drivers versus time for leaching of SON68 glass (simplified calculation without feedback, using the thermodynamic and kinetic parameters of leaching at pH 9 at 90°C). The expected *altered glass thickness* is the sum of the contributions of each mechanism: reactive diffusion, the quantity of altered glass necessary to reach silicon saturation with respect to the PRI formed in a closed system depending on the S/V ratio, and the effect of solution renewal versus flow rate per unit area (Q/S). *Example: for S/V = 100 cm^{-1} and Q/S = 10^{-6} m·d^{-1}, the diffusion mechanism predominates after 5 days of leaching, and the effect of solution renewal becomes significant only beyond 1000 days*

determines the altered glass thickness. This simplified calculation illustrates the orders of magnitude and the predominant mechanism. The calculations shown here are based on the solubility parameters and diffusion coefficients adopted for a temperature of 90°C and a pH of 9 at 90°C. Contrary to the full model, no feedback is taken into account between the mechanisms, and for the pH variations in particular. Figure 32 shows the same calculation expressed in terms of instantaneous rates. These schemes illustrate the importance of the effect of ion diffusion within the PRI on the concentrations of mobile elements (B, Na, Li, Mo), even at an S/V ratio of a few cm^{-1}. They show that diffusion cannot be disregarded in attempting to understand the geochemical evolution in a confined medium, such as a crack in a glass block, or a fractured glass block under geological repository conditions.

The model has been validated over the long term by comparison with archaeological analogs (Roman soda-lime glass leached for 1800 years in seawater) [141].

4.1.5 Concrete Hydrolysis

4.1.5.1 Introduction

After the repository is sealed, water will gradually saturate the site and structures until it eventually reaches the waste packages and saturates the porous cement

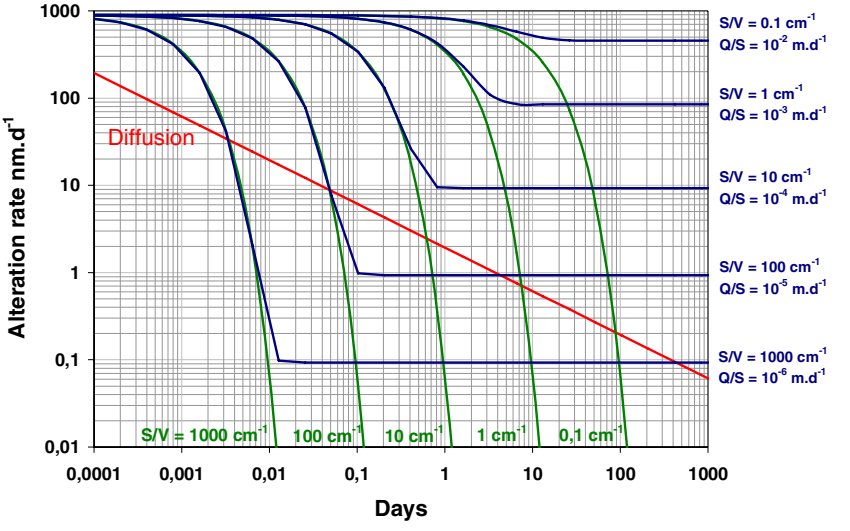

Fig. 32 Ranking of alteration drivers versus time for leaching of SON68 glass (simplified calculation without feedback, using the thermodynamic and kinetic parameters of leaching at pH 9 at 90°C). The expected *alteration rate* is the sum of the contributions of each mechanism: reactive diffusion, the quantity of altered glass necessary to reach silicon saturation with respect to the PRI formed in a closed system depending on the S/V ratio, and the effect of solution renewal versus flow rate per unit area (Q/S)

materials. The probable leaching process will then be related to the presence of water, both as an actual degradation agent or simply as a vector of aggressive ionic species. However, before chemically complex aggressive aqueous solutions can be taken into account it is indispensable to describe in detail the major hydrated phases (C-S-H, Portlandite, ettringite, AFm) under the simple chemical conditions of hydrolysis. In saturated media this process underlies all the other types of degradation related to the presence of aggressive species, and we have chosen here to limit the scope of this section to a study of hydrolysis of cement materials. The reader is invited to refer to specific documents and references concerning the alteration arising from:

- the presence of sulfate ions [29, 174, 175];
- the presence of carbonate, magnesium, or chloride ions alone or in coupled chemical corrosion [176];
- phenomena without external mass transfer (alkali-aggregate reaction [29], radiolysis [177, 178]).

4.1.5.2 Hydrolysis and Decalcification

Hydrolysis reactions in cement materials correspond to the action of dissociated water species on the hydrated solid phases of the cement matrix. Although the mineral phases are relatively stable in these materials in alkaline media, their stability is quite variable with the interstitial solution composition and especially with the pH [179, 180]. The chemical disequilibrium that may exist between the

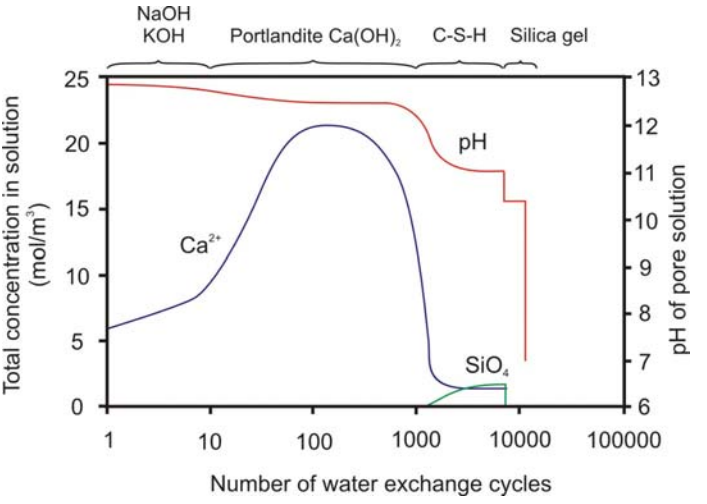

Fig. 33 Interstitial solution pH versus the leaching state of CEM I -based mortar (adapted from [179]). The major leached elements are identified on the graph

solid phases and the solutions with which they are in contact, related to mass transfer[9] between the material pore solution and a possibly aggressive external solution, may appreciably modify the mineral assemblage and lead to complete degradation of the binder.

The first elements leached as the pH diminishes are the alkali hydroxides, which are highly soluble and therefore not generally considered as belonging to the mineral assemblage of cement materials.

Strictly speaking, the first hydrate likely to be hydrolyzed is portlandite ($Ca(OH)_2$), the strongest mineral base. Near the stable pH for this compound (12.5), no other hydrate should be subject to significant degradation. Portlandite in this case acts like an inorganic buffer. The stability range of most hydrates lies between pH 12.5 and 10.5; the main relevant examples include C-S-H, ettringite and AFm. The stability of C-S-H diminishes with the pH, and incongruent dissolution results in a gradual decrease in the calcium/silicon ratio (Figure 34) to about 0.83, at which there structure is similar to that of tobermorite (Figure 38). In the same pH range the stability of the aluminates diminishes with the calcium stoichiometry. Only ettringite $[Ca_2Al(OH)_6]_2Ca_2(SO_4)_3$, $25H_2O$ remains more stable than its counterpart with a lower calcium content, calcium monosulfoaluminate hydrate (AFm) $[Ca_2Al(OH)_6]_2$, SO_4, $6H_2O$. At near-neutral pH values the residual material is a very porous silica and alumina gel containing variable traces of iron depending on the type of cement. [179, 181, 182].

In these systems only portlandite and C-S-H appear to have an actual role in controlling the interstitial solution pH; the other minerals, which are found in much smaller quantities, can be considered as “spectators”.

[9] As the kinetics of transport — especially diffusion — are much slower than the kinetics of the chemical reactions, a local chemical equilibrium is assumed. The leaching flows are therefore controlled by diffusion.

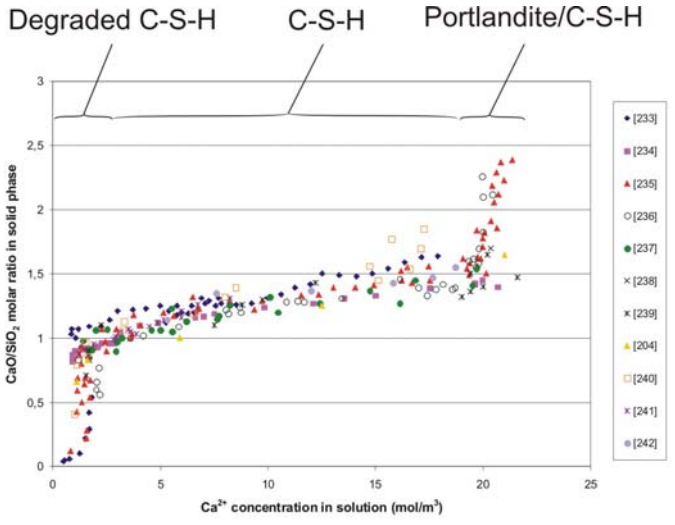

Fig. 34 CaO/SiO_2 ratio in solid phases versus calcium concentrations in solution at 25°C

4.1.5.3 Material Zonation

The degradation due to leaching by dissolution and precipitation processes develops from the cement material/solution interface and results in material zonation in which thicknesses of constant chemical composition are separated by dissolution-precipitation fronts (Figure 35) [181].

Each successive zone is characterized by a modified mineral assemblage and microstructure [183, 184], and more precisely by increased porosity. The successive layers each exhibit their own physicochemical and transport properties; the lower the porosity and the smaller its degree of interconnection, the denser the material and the less it is penetrated by the aggressive solutions.

The dissolution of massive crystals, as in the case of portlandite and calcium monosulfoaluminate hydrate, results in open porosity corresponding to the volume previously occupied by these hydrates. The decalcification of C-S-H phases that were much less crystallized is followed by internal structural reorganization with

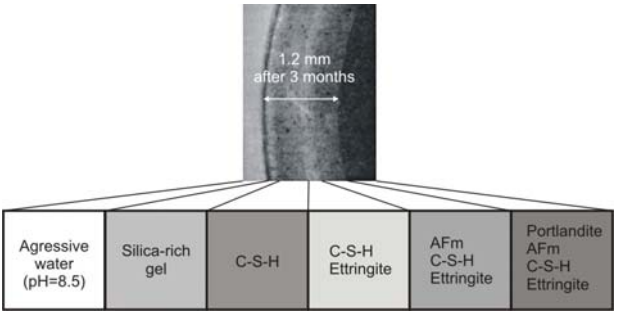

Fig. 35 Experimental results obtained with CEM I cement paste leached in a lightly mineralized solution at pH = 8.5, and detail of the resulting zonation (Adapted from [181])

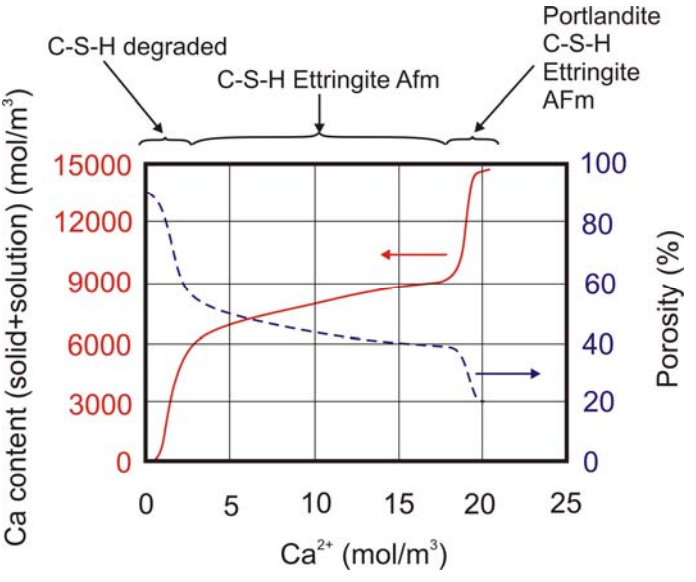

Fig. 36 Porosity versus total calcium concentration in the material (adapted from [185]). The mineral phases controlling the material chemistry are also indicated

little effect on their texture before the final stage of degradation (Figure 36). The fully degraded region then consists mainly of a porous silica gel containing traces of iron and aluminum. This layer tends to develop as the material degradation process advances.

Cement materials made from Portland clinker thus all exhibit the same degradation phenomenology; only the degradation kinetics vary with the type of cement and the leaching solution pH. The alteration of cement pastes by natural groundwater is related to the acidity of the solution with respect to the strong basicity (pH > 12.5) of the pore solution in cement materials. This results in dissolution of the Portlandite and residual anhydrides, and progressive decalcification of C-S-H between the pristine zone and the surface. Leaching also leads to segmentation of the mineral assemblage into mineralogically homogeneous zones separated by distinct degradation fronts parallel to the exposed sample surface. The alteration kinetics appear to increase with the Portlandite content, whose dissolution favors degradation by creating additional porosity. The alteration kinetics are also limited by diffusion and local chemical equilibria between the interstitial solution and the hydrated material. The zonation phenomenon described above causes the dissolution fronts to develop one-dimensionally, progressing at a rate proportional to the square root of time [181]. This phenomenological assessment now makes it possible to develop methods for modeling hydrolysis and decalcification of cement materials.

4.1.5.4 Approaches to Modeling Hydrolysis: Transport and Reaction

If an ion concentration gradient exists between two fluid zones, Brownian motion related to random thermal agitation results in a macroscopic effect, diffusion, that

involves an overall displacement of these ions toward the zone of lower concentration.

In the very general case of ion diffusion in a concentrated solution saturating a porous medium of porosity θ [%], the activity of the diffusing species cannot be equated with its concentration. Moreover, contrary to uncharged molecules such as the gas mentioned earlier, diffusing ions are subjected to ion-ion or ion-solvent electrical interactions. To maintain electroneutrality throughout the system, all the ions move in the direction of diffusion: the slower ions tend to slow down the faster-moving ones, and vice versa [186]. The ion flux of species *i* is then expressed by the Nernst-Planck equation:

$$\overrightarrow{J_i} = -De_i \left[\left(1 + \frac{\partial \ln \gamma_i}{\partial \ln C_i} \right) \overrightarrow{grad} C_i + \left(\frac{F}{RT} C_i z_i \right) \overrightarrow{grad} \varphi \right] \tag{38}$$

where

z_i valence of ion *i* [dimensionless]
F Faraday's constant [C/mol]
φ electrical potential due to the presence of other ionic species
R ideal gas constant [J/K/mol]
γ_i activity coefficient of diffusing species *i* [dimensionless]
J_i flux of diffusing species *i* in the porous medium [mol/m^2/s]
C_i concentration of diffusing species *i* [mol/kg^3]
De_i effective diffusion coefficient of species *i* in the porous medium [m^2/s]

Solving this equation requires a specific numeric approach because it must be solved for all the ionic species *i* in solution. In addition, if the liquid in which the diffusion process occurs is also in motion, convection phenomena can be integrated in the general equation by correcting the concentration variation over time using a term for the mean convection velocity. In the case of a geological repository in a clay formation, convection phenomena are negligible [187].

For reactive transport, in the case of hydrolysis in particular, chemistry-microstructure-transport feedback must be taken into account, making a numerical solution significantly more difficult. Mathematical methods and dedicated numerical tools must be developed to address chemistry-transport problems [181, 185, 188, 189]. The quality of the results also depends to a very large degree on the thermodynamic data supplied to the solid/solution equilibrium calculation codes.

For cement materials, which are intrinsically porous, chemical changes to the system modify the pore microstructure, which in turn leads to a variation in the diffusion coefficient of the species in the microstructure. The simplest approach is to estimate the feedback effects using empirical laws [181, 190, 191]. In the DIFFUZON model [181], for example, the solution is obtained through experimental zonation:

- Each zone, separated by a dissolution/precipitation front, represents a specific mineral assemblage, but in which the relative constituent proportions are variable.
- The porosity is determined from the nature and mean quantity of hydrates in each zone. The diffusion coefficient can then either be determined from the mineral composition, or maintained constant.

- Between each mobile dissolution front, the equation system based on diffusion phenomena, chemical equilibria, and material balances is solved with boundary conditions that remain constant over time.

This relatively simple method reproduces the increased diffusivity in the degraded zones of CEM I materials, as well as the experimentally observed zonation (Figure 37).

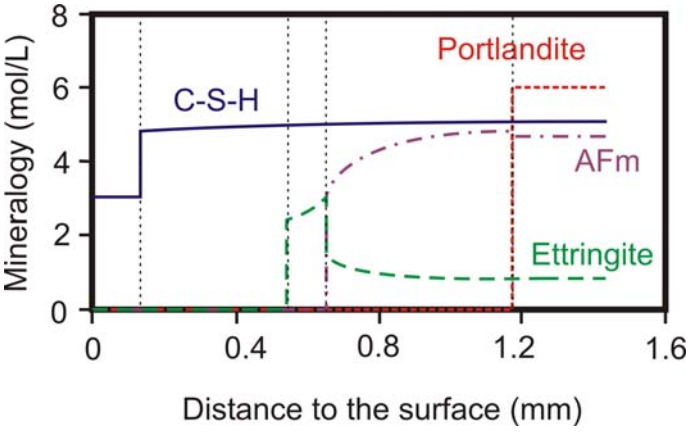

Fig. 37. DIFFUZON model of CEM I cement paste leaching in solution at pH = 8.5 (adapted from [181])

However, as the system becomes increasingly complex and precipitation reactions are superimposed on the phenomena already described, for example in the case of alteration by chemical species that are reactive with cement materials (sulfate, carbonate, etc.), these empirical approaches are insufficient. Two alternative strategies are currently adopted:

- The first is to estimate the macroscopic diffusivity with homogenizing models describing the heterogeneous system based on the basic constituents of the cement material, their physical and chemical characteristics and their volume fractions [192, 193].
- The second is to numerically generate a three-dimensional microstructure [194, 195] from which the material porosity and pore topology can be derived for use in estimating the transport properties.

With the computing resources available today, coupling between reactive transport codes and numerical models generating and modifying a three-dimensional microstructure at submicrometer scale can be expected to become a widespread approach.

4.2 Radionuclide Transport and Retention in These Matrices

The sorption of a dissolved element on a solid material can be due to various reversible or irreversible phenomena through different and independent mechanisms, including:

- physical adsorption involving Van der Waals forces;
- electrostatic interaction between ionic species and a surface-charged sorbent;
- chemisorption by interaction between solutes and complexation sites on the solid surface;
- substitution, the exchange of identical or similar species between the liquid phase and the solid phase;
- precipitation or coprecipitation of sparingly soluble products, capable of diminishing the quantity of matter in the soluble phase.

Some or all of these mechanisms can occur depending on the specific features of the conditioning materials and on the chemical nature of the elements considered. When a retention phenomenon cannot be clearly identified, a conservative approach can be adopted to assess the overall behavior of a specific radioelement in a particular material. In this context, the materials taken into consideration are glass, for which the passivating reaction interface has a fundamental role, and cement materials, in which the highly alkaline interstitial solution and the wide variety of hydrated mineralogical phases allow for many different types of interactions.

4.2.1 Radionuclide Retention Properties of the Gel (Adsorption and Coprecipitation)

Current HLW glass performance assessment models are based on the very conservative hypothesis that there is no retention of radionuclides in the glass alteration products. Experimental results have shown, however, that some elements are almost entirely retained in the gels, including the lanthanides (rare earth elements) and actinides. The degree of retention varies appreciably according to the environmental conditions. The pH and Eh, as well as the hydrolyzing and complexing species (H^+, OH^-, H_2O, carbonates, phosphates, sulfates, chlorides, organic acids, etc.) and solid materials, fundamentally constrain the distribution of the actinides and rare earth elements between the gel and solution, and the solubility of these elements is directly dependent on these constraints [168, 196].

4.2.1.1 Typical Radionuclide Retention for R7T7 Glass Leached in Pure Water

Retention is quantified by the retention factor (RF): the ratio between the normalized mass loss of a mobile element that is not retained in any glass alteration product (generally boron) and that of the element considered. A retention factor of 100 implies that 99% of the element is retained in the gel (the latter value represents the retention rate: RR).

The retention factors for various radionuclides were measured in pure water under oxidizing conditions at 50°C and 90°C during leaching of active R7T7 glass samples each containing 0.85 oxide wt% of a single radionuclide (^{237}Np, ^{238}Pu, ^{239}Pu or ^{241}Am) and an inactive glass control specimen (with 0.52 wt% UO_2 and 0.33 wt% ThO_2) [197]. Throughout the experiment the radionuclides were retained to a much greater degree than silicon (in the following order: Np < U < Pu < Am) and the retention factor within the alteration film remained roughly constant beyond the first month of leaching (Table 12). Only the neptunium release at 50°C was comparable to that of silicon. The relatively high mobility of Np is also confirmed by other authors [198, 199]. Retention was

generally greater at 90°C than at 50°C, but, for ^{238}Pu and ^{241}Am the low (acid) pH could account for the differences.

Table 12 Mean retention rates for U, Np, Pu and Am at 50°C and 90°C observed during leaching in static mode in pure water (mean values of analyses performed between 1 and 12 months, R7T7 glass). Slight differences were observed between ^{238}Pu and ^{239}Pu observed: they can be attributed to the effect of water radiolysis, which caused a decrease in the pH for the ^{238}Pu-doped glass (more pronounced at 50°C than at 90°C)

1–12 months	U	^{237}Np	^{238}Pu	^{239}Pu	^{241}Am
RR 90°C (%)	88.4	86.2	96.7	98.1	99.8
$RR_{(Si)}$ 90°C (%)	41.7	43.4	41.8	40.2	47.1
Final $pH_{(25°C)}$	9.7	9.4	8.6	8.6	8.5
RR 50°C (%)	80.2	55.8	88.1	93.5	95.7
$RR_{(Si)}$ 50°C (%)	40.6	46.0	27.4	41.9	36.6
Final $pH_{(25°C)}$	9.4	9.4	5.8	8.6	5.7

At high solution renewal rates, i.e. under aggressive conditions, the same type of behavior is observed as under steady-state conditions: strong Pu, Am and Cm retention, and lower retention of Np and U. Table 13 indicates the retention rates obtained during various 28-day Soxhlet tests [157, 197, 200, 201]:

Table 13 Retention rate of elements from R7T7 glass leached at 100°C in Soxhlet conditions

Soxhlet 28 d (100°C)	R7T7 glass	RR
Cs	Inactive	0
Mo	Inactive	7
Sr	Inactive	15
Np	Np-enriched	75
U	Inactive	87
Nd	Inactive	99.4
Ce	Inactive	99.6
Am	Np-enriched	99.8
Pu	Np-enriched	99.8
Zr	Inactive	99.8

In Pu-doped borosilicate glass leached in pure water renewed daily, the influence of the temperature on the Pu release between 25°C and 90°C was much lower (Ea = 22 kJ·mol^{-1}) than for other elements (Si, Na, Cs) (Ea = 78 kJ·mol^{-1}) because of different alteration mechanisms [202].

4.2.1.2 Effect of Redox Conditions on Radionuclide Retention

Variations in the redox conditions of the medium do not directly influence the glass alteration mechanisms. Although this parameter does affect the mobility of

some elements, and thus their retention in the alteration film, there is no experimental evidence of a loss of protectiveness of the gel as a result of preferential release of gel-forming elements.

The retention of Am, Cm and, to a lesser extent, Pu was relatively unaffected by the redox conditions — unlike Np, which was much more solidly retained under reducing conditions [203].

4.2.1.3 Mechanisms Involved in Radionuclide Retention

Radionuclides are found in solution as cations when they are not part of complexes, and they are characterized by very low solubility; the two principal mechanisms responsible for retention in the alteration film are physical or chemical adsorption on the surface of the gels and precipitation (or coprecipitation with other insoluble elements such as Fe, Zn, Zr) in the gels either by incorporation in the gel silicate network, or by segregation of small nodules.

Retention of the rare earth elements and actinides must be taken into account differently depending on whether the elements are adsorbed or precipitated. If the elements are retained in the gels by precipitation, they may be considered more durably immobilized than if they are simply adsorbed, in which case they can desorb and become mobile again if the environmental conditions are modified. Cesium, which is incorporated in the gel during glass alteration, should therefore be considered mobile when the gel itself is subjected to aqueous alteration. Complexation of the rare earth elements and actinides by various ligands is also a source of mobility and partitioning of these elements between the alteration solution and the gel.

In general, the *rare earth elements* (lanthanum, cerium and neodymium) and the *actinides* (americium and curium) exhibit comparable behavior during leaching. This could be due to the fact that these elements are all found in solution at oxidation state III (La^{3+}, Nd^{3+}, Am^{3+} and Cm^{3+}) or IV (Ce^{4+}). Their retention factors in the gel are very high: even in complexes they can conserve a positive total charge, maintaining a strong attraction to the negatively-charged gel.

Unlike the rare earth elements, both *uranium* and *neptunium* show much higher mobility. Both uranium and neptunium are found in solution (in oxidizing media) mainly as UO_2^{2+} and NpO_2^{+}. With their charges of only +1 or +2, when complexed their total charge is neutral or negative, leading in the latter case to strong repulsion. This could partially account for the behavior of U and Np compared with the rare earths and comparable transuranic elements.

Plutonium exhibits intermediate behavior between that of the rare earths and uranium.

In addition to element coordination studies in the gel, which provide data on the nature and incorporation of elements within the gel, a few experiments have been carried out in this area, including studies under the European contract Glastab [168], leading to the following conclusions concerning the mechanisms to be taken into account for radionuclide retention:

- Precipitation processes account for the long-term retention of elements such as Th, Am, U and REE, which precipitate in different combinations incorporating sparingly soluble elements such as Th, Ti, Zr, Al, Fe, Cr and Mo. These

findings were confirmed by a recent study in which gels formed by leaching α-doped SON68 glass at 300°C were then altered at 50°C, showing that they had a strong retention capacity for Pu and Am (> 99%, compared with 35% for Np), and that retention occurred within more stable phases than simple hydroxides or carbonates.

- Sorption processes are also involved in the retention of actinides and lanthanides, particularly for the short- and medium-term retention of trivalent species. The general trend for the retention of Pu, Am and Np follows the general sorption tendency of the actinides and lanthanides:

$$An(IV) > An(III) \geq Ln(III) > An(V).$$

- These processes are highly sensitive to the physical and chemical conditions of the medium: the presence of carbonate ligands or of specific elements in solution (e.g. Mg) significantly diminishes the retention of these radionuclides. Measurements of NpO_2^+ adsorption on a gel obtained by leaching SON68 glass under pseudo-dynamic conditions at 25° and 90°C with concentrations of 10^{-7} M and 10^{-5} M at variable pH showed that Np(V) adsorption on the gel is highly pH-dependent, especially between pH 6 and 9. Conversely, the temperature has little effect within this range.
- The gel structure and therefore the initial glass composition and the gel formation conditions have a major effect on its retention capacity. The percentage of adsorbed Np(V) and Am increases when their concentration in solution is low compared with the number of adsorption sites in the gel (surface complexes form between neptunium and ferrinol sites, for example). At high NpO_2^+ concentrations (i.e. about 1%) compared with the number of available sites, however, neptunium adsorbs on several types of sites. A predictive model of Np(V) and Am(III) sorption on a gel formed from R7T7-type glass according to the physical and chemical conditions of the medium was developed from the results of these studies. The model is based on an equation of this type:

$$S\text{-OH} + An^{m+} = S\text{-O}An^{(m-1)+} + H^+$$

where *S*=solid and *An* = actinide; the equilibrium constants $K = [H^+]/[An^{n+}]$ were determined for Np ($10^{-4.5}$) and Am ($10^{-4.2}$) [Ribet et al., 2004].

4.2.2 Radionuclide Retention and Transport in Cement Materials

4.2.2.1 Radionuclide Retention

4.2.2.1.1 Phenomena Involved. The radionuclide binding mechanisms at high interstitial solution pH are uncertain. Cation exchange and surface complexation mechanisms, which are generally representative at pH values ranging from 3 to 10 (refer to the section on glass, for example), are not necessarily the major

phenomena in basic media (pH > 11). Surface precipitation or the formation of solid solutions can become significant in this regard. In addition, many radioelements exhibit low solubility at high pH in the interstitial solution. Table 14 summarizes the principal interaction mechanisms between radionuclides and cement materials reported in the literature.

Table 14 Representative elements and retention mechanisms reported in the literature

Elements	Proposed mechanisms
Alkali metals	Sorption of C-S-H at silanol sites [204, 205]
	$H^+ \leftrightarrow M^+$ exchange within C-S-H layers [205]
Alkaline earths	$Ca^{2+} \leftrightarrow M^{2+}$ exchange [206]
	$Ca^{2+} \leftrightarrow M^{2+}$ substitution in the solid [207]
	Formation of a solid solution with $CaCO_3$ [208]
Ni, Zn, Pb	$Ca^{2+} \leftrightarrow M^{2+}$ substitution in the solid [209]
	Loading in the solid (C-S-H) matrix [210, 211].
	Formation of a solid solution with $CaCO_3$ [208]
	Precipitation of double Al-M hydroxides [212]
	Surface complexation [213]
Halogens	Formation of a solid solution
	$OH \leftrightarrow M$ substitution within C-S-H
	Formation of Friedel's salt [214]
	$SO_4 \leftrightarrow M$ substitution [215]
Trivalent actinides	Loading in the solid (C-S-H) matrix [216]
	Surface complexation [216]
Actinides at higher valence states	Adsorption at silanol sites [217]
	Formation of solid solutions [218].
	Coprecipitation [219]

The diversity of the proposed retention mechanisms adds to the difficulty of devising a thermodynamic representation of the mineral assemblage in cement materials and of their degradation (section 4.1.5). Two complementary approaches are possible:

- An overall assessment of the interactions between radionuclides and the cement matrix without any preconceived notions concerning the underlying mechanisms; this approach is easier to model, and is particularly suitable for conservative applications.
- A mechanistic description of retention based on an advanced physicochemical interpretation of the interactions between radioelements and the material; the resulting model is more representative of the reaction phenomena, but the knowledge level needed is more difficult to obtain.

4.2.2.1.2 Element Retention and Modeling. The retention capacity of a material for an element is determined by comparing two quantities:

- the element concentration in the sorbed phase [mol/kg of dry material]
- the element concentration in the liquid phase at equilibrium with the material [mol/m^3].

A partition coefficient, *Rd*, can then be defined for species *i* as equal to the ratio between the two concentrations [m^3/kg]; the higher the *Rd* value, the more sorbent the material.

4.2.2.1.3 Overall Approach. Under very specific conditions — for which sorption is reversible, chemical equilibria are reached instantaneously or at least very rapidly compared with transport, and the concentrations of sorbed species are directly proportional to the species in solution — the *Rd* ratio is designated *Kd*.

This parameter describes an exchange at macroscopic scale between the sorbed and dissolved species, without specifying the sorption mechanisms. This formalism is frequently used because of its simplicity. It also has the advantage of simply representing conservative conditions (low *Kd*), but is not very realistic since the conditions under which it can be used are rarely all met at the same time.

Although direct partition coefficient measurements can initially substantiate radionuclide sorption on relatively fresh cement materials, it is difficult to extrapolate them directly over the longer term. Two main approaches can be envisaged:

- The first is to measure the sorption on an assemblage of mineral phases considered representative of the material at a given state of degradation. This approach is dependent on the definition of arbitrary relations between the degradation states and the corresponding mineral assemblages.
- The second is to define empirical relations between the partition ratio and the composition of the fluids and solids versus key parameters such as the pH, the calcium concentration in the interstitial solution, or the calcium/silicon ratio in the solid phases.

4.2.2.1.4 Mechanistic Approach. A more precise representation of these interactions can be based on characterization and quantification of the binding mechanisms. This assumes detailed knowledge of the solid/fluid/radionuclide system, which is difficult to obtain in cement systems because of the wide range of mineral assemblages in such materials and the diversity of the minerals themselves. In fact, this approach is currently limited to conditions in which the behavior of a radionuclide can be represented by interactions with one or two fully characterizable mineral phases.

Ion retention at surface reaction sites is currently described by two complementary approaches: the theory of ion exchangers developed to analyze the interaction between radioelements and clay [220, 221], and surface complexation models, which are discussed below.

Table 15 Overview of solubility and retention of some radionuclides in pristine cement material (according to ANDRA, 2005)

Element	Solubility (mol/L)	*Kd* (m^3/kg)
Cl^{-I}	Infinite	0
I^{-I}	Infinite	~10^{-3}
Cs^{I}	Infinite	~10^{-2}
Tc^{IV}/Tc^{VII}	~10^{-7}/Infinite	~2/0
C^{IV}	~10^{-5} – ~10^{-6}	~1
Ni^{II}	~2×10^{-7}	~2
Se^{-IV}	~10^{-5}	~10^{-1}
Zr^{IV}	~10^{-8}	~40
Nb^{V}	~10^{-9}	~100
U^{VI}	~10^{-6}	~50
Sm^{III}	~10^{-10}	~100
Eu^{III}	~10^{-10}	~100
Tb^{III}	~10^{-10}	~100
Ho^{III}	~10^{-10}	~100
Th^{IV}	~10^{-10} – ~10^{-11}	~20
Np^{IV}	~5×10^{-9}	~20
Pu^{IV}	~10^{-9}	~20
Am^{III}	~10^{-10}	~30

In surface complexation models, the solid/solution interface is described at a microscopic level taking into account the ions on the material surface [222]. The material surface is not electrically neutral; each site is considered as weak diprotic acid [223], and the distribution of species in solution near the surface can be described in various ways [222, 224, 225]. In the case of cement matrices, the most widely used model is the Gouy-Chapman double layer model or one of its variants [226]. Depending on its dissociation state, each surface site can impart a positive or negative surface charge:

$$>MOH_2^+ \rightleftharpoons MOH + H^+ \quad \text{where} \quad Ka_1 = \frac{\{>MOH\}\left[H^+\right]}{\{>MOH_2^+\}} \tag{39}$$

$$>MOH \rightleftharpoons MO^- + H^+ \quad \text{where} \quad Ka_2 = \frac{\{>MO^-\}\left[H^+\right]}{\{>MOH\}} \tag{40}$$

For cement materials, and in particular C-S-H, the available silanol sites (>SiOH) can only sustain the second dissociation reaction for which the pKa can be estimated at 7.2 [223].

The apparent equilibrium constant for a sorption reaction K_a, can also be expressed in terms of the free energy of adsorption ΔG^0_{ads} [227]:

$$K_a = \exp\left(-\frac{\Delta G^0_{ads}}{RT}\right) = \exp\left(-\frac{\theta_i}{RT} - \frac{z_i F \Psi_0}{RT}\right) \tag{41}$$

where F is Faraday's constant, R the ideal gas constant, T the temperature, z_i the distance from the surface, θ_i the non-Coulomb chemical interaction between ion i and the surface site, Ψ_0 the surface potential directly related to the surface charge and thus to the surface saturation capacity and the specific surface area of the material. This relation can be written as follows:

$$K_a = K_a^{\text{int}} \exp\left(-\frac{z_i F \Psi_0}{RT}\right) \tag{42}$$

where K_a^{int} is the intrinsic equilibrium constant of adsorption.

It is difficult to determine parameters such as Ψ_0 directly, especially for cement materials whose composition varies with their equilibrium solution composition. To determine the specific binding constants of the species considered in this system, it must be described in the following terms [226]:

- the solubility of the solid phases, which is particularly important for C-S-H phases with incongruent solubility (Figure 34);
- the intrinsic charge of the C-S-H phases, which determines the surface potential Ψ_0; the surface charge density, based on structural knowledge concerning the C-S-H phases;
- the ion activity defining the thermodynamic properties of ions in solution, which determines the organization of the electrical double layer in both the compact and diffuse portions;
- the selected double layer model characterizing the solid/solution interface and determining the numerical development of the surface interactions;
- ion adsorption, i.e. the surface complexes likely to form and their equilibrium constants.

The prerequisite for developing a surface complexation model is to determine the system protonation/deprotonation constants by acid/base titration, zeta potential measurements, etc., on solid/solution suspensions. Only then can the binding constants of these species be calculated.

4.2.2.1.5 Example Applied to Cesium in Calcium Silicate Hydrates (C-S-H) [204]. In accordance with the preceding generic considerations, the first step in describing the interaction between C-S-H and cesium is to describe the solubility and surface charge of the C-S-H. The generic formula for calcium silicate hydrates is $x\text{CaO}\cdot\text{SiO}_2\cdot y\text{H}_2\text{O}$, where $0.7 < x < 1.8$ [21]. These materials exhibit a nanometric local structural order [228]. C-S-H has a layered structure with a double-layer octahedral calcium skeleton and, on either side, two partially

polymerized chains of silicon tetrahedra in a “dreierketten” pattern resembling tobermorite [229] (Figure 38).

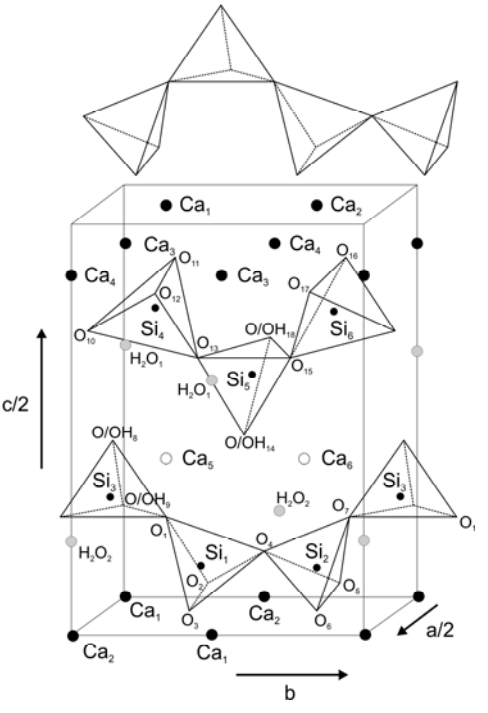

Fig. 38 Three-dimensional view of orthorhombic structure of tobermorite [229]. The lattice parameters are a/2 = 5.58 Å; b = 7.39 Å; c/2 = 11.389 Å. The calcium atoms (dotted lines) are statistically distributed between mesh points

Models can be proposed in which the solubility products are calculated by extrapolation from the extensive experimental solubility data reported in the literature [226]. Table 16 indicates the reaction equilibria and constants obtained by Pointeau through acid titration of C-S-H suspensions [204]. In the solid-solution equilibrium postulated by Pointeau, the charge deficit on the C-S-H surface and between the layers is assumed to be compensated by sorption at

Table 16 Reactions and constants determined by acid titration of C-S-H suspensions (from Pointeau, 2000)

	Reactions	Log *K*
Solubility equilibria	$CaH_2SiO_4 \leftrightarrow Ca^{2+}+H_2SiO_4^{2-}$	−8.12 ±0.05
	$Ca_4Si_5O_{15}H_2+8H^++5H_2O \leftrightarrow 4Ca^{2+}+5H_4SiO_4$	52.2 ±0.1
	$Ca_2Si_3O_9H_2+4H^++3H_2O \leftrightarrow 2Ca^{2+}+3H_4SiO_4$	24.7 ±0.1
	$SiO_2+2H_2O \leftrightarrow H_4SiO_4$	−2.75 ±0.05
Surface equilibria	$>SiOH \leftrightarrow SiO^-+H^+$	−12.0 ±0.2
	$>SiOH+Ca^{2+} \leftrightarrow SiOCa^++H^+$	−9.2 ±0.2

silanol sites of protons (>SiO^--H^+) or labile calcium ions (>SiO^--Ca^{2+}); these hypotheses appear to be validated by ^{29}Si MAS-NMR findings [230]. It is also possible, however, to estimate the C-S-H surface charge generated only by the silicon tetrahedra encircling the C-S-H layers; this charge is estimated at –0.66 C/m^2 [226].

The models are then validated on the C-S-H systems used to fit the data obtained from zeta potential measurements or titration of C-S-H suspensions. Figure 39 compares the titration values in the model developed by Pointeau with independent results.

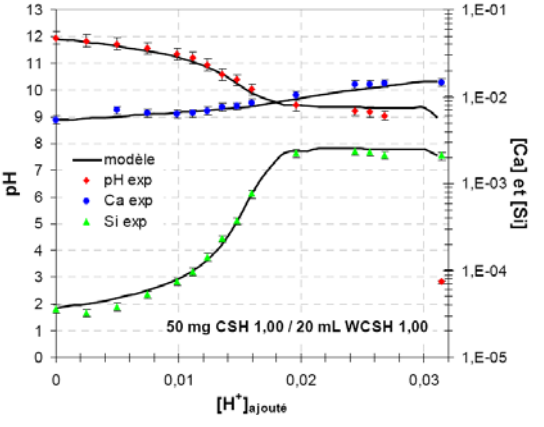

Fig. 39 Titration model of C-S-H system with a CaO/SiO_2 ratio of 1 [204]

Using these models and allowing for cesium sorption measurements by direct assay or determination of the isoelectric point, for example, it is possible to propose a description of cesium retention on C-S-H. Given the arbitrary character of some aspects (nature of the complexes taken into account, variability of experimental data reported in the literature, etc.) one [205, 213] or several [204] cesium sorption sites have been identified (Table 17).

Table 17 Surface complexation constants used for the interaction between Cs^+ with the C-S-H surface [231]

	[213]	[205]	[204]
>SiOH $\rightleftarrows$ SiO^-+H^+	$K=10^{-6.8}$	$K=10^{-12.3}$	$K=10^{-12.0}$
>SiOH+Ca^{2+} $\rightleftarrows$ $SiOCa^+$+H^+	-	$K=10^{-9.4}$	$K=10^{-9.2.}$
>SiOH+Ca^{2+}+H_2O $\rightleftarrows$ SiOCaOH+2H^+	$K=10^{-17}$ – $10^{-15.1}$	-	-
>SiOCaOH+H^+ $\rightleftarrows$ $SiOCaOH_2^+$	$K=10^{8.3}$ – $10^{12.6}$	-	-
>SiOH+Cs^+ $\rightleftarrows$ SiOCs+H^+	$K=10^{-4.6}$	$K=10^{-11.3}$	Strong site: $K=10^{-11.0}$
			Weak site: $K=10^{-6.2}$

Figure 40 illustrates the type of results given by these models, which are consistent with independent experimental data.

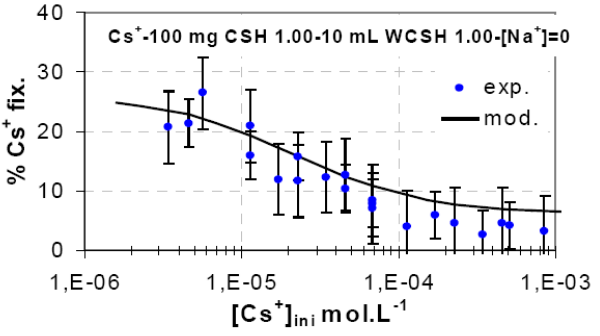

Fig. 40 Comparison between experimental and modeled Cs sorption isotherm for C-S-H with a CaO/SiO_2 ratio of 1.00 [204]

One of the principal objectives behind the development of a mechanistic modeling approach is, of course, to identify C-S-H sorption sites in order to quantify their evolution with the CaO/SiO_2 ratio in the solids, i.e. to assign parameter values for radionuclide retention versus one of the main factors of material degradation (refer to section 4.1.5).

4.2.2.2 Coupling of Transport and Retention

The fundamental equation for diffusive transport of an ionic species i in cement materials was discussed above (eq. (38)).

If interactions occur between the solid phase in the porous medium and the diffusing chemical species they must be taken into account. The total concentration of species *i* taken into account in equation (38) is therefore the sum of the concentration of species *i* in solution and its concentration in the solid phase. The quantity of ions *i* in the solid phase, $\overline{C}_i$, is generally measured per unit mass. The total concentration is thus:

$$C_{total_i} = \theta C_i + (1-\theta)\rho_s \overline{C}_i \tag{43}$$

where θ is the porosity of the medium, ρ_s the dry density of the material, and C_i the concentration of ionic species *i* in solution.

The equation of mass conservation can be written for a material of constant porosity ρ:

$$\frac{\partial C_{total}}{\partial t} = -div\left[\vec{J}\right] \tag{44}$$

The continuity equation, which must be written for each ionic species *i*, can be supplemented with the binding capacity, $\partial\overline{C_i}/\partial C_i$, which represents the ability of the porous medium to bind ions [232]:

$$\frac{\partial C_i}{\partial t} = De_i\left[\theta + (1-\theta)\rho_s \frac{\partial \overline{C_i}}{\partial C_i}\right]^{-1}\left[div\left[\left(1+\frac{\partial \ln \gamma_i}{\partial \ln C_i}\right)\overrightarrow{grad} C_i\right] + \frac{F}{RT} z_i div\left(C_i.\overrightarrow{grad}\phi\right)\right] \quad (45)$$

If the diffusing species is radioactive, radioactive decay can also be included in the preceding differential equation with a $\lambda C_{total,i}$ term, where λ is the radioactive half-life (s). The preceding equation must be solved for all species *i* in solution, whether or not they are likely to interact with the representative mineral assemblage of a cement material at a given degradation state, together with a given local porosity. In fact this type of model is still under development mainly because of the above-mentioned difficulty of accurately representing a cement material and its porosity.

A simpler conservative approach can nevertheless be adopted. Consider the diffusion of a single species *i* in a dilute medium in which electrodiffusion can be ignored and for which interactions between ionic species *i* and the cement material can be described by a partition coefficient K_d. The preceding equation becomes:

$$\frac{\partial C_i}{\partial t} = De_i\left[\theta + (1-\theta)\rho_s Kd\right]^{-1} \Delta C_i \quad (46)$$

Assuming diffusion phenomena occur in a porous medium, the effective diffusivity De_i of solute *i* can be defined thus:

$$De_i = \varepsilon \frac{\delta}{\tau^2} D\omega_i \quad (47)$$

where ε is the porosity accessible to ion *i*, δ the pore constrictivity, τ their tortuosity, and $D\omega_i$ the diffusion coefficient of ion *i* in free water. If the diffusing ion interacts with the porous medium, an apparent diffusivity can be defined thus:

$$Da_i = \frac{De_i}{\left(\varepsilon + \rho Kd\right)} \quad (48)$$

The apparent diffusion coefficients thus depend on two main factors:

- sorption of species in the porous medium. High *Kd* values result in a low apparent diffusion coefficient, hence slower ion transport.
- porosity accessible to the relevant ionic species, i.e. indirectly on the ion charge. Cement materials contain a large proportion of small pores, mainly between and within the C-S-H, with a negative surface charge imposed by the C-S-H. Because of electrostatic repulsion, all the pore volume is not accessible to anionic species which are forced into the pores, or even excluded from some transfer pathways. At macroscopic scale, this results in decreased diffusion coefficients for the anions compared with the cations.

Table 18 indicates orders of magnitude for the apparent diffusion coefficients obtained with CEM I paste.

Table 18 Apparent diffusion coefficient obtained for a CEM I paste, with water/cement ratio of 0.40. [231]

Element	Apparent diffusion coefficient (m^2/s)
HTO	10^{-13}–10^{-12}
Cs^+	10^{-13}
Sr^{2+}	10^{-16}
$Tc(TcO_4^-)$	10^{-14}–10^{-13}
Cl^-	10^{-15}
I^-	10^{-15}
Co	10^{-17}
Ni	10^{-19}
Mo, Pd	$<10^{-19}$–10^{-18}
Zr, Pd	10^{-22}–10^{-21}
Pu	10^{-22}–10^{-21}
Am, Np, U	$<10^{-19}$–10^{-18}

Studies of radionuclide retention and transport in cement matrices to date have shown that there are too many parameters involved to account for the retention of all the elements by all the potential mineral phases using a single model. Moreover, with regard to transfer processes the complexity of the mineral assemblages in cement materials is compounded by the difficulties involved in describing the evolution of the porosity with the solution chemistry and material alteration. Nevertheless, several features can be positively established: cement materials significantly delay the migration of radioelements both through retention of elements on the cement phases and because of the solubility limits at high interstitial solution pH values. Retention appears to be influenced both by the material formulation and to a greater extent by its degradation state. Surface chemistry models and thermodynamic models related to the formation of a solid solution can be used when the retention phenomena are known. In the absence of specific data, empirical or conservative relations are used to describe the material behavior material as accurately as possible.

Two different strategies can be applied to enhance the effectiveness of this modeling approach. The first is to carry out experimental studies on individual phases in the mineral assemblage representative of the cement degradation state. The retention data obtained on individual minerals are then used to establish a set of *Kd* values that can be organized according to the nature and quantity of phases present at a given state of degradation. The second strategy consists in a detailed investigation of the retention mechanisms with the objective of characterizing and quantifying them. Suitable thermodynamic models can subsequently be implemented.

The particularity of cement materials — multi-scale porous media in which the porosity depends on solid/solution chemical equilibria and is therefore subject to constant change — adds another degree of complexity to modeling. The strategies that can be adopted to deal with these features were mentioned above [section 4.1.4.4]. Despite these difficulties, numerical coupling of reactive transport codes and/or thermodynamic codes modeling sorption reactions with specific tools developed to create and modify a three-dimensional microstructure at submicrometer scale appears to be the most promising avenue of exploration for a performance assessment of cement materials over time.

5 Conclusion

The main objective of long-term radioactive waste management is to protect the population and environment against the risks arising from the existence of wasteforms over a time period according to their radiological half-life. The wasteforms are confined by multiple barriers to prevent the dispersal of the radionuclides they contain. The primary barrier is the waste package itself, i.e. the materials used to immobilize the waste together with the outer container. We have chosen to focus on transport phenomena in three constituent mineral materials of nuclear waste packages: ceramic materials (spent fuel in this case), as well as the cement materials and glass used to condition nuclear waste. In a deep geological repository context, these materials are exposed to environmental conditions that can vary significantly over time (water saturation, temperature, oxidation-reduction, etc.). The mass transfer phenomena and mechanisms to which these materials are subjected are controlled by the external context.

During the industrial operation of a deep geological repository, the container is leaktight and the waste conditioning matrices are exposed to unsaturated conditions. In this initial period the transport phenomena involved concern gas production by self-irradiation or corrosion, for example, and migration within the matrix (in spent fuel, for example) or release through the container walls.

The issues of gas production and transport within the matrix concern helium generated by alpha decay and released by diffusion. Although this behavior does not raise any direct radiological hazards, it affects the ceramic microstructure of the fuel and consequently the instant release inventory at the moment water comes into contact with the spent fuel. In the context of interim storage or final disposal of spent fuel, thermal diffusion of helium appears to be negligible; the helium remains essentially localized in the crystal lattice or trapped in irradiation defects. Only a small fraction of the helium appears to be released from the fuel, mainly in gaseous form at the grain boundaries or in intergranular bubbles.

The situation is very different for cement materials: these materials can be considered as multiphase porous media that are not completely water-saturated during the operational period. They are therefore liable to offer a pathway for gas transport through the unsaturated interconnected porosity. Depending on their production kinetics, the gases can migrate through the porosity in the materials by permeation (in which case transport appears to depend on the degree of saturation of the materials and on their total porosity) or by diffusion (for which transport

then depends on the material saturation and on the size distribution of the pore accessibility diameters).

Over the longer term, after closure of the repository, groundwater will inevitably come into contact with the waste packages. Water will then become the main material alteration vector. However the material alteration rates and retention properties can be considerably different depending on their specific physical and chemical characteristics and microstructure.

Borosilicate glass structures are amorphous materials with a remarkably capacity for incorporating chemical elements as cations while ensuring satisfactory chemical durability and strong irradiation resistance. Because of their amorphous nature these materials are difficult to characterize except by experimental spectroscopic techniques. It has been demonstrated, however, that aqueous alteration of glass involves four main phenomena:

- interdiffusion (exchange between protons and alkali ions),
- hydrolysis (rupture of Si-O-Si bonds, for example),
- recondensation of dissolved species to form an amorphous alteration gel constituting a diffusion barrier between the glass and solution,
- precipitation of crystallized secondary phases.

Depending on the glass composition and on the chemical composition and renewal rate of the leaching solution, any of these reactions can be favored, modifying the matrix alteration rate and thus the radionuclide release rate.

In any event these alteration processes result in the formation of a passivating reactive interface with properties, such as porosity and connectivity, that depend on the preceding parameters. Glass degradation is thus not controlled by the kinetics of hydrolysis reactions, but by limitations on the accessibility of water the reaction interface.

This phenomenological foundation was used to develop a nuclear glass alteration model allowing for coupling of chemistry and transport phenomena at microscopic scale. This model was then validated by comparison with archaeological analogs.

A significant body of knowledge has been established concerning this system because of the material homogeneity at mesoscopic scale — not only the composition but also the initial microstructure. These properties are compatible with a range of experimental techniques and atomistic models that have made it possible to clearly identify and understand in detail the basic mechanisms involved in the alteration processes.

Radionuclide release from the **UO_2 matrix** depends on:

- the instant release inventory, which comprises the radionuclides not localized in the UO_2 matrix and which will be released quickly after water comes into contact with the waste package; the source term varies according to the microstructure of the ceramic materials constituting the spent fuel, i.e. its leaching behavior in an unsaturated closed system.
- the chemical stability of the UO_2 ceramic matrix, largely controlled by the system redox conditions, which can be influenced by the fuel self-irradiation

field and by water radiolysis. The onset of oxidizing conditions is unfavorable since the UO_2 fuel matrix is altered by an oxidizing dissolution mechanism in which U(IV) is oxidized to U(VI). The latter species more readily forms complexes with some chemical species, such as carbonates, that are frequently found in groundwater.

Radionuclide release thus occurs both through leaching of the radioelements contained in the cracked or microstructural matrix pore network, and through oxidizing dissolution of the matrix. The complexity of the transport phenomena in this system is then due not only to the intrinsic chemical complexity of actinide oxides of the matrix, but also to the numerous radiolytic mechanisms occurring in the near field around spent fuel.

As for the other materials considered, the main alteration mechanisms of **cement materials** occur at the interfaces: both on the external surface and on the internal surfaces of capillary pores and nanopores. Interactions between hydrated phases and the outside environment, which are responsible for the major changes in the hardened cement paste, will be limited by segmentation of the capillary porosity, which is a characteristic of the microstructure and its evolution over time. Variations in the porosity of cement materials are therefore one of the keys to its behavior with regard to transport phenomena. In any event, aqueous leaching of these materials results in partial zonation and variations in the matrix mineral assemblage. Radionuclide retention varies according to their chemical properties and the hydrated phases present in the matrix at a given degradation state. When the mechanisms involved cannot be accurately identified, a conservative approach implies a comprehensive assessment of radionuclide behavior in all the material constituents.

In the context of a deep geological repository, the difficulty of investigating the phenomena related to cement materials is not due to the intrinsic complexity of the elementary processes — which can be accurately described for other materials — but from the inherent complexity of the cement paste itself:

- Anhydrous cement is a multiphase material in which the constituent phases react differently, resulting in an assemblage of hydrated mineral phases that can be difficult to characterize.
- The assemblage of mineral phases is at equilibrium with the interstitial solution in the material. Any change in this equilibrium, through the precipitation new phases or a change in the chemical composition of the pore solution, modifies the entire system.
- At mesoscopic scale, cement materials are heterogeneous multiphase materials with multi-scale porosity. Alteration phenomena, the precipitation of secondary mineral phases, or dissolution all modify the topological characteristics of the porosity over time, and it is difficult to account for these modifications accurately through experimentation.

In addition to a precise description of mass transfer phenomena involved within the scope of a geological repository for nuclear waste packages, this chapter highlights the specific physical and chemical features of each of the three matrices considered and their constraints as constituents of waste packages with variable

degrees of potential radiotoxicity. While the scientific issues and basic mechanisms involved are often similar, the unique aspects of each matrix as a transfer mass medium are identified.

Acknowledgments. The authors are grateful to Florence Bart (CEA, DEN, Head of the Waste Encapsulation Laboratory) for her attentive and constructive review, and to Aurélie Verney-Carron and Pierre Frugier (CEA, DEN, Conditioning Matrix Long-term Behavior Research Laboratory) for their contributions concerning the mechanisms of glass alteration and the GRAAL Model, respectively.

References

1. Bailly, H., Ménessier, D., Prunier, C.: Le combustible nucléaire des réacteurs à eau sous pression et des réacteurs à neutrons rapides. Eyrolles edn. (1996)
2. Poinssot, C., Toulhoat, P., Grouiller, J.P., Pavageau, J., Piron, J.P., Pelletier, M., Dehaudt, P., Cappelaere, C., Limon, R., Desgranges, L., Jégou, C., Corbel, C., Maillard, S., Faure, M.H., Cicariello, J.C., Masson, M.: Synthesis on the long term behaviour of the spent nuclear fuel. CEA-R-5958 (E), vol. I, II (2001)
3. Ferry, C., Poinssot, C., Cappelaere, C., Desgranges, L., Garcia, P., Jégou, C., Lovera, P., Marimbeau, P., Piron, J.P., Poulesquen, A., Roudil, D., Broudic, V., Gras, J.M., Bouffioux, P.: Synthesis on the spent fuel long term evolution, CEA-R-6084 (2004)
4. Ferry, C., Poinssot, C., Cappelaere, C., Desgranges, L., Jégou, C., Miserque, F., Piron, J.P., Roudil, D., Gras, J.M.: Major outcomes of the French research on the spent fuel long-term evolution in interim dry storage and deep geological disposal. Journal of Nuclear Materials 352, 246–253 (2006)
5. Poinssot, C., Ferry, C., Kelm, M., Grambow, B., Martinez-Esparza, A., Johnson, L., Andriambololona, Z., Bruno, J., Cachoir, C., Cavedon, J.M., Christensen, H., Corbel, C., Jégou, C., Lemmens, K., Loida, A., Lovera, P., Miserque, F., De Pablo, J., Poulesquen, A., Quinones, J., Rondinella, V., Spahiu, K., Wegen, D.: Final report of the European project spent fuel stability under repository conditions. Contract N°FIKW-CT-2001-00192 SFS (2005)
6. Elliot, M.N., Grover, J.R., Hardwick, W.H.: Fixation of radioactive waste in glass. Part II, The experimental evaluation of phosphate and borosilicate glasses. Treatment and Storage of High Level Radioactive Wastes, pp. 1–15. International Atomic Energy Agency (1962)
7. Bocola, W., Donato, A., Sgalambro, G.: Survey of the present state of study on the solidification of fission product solutions in Italy. OECD Paris (1973)
8. Blazewitz, A.G., et al.: The high level solidification demonstration program, OCDE Paris (1973)
9. Grover, J.R.: Glasses for the fixation of high level radioactive wastes. OECD Paris (1973)
10. Angeli, F.: Structure et réactivité aqueuse des verres silicatés. Apport de la résonance magnétique nucléaire haute-résolution. PhD Thesis, Université Denis Diderot, France (2000)
11. Delaye, J.M., Ghaleb, D.: Molecular dynamic simulation of a nuclear waste glass matrix. Materials Science and Engineering B 37, 232–236 (1996)

12. Delaye, J.M., Cormier, L., Ghaleb, D., Calas, G.: Investigation of multicomponent silicate glasses by coupling WAXS and molecular dynamics. Journal of Non-Crystalline Solids, 293–295 (2001)
13. Delaye, J.M., Louis Achile, V., Ghaleb, D.: Modeling oxide glasses with Born-Mayer-Huggins potentials, Effect of composition structural changes. Journal of Non-Crystalline Solids 210, 232–242 (1997)
14. Galoisy, L., et al.: Local structure of simplified waste glass, complementarity of XAS and MD calculations. In: McKinley, I.G., McCombie, C. (eds.) Scientific Basis for Nuclear Waste Management XXI, pp. 133–139. Mater. Res. Soc. (1998)
15. Galoisy, L., Pelegrin, E., Arrio, M.A., Ildefonse, P., Calas, G., Ghaleb, D., Fillet, C., Pacaud, F.: Evidence for 6-coordinated zirconium in inactive nuclear waste glasses. Journal of the American Ceramic Society 82, 2219–2224 (1999)
16. Cormier, G., Ghaleb, D., Delaye, J.M., Calas, G.: Competition for charge compensation in borosilicate glasses, a study by Wide Angle X ray Scattering and Molecular Dynamics calculation. Physical Review B 61, 1495–1499 (2000)
17. Angeli, F., Delaye, J.M., Charpentier, T., Petit, J.C., Ghaleb, D., Faucon, P.: Influence of glass chemical composition on the Na-O bond distance: a 23Na 3Q-MAS NMR and molecular dynamics study. Journal of Non Crystalline Solids 276, 132–144 (2000)
18. Cabaret, D., Le Grand, M., Ramos, A., Flank, A.M., Galoisy, L., Calas, G., Ghaleb, D.: Medium range structure of borosilicate glasses from Si K-edge XANES, a combined approach based on multiple scattering and molecular dynamics calculations. Journal of Non-Crystalline Solids 289(1-3), 1–8 (2001)
19. Cormier, L., Galoisy, L., Ghaleb, D., Calas, G.: Short-range and medium-range structural order around cations in glasses, a multidisciplinary approach. Comptes-rendus de l'Académie des Sciences de Paris - série IV Physique Astrophysique 2, 249–262 (2001)
20. Delaye, J.M.: Modeling of multicomponent glasses, A review. Current Opinion in Solid State and Materials Science 5, 451–454 (2001)
21. Taylor, H.F.W.: Cement Chemistry. Thomas Telford (1997)
22. Hadley, D.W., Dolch, W.L., Diamond, S.: On the occurrence of hollow-shell hydration grains in hydrated cement paste. Cement and Concrete Research 30, 1–6 (2000)
23. Mehta, P.K.: Concrete Structure Properties and Materials. Prentice-Hall, Englewood Cliffs (1986)
24. Feldman, R.F., Sereda, P.J.: A new model for hydrated Portland cement and its practical implications. Engineering Journal of Canada 53, 59–83 (1970)
25. Jennings, H.M., Tennis, P.D.: Model for the developing microstructure in Portland Cement pastes. Journal of the American Ceramic Society 77, 3161–3172 (1994); correction 78, 2575 (1995)
26. Baroghel-Bouny, V.: Caractérisation des pâtes de ciment et des bétons: méthodes, analyses, interprétations. Presses de l'Ecole Nationale des Ponts et Chaussées (1994)
27. Jennings, H.M.: A model for the microstructure of calcium silicate hydrate in cement paste. Cement and Concrete Research 30, 101–116 (2000)
28. Richardson, I.G.: The nature of C-S-H in hardened cements. Cement and Concrete Research 29, 1131–1147 (1999)
29. Baron, J., Ollivier, J.P.: La durabilité des bétons. Presses de l'École Nationale des Ponts et Chaussées, Paris, France (1992)

30. Roudil, D., Trocellier, P., Deschanels, X., Jégou, C., Peuget, S., Bart, J.M.: Helium thermal diffusion in a uranium dioxide matrix. Journal of Nuclear Materials 325, 148–158 (2004)
31. Guilbert, S., et al.: He migration in implanted UO_2 sintered disks. Journal of Nuclear Materials 327, 88–96 (2004)
32. Martin, G., et al.: A NRA study of temperature and heavy ion irradiation effects on helium migration in sintered uranium dioxide. Journal of Nuclear Materials 357, 198–205 (2006)
33. Martin, G., et al.: A quantitative μ-NRA study of helium intergranular and volume diffusion in sintered UO_2. Nuclear Instrumentations and Methods B 249, 509–512 (2006)
34. Martin, G.: Étude et modélisation de la diffusion sous irradiation de l'hélium dans le dioxyde d'uranium. PhD Thesis, Orléans University (2007)
35. Gosset, D., Trocellier, P., Serruys, Y.: Determination of the helium diffusion in nuclear waste storage ceramics by a nuclear reaction analysis method. Journal of Nuclear Materials 303, 115–124 (2002)
36. Mayer, M.: SIMNRA user's guide, Technical report IPP 9/113, Max-Planck-Institut für Plasmaphysik, Garching, Germany (1997)
37. Garcia, P., et al.: Étude par réactions nucléaires de la mobilité de l'hélium dans le dioxyde d'uranium, CEA Technical Report SESC/LLCC 08 03 (2008)
38. Sauvage, T., et al.: Profile measurement of helium implanted in UO_2 sintered pellets by using the $^3He(d, \alpha)^1H$ nuclear reaction analysis technique. Journal of Nuclear Materials 327, 159–164 (2004)
39. Rufeh, F., Olander, D.R., Pigford, T.H.: The solubility of helium in uranium dioxide. Nuclear Science And Engineering 23, 335–338 (1965)
40. Van Veen, A., Fedorov, A.V., Westerduin, K.T.: Thermal desorption study on helium implanted UO_2, Report IRI-DM-2001-004 (2001)
41. Pipon, Y., et al.: Conférence ATALANTE (France), 04-01 (2008)
42. Ronchi, C., Hiernaut, J.P.: Helium diffusion in uranium and plutonium oxides ». Journal of Nuclear Materials 325, 1–12 (2004)
43. Matzke, H.: Radiation enhanced diffusion in UO_2 and $(U, Pu)O_2$. Radiation Effects 75, 317 (1983)
44. Ferry, C., et al.: Enhanced diffusion under alpha self-irradiation in spent nuclear fuel, Theoretical approaches. Journal of Nuclear Materials 346, 48–55 (2005)
45. Lovera, P., et al.: Synthesis report on the relevant diffusion coefficients of fission products and helium in spent nuclear fuels, CEA-Report CEA-R-6039 (2003)
46. Mainguy, M.: Modèles de diffusion non linéaires en milieux poreux. Application à la dissolution et au séchage des matériaux cimentaires. PhD Thesis, École Nationale des Ponts et Chaussées, Paris, France (1999)
47. Groves, G.W., Rodway, D.I., Richardson, I.G.: The carbonation of hardened cement pastes. Advances in Cement Research 3, 117–125 (1990)
48. Groves, G.W., Brough, A., Richardson, I.G., Donson, C.M.: Progressive changes in the structure of hardened C_3S cement pastes due to carbonation. Journal of the American Ceramic Society 11, 2891–2896 (1991)
49. Houst, Y.F., Wittmann, F.H.: Influence of porosity and water content on the diffusivity of CO_2 and O_2 though hydrated cement paste. Cement and Concrete Research 24, 1165–1176 (1994)

50. Ngala, V.T., Page, C.L.: Effects of carbonation on pore structure and diffusional properties of hydrated cement pastes. Cement and Concrete Research 27, 995–1007 (1997)
51. Thierry, M.: Modélisation de la carbonatation atmosphérique des matériaux cimentaires – Prise en compte des effets cinétiques et des modifications microstructurales et hydriques. PhD thesis, Ecole Nationale des Ponts et Chaussées, Paris, France (2005)
52. Buil, M., Ollivier, J.P.: Conception des bétons, la structure poreuse. In: Baron, J., Ollivier, J.P. (eds.) La Durabilité des Bétons. Presses de l'École Nationale des Ponts et Chausses (1992)
53. Mindess, S., Young, J.F., Darwin, D.: Concrete, 2nd edn. Prentice-Hall, Englewood Cliffs (2001)
54. Winslow, D.N., Cohen, M.D., Bentz, D.P., Snyder, K.A., Garboczi, E.J.: Percolation and pore structure in mortars and concrete. Cement and Concrete Research 24, 25–37 (1994)
55. Liu, Z., Winslow, D.: Sub-distributions of pore size, a new approach to correlate pore structure in mortars and concrete. Cement and Concrete Research 25, 769–778 (1995)
56. Mason, E.A., Malinauskaus, A.P.: Gas Transport in Porous Media, the Dusty-Gas Model. Elsevier, Amsterdam (1983)
57. Frizon, F., Gallé, C.: Experimental investigations of diffusive and convective transport of inert gas through cement pastes. Journal of Porous Media 12, 221–237 (2009)
58. Atkinson, A., Nickerson, A.K.: The diffusion of ions through water-saturated cement. Journal of Materials Science 19, 3068–3078 (1984)
59. Gallé, C., Sercombe, J.: Permeability and pore structure evolution of silico-calcareous and hematite high-strength concretes submitted to high temperatures. Materials and Structures 34, 619–628 (2001)
60. Gallé, C., Peycelon, H., Le Bescop, P.: Effect of an accelerated chemical degradation on water permeability and pore structure of cement-based materials. Advances in Cement Research 16, 105–114 (2004)
61. Quenard, D., Carcasses, M.: Les résultats es essais croisés AFREM "perméabilité". In: Compte rendu des Journées Techniques AFPC-AFREM, Durabilité des bétons, Toulouse, France, Décember 11-12, AFPC-AFREM (1997)
62. Kropp, J., Hilsdorf, H.K.: Performance criteria for concrete durability. RILEM report 12, E. & FN Spon (1995)
63. Rondinella, V.V., Matzke, H., Cobos, J., Wiss, T.: Radiochim. Acta 88, 527–531 (2000)
64. Sattonnay, G., Ardois, C., Corbel, C., Lucchini, J.F., Barthe, M.F., Garrido, F., Gosset, D.: Journal of Nuclear Materials 288, 11–19 (2001)
65. Corbel, C., Sattonnay, G., Lucchini, J.F., Ardois, C., Barthe, M.F., Huet, F., Dehaudt, P., Hickel, B., Jégou, C.: Increase of the uranium release at an UO_2/H_2O interface under He^{2+} ion bean irradiation. Nuclear Instruments And Methods in Physics Research B 179, 225 (2001)
66. Cobos, J., Havela, L., Rondinella, V.V., De Pablo, J., Gouder, T., Glatz, J.P., Carbol, P., Matzke, H.J.: Corrosion and dissolution studies of UO_2 containing a-emitters. Radiochimica Acta 90, 597–602 (2002)
67. Stroes-Gascoyne, S., King, F., Betteridge, J.S., Garisto, F.: Radiochim. Acta 90, 603–609 (2002)

68. Jégou, C., Muzeau, B., Broudic, V., Poulesquen, A., Roudil, D., Jorion, F., Corbel, C.: Effect of alpha irradiation on UO_2 surface reactivity in aqueous media. Radiochimica Acta 93, 1–8 (2005)
69. Stroes-Gascoyne, S., Betteridge, J.S.: Mat. Res. Soc. Symp. Proc. 824, 175–181 (2004)
70. Muzeau, B., Jégou, C., Delaunay, F., Broudic, V., Brevet, A., Catalette, H., Simoni, E.: Radiolytic oxidation of UO_2 pellets doped with alpha-emitters (^{238}/^{239}Pu). Journal of Alloys and Compounds 467, 578–589 (2009)
71. Shoesmith, D.W.: Fuel corrosion processes under waste disposal conditions, Review. Journal of Nuclear Materials 282, 1 (2000)
72. Christensen, H., Sunder, S.: Current state of knowledge of water radiolysis effects on spent nuclear fuel corrosion. Nuclear Technology 131, 102 (2000)
73. Johnson, L.H., et al.: Spent fuel evolution under disposal conditions, Synthesis of results from the EU spent fuel stability (SFS) project, TR-04-09 Nagra report (2005)
74. Sunder, S., Schoesmith, D.W., Miller, N.H.: Journal of Nuclear Materials 244, 66–74 (1997)
75. Lundström, T.: PhD thesis, Linköpings Universitet, Sweden (2003)
76. Poulesquen, A., Jégou, C.: Influence of Alpha Radiolysis on Water on UO_2 Matrix Alteration, Chemical/Transport Model. Journal of Nuclear Technology 160, 337–345 (2007)
77. Christensen, H.: Calculation simulating spent fuel leaching experiments. Nuclear Technology 124, 165 (1998)
78. Kelm, M., Bohnert, E.: A kinetic model for the radiolysis of chloride brine, its sensitivity against model parameters and a comparison with experiments, FZKA 6977 report (2004)
79. Kirkegaard, P., Bjergbakke, E.: CHEMSIMUL, A simulator for chemical kinetics, Risø National Laboratory (2002)
80. Christensen, H., Sunder, S.: An evaluation of water layer thickness effective in the oxidation of UO_2 fuel due to radiolysis of water. Journal of Nuclear Materials 238, 70 (1996)
81. Vladimirova, M.V.: Recent advances in radiation chemistry of actinides. Radiochemistry 40, 395 (1998)
82. Christensen, H., Sunder, S., Shoesmith, D.W.: Oxidation of nuclear fuel (UO_2) by the products of water radiolysis, development of a kinetic model. J. Alloys. Comp. 213/214, 93–99 (1994)
83. Mendes, E.: Comportement des interfaces UO_2/H_2O de haute pureté sous faisceau d'ions He^{2+} en milieu désaéré. PhD thesis, Université de Paris XI Orsay, France (2005)
84. Spahiu, K., Carbol, P., Cobos, J., Glatz, J.P., Ronchi, C., Rondinella, V.V., Wegen, D., Wiss, T., Loida, A., Metz, V., Kienzler, B., Grambow, B., Quinones, J., Martinez Esparza Valiente, A.: The effect of dissolved hydrogen on the dissolution of ^{233}U doped UO_2(s), high burn-up spent fuel and MOX fuel, TR-05-09 SKB report (2005)
85. Pastina, B., LaVerne, J.A.: Effect of molecular hydrogen on hydrogen peroxide in water radiolysis. Journal of Physical Chmistry A 105, 9316–9322 (2001)
86. Conradt, R.: Chemical durability of oxide glasses in aqueous solution, a review. Journal of American Ceramic Society 91, 728–735 (2008)
87. Frugier, P., Gin, S., Minet, Y., Chave, T., Bonin, B., Godon, N., Lartigue, J.E., Jollivet, P., Ayral, A., De Windt, L., Santarini, G.: SON68 nuclear glass dissolution kinetics, Current state of knowledge and basis of the new GRAAL model. Journal of Nuclear Materials 380, 8–21 (2008)

88. Rebiscoul, D.: Étude de la pérennité des gels d'altération de verres nucléaires, PhD thesis, Université Montpellier II, France (2004)
89. Rana, M.A., Douglas, R.W.: The reaction between glass and water. Part I. Experimental methods and observations. Physics and Chemistry of Glasses 2, 179–195 (1961)
90. Rana, M.A., Douglas, R.W.: The reaction between glass and water. Part II. Discussion of the results. Physics and Chemistry of Glasses 2, 196–205 (1961)
91. Doremus, R.H.: Interdiffusion of hydrogen and alkali ions in a glass surface. Journal of Non-Crystalline Solids 19, 137–144 (1975)
92. White, A.F., Claasen, H.C.: Kinetic model for the short-term dissolution of a rhyolitic glass. Chemical Geology 28, 91–109 (1980)
93. Smets, R.M.J., Lommen, T.P.A.: The leaching of sodium aluminosilicate glasses studied by secondary ion mass spectrometry. Physics and Chemistry of Glasses 23, 83–87 (1982)
94. Dran, J.C., Petit, J.C., Trotignon, L., Paccagnella, A., Della Mea, G.: Hydration mechanisms of silicate glasses, discussion of the respective role of ion exchange and water permeation. Materials Research Society Symposia Proceedings 127, 25–32 (1989)
95. Geneste, G., Bouyer, F., Gin, S.: Hydrogen–sodium interdiffusion in borosilicate glasses investigated from first principles. Journal of Non-Crystalline Solids 352, 3147–3152 (2006)
96. Lanford, W.A., Davis, K., Lamarche, P., Laursen, T.: Hydration of soda-lime glass. Journal of Non-Crystalline Solids 33, 249–266 (1979)
97. Houser, C.A., Herman, J.S., Tsong, I.S.T., White, W.B., Lanford, W.A.: Sodium-hydrogen interdiffusion in sodium silicate glasses. Journal of Non-Crystalline Solids 41, 89–98 (1980)
98. Tsong, I.S.T., Houser, C.A., White, W.B.: Evidence for interdiffusion of hydronium and alkali ions in leached glasses. Applied Physics Letters 39, 669–670 (1981)
99. Ferrand, K., Abdelouas, A., Grambow, B.: Water diffusion in the simulated French nuclear waste glass SON 68 contacting silica rich solutions, Experimental and modeling. Journal of Nuclear Materials 355, 54–67 (2006)
100. Bunker, B.C.: Waste glass leaching, chemistry and kinetics. Materials Research Society Symposia Proceedings 84, 493–506 (1987)
101. Chave, T., Frugier, P., Ayral, A., Gin, S.: Solid state diffusion during nuclear glass residual alteration in solution. Journal of Nuclear Materials 362, 466–473 (2007)
102. Casey, W.: On the Relative Dissolution Rates of Some Oxide and Orthosilicates Minerals. Journal of Colloid and Interface Science 146, 586–589 (1991)
103. Oelkers, E.H.: General kinetic description of multioxide silicate mineral and glass dissolution. Geochimica et Cosmochimica Acta 65, 3703–3719 (2001)
104. Guy, C., Schott, J.: Multisite surface reaction versus transport control during the hydrolysis of a complex oxide. Chemical Geology 78, 181–204 (1989)
105. White, E., Brantley, S.: Chemical weathering rates of silicate minerals. Reviews in Mineralogy. 31. Mineralogical Society of America (1995)
106. Criscenti, L.J., Kubicki, J.D., Brantley, S.L.: Silicate Glass and Mineral Dissolution, Calculated Reaction Paths and Activation Energies for Hydrolysis of a Q^3 Si by H_3O^+ Using Ab Initio Methods. Journal of Physical Chemistry A 110, 198–206 (2006)
107. Icenhower, J.P., McGrail, B.P., Shaw, W.J., Pierce, E.M., Nachimuthu, P., Shuh, D.K., Rodriguez, E.A., Steele, J.L.: Experimentally determined dissolution kinetics of Na-rich borosilicate glass at far from equilibrium conditions, Implications for Transition State Theory. Geochimica et Cosmochimica Acta 72, 2767–2788 (2008)

108. Cailleteau, C., Angeli, F., Devreux, F., Gin, S., Jestin, J., Jollivet, P., Spalla, O.: Insight into silicate-glass corrosion mechanisms. Nature Materials (in press, 2008)
109. Advocat, T., Crovisier, J.L., Vernaz, E., Ehret, G., Charpentier, H.: Hydrolysis of R7T7 nuclear waste glass in dilute media: mechanisms and rate as a function of pH. Materials Research Society Symposia Proceedings 212, 57–64 (1991)
110. Valle, N.: Traçage isotopique (^{29}Si et ^{18}O) des mécanismes de l'altération du verre de confinement des déchets nucléaires, SON 68. PhD thesis, Université Poincaré, France (2001)
111. Le Gal, X.: Étude de l'altération de verres volcaniques du Vatnajökull (Islande). Mécanismes et bilans à basse température. PhD thesis, Université Louis Pasteur, France (1999)
112. Bunker, B.C., Tallant, D.R., Headley, T.J., Turner, G.L., Kirpatrick, R.J.: The structure of leached sodium borosilicate glass. Physics and Chemistry of Glasses 29, 106–121 (1988)
113. Angeli, F., Charpentier, T., Gin, S., Petit, J.C.: O-17 3Q-MAS NMR characterization of a sodium aluminoborosilicate glass and its alteration gel. Chemical Physics Letters 341, 23–28 (2001)
114. Ledieu, A., Devreux, F., Barboux, P.: Leaching of borosilicate glasses. I. Experiments. Journal of Non-Crystalline of Solids 343, 3–12 (2004)
115. Ledieu, A., Devreux, F., Barboux, P., Minet, Y.: Contribution of Monte Carlo modeling to understanding the alteration of nuclear glasses by water. Nuclear Science and Engineering 185, 285–300 (2006)
116. Spalla, O., Barboux, P., Sicard, L., Lyonnard, S., Bley, F.: Influence of insoluble elements on the nanostructure of water altered glasses. Journal of Non-Crystalline Solids 347, 56–68 (2004)
117. Cailleteau, C., Weigel, W., Ledieu, A., Barboux, P., Devreux, F.: On the effect of glass composition in the dissolution of glasses by water. Journal of Non-Crystalline Solids 354, 117–123 (2008)
118. Grambow, D.M., Strachan: Materials Research Society 112, 713–724 (1998)
119. Vernaz, E.: Estimating the lifetime of R7T7 glass in various media. C.R.Physique 3, 813–825 (2002)
120. Van Iseghem, A.M., Gin, S., Deneele, D., Grambow, B., McGrail, P., Strachan, D., Wicks, G.: A Critical Evaluation of the Dissolution Mechanisms of High-Level Waste Glasses in Conditions of Relevance for Geological Disposal (GLAMOR). In: SCK.CEN, CEA, Subatech, PNNL, SRNL (eds.). EUR 23097, 23097, pp. 1–164 (2007)
121. Gin, S., Jégou, C., Frugier, P., Minet, Y.: Theoretical consideration on the application of Aagaard-Helgelson rate law to dissolution of silicate minerals and glasses. Chemical Geology 255, 14–24 (2008)
122. Frugier, P., Gin, S., Lartigue, J.L., Deloule, E.: Mat. Res. Soc. Symp. Proc., 305–312 (2005)
123. Chave, T.: Étude des mécanismes d'altération par l'eau du verre R7T7 en milieu confiné. Compréhension et modélisation de la cinétique résiduelle, PhD thesis, Université de Montpellier II (2007)
124. Curti, E., Crovisier, J.L., Morvan, G., Karpoff, A.M.: Long-term corrosion of two nuclear waste reference glasses (MW and SON68), A kinetic and mineral alteration study. Applied Geochemistry 21, 1152–1168 (2006)
125. Cundy, C.S., Cox, P.A.: The hydrothermal synthesis of zeolites, Precursors, intermediates and reaction mechanism. Microporous and Mesoporous Materials 82, 1–78 (2005)

126. Gin, S., Mestre, J.P., Couillard, M.: SON 68 nuclear glass alteration kinetics between pH 7 and pH 11. 5. Journal of Nuclear Materials 295, 83–96 (2001)
127. Ribet, I., Gin, S.: Role of neoformed phases on the mechanisms controlling the resumption of SON68 glass alteration in alkaline media. Journal of Nuclear Materials 324, 152–164 (2004)
128. Gislason, S.R., Eugster, H.P.: Meteoritic water-basalt interactions. I, A laboratory study. Geochimica et Cosmochimica Acta 51, 2827–2840 (1987)
129. Jercinovic, M.J., Keil, K., Smith, M.R., Schmitt, R.A.: Alteration of basaltic glasses from north-central British Columbia, Canada. Geochimica Cosmochimica Acta 54, 2679–2696 (1990)
130. Verney-Carron, A., Gin, S., Libourel, G.: Use of natural and archeological analogs to validate long term behaviour of HLW glass in geological disposal conditions. Water Rock Interaction 12, 659–662 (2007)
131. Bunker, B.C.: Molecular mechanisms for corrosion of silica and silicate glasses. Journal of Non-Crystalline Solids 179, 300–308 (1994)
132. Bakos, T., Rashkeev, S.N., Pantelides, S.T.: Reactions and diffusion of water and oxygen molecules in amorphous SiO_2. Physical Review Letters 88 (2002)
133. Hellmann, R.: The albite-water system, Part IV. Diffusion modeling of leached and hydrogen-enriched layers. Geochimica et Cosmochimica Acta 61, 1595–1611 (1997)
134. Crank, J.: The mathematics of diffusion, 2nd edn. Oxford University Press, Oxford (1975)
135. Boksay, Z., Bouquet, G., Dobos, S.: Diffusion processes in the surface layer of glass. Physics and Chemistry of Glasses 8, 140–144 (1967)
136. Boksay, Z., Bouquet, G., Dobos, S.: The kinetics of the formation of leached layers on glass surfaces. Physics and Chemistry of Glasses 9, 69–71 (1968)
137. Bunker, B.C.: Waste glass leaching, chemistry and kinetics. Materials research Society Symposia Proceedings 84, 493–506 (1987)
138. Grambow, B., Müller, R.: First-order dissolution rate law and the role of surface layers in glass performance assessment. Journal of Nuclear Materials 298, 112–124 (2001)
139. McGrail, B.P., Icenhower, J.P., Darab, J.G., Shuh, D.K., Baer, D.R., Shutthanandan, V., Thevuthasan, S., Engelhard, M.H., Steele, J.L., Rodriguez, E.A., Liu, P., Ivanov, K.E., Booth, C.H., Nachimuthu, P.: Ion-Exchange Processes and Mechanisms in Glasses. U.S. DOE report, Pacific Northwest Laboratory (2001)
140. Sterpenich, J., Libourel, G.: Water diffusion in silicate glasses under natural weathering conditions, evidence from buried medieval stained glasses. Journal of Non-Crystalline Solids 352, 5446–5451 (2006)
141. Verney-Carron, A.: Étude d'analogues archéologiques pour la validation des modèles de comportement à long terme des verres nucléaires. PhD thesis, Université Poincaré, France (2008)
142. Boksay, Z., Varga, M., Wikby, A.: Surface conductivity of leached glass. Journal of Non-Crystalline Solids 17, 349–358 (1975)
143. Smit, W., Stein, H.N.: Interdiffusion of hydrogen and alkali ions in glass surfaces. Journal of Non-Crystalline Solids 34, 357–370 (1979)
144. McGrail, B.P., Kumar, A., Day, D.E.: Sodium Diffusion and Leaching of Simulated Nuclear Waste Glass. Journal of the American Ceramic Society 67, 463–467 (1984)
145. Friedman, I., Smith, R.L., Long, W.D.: Hydration of natural glass and formation of perlite. Geological Society of America Bulletin 77, 323–327 (1966)

146. McGrail, B.P., Icenhower, J.P., Shuh, D.K., Liu, P., Darab, J.G., Baer, D.R., Thevuthasen, S., Shutthanandan, V., Engelhard, M.H., Booth, C.H., Nachimuthu, P.: The structure of Na_2O-Al_2O_3-SiO_2 glass, impact on sodium ion exchange in H_2O and D_2O. Journal of Non-Crystalline Solids 296, 10–26 (2001)
147. Friedman, I., Long, W.: Hydration rate of obsidian. Science 191, 347–352 (1976)
148. Petit, J.C., Della Mea, G., Dran, J.C., Magonthier, M.C., Mando, P.A., Paccagnella, A.: Hydrated-layer formation during dissolution of complex silicate glasses and minerals. Geochimica et Cosmochimica Acta 54, 1941–1955 (1990)
149. Roggendorf, H.: Corrosion of the borosilicate glass R7T7 in a concentrated NaCl-brine – Experimental data and surface characterization. In: International Symposium on Ceramics in Nuclear and Hazardous Waste Management Proceedings, pp. 675–684 (1991)
150. Stillings, L.L., Brantley, S.L., Machesky, M.L.: Proton adsorption at an adularia feldspar surface. Geochimica et Cosmochimica Acta 59, 1473–1482 (1995)
151. McGrail, B.P., Pederson, L.R., Petersen, D.A.: The influence of surface potential and pH on the release of sodium from $Na_2O{\cdot}3SiO_2$ glass. Physics and Chemistry of Glasses 27, 59–64 (1986)
152. Pederson, L.R., McGrail, B.P., McVay, G.L., Petersen-Villalobos, D.A., Settles, N.S.: Kinetics of alkali silicate and aluminosilicate glass reactions in alkali chloride solutions, influence of surface charge. Physics and Chemistry of Glasses 34, 140–148 (1993)
153. Crovisier, J.L.: Dissolution du verre basaltiques dans l'eau de mer et dans l'eau douce. Essai de modélisation. PhD thesis, Université Louis Pasteur, France (1989)
154. Crovisier, J.L., Atassi, H., Daux, V., Eberhart, J.P.: Hydrolyse d'un verre basaltique tholéiitique à 60°C. Dissolution sélective puis congruente par élévation du pH. Comptes-Rendus de l'Académie des Sciences de Paris 310, 941–946 (1990)
155. Techer, I.: Apports des analogues naturels vitreux à la validation des codes de prédiction du comportement à long terme des verres nucléaires. PhD thesis, Université Montpellier II, France (1999)
156. Grambow, B.: A general rate equation for nuclear waste glass corrosion. Materials Research Society Symposia Proceedings 44, 15–27 (1985)
157. Advocat, T.: Les mécanismes de corrosion en phase aqueuse du verre nucléaire R7T7. Approche expérimentale. Essai de modélisation thermodynamique et cinétique. PhD thesis, Université Louis Pasteur, France (1991)
158. Daux, V., Guy, C., Advocat, T., Crovisier, J.L., Stille, P.: Kinetic aspects of basaltic glass dissolution at 90°C, role of aqueous silicon and aluminum. Chemical Geology 142, 109–126 (1997)
159. Techer, I., Advocat, T., Lancelot, J., Liotard, J.M.: Chemical Geology, Dissolution kinetics of basaltic glasses, control by solution chemistry and protective effect of the alteration film. Chemical Geology 176, 235–263 (2001)
160. Jégou, C.: Mise en évidence expérimentale des mécanismes limitant l'altération du verre R7T7 en milieu aqueux. Critique et proposition d'évolution du formalisme cinétique. PhD thesis, Université de Montpellier II, France (1998)
161. Linard, Y., Yamashita, I., Atake, T., Rogez, J., Richet, P.: Thermochemistry of nuclear waste glasses, an experimental determination. Journal of Non-Crystalline Solids 286, 200–209 (2001)
162. Linard, Y., Advocat, T., Jégou, C., Richet, P.: Thermochemistry of nuclear waste glasses, application to weathering studies. Journal of Non-Crystalline Solids 289, 135–143 (2001)

163. Gin, S.: Protective Effect of the Alteration Gel, A Key Mechanism in the Long-Term Behavior of Nuclear Waste Glass. Materials Research Society Symposia Proceedings 663, 207–215 (2001)
164. Chick, L.A., Pederson, L.R.: The relationship between reaction layer thickness and leach rate for nuclear waste glasses. In: Mc Vay, G.L. (ed.) Mat. Res. Soc. Symp. Proc., vol. 26, pp. 635–642 (1984)
165. Deruelle, O.: Etude in-situ de la couche d'altération de verres, PhD thesis, Université Pierre et Marie Curie, France (1997)
166. Devreux, F., Ledieu, A., Barboux, P., Minet, Y.: Leaching of borosilicate glasses. II. Model and Monte Carlo simulations. Journal of Non-Crystalline Solids 343, 13–25 (2004)
167. Ribet, I., Gin, S., Vernaz, E., Do Quang, R.: Long-term behavior of nuclear glass, the r(t) operational model. In: GLOBAL 2001, Paris, pp. 1–9 (2001)
168. Ribet, I., Gin, S., Godon, N., Jollivet, P., Minet, Y., Grambow, B., Abdelouas, A., Ferrand, K., Lemmens, K., Aertsens, M., Pirlet, V., Jacques, D., Crovisier, J.L., Clément, A., Aouri, M., Aouad, G., Fritz, B., Arth, A., Morvan, G., Munier, I., Del Nero, M., Ozgümüs, A., Curti, E., Luckscheiter, B., Schwyn, B.: Long-term behavior of glass, improving the glass source term and substantiating the basic hypotheses. Final technical report 2004, European Commission CONTRACT N°FIKW-CT-2000 00007 (2004)
169. Gin, S., Ribet, I., Frugier, P., Chave, T., Angeli, F., Lartigue, J.E., de Combarieu, G., Godon, N.: Assessment of nuclear glass behavior in a geological disposal conditions, Current state of knowledge and recent advances. In: European Nuclear Conference Proceeding 2005 (2005)
170. Zhang, L., Lüttge, A.: Aluminosilicate Dissolution Kinetics, A General Stochastic Model. Journal of Physical Chemistry B 112, 1736–1742 (2008)
171. McGrail, B.P., Bacon, D.H., Icenhower, J., Mann, F.M., Puigh, R.J., Schaef, H.T., Mattigod, S.V.: Near-Field performance assessment for a low-activity waste glass disposal system, laboratory testing to modeling results. Journal of Nuclear Materials 298, 95–111 (2001)
172. Munier, I., Crovisier, J.L., Grambow, B., Fritz, B., Clement, A.: Modeling the alteration gel composition of simplified borosilicate glasses by precipitation of an ideal solid solution in equilibrium with the leachant. Journal of Nuclear Materials 324, 97–115 (2004)
173. Van der Lee, J., De Windt, L.: Chess tutorial and Cookbook, Updated version for 3.0, Ecole des Mines de Paris, LHM/RD/02/13 (2002)
174. Taylor, H.F.W., Famy, C., Scrivener, K.L.: Delayed Ettringite Formation. Cement and Concrete Research 31, 683–693 (2001)
175. Collepardi, M.: A state of the art review on delayed ettringite attack on concrete. Cement and Concrete Composites 25, 401–407 (2003)
176. Escadeillas, G., Hornain, H.: La durabilité des bétons vis-à-vis des environnements agressifs. In: Ollivier, J.P., Vichot, A. (eds.) La durabilité des bétons. Presses de l'Ecole Nationale des Ponts et Chaussées (2008)
177. Bouniol, P.: État des connaissances sur la radiolyse de l'eau dans les colis de déchets cimentés et son approche par simulation. Report CEA-R-6069 (2004)
178. Bouniol, P., Bjergbakke, E.: A comprehensive model to describe radiolytic processes in cement medium. Journal of Nuclear Materials 372, 1–15 (2008)

179. Berner, U.: A thermodynamic description of the evolution of the pore water chemistry and uranium speciation during the degradation of cement. Nagra technical Report 90-12 (1990)
180. Bennett, D.G., Read, D., Atkins, M., Glasser, F.P.: A thermodynamic model for blended cement. II. Cement hydrate phases; thermodynamic values and modeling studies. Journal of Nuclear Materials 190, 315–325 (1992)
181. Adenot, F.: Durabilité du béton: caractérisation et modélisation des processus physiques et chimiques de dégradation du ciment. PhD Thesis, Orléans University, France (1992)
182. Faucon, P., Le Bescop, P., Adenot, F., Bonville, P., Jacquinot, J.F., Pineau, F., Felix, B.: Leaching of cement, study of the surface layer. Cement and Concrete Research 26, 1707–1715 (1996)
183. Bentz, D.P., Garboczi, E.: Modeling the leaching of calcium hydroxide from cement paste: effects on pore space percolation and diffusivity. Materials and Structure 25, 523–533 (1992)
184. Delagrave, A., Pigeon, M., Marchand, J., Revertegat, E.: Influence of chloride ions and pH level on the durability of high performance cement pastes. Cement and Concrete Research 26, 749–760 (1996)
185. Gerard, B.: Contribution des couplages mécanique/chimie/transfert dans la tenue à long terme des ouvrages de stockage de déchets radioactifs. PhD Thesis. ENS Cachan (France) et Laval University, Québec (1996)
186. Truc, O., Ollivier, J.P., Nilsson, L.O.: Numerical simulation of multi-species transport through saturated concrete during a migration test. Ms. Diff. code. Cement and Concrete Research 30, 1581–1592 (2000)
187. Andra, Dossier, Argile – Tome Évolution phénoménologique du stockage géologique, ANDRA, Châtenay-Malabry, France (2005)
188. Marchand, J.: Modeling the behavior of unsaturated cement systems exposed to aggressive chemical environment. Materials and Structures 34, 195–200 (2001)
189. Van der Lee, J., De Windt, L., Lagneau, V., Goblet, P.: Module-oriented modeling of reactive transport with HYTEC. Computers and Geosciences 29, 265–275 (2003)
190. Tognazzi, C.: Couplage fissuration/dégradation chimique dans les matériaux cimentaires, caractérisation et modélisation. PhD Thesis, Institut National des Sciences Appliquées de Toulouse, France (1998)
191. Mainguy, M., Tognazzi, C., Torrenti, J.M., Adenot, F.: Modeling of leaching in pure cement paste and mortar. Cement and Concrete Research 30, 83–90 (2000)
192. Garboczi, E.J., Bentz, D.P.: Multiscale analytical/numerical theory of the diffusivity of concrete. Advanced Cement Based Materials 8, 77–88 (1998)
193. Pivonka, P., Hellmich, C., Smith, D.: Microscopic effects on chloride diffusivity of cement pastes, a scale-transition analysis. Cement and Concrete Research 34, 2251–2260 (2004)
194. Bentz, D.P.: Three-dimensional computer simulation of cement hydration and microstructure development. Journal of the American Ceramic Society 80, 3–21 (1997)
195. Ye, G., Van Breugel, K., Fraaij, A.L.A.: Three-dimensional microstructure analysis of numerically simulated cementitious materials. Cement and Concrete Research 33, 215–222 (2003)
196. Ménard, O., Advocat, T., Ambrosi, J.P., Michard, A.: Behavior of actinides (Th, U, Np and Pu) and rare earths (La, Ce and Nd) during aqueous leaching of a nuclear glass under geological disposal conditions. Applied Geochemistry 13, 105–126 (1998)

197. Fillet, C.: Mécanismes de corrosion et comportement des actinides dans le verre nucléaire R7T7. PhD thesis, Université de Montpellier II, France (1987)
198. Grambow, B.: Borosilicate glass, future research requirements or what we don't know. MRS Bulletin (1994)
199. Pirlet, V., Van Iseghem, P., Dierckx, A., Desreux, J.F.: The investigation of the neptunium complexes formed upon the interaction of high level waste glass and Boom clay media. Journal of Alloys and Compounds, 271–273, 267-271 (1998)
200. Noguès, J.L.: Les mécanismes de corrosion des verres de confinement des produits de fission. PhD thesis, Université de Montpellier II, France (1984)
201. Vernaz, E., Godon, N.: Leaching of actinides from nuclear waste glass, French experience. Mater. Res. Soc., Scientific Basis for Nuclear Waste Management XV 257, 37–48 (1992)
202. Bamba, T., Nukaga, K., Sagawa, T.: Temperature effect on plutonium leach rate of nuclear waste glasses. Journal of Nuclear Science and Technology 26, 705–711 (1989)
203. Inagaki, Y., Furuya, H., Idemitsu, K., Arima, T., Osako, H., Banba, T., Maeda, K., Matsumoto, S., Nomura, I., Kikkawa, S., Saito, M., Okamoto, H.: Leaching and migration of neptunium in a simulated engineered barrier system consisting of HLW glass and compacted bentonite. Journal of Nuclear Materials 298, 168–173 (2001)
204. Pointeau, I.: Étude mécanistique et modélisation de la rétention de radionucléides par las silicates de calcium hydratés (CSH) des ciments. PhD Thesis, Université de Champagne-Ardenne, Reims, France (2000)
205. Viallis-Terrisse, H.: Interaction des Silicates de Calcium Hydratés, principaux constituants du ciment, avec les chlorures d'alcalins. Analogie avec les argiles, PhD Thesis, Université de Bourgogne (2000)
206. Landesman, C., Le Callonec, C., Richet, C., Ayache, R., Belkhadem, M., Domergue, C., Solet, C., Ly, J., Meier, P.: Rétention des radionucléides sur les matériaux cimentaires (C-S-H, Pâtes CPA et CLC) sains et dégradés, CEA Technical Note, NT SESD, pp. 99–95 (1999)
207. Iwada, T., Nagasaki, S., Tanaka, S.: Sorption study of Strontium onto hydrated cement phases using a sequential desorption method. Radiochimica Acta 88, 483–486 (2000)
208. Curti, E.: Coprecipitation of radionuclides, basic concepts, literature reviews and first applications. PSI Report 97-10 (1997)
209. Komarneni, S., Breval, E., Roy, D.M., Roy, R.: Reactions of some calcium silicates with metal cations. Cement and Concrete Research 18, 204–220 (1988)
210. Ziegler, F.: Heavy metal binding in cement-based waste materials, an investigation of the mechanism of Zinc sorption to calcium silicate hydrate. PhD Thesis, Swiss Federal Institute of Technology, Zurich, Switzerland (2000)
211. Ziegler, F., Scheidegger, M., Johson, C.A., Dähn, W.E.: Sorption mechanism of Zinc to calcium silicate hydrate, X-ray absorption fine structure (XAFS) investigation. Environmental Science and Technology 35, 1550–1555 (2001)
212. Wieland, E., Spieler, P.: Colloids in the mortar backfill of a cementitious repository for radioactive waste. In: Birchley, J., Ringele, R. (eds.) PSI Scientific Report 1998. Nuclear Energy and Safety, vol. IV. PSI Viligen (1998)
213. Heath, T.G., Ilett, D.J., Tweed, J.C.: Thermodynamic Modeling of the sorption of radioelements onto cementitious materials. In: MRS Symposium Proceedings, vol. 412, pp. 443–449 (1996)

214. Brown, D.R., Grutzek, M.W.: Iodine waste forms, calcium aluminate hydrate analogs. In: MRS Symposium Proceedings, vol. 44, pp. 911–918 (1985)
215. Liu, Y., Von Gunten, H.R.: Migration chemistry and behavior of iodine relevant to geological disposal of radioactive wastes. A literature review with a compilation of sorption data. PSI Report No. 19 (1988)
216. Pointeau, I., Piriou, B., Fedoroff, M., Barthes, M.G., Marmier, N., Fromage, F.: Sorption mechanisms of Eu3+ on C-S-H phases of hydrated cements. Journal of Colloid and Interface Science 236, 252–259 (2001)
217. Marx, G., Althenhein-Haese, C., Bischoff, H., Engelhardt, J., Feldmaier, F.: Investigations into speciation, sorption and corrosion of actinides in systems of high ionic strength. Journal of Radioanalytical and Nuclear Chemistry 194, 95–105 (1995)
218. Gougar, M., Scheetz, B., Roy, D.: Ettringite and CSH Portland cement phases for waste ion immobilization, a review. Waste Management 16, 182–188 (1996)
219. Atkins, M., Damidot, D., Glasser, F.: Performance of cementitious systems in the repository. In: MRS Symposium Proceeding, vol. 333, pp. 315–326 (1994)
220. Gorgeon, L.: Contribution à la modélisation physico-chimique de la rétention de radioéléments à vie longue par les matériaux argileux. PhD Thesis, Université Pierre et Marie Curie (Paris VI), Paris, France (1994)
221. Nolin, D.: Influence des anions sur la rétention de radioéléments par les matériaux argileux, PhD thesis, Université Pierre et Marie Curie (Paris VI), Paris, France (1997)
222. Davis, J.A., Kent, D.B.: Surface complexation modeling in aqueous chemistry. In: Hochella, M.F., White, A.F. (eds.) Mineral-water interface geochemistry, Reviews in mineralogy, vol. 23 (1990)
223. Lyklema, J.: Fundamentals of interface and colloid science. Solid-liquid interface, vol. II. Academic Press, London (1995)
224. Gileadi, E., Kirowa-Eisner, E., Penciner, J.: Interfacial Electrochemistry, An Experimental Approach. Addison-Wesley, Reading (1975)
225. Bockris, J.O., Conway, B.E., Yeager, E.: The Double Layer. Comprehensive Treatise of Electrochemistry, vol. 1. Plenum Press (1980)
226. Henocq, P.: Modélisation des interactions ioniques à la surface des Silicates de Calcium Hydratés, PhD Thesis, Université de Laval, Québec
227. Hunter, R.J.: Foundations of Colloid Science, 2nd edn. Oxford University Press, Oxford (2001)
228. Nonat, A.: The structure and stoichiometru of C-S-H. Cement and Concrete Research 34, 1521–1528 (2004)
229. Hamid, S.A.: The crystal structure of the 11 Å natural tobermorite $Ca_{2\cdot25}(Si_3O_{7.5}(OH)_{1.5})(H_2O)$. Zeischrift für Kristallographie 154, 189–198 (1981)
230. Klur, I.: Etude par RMN de la structure des silicates de calcium hydrates, PhD Thesis, Université Pierre et Marie Curie, Paris, France (1996)
231. Richet, C., Le Bescop, P., Gallé, C., Peycelon, H., Bejaoui, S., Pointeau, I., L'Hostis, V., Bary, B.: Dossier de synthèse sur le comportement à long terme des colis, dossier de référence phénoménologique colis béton, CEA Technical Report RT 04-679-A (2004)
232. Frizon, F.: Décontamination électrocinétique des milieux poreux. Étude expérimentale et modélisation appliqués au césium dans les matériaux cimentaires, PhD Thesis, Institut National des Sciences Appliquées de Toulouse, France (2003)
233. Flint, E.P., Wells, L.S.: Study of the system $CaO\text{-}SiO_2\text{-}H_2O$ at 30°C and of the reaction of water on the anhydrous calcium silicates. Journal of Research - National Bureau of Standards 12, 751–783 (1934)

234. Roller, P.S., Ervin Jr., G.: The system calcium oxide-silica-water at 30°C. The association of silicate ion in dilute alkaline solution. Journal of American Chemical Society 62, 461–471 (1940)
235. Taylor, H.F.W.: Hydrated Calcium Silicates. Part I. Compound Formation at Ordinary Temperatures. Journal of Chemical Society, 3682–3690 (1950)
236. Kalousek, G.L.: Application of differential thermal analysis in a study of the system lime-silioca-water. In: Proceedings of the 3rd international symposium on chemistry of cements, London, pp. 296–311 (1952)
237. Fui, K., Kondo, W.: Heterogeneous equilibria of calcium silicate hydrate in water at 30°C. Journal of Chemical Society Dalton Trans. V. 2, 645–651 (1981)
238. Atkins, M., Glasser, F.P., Kindness, A.: Cement hydrate phases: solubility at 25°C. Cement and Concrete Research 22, 241–246
239. Courault, A.C.: Simulation expérimentale des C-S-H dans les bétons modernes: Etude de la composition et des propriétés à l'équilibre dans des milieux complexes. PhD thesis, Université de Bourgogne, France (2000)
240. Cong, X., Kirkpatrick, R.J.: ^{29}Si MAS NMR study of the structure of calcium silicate hydrate. Advanced Cement Based Materials 3, 144–156 (1996)
241. Grutzek, M., Benesi, A., Fanning, B.: Silicon-29 magic angle spinning nuclear magnetic resonance study of calcium silicate hydrates. Journal of American Ceramic Society 72, 665–668
242. Barret, P., Bertrandie, D.: Fundamental hydration kinetic features of the major cement constituents: Ca_3SiO_5 and beta-Ca_2SiO_4. Journal de Chimie Physique 83, 765–775 (1983)

Heat Transfer and Rheological Behaviour of Nanofluids – A Review

Haisheng Chen and Yulong Ding*

Abstract. Nanofluids refer to dilute liquid suspensions of nanoparticles. Over the past decade, such materials generated lots of excitement mainly because a number of researchers reported drastic thermal conductivity enhancement with very small particle loadings. This also sparked hot debates on the underlying physics governing the experimentally observed phenomena. This paper gives an updated review on the topic. It is not intended to be exhaustive but meant to cover the main aspects associated with nanofluids with a specific focus on heat transfer applications. The review covers transport properties of nanofluids in particular thermal conductivity and shear viscosity, and heat transfer of nanofluids under convective and boiling conditions. No new physics appears to be behind the experimentally observed thermal conductivity enhancement as the vast majority of the experimental data fall within the range predicted by the conventional effective medium theory in combination with information of nanoparticle structuring. There seems to be no new physics either in terms of the experimentally observed increase in the shear viscosity of nanofluids as almost all the experimental data can be quantitatively interpreted by the conventional rheological and colloidal theories. There is no sufficient quantitative information, however, to infer the dominant mechanisms for heat transfer enhancement under convective and boiling conditions, where many controversies remain and require further research.

1 Introduction

Nanofluids are dilute colloidal suspensions containing nanoparticles. The base suspending liquid media can be water, ethylene glycol, mineral oil, refrigerant, or mixtures of one or more liquids. The nanoparticles can be made of metal, metal oxide, carbide, nitride, carbon and even immiscible nanoscale liquid droplets. They can take spherical, rod-like or tubular shapes and can be dispersed individually, or in the form of aggregates (several individual particles stick together), or in an entangled form (entanglement of long tubes or fibers). Nanofluids can be transparent, semi-transparent and opaque depending the properties and concentration of the dispersed particles and

Haisheng Chen · Yulong Ding
Institute of Particle Science & Engineering, University of Leeds, Leeds LS2 9JT, UK
Tel.: +44 (0) 113 343 2747; Fax: +44(0113 343 2405
y.ding@leeds.ac.uk

* Corresponding author.

L.Q. Wang (Ed.): Advances in Transport Phenomena 2009, ADVTRANS 1, pp. 135–177.
springerlink.com

they may contain a certain amount of surfactants or dispersants to enhance their stability. The concept of nanofluids was first put forward by Dr Stephen Choi [1] although there was an earlier and independent report by Masuda et al. [2]. The initial stage of research on nanofluids was mainly done at the US Argonne National Laboratories with a focus on thermal conductivity under macroscopically static conditions. The topic gained worldwide attention from later 1990s and became a very hot topic from around 2002 when the exponential growth in the number of publications started. The popularity of the topic of nanofluids is associated with some early experimental observations of enhanced properties and behaviour in heat transfer [3], mass transfer [4-5], wetting and spreading [6], and antimicrobial activities [7]. This paper reviews the most recent studies on the flow and heat transfer behaviour of nanofluids. It does not aim to be exhaustive, but pays specific attention to the mechanistic understanding of experimentally observed phenomena, and establishment of a relationship between flow and heat transfer properties and behaviour. It is therefore different from the scopes of most of the recently published reviews [8-14]. The paper is organised in the following manner. Section 2 is devoted to the transport properties of nanofluids. Heat transfer under convective heat transfer conditions will be covered in Section 3. Section 4 discusses heat transfer under the boiling conditions. Finally, a summary will be given in Section 5.

2 Transport Properties of Nanofluids

Transport properties most relevant to the flow and heat transfer of nanofluids include thermal conductivity and viscosity. This section will discuss the two transport properties in a great detail.

2.1 Thermal Conductivity of Nanofluids

Thermal energy transfer takes place through three modes, conduction, convection and radiation [15]. This sub-section deals with heat transfer of nanofluids through the thermal conduction mode, whereas heat transfer via the convection mode will be discussed in Section 3. Heat transfer via the radiation mode is less relevant under the conditions of experimental work reported in the literature and will not be discussed further. Published studies on the thermal conduction of nanofluids under macroscopically static conditions have been dominating the nanofluids literature over the past decades though the pattern starts to change a couple of years ago. The published studies on thermal conduction of nanofluids can be categorized into four groups, methods and devices for thermal conductivity measurements, experimental measurements of thermal conductivity of various nanofluids, models for predicting thermal conductivity, and mechanistic understanding of thermal conduction enhancement of nanofluids. These are reviewed in the following.

2.1.1 Methods and Devices for Measuring Thermal Conductivity of Nanofluids

A number of techniques have been used to measure the effective thermal conductivity of nanofluids, including the conventional state-state parallel-plate

method [16-17], and transient-based hot-wire [18], oscillation [19], and 3ω methods [20-23]. Of these methods, transient hot-wire method is the most frequently used mainly due to simplicity of the system and fast measurements, whereas the 3ω method is being increasingly adopted recently due to its accuracy. As a consequence, only the two methods are briefly discussed.

Transient hot wire methods. The hot wire method is based on the measurement of temperature rise in a defined distance from a linear heat source (hot wire) embedded in a test sample (e.g. nanofluids). If the heat source is assumed to have a constant and uniform output along the length of the test sample, the thermal conductivity can be derived directly from the resulting change in the temperature over a known time interval [18]. Practical applications of the method, however, require very high precision measurement of the absolute temperature rise with time. The finite length and heat capacity of the hot wire, the finite size of the container, the orientation of the wire or probe, and possibly natural convection effects are examples of possible causes for deviations of realistic measurement systems for thermal conductivity of single phase fluids from the one used in deriving the principle. For nanofluids, motion of nanoparticles due to for example thermophoresis can cause a decrease in the thermal conductivity [24]. The measuring time is also an important aspect of consideration. If the time is too long, the temperature difference between the hot wire and the sample fluid increases and free convection takes place which may result in significant error. In addition, for electrically conductive and highly corrosive fluids, this method can be difficult to apply as the wire / probe has to be insulated with anti-corrosive and electrically insulating coatings. Such coatings can create additional resistance, which are difficult to determine as their thickness and uniformity are difficult to control. These could be reasons for the much scattered thermal conductivity data reported in the literature; see later for more discussion.

3ω method. The 3ω method was originated by Cahill [20]. It uses a fine wire conductor, usually platinum, suspended in a liquid sample to be measured, serving both as a heater and a thermometer. A sinusoidal current passes through the wire at a frequency of ω leading to Joule heating containing a 2ω component. The magnitude and phase of the resulting temperature rise at the 2ω frequency depend on the thermal resistance pertaining to the thermal conductivity and heat capacity of the wire. Due to the linear temperature dependence, the electrical resistance of the wire is modulated at 2ω. Consequently, the current at ω is mixed with the resistance at 2ω leading to a voltage signal at 3ω, and hence providing information of thermal conductivity and thermal diffusivity of the liquid [22]. For electrically conductive liquids, an insulating layer is required. As mentioned above, the insulation layer will introduce a temperature drop. However, such a temperature drop is independent of frequency and can be accurately determined by Fourier's law if the heating power and the thermal conductivity of the coating are known. The uncertainty of thermal conductivity measurements using the 3ω method mainly arises from the temperature coefficient of the electrical resistance of the fine wire and is reported to be within 1.5%. The uncertainty of thermal diffusivity measurements is mainly due to the uncertainties of the properties of the

fine wire, the temperature coefficient of the electrical resistance of the fine wire, and the thermal conductivity, and is reported to be within 6.5% [22]. The 3ω method uses a very small amount liquid sample and can be very fast. However, for nanofluids measurements, the thermophoretic issue remains and requires more and further work in the area.

2.1.2 Experimental Data of Thermal Conductivity of Nanofluids

As mentioned above, heat transfer via the conduction mode has been dominating the nanofluids literature over the past decade though this pattern starts to change recently. A few reviews have been published over the period; see for example [8-11, 14, 25]. The published data of thermal conductivity of nanofluids are mostly obtained at the room temperature. Figure 1 shows a collection of representative data obtained at the room temperature [3, 26-42]. In Figure 1(a), the data are plotted in the form of thermal conductivity enhancement as a function of particle volume fraction, whereas the normalised thermal conductivity enhancement with respect to particle volume fraction is plotted against particle volume fraction in Figure 1(b). These data include aqueous, ethylene glycol and minerals oil based nanofluids made from different types of nanoparticle materials. For comparison, a set of data for polymer-based carbon nanotube composite materials are also included [30]. This type of materials can be argued to be similar to nanofluids from fundamental physics though there are two important differences – the mobility of nanoparticles in the composite is much lower than that in a nanofluids, and the interfacial phenomena can be very different in the two cases. As will be discussed in Section 2.1.4, the effect of nanoparticle mobility on the effective thermal conductivity of nanofluids is still an on-going debate. However, the fundamental physics seems to indicate that nanoparticle mobility plays a small role. An inspection of Figure 1 suggests the following:

- There is a significant level of data scattering in the measured thermal conductivity of nanofluids. In spite of the scatter, the presence of nanoparticles in fluids is seen to enhance the thermal conductivity in many cases.
- The extent of thermal conductivity enhancement depends on the nanoparticle material type and volume fraction. A higher volume fraction gives a greater enhancement.
- The data points shown in Figure 1a can be approximately divided into two groups separated by two demarcation lines. The data points on the left hand side of the right demarcation are for nanofluids made of metal nanoparticles and carbon nanotubes, whereas those on the right hand side of the left demarcation are for nanofluids made of metal oxide and carbide nanoparticles. The region between the two demarcation lines represents overlapping between the two groups. Broadly speaking, the demarcation lines seem to indicate that nanofluids made with higher thermally conductive materials give a higher effective thermal conductivity.

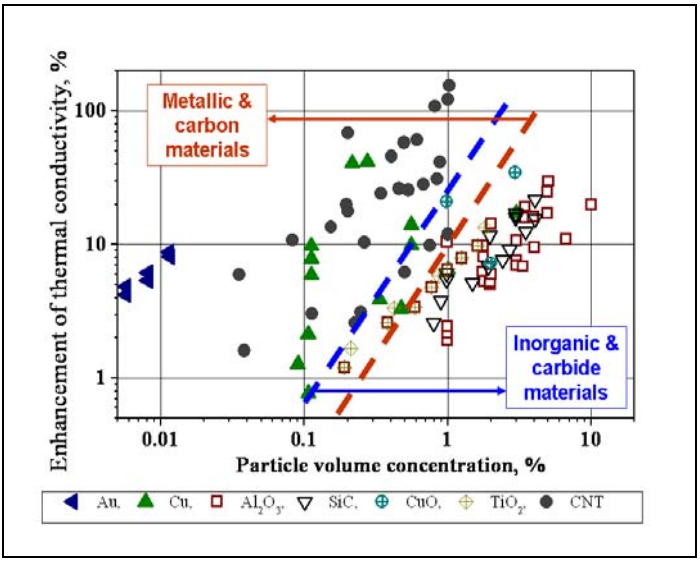

(a) Thermal conductivity enhancement as a function of particle volume fraction

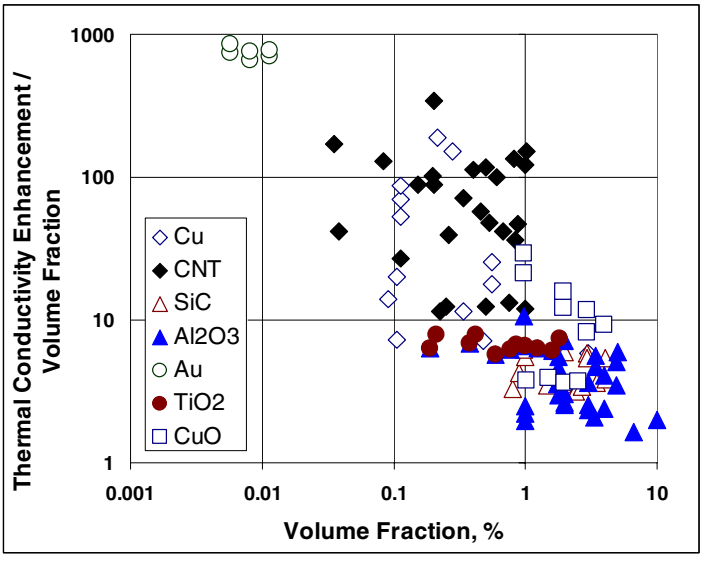

(b) Thermal conductivity enhancement normalized by particle volume fraction plotted against the particle volume fraction

Fig. 1 Effective thermal conductivity of nanofluids reported in the literature: Representative data only extracted from [3, 26-27, 30-39, 41-42]

- There are deviations within each of the two regions separated by the demarcation lines. For example, the thermal conductivities of gold and copper are respectively 317 and 401 W/m.K at the room temperature, whereas the thermal conductivity of carbon nanotubes can be up to 3000-6000 W/m.K [43-44]. The sequence of the three materials as shown in the left hand side of the overlapping region is gold, carbon nanotubes and copper. On the other hand, the thermal conductivities of CuO, alumina and SiC at the room temperature are approximately 20, 40 and 120 W/m.Km, respectively. However, the experimental data shown in the figure indicate that copper oxide nanofluids give the highest enhancement and little difference is seen between SiC and alumina nanofluids. Apart from possible measurement errors and fluid property effects, particle size, shape and aggregation / entanglement are believed to play important roles. However, most publications only contain information of primary size of nanoparticles and / or shape obtained by electron microscopes. This may not be the actual status of nanoparticles as they are prone to agglomerating and/or aggregating (and also entangling for nanotubes and nanofibres).

Temperature has also been found to affect the thermal conductivity of nanofluids; see Section 2.1.4 for more discussion. Additionally, various models have been proposed to predict the thermal conductivity of nanofluids, which will be briefly discussed in the following Section 2.1.3.

2.1.3 Models for the Thermal Conductivity of Nanofluids

A number of theoretical models have been proposed for predicting the thermal conductivity of nanofluids; see for example [8, 17, 45-48]. Table 1 gives a list of representative models, where k_{eff}, k_l and k_p are respectively the thermal conductivities of nanofluids, base liquid and nanoparticles, φ is the volume fraction of nanoparticles in nanofluids and other symbols are explained in the third column of the table. The first five models listed in Table 1 are the original form of conventional models and the rest are newly proposed ones. One can see that the new models are modified versions of the conventional effective medium theory and the modifications are based on various mechanisms proposed to interpret the experimentally observed thermal conduction enhancement; see Section 2.1.4 for a detailed discussion.

It is interesting to note that the original form of the classical models for spherical particles gives a predicted line that is slightly lower than the right demarcation line and there is a very small difference between these classical models within the range of particle concentration shown in Figure 1. This indicates that the original form of the conventional models gives an underprediction for most nanofluids particularly for Au, Cu and CuO nanofluids. For carbon nanotube nanofluids, the original form of the conventional models is found to provide an overprediction [11, 36]. Currently available evidence seems to indicate the underprediction is due to nanoparticle structuring, whereas the

Table 1 A list of theoretical models for thermal conductivity of nanofluids

Models	Expression	Remarks
Maxwell (1873)[140]	$\frac{k_{eff}}{k_l} = \frac{k_p + 2k_l - 2\varphi(k_l - k_p)}{k_p + 2k_l + \varphi(k_l - k_p)}$	For well-dispersed spherical particles with vanishing interfacial thermal resistance
Hamilton& Crosser (1962)[141]	$\frac{k_{eff}}{k_l} = \frac{k_p + (n-1)k_l - (n-1)\varphi(k_l - k_p)}{k_p + (n-1)k_l + \varphi(k_l - k_p)}$	For well dispersed particles with vanishing interfacial thermal resistance, n is the shape factor given by $n=3/\psi$ with ψ the sphericity
Jeffrey (1973)[142]	$\frac{k_{eff}}{k_l} = 1 + \frac{3\varphi(k_p/k_l - 1)}{k_p/k_l + 2} + 3\varphi^2\left(\frac{k_p/k_l - 1}{k_p/k_l + 2}\right)^2 [1 + \frac{1}{4}\left(\frac{k_p/k_l - 1}{k_p/k_l + 2}\right) + \frac{3}{16}\left(\frac{k_p/k_l - 1}{k_p/k_l + 2}\right)\left(\frac{k_p/k_l + 2}{2k_p/k_l + 3}\right) + \ldots$	High order terms represent pair interactions of randomly dispersed particles; vanishing interfacial thermal resistance
Davis (1986)[143]	$\frac{k_{eff}}{k_l} = 1 + \frac{3\varphi(k_p/k_l - 1)[\varphi + f\varphi^2 + O(\varphi^3)]}{(k_p/k_l + 2) - (k_p/k_l - 1)\varphi}$	High order terms due to pair interactions of randomly dispersed spheres, f= 2.5 & 0.5 for k_p/k_l = 10 and ∞ respectively; vanishing interfacial thermal resistance
Bruggenman (1935)[100]	$\frac{k_{eff}}{k_l} = \frac{1}{4}\{(3\varphi - 1)\frac{k_p}{k_l} + (3(1-\varphi) - 1) + [((3\varphi - 1)\frac{k_p}{k_l} + (3(1-\varphi) - 1))^2 + 8\frac{k_p}{k_l}]^{\frac{1}{2}}\}$	For concentrated suspensions of interacting particles; vanishing interfacial thermal resistance
Yu and Choi (2003 & 2004)[51,144]	(i) $\frac{k_{eff}}{k_l} = \frac{k_{pe} + 2k_l - 2\varphi(k_l - k_{pe})(1+\beta)^3}{k_{pe} + 2k_l + \varphi(k_l - k_{pe})(1+\beta)^3}$ (ii) $\frac{k_{eff}}{k_l} = 1 + \frac{n\varphi_{eff}A}{1 - \varphi_{eff}A}$ with $A = \frac{1}{3}\sum_{j=a,b,c}\frac{k_{pj} - k_l}{k_{pj} + (n-1)k_f}$	Well-dispersed nanopaticles with a 'crystalline' liquid nanolayer surrounding each nanoparticles: (i) spherical and (ii) non-spherical; β – ratio of nanolayer thickness to particle radius for spherical particles; k_{pe} – effective thermal conductivity of nanoparticle-nanolayer composite for spherical particles; k_{pj} – effective thermal conductivity of non-spherical particles including nanolayer in j direction; φ_{eff} -effective particle volume fraction including nanolayer

Table 1 (*continued*)

Wang et al. (2003)[17]	$\frac{k_{eff}}{k_l} = \frac{(1-\varphi)+3\varphi\int_0^{\infty} k_{cl}(r)n(r)/[k_{cl}(r)+2k_l]dr}{(1-\varphi)+3\varphi\int_0^{\infty} k_l(r)n(r)/[k_{cl}(r)+2k_l]dr}$	A fractal model based on the multi-component Maxwell model by substituting the effective thermal conductivity of nanoparticle clusters, $k_{cl}(r)$, and the radius distribution function, $n(r)$
Xue (2003) [145]	$0 = 9(1-\frac{\varphi}{\lambda})\frac{k_{eff}-k_l}{2k_{eff}+k_l} + \frac{\varphi}{\lambda}[\frac{k_{eff}-k_{c,x}}{k_{eff}+B_{2,x}(k_{c,x}-k_{eff})} + 4\frac{k_{eff}-k_{c,y}}{2k_{eff}+(1-B_{2,x})(k_{c,y}-k_{eff})}]$ with $\lambda = abc/(a+t)(b+t)(c+t)$	Model for elliptical nanoparticles with radii in three directions of x, y and z respectively as *a, b* and *c*; model based on the average polarization theory taking into account the effect of an interfacial shell of a thickness *t* between nanoparticles and base liquid; $k_{c,x}$ - effective dielectric constant and $B_{2,x}$ - depolarization factor along *x*-symmetrical axis
Xue and Xu (2005) [146]	$0 = (1-\frac{\varphi}{\alpha})\frac{k_{eff}-k_l}{2k_{eff}+k_l} + \frac{\varphi}{\alpha}\cdot [\frac{(k_{eff}-k_2)(2k_2+k_1)-\alpha(k_1-k_2)(2k_2+k_{eff})}{(2k_{eff}+k_2)(2k_2+k_p)+2\alpha(k_p-k_2)(k_2-k_{eff})}]$	α - volume ratio of spherical nanoparticle and complex nanoparticles containing an interfacial shell; k_1 - thermal conductivities of nanoparticles; k_2 – thermal conductivity of interfacial shell
Xuan et al. (2003)[69]	$k_{eff} = \frac{k_p+2k_l-2(k_l-k_p)\varphi}{k_p+2k_l+(k_l-k_p)\varphi}k_l + \frac{\rho_p\varphi C_p}{2}\sqrt{\frac{k_BT}{3\pi r_c\mu}}$	Model taking into account Brownian motion and clusters of nanoparticles; r_c – radius of clusters; k_B – Boltzmann constant; ρ_p – particle density; μ – fluid viscosity; C_p – heat capacity; *T*- absolute temperature
Kumar et al. (2004) [33]	$k_{eff} = k_l + c\frac{2k_BT}{\pi\mu d_p^2}\frac{\varphi r_f}{(1-\varphi)r_a}$	Model taking into account Brownian motion; d_p – particle diameter; μ - fluid viscosity; r_f – fluid particle radius

Table 1 (*continued*)

Jang and Choi (2004) [147]	$k_{eff} = k_l(1-\varphi) + k_p\varphi + 3C\frac{d_l}{d_p}k_l \,\mathrm{Re}^2 \,\mathrm{Pr}\,\varphi$	Model taking into account micro-convection; C – constant; d_l – liquid molecule diameter; Re – particle Reynolds number; Pr – Prandtle number
Prasher et al. (2005) [57]	$\frac{k_{eff}}{k_l} = (1 + A\,\mathrm{Re}^m\,\mathrm{Pr}^{0.333}\,\varphi)\cdot [\frac{k_p + 2k_l + 2(k_p - k_l)\varphi}{k_p + 2k_l - (k_p - k_l)\varphi}]$	Model taking into account micro-convection induced by Brownian motion; A – constant; m - constant
Koo and Kleinstreuer (2004 & 2005) [148]	$\frac{k_{eff}}{k_l} = \frac{k_p + 2k_l - 2\varphi(k_l - k_p)}{k_p + 2k_l + \varphi(k_l - k_p)} + 5\times10^4 \beta\varphi\rho_p C_p \sqrt{\frac{k_B T}{\rho_p d_p}} \frac{f(T,\varphi)}{k_l}$	Model taking into account micro-convection due to the Brownian motion; β – volume fraction of fluid moving with a particle; $f(T, \varphi)$ – factorial function depending on fluid properties and interparticle interactions

overprediction is due to the effect of interfacial resistance, both of which are not included in the original form of the conventional models. More discussion is given in Section 2.1.4.

2.1.4 Mechanisms of Thermal Conductivity Enhancement / Deterioration of Nanofluids

A number of mechanisms have been proposed for interpreting the experimentally observed thermal conduction enhancement [48-49]. The most popular mechanisms include Brownian motion of nanoparticles [32-33, 46, 50], interfacial ordering of liquid molecules at nanoparticle surfaces [17, 49, 51], ballistic transport of energy carriers within individual nanoparticles [49], as well as nanoparticle structuring / networking [17, 45, 49, 52]. They are briefly discussed in the following.

Ballistic transport of energy carriers. Ballistic transport of energy carriers occurs when the mean free path of the energy carriers is larger than the characteristic length of nanoparticles. Such a mechanism has been excluded as a possible mechanism for the enhanced thermal conductivity because the thermal conductivity of nanoparticles decreases with deceasing particle size when the size becomes comparable to the mean free path of the energy carriers [53].

Brownian motion. Brownian motion of nanoparticles could contribute to the thermal conduction enhancement through two ways, direct contribution due to motion of nanoparticles that transports heat, and indirect contribution due to micro-convection of fluid surrounding individual nanoparticles. The direct contribution of Brownian motion has been shown theoretically to be negligible as the time scale of the Brownian motion is about 2 orders of magnitude larger than that of the thermal diffusion in the base liquid at low to medium temperatures [49]. The indirect contribution has also been shown to play a minute role through the same reasoning for the direct contribution and also through molecular modelling [54]. Furthermore, nanoparticles are often in the form of agglomerates and / or aggregates, so the Brownian motion is expected to play an even less role. This conclusion is supported by experimental data shown in Figure 2, where the thermal conductivity enhancement is plotted as a function of temperature for nanofluids made of three types of metal-oxide nanoparticles. One can see that, except for the data reported in [31] for CuO/H_2O nanofluids, the thermal conductivity enhancement is almost independent of temperature. Such weak temperature dependence suggests that the Brownian motion of nanoparticles be not a dominant mechanism for the enhanced thermal conductivity of nanofluids. The minor role of the Brownian motion is also supported by the lack of clear effect of the base liquid viscosity on the thermal conductivity enhancement of alumina based nanofluids [11].

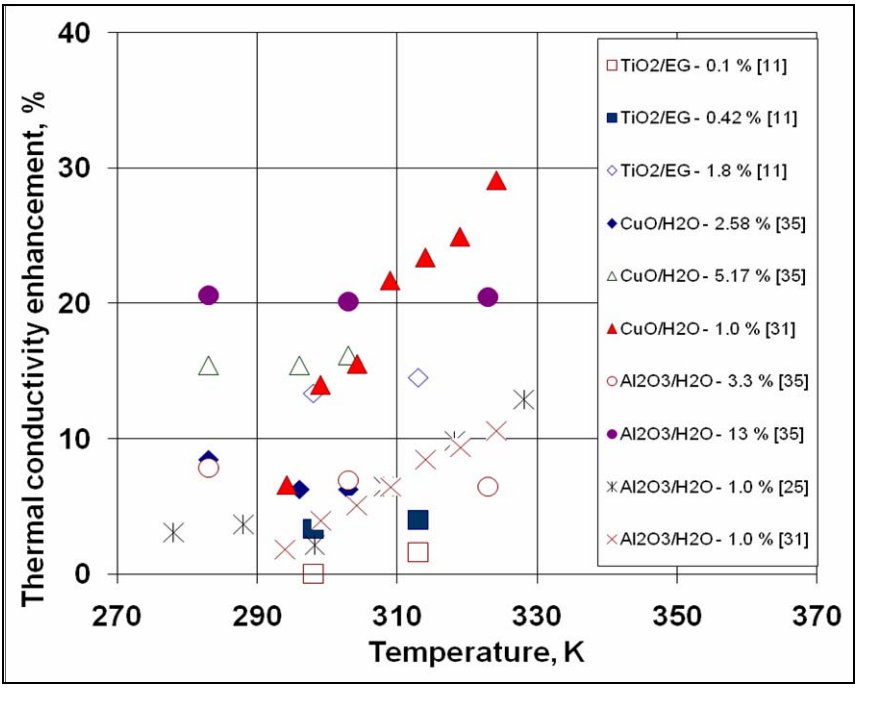

Fig. 2 Effect of temperature on the thermal conductivity enhancement of nanofluids

Liquid molecular layering. At the solid-liquid interface, liquid molecules could be significantly more ordered than that in the bulk liquid. By analogy to the thermal behaviour of crystalline solids, the ordered structure could give thermal conductivity enhancement [49]. Such a suggestion inspired a number of researchers to develop theoretical models to explain the experimentally observed thermal conduction enhancement; see Table 1. However, it is now clear that liquid-nanoparticle interface is one of the main factors that decrease (rather than increase) the effective thermal conductivity due to the so-called Kapita interfacial resistance [45, 47, 55-56], and the effect of interfacial resistance on the overall effective thermal conductivity depends on particle size [8, 47, 57-58]. When particle size is relatively small in comparison with the characteristic length scale for the interfacial resistance, nanoparticles act as insulators. This can lead to deterioration of the thermal conduction of nanofluids [35, 58].

Nanoparticle structuring / aggregation. Recent studies have suggested that nanoparticle structuring / aggregation be a dominant mechanism for the experimentally observed thermal conductivity enhancement of nanofluids [17, 45, 48, 51-52, 59-62]. Using such a mechanism, well-dispersed nanoparticles in a fluid matrix gives the lowest thermal conductivity, whereas interconnected nanoparticles in the liquid enhances the thermal conduction. This can be understood from the viewpoint of circuit analyses; the well-dispersed situation is closer to conductors connected in a series mode, while the interconnected case is closer to those in a parallel mode [48]. It is to be noted that although nanoparticle structuring is able to explain the experimentally observed thermal conduction enhancement, it does not necessarily mean nanoparticle structuring is the only dominant mechanism and this remains to be proved.

If nanoparticle structuring is the only dominant mechanism, then the key issue is to obtain nanoparticle structural information, which can be fed to the conventional effective medium theories to give predictive models for the effective thermal conductivity of nanofluids. One of the methods for obtaining the nanoparticle structural information is through the rheological analyses; see Section 2.2 for details.

2.2 Rheological Behaviour of Nanofluids

Rheological behavuour of nanofluids affects the convective heat transfer and pressure drop of nanofluids. In addition, as mentioned above, the rheological behaviour provides nanoparticle structuring information, which can then be used for predicting the thermal conductivity of nanofluids. However, only a small number of studies have been found in the literature on the rheological behaviour of nanofluids and there are inconsistencies in the few publications [41, 63-66]. In the following, experimentally measured rheological data for nanofluids are summarised first. Efforts are then made to analyse the data and to interpret the inconsistent results reported in the literature using the conventional rheological and colloidal theories (or semi-theories).

2.2.1 Experimentally Measured Rheological Data for Nanofluids

The rheological behaviour of nanofluids can be measured by using rheometers [41-42, 63-65]. There are also reports on the use of viscometers [66-67], which, as will be discussed in the following, are mostly inadequate as they cannot catch the feature of the shear dependence particularly for low viscosity liquid (e.g. water) based nanofluids containing non-spherical particles. In the following, experimental observations are presented and the high shear viscosity values reported in the literature are summarised and compared with the original form of the conventional theories.

Newtonian and non-Newtonian behaviour of nanofluids. There have been debates on shear-dependent behaviour of nanofluids. The Newtonian behaviour has been reported in [16] and [68] for water-Al_2O_3 nanofluids, [16] for EG-Al_2O_3 nanofluids, [69] for Cu-water nanofluids and [64] for Al_2O_3-PG (Propylene glycol) nanofluids, whereas the non-Newtonian behaviour of nanofluids has been reported in [41-42, 63, 65, 70-71]. Detailed rheological analyses show that nanofluids can exhibit either or both Newtonian and non-Newtonian behaviour depending on particle size and shape, particle concentration, base liquid viscosity, solution chemistry, etc. For example, Figures 3(a) and 3(b) show respectively the shear viscosity as a function of shear rate for an aqueous based carbon nanotube nanofluid [41] and an ethylene glycol based titaina nanofluids [65]. The measurements are based on the controlled stress model using a Bolin CVO rheometer with cone-plate geometry. One can see a clear non-Newtonian shear-thinning behaviour of the carbon nanotube nanofluids, and Newtonian shear-independent behaviour of the ethylene glycol - titania nanofluid. An inspection of the literature on the rheological behavior of nanofluids suggests the following:

- The shear-dependence of viscosity of very dilute nanofluids is negligible, while nanofluids with a relatively high concentration are more likely to exhibit shear thinning behaviour.
- Nanofluids made of low viscosity fluids (e.g. water) are more likely to exhibit the non-Newtonian behaviour than those made of highly viscous base fluids (e.g. ethylene glycol and propylene glycol)
- Particle shape plays a strong effect on the shear dependent behaviour of nanofluids. Nanofluids containing rod-like nanoparticles, particularly rods with large aspect ratios, are most likely to show strong shear thinning behaviour.
- For highly concentrated suspensions containing non-spherical particles, shear thickening may occur at high shear rates; see for example [72]. This is beyond the normal concentration range for nanofluids for heat transfer applications as the penalty due to viscosity increase outweighs the benefits of heat transfer performance increase.

Effects of temperature. The temperature dependence of viscosity of nanofluids has been investigated experimentally over the last couple of years; see for example [60-62, 66-67]. These studies show that temperature can have a very strong effect

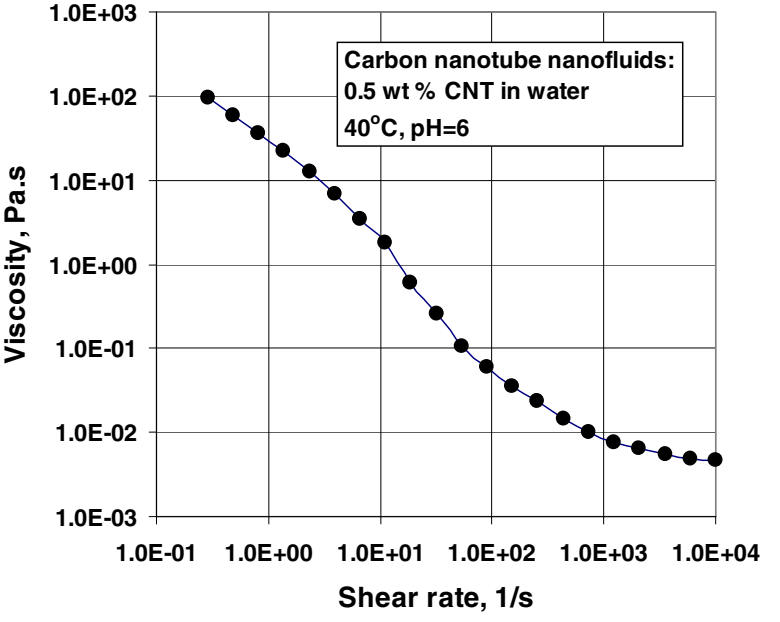

(a) Water - carbon nanotube nanofluid

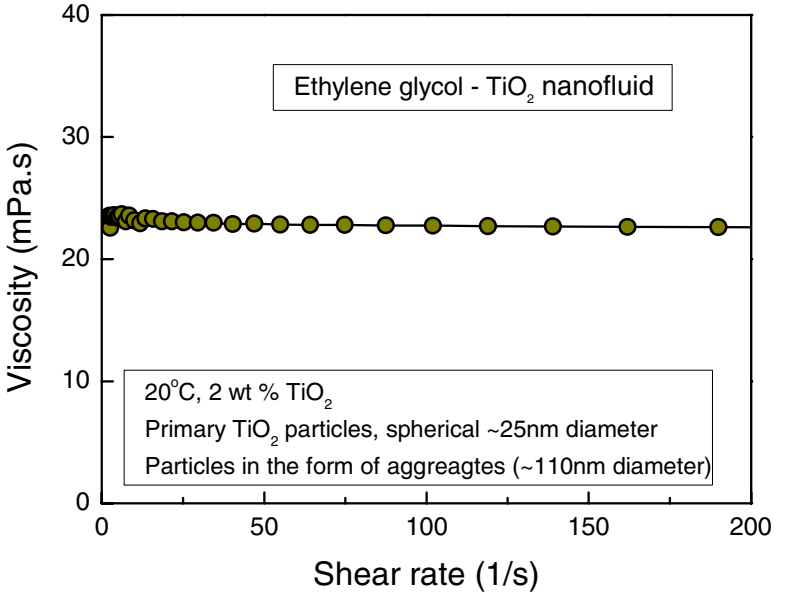

(b) Ethylene glycol – titania nanofluids

Fig. 3 Shear viscosity as a function of shear rate for (a) aqueous based carbon nanotube nanofluids and (b) ethylene glycol based titania nanofluid

on the shear viscosity of nanofluids. At low shear rates, the viscosity of nanofluids increases with increasing temperature, exhibiting a stronger shear-thinning behaviour. In high shear rate region where the shear viscosity approaches a constant value (called high shear viscosity), the viscosity scales with temperature in a similar fashion to that of the base liquid. The experimental results also show that both the high shear viscosity of nanofluids and the base liquids follow well the classical Vogel-Tammann-Fulcher (VTF) equation [15, 60]. Interestingly, however, the relative increment of high shear viscosity at a given particle concentrations is almost independent of temperature [60, 65].

Effects of particle size and shape. Very few studies have been found in the literature that deals with the effects of particle size and shape on the rheological behaviour of nanofluids. He et al. (2007) showed experimentally that an increase in particle size led to an increase in the shear viscosity [42], whereas Chen et al. demonstrated that nanofluids containing rod-like particles had a much stronger shear thinning in comparison with those containing spherical nanoparticles [62].

High shear viscosity. For shear thinning nanofluids, the shear viscosity approaches a constant at high shear rates as mentioned above. Such a constant is termed the high shear viscosity and is very relevant to the convective heat transfer applications where heat transfer fluids are often in vigorous motion and subject to very high shear. Figure 4 summarises the room temperature data of high shear viscosity reported in the literature [16, 31, 42, 60, 64-65, 71] together with predictions by various classical models in their original forms including Einstein equation [73, 74] for dilute non-interacting suspensions of spherical particles, Batchelor equation [75] for semi-dilute suspensions of spherical particles and Brenner-Condiff equation (B-C equation) [76] for dilute suspensions of rod-like particles. The details of these models are given in Table 2. In spite of the data scattering, the following observations can be made from Figure 4:

- The presence of nanoparticles in fluids increases the high shear viscosity and the extent of increment depends on nanoparticle shape and volume fraction. Given other conditions, the high shear viscosity of nanofluids containing rod-like particles is much higher than those containing spherical nanoparticles.
- The high shear viscosity of nanofluids increases with increasing nanoparticle volume fraction in a nonlinear manner; the original form of the conventional models as listed in Table 2 fails, by a large margin, to provide an adequate prediction.
- Regression of the measured high shear viscosity of nanofluids containing spherical nanoparticles gives an binomial relationship, $\eta = \eta_0(1+10\varphi+(10\varphi)^2)$, where η and η_0 are the shear viscosity of nanofluids and base liquids, respectively [65].

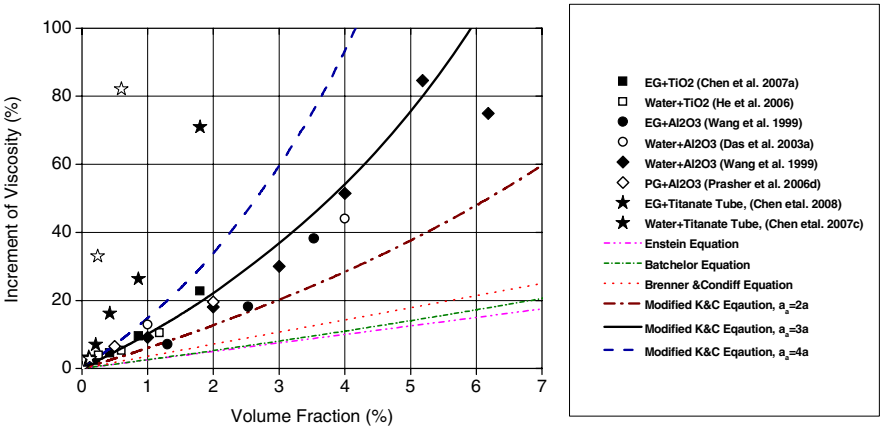

Fig. 4 Increment of high shear viscosity of nanofluids as a function of nanoparticle concentration, data from Refs [16, 31, 42, 60, 62, 64, 71]

2.2.2 Analyses and Interpretation of the Experimental Data

In this section, efforts are made to analyse and interpret the experimental observations presented in Section 2.2.1. Some theoretical background will also be reviewed first, which is essential for the analyses and interpretation of the experimental data.

Theoretical background of suspension rheology. The theories of rheology of colloid dispersions have been well documented; see for example [77-83]. Investigation of the rheology of colloid dispersions is started from the Einstein's analysis of infinitely dilute suspensions of hard spheres [73-74]. This leads to the rotational motion of the particle known as the vorticity of the shear field and hence the following dispersion viscosity (η): $\eta = \eta_0\left(1+[\eta]\varphi + O(\varphi^2)\right)$, where $[\eta]$ is the intrinsic viscosity having a typical value of 2.5 for monodisperse dispersions of hard spheres. This equation is the well-known Einstein Equation and applies to φ <~0.01.

For φ>~0.01, hydrodynamic interactions between particles become important as the disturbance of the fluid around one particle interacts with that around other particles. The viscosity in such a case is given by Batchelor (1977): $\eta/\eta_0 = 1+[\eta]\varphi + k_H\left([\eta]\varphi\right)^2 + O(\varphi^3)$. The Batchelor Equation is validated to φ=0.1 for flows dominated by single particles and pair-particle microstructures. k_H in the above expression is the Huggin's coefficient and can be considered as the interaction parameter characterising the colloidal interactions between particles as opposed to the purely hydrodynamic effect [81].

For φ>~0.1, three-particle and multi-particle collisions become increasingly important and hence terms with an order of 3 and higher have to be considered for which there is no rigorous analysis. Krieger & Dougherty (1959) proposed a

Table 2 A list of classical viscosity models for suspensions

Model	Expression	Description
Einstein (1906&1911) [73-74]	$\eta = \eta_0\left(1+[\eta]\varphi+O(\varphi^2)\right)$	Spherical particles and dilute suspensions, $[\eta]$ the intrinsic viscosity with a typical value of 2.5
Batchelor (1977) [75]	$\frac{\eta(0)}{\eta_0} = 1+[\eta]\varphi+k_H\left([\eta]\varphi\right)^2+O(\varphi^3)$	Spherical particles and semi-dilute suspensions, interaction of pair-particles are considered, k_H is the Huggin's coefficient
Brenner and Condiff (1974) [76]	$\eta = \eta_0\left(1+[\eta]\varphi+O(\varphi^2)\right)$ $[\eta](0) = 5Q_1 - Q_2 + 2Q_3$ $Q_1 = \frac{2}{5} - \frac{6\ln 2r}{5r}$ $Q_2 = -\frac{r^2}{15(\ln 2r - 1.5)} + \frac{2}{5}$ $Q_3 = \frac{r^2}{10(\ln 2r - 0.5)}$ $[\eta](\infty) = \frac{0.312r}{\ln 2r - 1.5} + 2 - \frac{0.5}{\ln 2r - 1.5} - \frac{1.872}{r}$	Rod-like particles and dilute suspensions; r is the aspect ratio;
Krieger & Dougherty (1959) [84]	$\frac{\eta}{\eta_0} = \left(1-\frac{\varphi}{\varphi_m}\right)^{-[\eta]\varphi_m}$	Spherical particles, full range of concentration, φ_m has a different value for high and low shear rates
Modified Krieger & Dougherty (2007) [65]	$\frac{\eta}{\eta_0} = \left(1-\frac{\varphi_a}{\varphi_m}\right)^{-[\eta]\varphi_m}$, $\varphi_a = \varphi\left(\frac{a_a}{a}\right)^{3-D}$	Spherical particles with aggregation, a_a and a are the radii of aggregate and primary particles, D is the fractural index

semi-empirical relationship for the high shear viscosity covering the full range of particle volume concentration: $\eta/\eta_0 = (1-\varphi/\varphi_m)^{-[\eta]\varphi_m}$, where φ_m is the maximum particle packing fraction. φ_m has a value in a range of 0.495 - 0.54 under quiescent conditions and is approximately 0.605 at high shear rates [84]. Inserting the two φ_m values into Krieger & Dougherty equation gives the limiting viscosities at low and high shear conditions, $\eta(0)$ and $\eta(\infty)$, for monodisperse suspensions: $\eta(0)/\eta_0 = (1-\varphi/\varphi_m(0))^{-[\eta]\varphi_m(0)} \approx (1-\varphi/0.5)^{-1.25}$ and $\eta(\infty)/\eta_0 = (1-\varphi/\varphi_m(\infty))^{-[\eta]\varphi_m(\infty)}$ or $\eta(\infty)/\eta_0 = (1-\varphi/0.605)^{-1.5125}$. It is interesting to note that, when the particle volume fraction approaches zero, the Krieger-Dougherty equation reduces to the Einstein equation if a monomial expansion is performed, whereas a binomial expansion of the equation will lead to the Batchelor Equation as discussed before.

The difference between $\eta(\infty)$ and $\eta(0)$ as discussed above can be used to illustrate the shear dependent behaviour of suspensions. Figure 5 shows such a difference as a function of particle volume fraction. Little difference is seen when φ <0.2 and hence no discernible non-Newtonian behaviour is expected. When the volume fraction exceeds about 0.2, however, the difference between the two limiting shear viscosities becomes increasingly significant and the shear-thinning behaviour is expected. From the above analyses, it appears that the volume fraction of 0.2 is a demarcation for the shear dependent behaviour. However, experimental results show that the shear thinning behaviour can occur at a much lower particle volume fraction; see for example Figure 3(a). The reason for this will be discussed later in this section.

Using the two limiting shear viscosities discussed above, the shear viscosity, η, as a function of shear rate can be given as $\eta = \eta(\sigma_r) = \eta(\infty) + \dfrac{(\eta(0)-\eta(\infty))}{1+(\sigma_r/\sigma_c)^n}$ [80]. This expression can be recast to give $\eta = \eta(Pe) = \eta(\infty) + \dfrac{(\eta(0)-\eta(\infty))}{1+(Pe/Pe_c)^m}$. Here, σ_r is the reduced shear stress defined by $\sigma_r = \sigma a^3/k_BT$, σ is the shear stress that relates to the shear rate, $\dot{\gamma}$, according to $\sigma = \eta\dot{\gamma}$, a is the particle radius, k_B is the Boltzmann constant, T is the absolute temperature, m and n are power law indices (equal to 1 for monodisperse spherical particles), Pe is the Péclet number defined as $Pe = 6\pi a^3\sigma/k_BT$, and the subscript, c, represents the characteristic point in the shear dependent viscosity curve at which Pe=~1 (Pe=*1* implies physically that the diffusive and convective timescales are equal, which also gives a value of σ_c~0.053 at the ambient temperature. Cross (1965) indicated that m should approach 2/3 with increasing polydispersity [85].

Rheological behaviour of nanofluids containing spherical nanoparticles. As discussed earlier in Section 2.1, nanoparticles in nanofluids are prone to

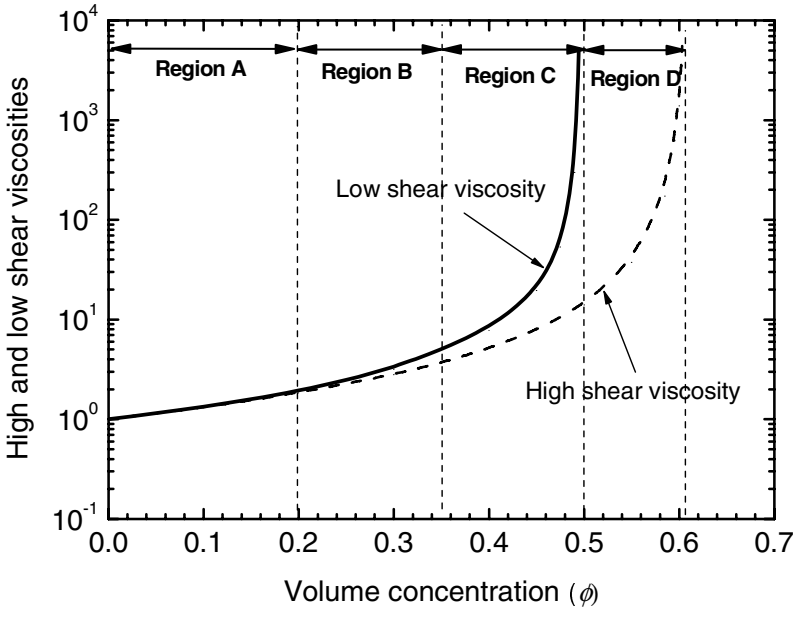

Fig. 5 Ratio of the high to low shear viscosity as a function of volume fraction

aggregation due to large surface energy of nanoparticles. This has been experimentally observed; see for example [39, 42, 63]. In the following, it will be shown that rheological analyses incorporating nanoparticle aggregation can explain the experimental observations.

Let's consider nanofluids containing spherical nanoparticles first and assume that hydrodynamic forces are insufficient to break the network of particles in individual aggregates down to individual primary particles, but only make the aggregates form spherical flow units with an effective volume faction of φ_a. Under such conditions, the Krieger & Dougherty equation presented above takes the form of $\eta/\eta_0 = \left(1-\varphi_a/\varphi_m\right)^{-[\eta]\varphi_m(\infty)}$, where the effective volume fraction of nanoparticles is given by $\varphi_a = \varphi\left(a_a/a\right)^{3-D}$ according the fractal theory, a_a is the radius of aggregates, and the term D is the so-called fractal index with a value ranging from 1.8 to 2.5 according to the colloidal literature. For nanofluids containing spherical nanoparticles, a typical value of *D=1.8* has been suggested [17, 51, 65, 80, 86]. As a consequence, the effective volume fraction of nanoparticles can be much higher than the actual solid volume fraction due to the aggregation and the resulting nanofluids viscosity can be much higher than predictions by the original forms of various conventional theories. This is indeed the case as shown in Figure 4, where the modified Krieger & Dougherty equation $\eta/\eta_0 = \left(1-\varphi_a/\varphi_m\right)^{-[\eta]\varphi_m(\infty)}$ is plotted for three effective aggregate radii of

2*a, 3a,* and *4a*. It can be seen that the data points for nanofluids containing spherical particles are bound by the curves for $a_a=2a$ and $a_a=4a$, and are very close to the curve for $a_a=3a$. It is interesting to note that the best curve-fitting gives a value of $a_a=3.3a$, which agrees well with the SEM and dynamic light scattering measurements [65]. The above analyses provide an explanation for the experimentally observed higher viscosity than predictions by the original forms of classical theories for suspension rheology.

The analyses also provide an explanation for experimentally observed shear thinning behaviour of nanofluids with an actual particle volume fraction much lower than 0.2 (Figures 3 and 5). As a consequence, classification of nanofluids needs to take into account of nanoparticle aggregation. Further analyses suggest the following for nanofluids containing spherical nanoparticles [65]:

- *Dilute nanofluids* ($0<\varphi<\sim0.001$) containing well dispersed nanoparticles with no discernible shear-thinning behaviour. Shear viscosity can be described by the Einstein equation.
- *Semi-dilute* nanofluids ($\sim0.001<\varphi<\sim0.05$) containing aggregates of nanoparticles with no obvious shear-thinning behaviour. Shear viscosity fits the modified Krieger & Dougherty equation
- *Semi-concentrated* nanofluids ($\sim0.05<\varphi<\sim0.10$) containing aggregates of nanoparticles with clear shear thinning behaviour. Shear viscosity fits the modified Krieger & Dougherty equation
- *Concentrated* nanofluids ($\varphi>\sim0.10$) with interpenetration of aggregates. It is out of the normal range of nanofluids for heat transfer applications

Nanofluids containing rod-like nanoparticles. Nanofliuds containing rod-like nanoparticles are more complicated and less researched so far. Chen et al. (2009) found that such nanofluids showed much stronger shear dependence of their viscosity [62]. They used a similar approach as that for nanofluids containing spherical nanoparticles with an aim to interpret the experimental observations. They first considered a case with well dispersed rod-like naoparticles with an aspect ratio of $r = L/b$, where L and b are respectively the length and diameter of the rods. The number concentration of particles (number of particles per unit volume), c, was given as $c = \varphi/(\pi b^2 L/4) \approx \varphi/b^2 L$. In a quiescent state, the rod-like particles can make three types of motion due to the Brownian diffusion, rotational (end-over-end) motion around mid-point of rods, and translational motion either parallel or perpendicular to the long axis of the rods. Accordingly, nanofluids containing well dispersed nano-rods can be classified into three categories. The first category is d*ilute nanofluids* with $0<c<1/L^3$ $(0<\varphi<1/r^2)$ and the average interparticle spacing being much larger than the largest dimension of the rod-like particles. In this case, the Brownian motion is determined by the base liquid viscosity and the suspension viscosity can be calculated by: $\eta(0) \approx \eta_0(1 + A \cdot cL^3)$ where A is a numerical constant [87]. As $\varphi \propto c$, this equation can be recast to give the Brenner & Condiff equation as given in Table 2

and discussed above. The second category is s*emi-dilute nanofluids* with $1/L^3<c<1/bL^2$ $(1/r^2<\varphi<1/r)$ and interactions between the rod-like particles. The rotational motion in this case is restricted, so does the translational motion perpendicular to the rod axis. If the rods are treated as a line without thickness, the viscosity takes the form of $\eta(0) \approx \eta_0(1+(BcL^3)^3)$, with B a numerical constant [88]. As $c>1/L^3$, this expression shows that $\eta(0)$ can be much larger than the base liquid viscosity. Such a large shear viscosity is due to the shape of the rods (or tubes) that have a rotational degree of freedom and the viscosity is very sensitive to the shear. This explains the strong shear thinning behaviour of suspensions of tube / rod-like particles. The third category is c*oncentrated nanofluids* with $c>1/bL^2$ $(\varphi>1/r)$ and rod particles likely to align and/or entangle. The rod-like particles still show a degree of disorder but only over a limited concentration range and both the dynamics and distribution of particles in space are substantially modified. The isotropic state is maintained up to a concentration of c^r (φ^r) which is normally of the same order as $1/bL^2$ [81]. The rheological behaviour of the concentrated nanofluids is likely to be similar to the semi-dilute suspensions [79, 89-91]. This is, however, out of the normal range of particle concentration of nanofluids for heat transfer applications.

Rod-like nanoparticles are also often found to aggregate in nanofluids [61-62]. This implies the experimentally observed rheological behaviour of nanofluids containing rod-like particles cannot be explained purely by the shape effect, particle aggregation should be considered. If the aggregates of the rod-like particles form flow units with an ellipsoidal or rod-like morphology with an effective volume fraction of φ_a, an effective aspect ratio of $r_a = L_a / b_a$, where L_a and b_a are respectively effective length and diameter, then the classification of the nanofluids containing aggregated nano-rods will become:

- *Dilute nanofluids* $(0<\varphi_a<1/r_a^2)$ with the primary rod-like nanoparticles either well dispersed in the base liquid or in the format of aggregates. Due to the low concentration, the hydrodynamic interactions between the primary nanoparticles or aggregates are negligible. The rheological behaviour can be represented by the Brenner & Condiff equation, where a different intrinsic viscosity [η] has to be used, which depends on particle shape and/or structure of aggregates. Also, the volume fraction φ in Brenner & Condiff equation should be replaced by the effective volume fraction φ_a if aggregates exist.
- *Semi-dilute nanofluids* $(1/r_a^2<\varphi_a<1/r_a)$ with the rod-like nanoparticles in the format of aggregates. Besides the motion of individual primary particles inside the aggregates, the motion of individual aggregates is also restricted as the hydrodynamic interactions between aggregates become increasingly strong as the particle concentration increases. The rheological behaviour of such nanofluids is similar to nanofluids consisting of individual rod-like nanoparticles. However, the effective aspect ratio r_a and effective volume fraction φ_a should be used for the analyses. In a quiescent state, the shear viscosity can be expressed by

$\eta(0) \approx \eta_0(1+(C\varphi_a r_a^2)^3)$, which implies the low shear viscosity is proportional to φ_a^3 and hence to φ^3. At high limit shear rates, the (high) shear viscosity normally fits the Krieger & Dougherty equation. However, the intrinsic viscosity, [η], and the fractal index, D, are different [92].

- *Semi-concentrated nanofluids ($1/r_a<\varphi_a<\varphi_a^r$)* with rod-like particles tending to align and/or entangle and the low shear visocisty being proportional to φ^n (n=*4-6*) [80].

Effects of temperature. The effect of temperature depends on the relative importance of the Brownian diffusion and the shear flow convection. At low shear rates and high temperatures, the Brownian diffusion can be stronger in comparison with the convection, a stronger shear thinning behaviour is expected [62, 65, 71].

Effects of other factors. There are some other important factors that may affect the rheological behaviour of nanofluids. These include solution chemistry related surface layer and electro-viscous effects [81, 93-94], and high shear effects [79, 95-99].

2.3 Thermal Conductivity Prediction Based on the Rheological Information

As mentioned before, current experimental and theoretical evidence suggests nanoparticle structuring be a most likely dominant mechanism for the experimentally observed thermal conduction in nanofluids. This has been demonstrated in [17] and [52], and more recently by Chen et al. [60-62], who extracted nanoparticle structuring information directly from the measured rheological behaviour of various nanofluids and used such information for the prediction of thermal conductivity of nanofluids. Figure 6 shows the methodology used in [60-62], which also includes validation of the size of structured nanoparticles using particle characterisation techniques. In the following, their work on the prediction of nanofluids containing both spherical and rod-like nanoparticles is briefly summarised.

From the rheological behaviour, Chen et al. estimated the effective size of structured (aggregated) nanoparticles and the effective volume fraction of nanofluids [60, 62]. They then modified the conventional form of H-C model using the effective parameters to obtain the effective thermal conductivity of nanofluids, $k_{eff}/k_l = \dfrac{k_a+(n-1)k_l-(n-1)\varphi_a(k_l-k_a)}{k_a+(n-1)k_l+\varphi_a(k_l-k_a)}$, where k_{eff}, k_l and k_a are respectively the thermal conductivities of nanofluids, base liquid and aggregates of nanoparticles, n is the shape factor given by $n=3/\psi$ with ψ the surface area based sphericity (ψ = 1.0 for spheres). For aggregates consisting of spherical nanoparticles, their thermal conductivity

is estimated by using the following Bruggeman model [100], $\frac{k_a}{k_l}=\frac{1}{4}\{(3\varphi_{in}-1)\frac{k_p}{k_l}+(3(1-\varphi_{in})-1)+[((3\varphi_{in}-1)\frac{k_p}{k_l}+(3(1-\varphi_{in})-1))^2+8\frac{k_p}{k_l}]^{\frac{1}{2}}\}$, where k_p is the thermal conductivity of nanoparticles, φ_{in} is the solid volume fraction of aggregates given by $\varphi_{in}=(a_a/a)^{D-3}$. For the rod-like particles, the Nan's model has been shown to give good representation of the experimental results for randomly dispersed nanotubes [45], $k_a/k_l=\frac{3+\varphi_{in}[2\beta_x(1-L_x)+\beta_z(1-L_z)]}{3-\phi_{in}[2\beta_x L_x+\beta_z L_z]}$, where $\beta_x=(k_x-k_l)/[k_l+L_x(k_t-k_l)]$ and $\beta_z=(k_z-k_l)/[k_l+L_z(k_t-k_l)]$ with k_x, k_z and k_t being the thermal conductivities of nanotubes along transverse and longitudinal directions and isotropic thermal conductivity of the nanotube respectively, and L_x and L_z are geometrical factors depending on the aspect ratio of the particles and given by $L_x=0.5r^2/(r^2-1)-0.5r\cosh^{-1}r/(r^2-1)^{3/2}$ and $L_z=1-2L_x$.

The predictions using the method shown in Figure 6 are compared with the experimental data in Figures 7 and 8 for nanofluids containing spherical titania and rod-like titanate particles in both ethylene glycol and water, respectively. In Figure 8, k_x, k_z and k_t are assumed to be the same as k_p for the first order of approximation due to lack of heterogeneous thermal conductivity data of the titanate particles. One can see that the calculated thermal conductivity agrees reasonably well with the experimental measurements.

It should be noted that the effect of interfacial thermal resistance was not accounted in the method proposed in [61]. The incorporation of the interfacial resistance into their method is straightforward, which, in theory, should lead to a decrease in the predicted enhancement of the thermal conductivity for the materials used in their work. In addition, a more complicated method (the three-level homogenization model) can be adopted to extract information of nanoparticle structuring [52].

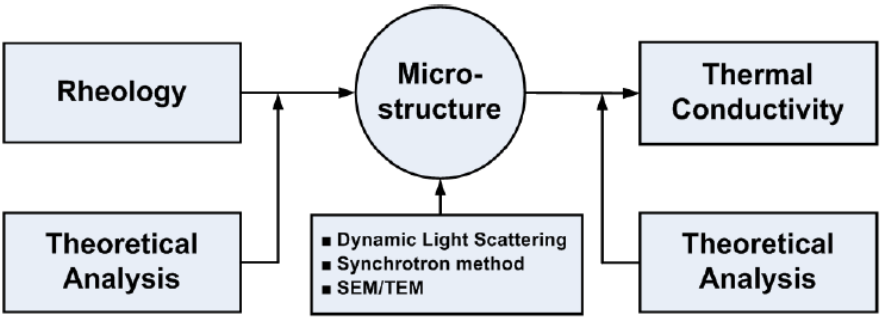

Fig. 6 Methodology for predicting the thermal conductivity of nanofluids based on their rheological behaviour [61]

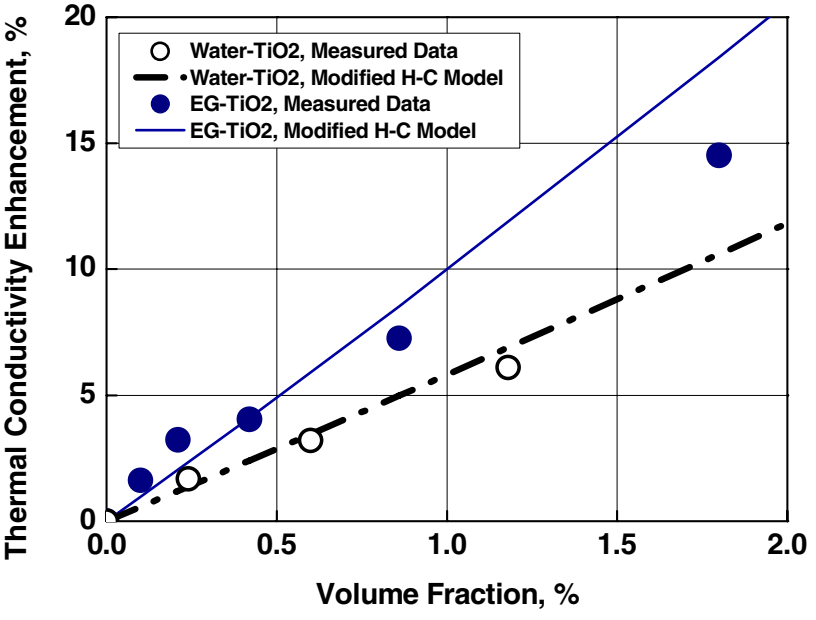

Fig. 7 Prediction of thermal conductivity enhancement based on rheological data: comparison with experimental results for nanofluids containing spherical titania particles

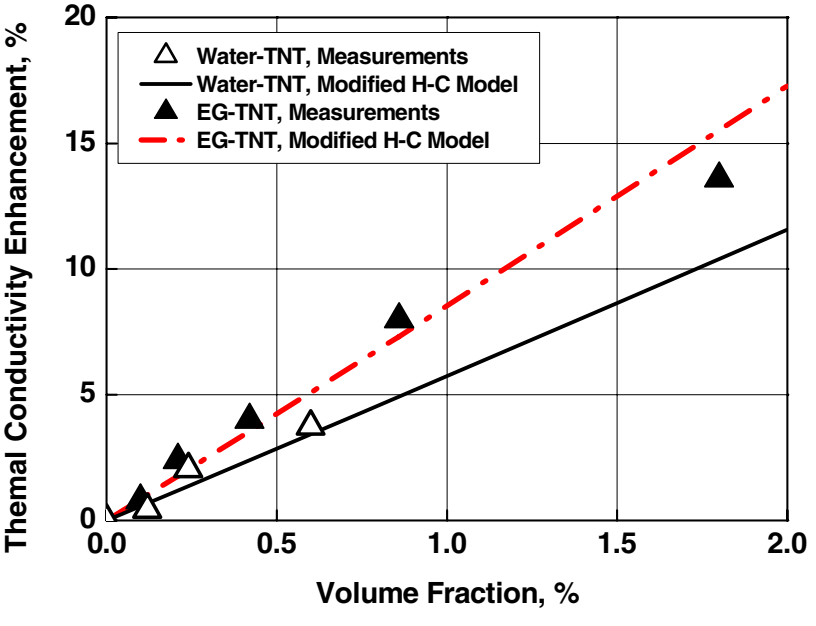

Fig. 8 Prediction of thermal conductivity enhancement based on rheological data: comparison with experimental results for nanofluids containing rod-like titanate particles

3 Convective Heat Transfer of Nanofluids

Convective heat transfer refers to heat transfer between a fluid and a surface due to macroscopic motion of the fluid relative to the surface [101]. Convective heat transfer can be divided into two types, natural convective heat transfer where fluid motion is induced by buoyancy and forced convective heat transfer where fluid is forced through a confined region (internal flows) or across an object (external flows). This section will review the work on both the forced and natural convection of nanofluids.

3.1 Forced Convective Heat Transfer of Nanofluids

The forced convective heat transfer is quantified by the convective heat transfer coefficient, h, defined by Newton's cooling law, $q = h \cdot (T_w - T_f)$, where q is the heat flux in W/m^2, and T_w and T_f are respectively surface and fluid temperatures in K. The heat transfer coefficient has a unit of W/m^2•K. Due to the viscous effect and temperature difference, both hydrodynamic and thermal boundary layers form on the solid surface. A heat balance over a thin layer of fluid on the surface gives $h = k_f / \delta_t$ with k_f the thermal conductivity of the fluid (=k_{eff} for nanofluids) and δ_t the boundary layer thickness. As the boundary layer thickness is affected by the flow and temperature fields of nanofluids, the heat transfer coefficient is obviously not a material property. In the following, experimental results of the forced convective heat transfer of nanofluids are reviewed first, discussion is then on the experimental results with a particular focus on possible mechanisms of the heat transfer enhancement.

3.1.1 Experimental Results of Forced Convective Heat Transfer of Nanofluids

Very limited amount of work has been found in the literature on the forced convective heat transfer of nanofluids. Most of the reported studies show an enhancement of convective heat transfer by using nanofluids [37, 42, 69, 102-107]. A few studies show inconsistencies, i.e. enhancement under certain conditions but little enhancement under other conditions [70, 108-110]. There are also studies that show little or even decrease in the convective heat transfer coefficient when nanoparticles are added to the base liquids [70, 111]. These studies used pipe or channel flows and experiments were mostly done under the constant heat flux conditions. Figures 9 and 10 summarise the experimental data of the convective heat transfer coefficient in the form of Nusselt number as a function of Reynolds number in the laminar and turbulent flow conditions, respectively. The data shown in Figures 9 and 10 are not exhaustive but are meant to represent the majority of the data available in the literature. For turbulent flow regime (Figure 10), the trend that Nusselt number increases with increasing Reynolds number is expected in spite of considerable data scattering. The data in Figure 9 indicates that Nusselt number also increases with increasing Reynolds

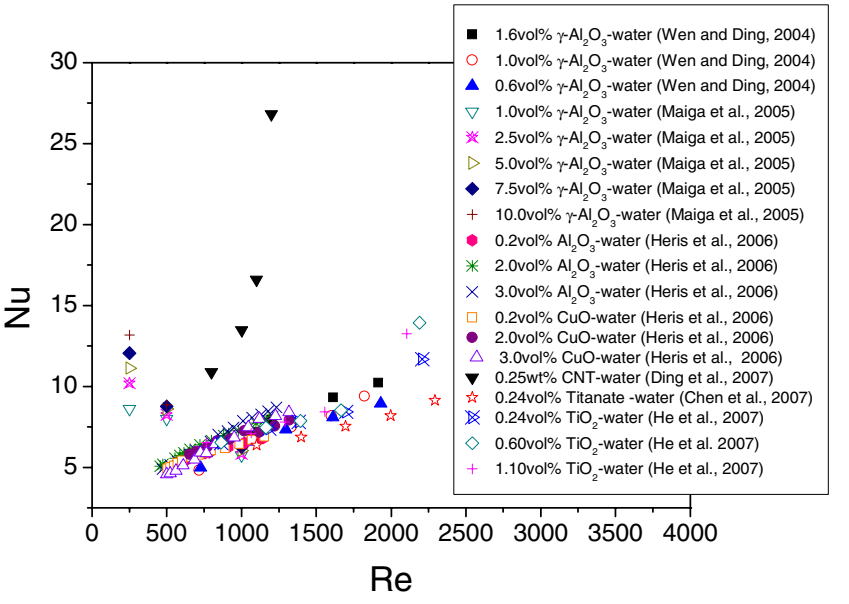

Fig. 9 Nusselt number as a function of Reynolds number: summary of literature data for laminar flows, data from Refs [37, 42, 70, 71, 105, 138]

number for laminar flows under constant heat flux conditions. This causes controversy because, for Newtonian fluids under constant wall heat flux conditions, the Nusselt number in the fully developed flow regime should be a constant of 4.36 and this has indeed been experimentally demonstrated for zirconia and alumina nanofluids [112]. This will be discussed further in Section 3.1.2. In the following, some general observations of the studies reported in the literature are summarized:

- The convective heat transfer coefficient of nanofluids flowing through straight tubes has the highest value at the entrance but it decreases with increasing axial distance and tends to approach a constant value in the fully developed flow region. Given the pipe geometry, the entrance length for nanofluids is longer than that for the base liquids and the increase in the entrance length depends on the properties and behaviour of nanofluids.
- Convective heat transfer coefficient can be enhanced and deteriorated depending on the nanofluids formulations and experimental conditions.
- For cases where heat transfer enhancement is observed, nanofluids containing tubular or rod-like nanoparticles often give a higher enhancement of convective heat transfer coefficient in comparison with spherical or disc-like nanoparticles. Nanofluids made of less viscous liquids (e.g. water) give a higher heat transfer coefficient in comparison to those made of highly viscous liquids (e.g. mineral oil).

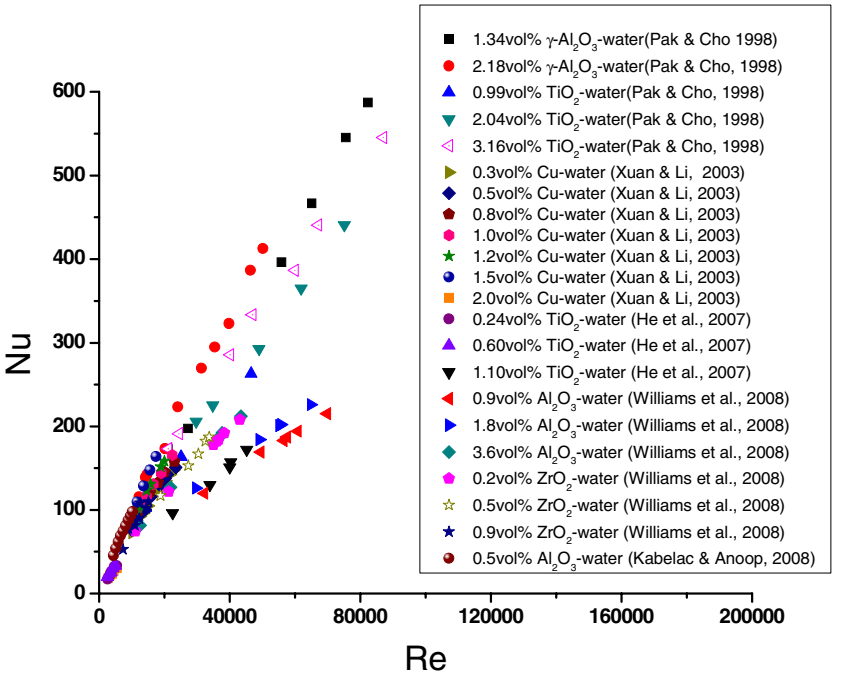

Fig. 10 Nusselt number as a function of Reynolds number: summary of literature data for turbulent flows, data from Refs [25, 42, 69, 108, 139]

- For cases where heat transfer enhancement is observed, the convective heat transfer coefficient generally increases with increasing flowrate or increasing particle concentration, and the enhancement may exceed the extent of the thermal conduction enhancement.
- No clear trend has been found in the effect of particle size on the convective heat transfer coefficient of nanofluids.
- For nanofluids made of particles with large aspect ratios, e.g. carbon nanotubes, there seems to be a relationship between the rheological behaviour and convective heat transfer behaviour.
- Given a nanofluid and pipe geometry, heat transfer enhancement in the turbulent flow regime is less significant than that in the laminar flow regime.

In the following section, attempts are made to explain the experimental observations as summarised in this section.

3.1.2 Interpretations of the Experimental Observations of Convective Heat Transfer of Nanofluids

First, discussion is made on the controversial dependence of Nusselt number on Reynolds number for laminar flows under constant wall heat flux conditions. A

number of reasons could be responsible for the experimentally observed phenomena:

- ***Non-Newtonian behaviour of nanofluids.*** If nanofluids are non-Newtonian, then the analysis that leads to the constant Nusselt number is invalid. As discussed in Section 2, even very dilute nanofluids can be non-Newtonian, particularly for the water based nanofluids.
- ***Entrance region effect.*** Lots of data reported in the literature are not entirely for the fully developed flow regime but rather for a combination of both the entrance and fully developed regimes. As a consequence, caution should be taken when using the data from Figures 9 and 10 (particularly Figure 9 due to longer entrance length for the laminar flow conditions).
- ***Accuracy of measurements.*** Most of the reported data do not include error bars so it is difficult to assess the reliability of the data.

Further work is therefore needed on clarifying the above aspects. In the following, attempts are made to explain the experimental observations if the data shown in Figures 9 & 10 were genuinely correct. They are therefore on a more speculative side. The explanation will be done from both macroscopic and microscopic aspects. Considering a flow with uniform velocity and temperature distributions entering a pipe, the flow has a different temperature from the wall temperature. Due to friction between the fluid and the pipe wall, a hydrodynamic boundary layer will form at the wall region in which the flow velocity increases from zero at the wall to maximum in a radial position depending on the axial position from the entrance. At a certain axial position from the entrance, the thickness of the boundary layer approaches constant and the flow is regarded as fully developed. Similarly, as the temperature of the fluid differs from the pipe wall, a thermal boundary layer is developed, though its thickness and the entrance length can be different from the hydrodynamic boundary layer. Macroscopically, as mentioned previously, the forced convective heat transfer coefficient is given by $h = k_f / \delta_t$. This indicates that either or both of an increase in k_f and a decrease in ∂_t can result in an increase the convective heat transfer coefficient. This explains why the entrance region gives the highest convective heat transfer coefficient (Boundary layer thickness is the thinnest). As nanofluids may have a higher thermal conductivity in comparison with the base liquid, the above expression also partially explains the enhanced convective heat transfer coefficient. However, it cannot provide an adequate explanation to the experimental observations that, in some cases, the convective heat transfer coefficient enhancement is higher than the thermal conduction enhancement, while in other cases, there is no convective heat transfer enhancement despite considerable thermal conduction enhancement. In the following, explanation is made from the microscopic point of view.

Microscopically, nanofluids may be inhomogeneous. There are at least two possible reasons for the inhomogeneity [11, 41]. One is the presence of agglomerates in nanofluids, which can be associated with either sintering during nanoparticle manufacturing or solution chemistry during nanofluids formulation.

The former is often seen in processes involving elevated temperatures e.g. aerosol reactors. The resulting agglomerates are too strong to be broken down to primary nanoparticles even with prolonged high energy processing. The latter is due to attraction between nanoparticles e.g. van der waals attractive force and depletion phenomena [77]. The agglomerates (aggregates) can be controlled by adjusting solution chemistry and applying mechanical energy. The second reason is particle migration due to viscosity and velocity gradients. Experimental evidence of particle migration includes a longer entrance length for nanofluids [37, 113]. There are also plenty of theoretical studies on particle migration; see for example [114-116]. If particles are very small, Brownian motion is strong and the effect of particle migration is negligible. If particles are large, e.g. aggregates of hundreds of nanometres, the contribution of the Brownian motion can be significantly reduced, and a particle depletion region may exist at the wall region, which gives non-uniform distributions of particle concentration, viscosity and thermal conductivity. The direct results of particle migration are lower particle concentration at the wall region and a thinner boundary thickness due to disturbance by the moving particles. This, according to $h = k_f / \delta_t$, could lead to three possible scenarios: (i) h is enhanced if the decrease in δ_t exceeds the decrease in k_f; (ii) h does not change if the decrease in δ_t is equal to the decrease in k_f; and (iii) h is reduced if the decrease in δ_t is lower than the decrease in k_f. The above arguments provide possible (qualitative) explanations to the experimentally observed results.

3.2 Natural Convective Heat Transfer of Nanofluids

Natural convective heat transfer is caused by convection currents induced in a fluid surrounding a body without application of external flow means. The convection currents are set up as a result of the temperature difference between the body and the fluid which causes a change in the density of the fluid in the vicinity of the surface. Very few studies have been found in the literature on natural convection of nanofluids. This is mainly because the fluid mixing intensity in natural convection and hence the heat transfer coefficient is far less than that of forced convection. These studies are briefly reviewed in the following.

The published few studies can be grouped into two categories, numerical modeling and experimental work. Khanafer et al. (2003) studied natural convection of nanofluids by numerical modeling [117]. They found that nanofluids enhanced natural convective heat transfer. The modeling results reported recently by [118], however, showed that both enhancement and deterioration could occur depending on particle concentration, Rayleigh number and geometry of the cavity containing the nanofluids. A similar controversy has been reported in the experimental studies. Enhancement of natural convection was experimentally observed and reported in [119] and [120], and systematic deterioration was seen by Wen and Ding [39-40] and Putra et al. [121], whereas both enhancement and deterioration were reported in [122]. In the following, a theoretical analysis on natural convection of nanofluids between two parallel plates is used to interpret the controversy.

It is well known that natural convective heat transfer can be described well by $Nu = CRa^n$ [123], where C and n are constants with n ranging between 1/4 and 1/3. In this equation, Nu and Ra are the Nusselt and Rayleigh numbers respectively defined as $Nu = hd_g / k_f$ and $Ra = g\beta(\Delta T)d_g^3 /(\nu\alpha)$ with d_g the separation between heating and cooling plates, ν the kinematic viscosity, α the fluid thermal diffusivity, g the gravitational acceleration, β the fluid volume expansion coefficient and ΔT the temperature difference between the heating and cooling plates. Let subscripts nf and f denote, respectively, nanofluid and base liquid, the use of the above definitions gives the ratio of the heat transfer coefficient ratio: $\frac{h_{nf}}{h_f} = (\frac{k_{nf}}{k_f})(\frac{\beta_{nf}}{\beta_f})^n(\frac{\Delta T_{nf}}{\Delta T_f})^n(\frac{\nu_f}{\nu_{nf}})^n(\frac{\alpha_f}{\alpha_{nf}})^n$. Consider $C_{pnf} = [\rho_p C_{pp}\varphi + \rho_f C_{pf}(1-\varphi)]/\rho_{nf}$ and $\alpha = k/(\rho C_p)$, one has $\frac{h_{nf}}{h_f} = (\frac{k_{nf}}{k_f})^{1-n}(\frac{\beta_{nf}}{\beta_f})^n(\frac{\Delta T_{nf}}{\Delta T_f})^n(\frac{\nu_f}{\nu_{nf}})^n[(1-\varphi)+(\frac{\rho_p}{\rho_f})(\frac{C_{pp}}{C_{pf}})\varphi]^n$, where ρ_f and ρ_p are respectively the fluid and particle densities, and C_{pf} and C_{pp} are the base fluid and particle heat capacities, respectively. This indicates that the convective heat transfer coefficient ratio of nanofluid to the base liquid depends on thermal conductivity ratio (k_{nf}/k_f), thermal expansion ratio (β_{nf}/β_f), viscosity ratio (ν_f/ν_{nf}), density ratio (ρ_p/ρ_f), heat capacity ratio (C_{pp}/C_{pf}), particle volume fraction (φ) and temperature difference ratio $(\Delta T_{nf}/\Delta T_f)$. Of these dimensionless numbers, (k_{nf}/k_f) and (ν_f/ν_{nf}) appear to be the most important given the base liquid and nanoparticle properties and they change in an opposite direction when particle volume fraction changes. As a consequence, one would expect both enhancement and deterioration could occur [39-40, 122].

4 Boiling Heat Transfer of Nanofluids

A number of studies have been performed on the boiling heat transfer of nanofluids [38, 68, 124-137]. These studies can be broadly divided into two groups, boiling heat transfer under the nucleate regime and critical heat flux. A brief review on the two aspects is given in the following.

Critical heat flux (CHF) of nanofluids. A number of studies have been carried on the critical heat flux of nanofluids and they are summarised in the following:

- You et al. (2003) boiled aluminum - water nanofluids on a horizontal plate heater under sub-atmospheric pressure conditions and observed can enhancement of 200% in the CHF with nanoparticle volume

concentration of 0.001% [125]. Their study also indicated the use of nanofluids increased bubble size and decreased bubble departure frequency.

- Milanova and Kumar (2005) studied pool boiling of water based silica nanofluids on horizontal heating wires under atmospheric pressure conditions and observed ~300% enhancement for the nanofluids containing 0.2% 20 nm silica [135]. They attributed different ionic strengths and electrolyte concentrations to being responsile for the observed enhancement of CHF.
- Vassallo et al. (2004) also studied pool boiling of water based nanofluids containing silica particles of 10-3000nm diameter on horizontal heating wires under atmospheric pressure conditions [127]. They observed ~200% enhancement in CHF for the nanofluids containing 0.5 vol % 15 nm silica particles. Their results, however, did not show a clear influence of particle size. Vassallo et al. (2004) also observed layers of silica (0.025–0.05 mm) coated on the boiled surface and therefore suggested that the coating cause surface roughness change and hence contribute to the enhancement of CHF [127].
- Bang and Chang (2005) studied boiling of alumina-water nanofluids on a horizontal plate and observed a maximum increase of ~50% in CHF for 1% alumina–water nanofluids [128]. High nanoparticle concentrations were found to give a reduced CHF enhancement.
- Kim et al. (2006) boiled aqueous based titania and alumina nanofluids on thin wires under atmospheric pressure conditions and obtained a maximum CHF enhancement of ~100% with a volume concentration 0.1% for titania nanofluids [130]. They suggested that CHF enhancement be mainly due to formation of a layer of nanoparticles coated on the heating surface.
- Coursey and Kim (2008) studied the boiling of both water and ethanol based alumina nanofluids of different concentrations [136]. Ethanol nanofluids were found to give little enhancement of the CHF while the water based nanofluids gave a modest increase (up to ~37%) in the CHF. They concluded that poorly wetting systems (e.g. water on polished copper) could be enhanced by the addition of nanoparticles, whereas better wetting systems (e.g. ethanol on glass) showed no improvement or even considerable deterioration. Interestingly, they achieved a similar extent of CHF enhancement with the base liquid on an oxidized surface, indicating important roles played by the properties of the boiling surface.
- Lv and Liu (2008) boiled water-CuO nanofluids on a vertical tube and found a small extent of enhancement ranging between ~4 (for ~ 0.013 vol % CuO) and 20% (for ~0.08 vol% CuO) [137].

Figure 11 shows a summary of the literature data for the CHF. One can see that the addition of nanoparticles into the base liquid enhances the CHF in the vast majority of the cases. However, the extent of the enhancement differs significantly. For a similar particle concentration, the enhancement can range from ~0% to ~300%, indicating effects of other factors such as type and properties of

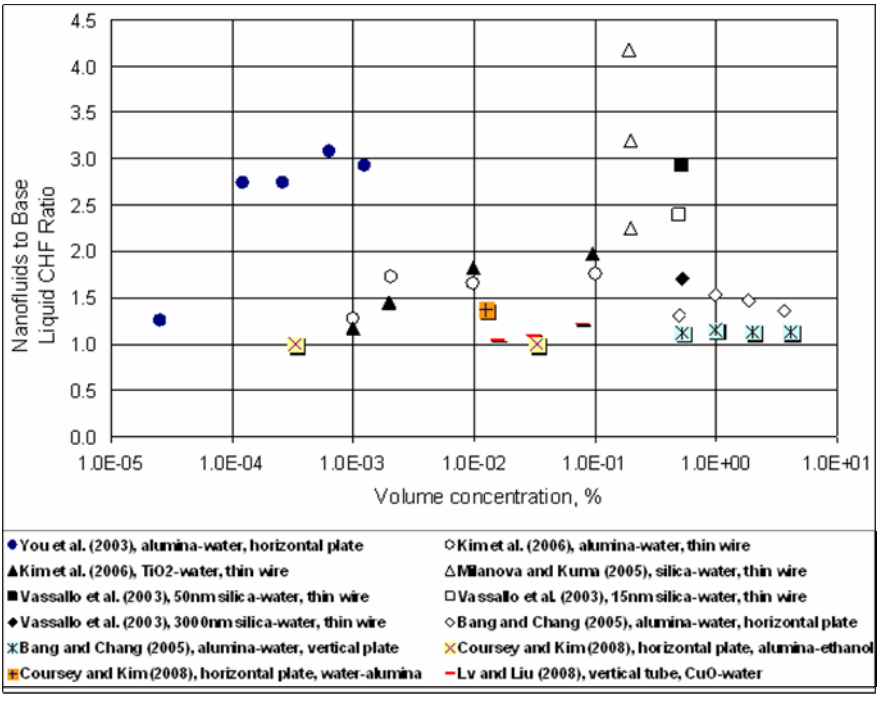

Fig. 11 Critical heat flux data reported in the literature for pool boiling, data from Refs [125, 127, 128, 130, 135, 136, 137]

nanoparticles and the boiling surfaces, boiling conditions and geometries of the boiling surfaces. Wen (2008) proposed that the disjoining pressure caused by nanoparticle structuring in the confined wedge of bubbles could be a reason [134], while others concluded that surface modification due to the presence of nanoparticles play a major role [132, 136]. Further work is clearly needed to elucidate the mechanisms through theoretical analyses, mathematical modeling and more controlled experiments.

Boiling heat transfer of nanofluids in nucleate regime. Lots of studies have been carried out on the pool boiling in the nucleate regime and these studies show a disagreement in the heat transfer performance. Wen and Ding (2005) [38] and Wen et al. (2006) [129] observed enhancement of boiling heat transfer for both titania and alumina nanofluids. This agrees with the observations reported in [125] and [126], but disagrees with those in [68, 123, 128, 131] where deterioration of boiling heat transfer in the nucleate regime is reported. The exact reason requires further investigation but the following are possible reasons according to the current understanding:

a) As thermal conductivity and viscosity affect the heat transfer behaviour of nanofluids in opposite ways, a combination of thermal conductivity

enhancement and increase in the viscosity can give either enhancement or deterioration of the heat transfer coefficient. However, there is little information in the published studies for making a conclusive assessment.

b) Stability of nanofluids and the presence of dispersant / surfactant affect the behaviour of nanofluids, which are often not provided in the published studies. For example, settling of nanoparticles in nanofluids with poor stability can change the properties of the boiling surface, and surfactant / dispersant may fail at elevated temperatures. This is supported by the recent work reported in [133].

c) Boiling heat transfer consists of a number of sub-processes in parallel and/or series, including unsteady-state heat conduction, growth and departure of bubbles, and convection due to bubble motion and liquid re-filling. These sub-processes are affected by parameters such as heater geometry, properties of the boiling surface, orientation of the heater, liquid sub-cooling, system pressure, and the mode in which the system is operated. Among these, the boiling surface properties are among the key factors that influence the boiling heat transfer. The surface properties include surface finish (roughness), surface wettability, and surface contamination as they all influence the number and distribution of active nucleation sites for bubbles and their subsequent growth. In the published studies, however, surface roughness is the most often used parameter, and interpretation of the effect of surface roughness on the boiling heat transfer has been based on the relative size of the suspended particles to the surface roughness. For example, Bang and Chang (2005) used a boiling surface of nanometre scale roughness hence sedimentation of particles was regarded to effectively increase the roughness of the surface [128], whereas a commercial cartridge heater with a micron scale surface roughness was employed in [68] onto which sedimentation of nanoparticles was thought to decrease the effective surface roughness.

d) Different temperature measurement methods may lead to the different experimental results obtained by different investigators. For example, all thermocouples were welded on the outer surface of the cartridge heater in the work reported in [68]. This may influence surface characteristics of the boiling surface as bubbles have a tendency to nucleate on the welded positions and the measured temperature may not be representative of the boiling surface. Vassalao et al. (2004) used fine resistance wires for temperature measurements [127]. Large uncertainties are expected for this sort of method as temperature is converted from the measured resistance of the heating wire against the standard temperature-resistance curve. Indeed, for boiling with pure water, more than 10^{o}C deviance of superheat was observed under a fixed heat flux condition in different runs; see Figure 1 of [127].

5 Concluding Remarks

This paper gives an updated review on nanofluids with a specific focus on heat transfer applications. It covers transport properties of nanofluids in particular

thermal conductivity and shear viscosity, and heat transfer of nanofluids under convective and boiling conditions. No new physics appears to be behind the experimentally observed thermal conductivity enhancement as the vast majority of the experimental data fall within the range of predictions of modified effective medium based theories taking into account nanoparticle structuring. There seems to be no new physics either in terms of the experimentally observed increase in the shear viscosity as the data can be quantitatively interpreted by the conventional rheology and colloidal theories. No sufficient quantitative information, however, is available in the literature that can be used to infer the dominant mechanisms for heat transfer enhancement / deterioration under convective and boiling heat transfer conditions, where many controversies remain and require further research.

6 Symbols

A	constant coefficient
a	radius of particles
a_a	effective radius of aggregates
b	rod diameter, radius of elliptical particles
b_a	effective rod diameter
B	constant coefficient
$B_{2,x}$	depolarization factor
c	number concentration of particles, radius of elliptical particles
c^r	critical particle concentration
C	constant coefficient
C_p	heat capacity
C_{Pnf}	heat capacity of nanofluid
C_{PP}	heat capacity of particles
d_g	separation between heating and cooling plates
d_l	liquid molecule diameter
d_p	particle diameter
D	fractal index
f	parameter used in the equation of Davis (1986)
g	gravitational acceleration
h	heat transfer coefficient
h_{nf}	heat transfer coefficient of nanofluids
h_f	heat transfer coefficient of base fluid
k	thermal conductivity
k_2	thermal conductivity of nanolayer
k_a	effective thermal conductivity of aggregates
k_B	Boltzmann constant
k_{cl}	thermal conductivity of cluster$_s$
k_{cx}	effective dielectric constant
k_{nf}	thermal conductivity of nanofluids

k_{eff} effective thermal conductivity
k_{f} fluid thermal conductivity
k_H Huggins's coefficient
k_l liquid thermal conductivity
k_p particle thermal conductivity
k_{pe} effective thermal conductivity of spherical nanoparticles with a nanolayer
k_{pj} thermal conductivity of non-spherical particles including a nanolayer in *j* direction
k_x thermal conductivity in x direction
k_z thermal conductivity in z direction
k_t isotropic thermal conductivity
L rod length
L_b effective rod length
L_i *i =x, z,* geometrical factors
m power law index
n power law index and shape factor of particles
$n(r)$ radial distribution function
Nu Nusselt number
Pe Péclet number
Pe_{c} characteristic Peclet number
Pr Prandtl number
q heat flux
Q_i *i=1-3*, parameters used in Brenner and Condiff equation
r aspect ratio
r_a effective aspect ratio
r_f radius of liquid molecules
r_c radius of clusters
R_a Rayleigh number
Re Reynolds number
t thickness of nanolayer
T absolute temperature
T_w wall temperature
T_f fluid temperature

Greek

α thermal diffusivity, volume ratio of core part of a particle to the composite particle
β thermal expansion coefficient, ratio of nanolayer thickness to particle radius, volume fraction of fluid moving with the particle
β_f thermal expansion coefficient of base fluid
β_{nf} thermal expansion coefficient of nanofluids
β_x parameter in Nan's model
β_z parameter in Nan's model
v kinematic viscosity
v_f kinematic viscosity of base fluid
v_{nf} kinematic viscosity of nanofluids

ρ density
ρ_f fluid density
ρ_{nf} nanofluid density
ρ_p particle density
φ particle volume fraction
φ_a effective volume concentration of aggregated suspensions
φ_m maximum particle packing fraction
φ_{eff} effective particle volume fraction including nanolayer
φ^r critical particle volume fraction
φ_{in} solids volume fraction of aggregates
$\dot{\gamma}$ shear rate
σ shear stress
σ_c characteristic shear stress
σ_r reduced shear stress
δ_t thermal boundary layer thickness
η_0 viscosity of base liquid
η viscosity of suspension
$[\eta]$ intrinsic viscosity
ψ sphericity
μ fluid viscosity

References

1. Choi, S.U.S.: Enhancing thermal conductivity of fluids with nanoparticles. In: Siginer, D.A., Wang, H.P. (eds.) Developments Applications of Non-Newtonian Flows. FED, MD, vol. 231, 66, pp. 99–105. ASME, New York (1995)
2. Masuda, H., Ebata, A., Teramae, K., Hishiunma, N.: Alteration of thermal conductivity and viscosity of liquid by dispersed by ultra-fine particles(dispersion of γ-Al2O3 SiO2 and TiO2 ultra-fine particles). Netsu Bussei (Japan) 4, 227–233 (1993)
3. Choi, S.U.S., Zhang, Z.G., Yu, W., Lockwood, F.E., Grulke, E.A.: Anomalous thermal conductivity enhancement in nano-tube suspensions. Applied Physics Letters 79, 2252–2254 (2001)
4. Krishnamurthy, S., Lhattacharya, P., Phelan, P.E., Prasher, R.S.: Enhanced mass transport in nanofluids. Nano Letter 6(3), 419–423 (2006)
5. Olle, B., Bucak, S., Holmes, T.C., Bromberg, L., Hatton, T.A., Wang, D.I.C.: Enhancement of oxygen mass trnafser using functionalized magnetic nanoparticles. Ind. Eng. Chem. Res. 45, 4355–4363 (2006)
6. Wasan, D.T., Nikolov, A.D.: Spreading of nanofluids on solids. Nature 423, 156–159 (2003)
7. Zhang, L.L., Jiang, Y., Ding, Y.L., Povey, M., York, D.W.: Investigation into the antibacterial behaviour of suspensions of ZnO nanoparticles (ZnO nanofluids). Journal of Nanoparticle Research 9, 479–489 (2007)

8. Keblinski, P., Eastman, J.A., Cahill, D.G.: Nanofluids for thermal transport. Materials Today June Issue, 36–44 (2005)
9. Das, S.K., Choi, S.U.S., Patel, H.E.: Heat transfer in nanofluids-a review. Heat Transfer Engineering 27(10), 2–19 (2006)
10. Wang, X.Q., Mujumdar, A.S.: Heat transfer characteristics of nanofluids: a review. International Journal of Thermal Sciences 46, 1–19 (2007)
11. Ding, Y.L., Chen, H., Wang, L., Yang, C.Y., He, Y., Yang, W., Lee, W.P., Zhang, L.L., Huo, R.: Heat transfer intensification using nanofluids. KONA Powder and Particle 25, 23–38 (2007)
12. Trisaksri, V., Wongwises, S.: Critical review of heat transfer characteristics of nanofluids. Renewable & Sustainanble Energy Reviews 11, 512–523 (2007)
13. Murshed, S.M.S., Leong, K.C., Yang, C.: Thermophysical and electrokinetic properties of nanofluids – A critical review. Applied Thermal Engineering 28, 2109–2125 (2008)
14. Yu, W., France, D.W., Routbort, J.L., Choi, S.U.S.: Review and comparison of nanofluids thermal conductivity and heat transfer enhancements. Heat Transfer Engineering 29, 432–460 (2008)
15. Bird, R.B., Stewart, W.E., Lightfoot, E.N.: Transport Phenomena, 2nd edn. Wiley & Sons Inc., Chichester (2002)
16. Wang, X., Xu, X., Choi, S.U.S.: Thermal conductivity of nanoparticle-fluid mixture. Journal of Thermophysics and Heat Transfer 13, 474–480 (1999)
17. Wang, B.X., Zhou, L.P., Peng, X.F.: A fractal model for predicting the effective thermal conductivity of liquid with suspension of nanoparticles. International Journal of Heat and Mass Transfer 46, 2665–2672 (2003)
18. Nagasaka, Y., Nagashima, A.: Absolute measurement of the thermal conductivity of electrically conducing liquids by the transient hot-wire method. Journal of Physics E: Scientific Instruments 14, 1435–1440 (1981)
19. Czarnetzki, W., Roetzel, W.: Temperature oscillation techniques for simultaneous measurement of thermal-diffusivity and conductivity. International Journal of Thermophysics 16, 413–422 (1995)
20. Cahill, D.G.: Thermal conductivity measurement from 30 to 750K: the 3ω method. Review of Scientific Instruments 61, 802–808 (1990)
21. Yang, B., Han, Z.H.: Temperature-dependent thermal conductivity of nanorod-based nanofluids. Applied Physics Letters 89, 083111 (2006)
22. Wang, Z.L., Tang, D.W., Liu, S., Zheng, X.H., Araki, N.: Thermal conductivity and thermal diffusivity measurements of nanofluids by 3ω method and mechanism analysis of heat transport. International Journal of Thermophysics 28, 1255–1268 (2007)
23. Oh, D.W., Jain, A., Eaton, J.K., Goodson, K.E., Lee, J.S.: Thermal conductivity measurement and sedimentation detection of aluminum oxide nanofluids by using the 3ω method. International Journal of Heat and Fluid Flow 29, 1456–1461 (2008)
24. Louge, M., Chen, X.: Heat transfer enhancement in suspensions of agitated solids. Part II: Thermophoretic transport of nanoparticles in the diffusion limit. International Journal of Heat and Mass Transfer 51, 5130–5243 (2008)
25. Kabelac, K., Kuhnke, J.F.: Heat transfer mechanisms in nanofluids – experimental and theory. In: de Vahl Davis, G., Leonardi, E. (eds.) Proceedings of 13th International Heat Transfer Conference, Sydney, Australia, August 13-18, pp. 110–111 (2006)

26. Lee, S., Choi, S., Li, S., Eastman, J.: Measuring thermal conductivity of fluids containing oxide nanoparticles. Journal of Heat Transfer 121, 280–289 (1999)
27. Eastman, J.A., Choi, S.U.S., Li, S., Yu, W., Thompson, L.J.: Anomalously increased effective thermal conductivities of ethylene glycol-based nanofluids containing copper nanoparticles. Applied Physical Letter 78, 718–720 (2001)
28. Xie, H.Q., Wang, J., Xi, T., Liu, Y., Ai, F.: Thermal conductivity enhancement of suspensions containing nanosized alumina particles. Journal of Applied Physics 91, 4568–4572 (2002)
29. Xie, H.Q., Wang, J., Xi, T., Liu, Y.: Thermal conductivity of suspensions containing nanosized SiC particles. International Journal of Thermophysics 23, 571–580 (2002)
30. Biercuk, M.J.: Carbon nanotube composites for thermal management. Applied Physics Letters 80, 2767–2769 (2002)
31. Das, S.K., Putra, N., Thiesen, P., Roetzel, W.: Temperature dependence of thermal conductivity enhancement for nanofluids. Journal of Heat Transfer 125, 567–574 (2003)
32. Patel, H.E., Das, S.K., Sundararajan, T., Nair, A.S., George, B., Pradeepa, T.: Thermal conductivities of naked and monolayer protected metal nanoparticle based nanofluids: Manifestation of anomalous enhancement and chemical effects. Applied Physical Letters 83, 2931–2933 (2003)
33. Kumar, D.H., Patel, H.E., Kumar, V.R.R., Sundararajan, T., Pradeep, T., Das, S.K.: Model for heat conduction in nanofluids. Physical Review Letter 93, 144301 (2004)
34. Assael, M.J., Chen, C.F., Metaxa, I., Wakeham, W.A.: Thermal conductivity of suspensions of carbon nanotubes in water. International Journal of Thermophysics 25, 971–985 (2004)
35. Zhang, X., Gu, H., Fujii: Effective thermal conductivity and thermal diffusivity of nanofluids containing spherical and cylindrical nanoparticles. Experimental Thermal and Fluid Science 31, 593–599 (2007)
36. Wen, D.S., Ding, Y.L.: Effective thermal conductivity of aqueous suspensions of carbon nanotubes (Nanofluids). Journal of Thermophysics and Heat Transfer 18(4), 481–485 (2004)
37. Wen, D.S., Ding, Y.L.: Experiment investigation into convective heat transfer of nanofluids at the entrance region under laminar flow conditions. Int. Journal of Heat and Mass Transfer 47, 5181–5188 (2004)
38. Wen, D.S., Ding, Y.L.: Experimental investigation into the pool boiling heat transfer of aqueous based γ -Alumina nanofluids. Journal of Nanoparticle Research 7, 265–274 (2005)
39. Wen, D.S., Ding, Y.L.: Formulation of nanofluids for natural convective heat transfer applications. International Journal of Heat and Fluid Flow 26, 855–864 (2005)
40. Wen, D.S., Ding, Y.L.: Natural convective heat transfer of suspensions of TiO2 nanoparticles (nanofluids). Transactions of IEEE on Nanotechnology 5, 220–227 (2006)
41. Ding, Y.L., Alias, H., Wen, D.S., Williams, R.A.: Heat transfer of aqueous suspensions of carbon nanotubes (CNT nanofluids). International Journal of Heat and Mass Transfer 49, 240–250 (2006)
42. He, Y.R., Jin, Y., Chen, H.S., Ding, Y.L., Cang, D.Q., Lu, H.L.: Heat transfer and flow behaviour of aqueous suspensions of TiO_2 nanoparticles (nanofluids) flowing upward through a vertical pipe. International Journal of Heat and Mass Transfer 50, 2272–2281 (2007)

43. Kim, P., Shi, L., Majumdar, A., McEuen, P.L.: Thermal transport measurements of individual multiwalled nanotubes. Physical Review Letters 87, 215502 (2001)
44. Berber, S., Kwon, Y.K., Tomanek, D.: Unusually high thermal conductivity of carbon nanotubes. Physical Review Letter 84(20), 4613–4616 (2000)
45. Nan, C.W., Shi, Z., Lin, Y.: A simple model for thermal conductivity of carbon nanotube-based composites. Chemical Physics Letters 375, 666–669 (2003)
46. Koo, J., Kleinstreuer, C.: A new thermal conductivity model for nanofluids. Journal of Nanoparticle Research 6, 577–588 (2004)
47. Gao, L., Zhou, X., Ding, Y.L.: Effective thermal and electrical conductivity of carbon nanotube composites. Chemical Physics Letters 434, 297–300 (2007)
48. Keblinski, P., Prasher, R., Eapen, J.: Thermal conductance of nanofluids: is the controversy over? Journal of Nanoparticle Research 10, 1089–1097 (2008)
49. Keblinski, P., Phillpot, S.R., Choi, S.U.S., Eastman, J.A.: Mechanisms of heat flow in suspensions of nano-sized particles (nanofluids). International Journal of Heat and Mass Transfer 45, 855–863 (2002)
50. Prasher, R., Bhattacharya, P., Phelan, P.E.: Brownian-Motion-Based Convective-Conductive Model for the effective thermal conductivity of nanofluids. Journal of Heat Transfer 128, 588–595 (2006)
51. Yu, W., Choi, S.U.S.: The role of interfacial layers in the enhanced thermal conductivity of nanofluids: a renovated Maxwell model. Journal of Nanoparticle Research 5, 167–171 (2003)
52. Prasher, R., Phelan, P.E., Bhattacharya, P.: Effect of aggregation kinetics on thermal conductivity of nanoscale colloidal solutions (nanofluids). Nano Letters 6(7), 1529–1534 (2006)
53. Chen, G.: Nonlocal and nonequilibrium heat conduction in the vicinity of nanoparticles. ASME Journal of Heat Transfer 118, 539–545 (1996)
54. Evans, W., Fish, J., Keblinski, P.: Role of Brownian motion hydrodynamcis on nanofluids thermal conductivity. Applied Physical Letters 88, 093116 (2006)
55. Shenogin, S., Bodapati, A., Xue, L., Ozisik, R., Keblinski, P.: Effect of chemical functionalization on thermal transport of carbon nanotube composites. Applied Physics Letters 85, 2229–2231 (2004)
56. Shenogin, S., Xue, L.P., Ozisik, R., Keblinski, P., Cahill, D.G.: Role of thermal boundary resistance on the heat flow in carbon nanotube composites. Journal of Applied Physics 95, 8136–8144 (2004)
57. Prasher, R., Bhattacharya, P., Phelan, P.E.: Thermal conductivity of nanoscale colloidal solutions (nanofluids). Physical Review Letters 94, 025901 (2005)
58. Putnam, P.A., Cahill, D.G., Braun, P.V., Ge, Z., Shimmin, R.G.: Thermal conductivity of nanoparticle suspensions. Journal of Applied Physics 99, 084308 (2006)
59. Hong, K.S., Hong, T.K., Yang, H.S.: Thermal conductivity of Fe nanofluids depending on the cluster size of nanoparticles. Applied Physics Letter 88, 031901 (2006)
60. Chen, H.S., Ding, Y.L., He, Y.R., Tan, C.Q.: Rheological behaviour of ethylene glycol based titania naofluids. Chemical Physics Letters 444, 333–337 (2007)
61. Chen, H.S., Witharana, S., Jin, Y., Kim, C., Ding, Y.L.: Predicting the thermal conductivity of liquid suspensions of nanoparticles (nanofluids) based on rheology. Particuology 7, 151–157 (2009)

62. Chen, H.S., Ding, Y.L., Lakpin, A.A., Fan, X.L.: Rheological behaviour of ethylene glycol - titanate nanotube nanofluids. Journal of Nanoparticle Research (available online) (in press, 2009)
63. Kwak, K., Kim, C.: Viscosity and thermal conductivity of copper oxide nanofluid dispersed in ethylene glycol. Korea-Australia Rheology Journal 17, 35–40 (2005)
64. Prasher, R., Song, D., Wang, J.: Measurements of nanofluid viscosity and its implications for thermal applications. Applied Physics Letter 89, 133108 (2006)
65. Chen, H.S., Ding, Y.L., He, Y.R., Tan, C.Q.: Rheological behaviour of nanofluids. New Journal of Physics 9, 367, 1–25 (2007)
66. Namburu, P.K., Kulkarni, D.P., Misra, D., Das, D.K.: Viscosity of copper oxide nanoparticles dispersed in ethylene glycol and water mixture. Experimental Thermal and Fluid Science 32, 397–402 (2007)
67. Nguyen, C.T., Desgranges, F., Galanis, N., Roy, G., Maré, T., Boucher, S., Angue Mintsa, H.: Viscosity data for Al_2O_3-water nanofluids - hysteresis: is heat transfer enhancement using nanofluids reliable? International Journal of Thermal Sciences 47, 103–111 (2008)
68. Das, S.K., Putra, N., Roetzel, W.: Pool boiling characteristics of nano–fluids. International Journal of Heat and Mass Transfer 46, 851–862 (2003)
69. Xuan, Y.M., Li, Q.: Investigation on convective heat transfer and flow features of nanofluids. Journal of Heat transfer 125, 151–155 (2003)
70. Ding, Y.L., Chen, H.S., He, Y.R., Lapkin, A.A., Yeganeh, M., Siller, L., Butenko, Y.: Forced convective heat transfer of nanofluids. Advanced Powder Technology 18, 813–824 (2007)
71. Chen, H.S., Yang, W., He, Y.R., Ding, Y.L., Lapkin, A.A., Bavykin, D.V., Tan, C.Q.: Heat transfer and flow behaviour of aqueous suspensions of titanate nanotubes under the laminar flow conditions. Powder Technology 183(1), 63–72 (2008)
72. Egres, R.G., Wagner, N.J.: The rheology and microstructure of acicular precipitated calcium carbonate colloidal suspensions through the shear thickening transition. Journal of Rheology 49, 719–746 (2005)
73. Einstein, A.: Eine neue Bestimmung der Molekul-dimension (A new determination of the molecular dimensions). Annalen der Physik 19(2), 289–306 (1906)
74. Einstein, A.: Berichtigung zu meiner Arbeit: Eine neue Bestimmung der Molekul-dimension (Correction of my work: A new determination of the molecular dimensions). Annalen der Physik 34(3), 591–592 (1911)
75. Batchelor, G.K.: Effect of brownian-motion on bulk stress in a suspension of spherical-particles. Journal of Fluid Mechanics 83(1), 97–117 (1977)
76. Brenner, H., Condiff, D.W.: Transport mechanics in systems of orietable particles, Part IV. Convective Transprort. Journal of Colloid and Interface Science 47(1), 199–264 (1974)
77. Russel, W.B., Saville, D.A., Scholwater, W.R.: Colloidal Dispersions. Cambridge University Press, Cambridge (1991)
78. Chow, T.S.: Viscosities of concentrated dispersions. Physical Review E 48(3), 1977–1983 (1993)
79. Petrie, C.J.S.: The rheology of the fibre suspensions. Journal of Non-Newtonian Fluid Mechnanics 87, 369–402 (1999)
80. Goodwin, J.W., Hughes, R.W.: Rheology for Chemists-An introduction. The Royal Society of Chemistry (2000)
81. Goodwin, J.W.: Colloids and interfaces with surfactants and polymers-An introduction. John Wiley & Sons, Chichester (2003)

82. Larson, R.G.: The rheology of dilute solutions of flexible polymers: progress and problems. Journal of Rheology 49(1), 1–70 (2005)
83. Abdulagatov, I.M., Azizov, N.D.: Experimental study of the effect of temperature, pressure and concentration on the viscosity of aqueous NaBr solutions. Journal of Solution Chemistry 35(5), 705–738 (2006)
84. Krieger, I.M., Dougherty, T.J.: A mechanism for non-newtonian flow in suspensions of rigid spheres. Transactions of the Society of Rheology 3, 137–152 (1959)
85. Cross, M.M.: Rheology of non-Newtonian fluids - a new flow equation for pseudoplastic systems. Journal of Colloid Science 20(5), 417–437 (1965)
86. Xuan, Y., Li, Q., Hu, W.: Aggregation structure and thermal conductivity of nanofluids. AIChE Journal 49, 1038–1043 (2003)
87. Doi, M., Edwards, S.F.: Dynamics of rod-like macromolecules in concentrated solution, Part 1. Journal of Colloid Science 74, 560–570 (1978)
88. Doi, M., Edwards, S.F.: Dynamics of rod-like macromolecules in concentrated solution, Part 2. Journal of Colloid Science 74, 918–932 (1978)
89. Doi, M., Edwards, S.F.: Dynamics of concentrated polymer systems, Part 1: Brownian motion in the equilibrium state. Journal of Colloid Science 74, 1789–1801 (1978)
90. Doi, M., Edwards, S.F.: Dynamics of concentrated polymer systems, Part 2: Molecular motion under flow. Journal of Colloid Science 74, 1802–1817 (1978d)
91. Doi, M., Edwards, S.F.: Dynamics of concentrated polymer systems, Part 3: The constitutive Equation. Journal of Colloid Science 74, 1818–1832 (1978)
92. Mohraz, A., Moler, D.B., Ziff, R.M., Solomon, M.J.: Effect of monomer geometry on the fractal structure of colloidal rod aggregates. Physical Review Letters 92, 155503 (2004)
93. Lee, D., Kim, J., Kim, B.: A new parameter to control heat transport in nanofluids: surface charge state of the particle in suspension. Journal of Physical Chemistry B 110, 4323–4328 (2006)
94. Mary, B., Dubois, C., Carreau, P.J., Brousseau, P.: Rheological properties of suspensions of polyethylene-coated aluminum nanoparticles. Rheology Acta 45, 561–573 (2006)
95. Sonntag, R.C., Russel, W.B.: Structure and Breakup of Flocs subjected to Fluid Stresses: I. Shear experiments. Journal of Colloid and Interface Science 113(2), 399–413 (1986)
96. Sonntag, R.C., Russel, W.B.: Structure and Breakup of Flocs subjected to Fluid Stresses: II. Theory. Journal of Colloid and Interface Science 115(2), 378–389 (1987)
97. Sonntag, R.C., Russel, W.B.: Structure and Breakup of Flocs subjected to Fluid Stresses: III. Converging flow. Journal of Colloid and Interface Science 115(2), 390–395 (1987)
98. Sonntag, R.C., Russel, W.B.: Elastic properties of flocculated networks. Journal of Colloid and Interface Science 116(2), 485–489 (1987)
99. Mills, P.D.A., Goodwin, J.W., Grover, B.W.: Shear field modification of strongly flocculated suspensions-aggregate morphology. Colliod & Polymer Science 269, 949–963 (1991)
100. Bruggeman, D.A.G.: Calculation of various physics constants in heterogenous substances I Dielectricity constants and conductivity of mixed bodies from isotropic substances. Annalen der Physik 24(7), 636–664 (1935)
101. Rohsenow, W.M., Hartnett, J.P.: Handbook of Heat transfer. McGraw Hill, New York (1973)

102. Xuan, Y.M., Roetzel, W.: Conceptions for heat transfer correlation of nanofluids. International Journal of Heat and Mass Transfer 43, 3701–3707 (2000)
103. Li, Q., Xuan, Y.M.: Convective heat transfer and flow characteristics of Cu-water nanofluids. Science in China, Series E 45, 408–416 (2002)
104. Jang, S.P., Choi, S.U.S.: Cooling performance of a microchannel heat sink with nanofluids. Applied Thermal Engineering 26, 2457–2463 (2006)
105. Heris, S.Z., Esfahany, M.N., Etemad, S.G.: Experimental investigation of convective heat transfer of Al_2O_3/water nanofluid in a circular tube. International Journal of Heat and Fluid Flow 28, 203–210 (2007)
106. Hwang, K.S., Jang, S.P., Choi, S.U.S.: Flow and convective heat transfer characteristics of water-based Al_2O_3 nanofluids in fully developed laminar flow regime. International Journal of Heat and Mass Transfer 52, 193–199 (2009)
107. Jung, J.Y., Oh, H.K., Kwak, H.Y.: Forced convective heat transfer of nanofluids in microchannels. International Journal of Heat and Mass Transfer 52, 466–472 (2009)
108. Pak, B.C., Cho, Y.I.: Hydrodynamic and heat transfer study of dispersed fluids with submicron metallic oxide particles. Experimental Heat Transfer 11, 150–170 (1998)
109. Chein, R., Chuang, J.: Experimental microchannel heat sink performance studies using nanofluids. International Journal of Thermal Sciences 46, 57–66 (2007)
110. Lee, J., Mudawar, I.: Assessment of the effectiveness of nanofluids for single phase and two-phase heat transfer in micro-channels. International Journal of Heat and Mass Transfer 50, 452–463 (2007)
111. Yang, Y., Zhong, Z.G., Grulke, E.A., Anderson, W.B., Wu, G.: Heat transfer properties of nanoparticle-in-fluid dispersion (nanofluids) in laminar flow. International Journal of Heat and Mass Transfer 48, 1107–1116 (2005)
112. Rea, U., McKrell, T., Hu, L.W., Buongiorno, J.: Laminar convective heat transfer and viscous pressure loss of alumina–water and zirconia–water nanofluids. International Journal of Heat and Mass Transfer 52, 2043–2048 (2009)
113. Merhi, D., Lemaire, E., Bossis, G., Moukalled, F.: Particle migration in a concentrated suspension flowing between rotating parallel plates: Investigation of diffusion flux coefficients. Journal of Rheology 49, 1429–1448 (2005)
114. Phillips, R.J., Armstrong, R.C., Brown, R.A., Graham, A.L., Abbott, J.R.: A constitutive equation for concentrated suspensions that accounts for shear-induced particle migration. Physics of Fluids 4, 30–40 (1992)
115. Frank, M., Anderson, D., Weeks, E.R., Morris, J.F.: Particle migration in pressure-driven flow of a Brownian suspension. Journal of Fluid Mechanics 493, 363–378 (2003)
116. Wen, D.S., Ding, Y.L.: Effect on heat transfer of particle migration in suspensions of nanoparticles flowing through minichannels. Microfluidics and Nanofluidics 1&2, 183–189 (2005)
117. Khanafer, K., Vafai, K., Lightstone, M.: Buoyancy-driven heat transfer enhancement in a two-dimensional enclosure utilizing nanofluids. International Journal of Heat and Mass Transfer 46, 3639–3653 (2003)
118. Abu-Nada, E., Masoud, Z., Hijazi, A.: Natural convection heat transfer enhancement in horizontal concentric annuli using nanofluids. International Communications in Heat and Mass Transfer 35, 657–665 (2008)
119. Nanna, A.G.A., Fistrovich, T., Malinski, K., Choi, S.U.S.: Thermal transport phenomena in buoyancy-driven nanofluids. In: Proceedings of 2005 ASME International Mechanical Engineering Congress and RD&D Exposition, Anaheim, California, USA, November 15-17, 2004 (2005)

120. Nnanna, A.G.A., Routhu, M.: Transport phenomena in buoyancy-driven nanofluids – Part II. In: Proceedings of 2005 ASME Summer Heat Transfer Conference, San Francisco, California, USA, July 17-22 (2005)
121. Putra, N., Roetzel, W., Das, S.K.: Natural convection of nano-fluids. Heat and Mass Transfer 39, 775–784 (2003)
122. Nnanna, A.G.A.: Experimental model of temperature-driven nanofluid. Journal of Heat Transfer 129, 697–704 (2007)
123. Inaba, H.: Experimental study of natural convection in an inclined air layer. International Journal of Heat and Mass Transfer 27, 1127–1139 (1984)
124. Tsai, C.Y., Chien, H.T., Ding, P.P., Chan, B., Luh, T.Y., Chen, P.H.: Effect of structural character of gold nanoparticles in nanofluid on heat pipe thermal performance. Materials Letters 58, 1461–1465 (2003)
125. You, S.M., Kim, J.H., Kim, K.H.: Effect of nanoparticles on critical heat flux of water in pool boiling heat transfer. Applied Physics Letters 83, 3374–3376 (2003)
126. Tu, J.P., Dinh, N., Theofanous, T.: An experimental study of nanofluid boiling heat transfer. In: Proceedings of 6th International Symposium on Heat Transfer, Beijing, China (2004)
127. Vassallo, P., Kumar, R., Damico, S.: Pool boiling heat transfer experiments in silica-water nano-fluids. International Journal of Heat and Mass Transfer 47, 407–411 (2004)
128. Bang, I.C., Chang, S.H.: Boiling heat transfer performance and phenomena of Al_2O_3–water nano-fluids from a plain surface in a pool. International Journal of Heat and Mass Transfer 48, 2407–2419 (2005)
129. Wen, D.S., Ding, Y.L., Williams, R.A.: Pool boiling heat transfer of aqueous based TiO_2 nanofluids. Journal of Enhanced Heat Transfer 13, 231–244 (2006)
130. Kim, H., Kim, J., Kim, M.: Experimental study on CHF characteristics of water-TiO_2 nanofluids. Nuclear Engineering and Technology 38, 61–68 (2006)
131. Kim, S.J., Bang, I.C., Buongiorno, J., Hu, L.W.: Effects of nanoparticle deposition on surface wettability influencing boiling heat transfer in nanofluids. Applied Physics Letters 89, 153107 (2006)
132. Kim, S.J., Bang, I.C., Buongiorno, J., Hu, L.W.: Surface wettability change during pool boiling of nanofluids and its effect on critical heat flux. International Journal of Heat and Mass Transfer 50, 4105–4116 (2007)
133. Chopkar, M., Das, A.K., Manna, I., Das, P.K.: Pool boiling heat transfer characteristics of ZrO_2-water nanofluids from a flat surface in a pool. Heat and Mass Transfer 44, 999–1004 (2008)
134. Wen, D.S.: Mechanisms of thermal nanofluids on enhanced critical heat flux (CHF). International Journal of Heat and Mass Transfer 51, 4958–4965 (2008)
135. Milanova, D., Kumar, R.: Role of ions in pool-boiling heat transfer of pure and silica nanofluids. Applied Physical Letters 87, 233107 (2005)
136. Coursey, J.S., Kim, J.: Nanofluid boiling: the effect of surface wettability. International Journal of Heat and Fluid Flow 29, 1577–1585 (2008)
137. Lv, L.C., Liu, Z.H.: Boiling characteristics in small vertical tubes with closed bottom for nanofluids and nanoparticle-suspensions. Heat Mass Transfer 45, 1–9 (2008)
138. Maiga, S.E., Palm, S.J., Nguyen, C.T., Roy, G., Galanis, N.: Heat transfer enhancement by using nanofluids in forced convection flows. International Journal of Heat and Fluid Flow. 26, 530–546 (2005)

139. Williams, W., Buongiorno, J., Hu, L.W.: Experimental investigation of turbulent convective heat transfer and pressure loss of alumina/water and zirconia/water nanoparticle colloids (nanofluids) in horizontal tubes. Journal of Heat Transfer – Transaction of ASME 130, 042412 (2008)
140. Maxwell, J.C.: A treatise on electricity and magnetism. Clarendon Press, Oxford (1873)
141. Hamilton, R.L., Crosser, O.K.: Thermal conductivity of heterogeneous two-component systems. I & EC Fundamentals 1, 187–191 (1962)
142. Jeffrey, D.J.: Conduction through a random suspension of spheres. Proceedings of Royal Society of London Series A 335, 355–367 (1973)
143. Davis, R.H.: The effective thermal conductivity of a composite material with spherical inclusions. International Journal of Thermophysics 7(3), 609–620 (1986)
144. Yu, W., Choi, S.U.S.: The role of interfacial layers in the enhanced thermal conductivity of nanofluids: a renovated Hamilton–Crosser model. Journal of Nanoparticle Research 6, 355–361 (2004)
145. Xue, Q.Z.: Model for effective thermal conductivity of nanofluids. Physics Letters A 307, 313–317 (2003)
146. Xue, Q., Xu, W.M.: A model of thermal conductivity of nanofluids with interfacial shells. Materials Chemistry and Physics 90, 298–301 (2005)
147. Jang, S.P., Choi, S.U.S.: Role of Brownian motion in the enhanced thermal conductivity of nanofluids. Applied Physics Letters 84, 4316–4318 (2004)
148. Koo, J., Kleinstreuer, C.: Laminar nanofluid flow in micro-heat sinks. International Journal of Heat and Mass Transfer 48, 2652–2661 (2005)

Nanofluids of the Future

Liqiu Wang* and Michel Quintard

Abstract. Nanofluids are a new class of fluids engineered by dispersing nanometer-size structures (particles, fibers, tubes, droplets) in base fluids. The very essence of nanofluids research and development is to enhance fluid macroscale and megascale properties such as thermal conductivity through manipulating microscale physics (structures, properties and activities). Therefore, the success of nanofluid technology depends very much on how well we can address issues like effective means of microscale manipulation, interplays among physics at different scales, and optimization of microscale physics for the optimal megascale properties. In this chapter we review methodologies available to effectively tackle these central but difficult problems and identify the future research needs as well. The reviewed techniques include nanofluids synthesis through liquid-phase chemical reactions in continuous-flow microfluidic microreactors, scaling-up by the volume averaging, and constructal design with the constructal theory. The identified areas of future research contain microfluidic nanofluids, thermal waves, and constructal nanofluids. While our focus is on heat-conduction nanofluids, the methodologies are equally valid for the other types of nanofluids. The review could serve as a coherent, inspiring and realistic plan for future research and development of nanofluid technology.

1 Introduction

Nanofluids, fluid suspensions of nanometer-sized particles, find numerous applications in various fields as heat transfer fluids [1-4], ferromagnetic fluids [5], superwetting fluids and detergents [6-8], biomedical fluids [9], polymer nanocomposites [10], gain media in random lasers [11], and as building blocks for electronic and optoelectronic devices [12, 13]. This is due to their unique thermal, electronic, magnetic, wetting and optical properties that can be obtained via engineering

Liqiu Wang
Department of Mechanical Engineering, the University of Hong Kong,
Pokfulam Road, Hong Kong
lqwang@hku.hk

Michel Quintard
Institut de Mécanique des Fluides, C.N.R.S., Toulouse, France

* Corresponding author.

L.Q. Wang (Ed.): Advances in Transport Phenomena 2009, ADVTRANS 1, pp. 179–243.
springerlink.com

particles' structures and properties. Recent experiments on nanofluids have shown, for example, up to two-fold increases in thermal conductivity [2, 14-20], strong temperature dependence of thermal conductivity [3, 21], substantial increases in convective heat transfer coefficient [4, 22-25], and three-fold increases in critical heat flux (CHF) in boiling heat transfer [1-3, 26-29]. State-of-the-art expositions of major advances on the synthesis, characterization and application of nanofluids are available, for example, in [1-3, 16, 30-34].

Nanofluids are research challenges of rare potential but daunting difficulty. The potential comes from both scientific and practical opportunities in many fields. The difficulty reflects the issues related to multiscales. Nanofluids involve at least four relevant scales: the molecular scale, the microscale, the macroscale and the megascale. The molecular scale is characterized by the mean free path between molecular collisions, the microscale by the smallest scale at which the law of continuum mechanics apply, the macroscale by the smallest scale at which a set of averaged properties of concern can be defined and the megascale by the length scale corresponding to the domain of interest [35, 36]. By their very nature, research and engineering practice in nanofluids are to enhance fluid macroscale and megascale properties through manipulating microscale physics (structures, properties and activities). Therefore, interest should focus on addressing questions like: (i) how to effectively manipulate at microscale, (ii) what are the interplays among physics at different scales, and (iii) how to optimize microscale physics for the optimal megascale properties. In this chapter we summarize methodologies available to effectively address these central problems and identify the future research needs by taking heat-conduction nanofluids as examples.

2 Microscale Manipulation: Microfluidic Nanofluids

The ability to manipulate at microscale depends very much on nanofluids synthesis techniques. Nanofluids have been synthesized by either a two-step approach that first generates nanoparticles and subsequently disperses them into base fluids [1-3, 30-34] or a one-step *physical* method that simultaneously makes and disperses the nanoparticles into base fluids [37-41]. An advantage of the two-step method is that the inert gas condensation technique has already been scaled up to commercial nano-powder production [42]. Because of this and the ease with which the particle concentration and size distribution can be manipulated, most of the experimental investigations have used the two-step method [1-3, 30-34]. A deficiency of the two-step technique is particles' agglomeration during storage and dispersion in the base fluids, as a result of their high surface-to-volume ratio. Such agglomerates, in most cases, negate the unique properties associated with nanoparticles and nanofluids [1-3, 30-34]. Changing the nanofluids' PH value, adding surfactants or a suitable surface activator, or using ultrasonic or microwave vibration have been used with the two-step method to prevent nanoparticles from agglomerating [1-3, 30-34]. However, typically it is rare to maintain so-synthesized nanofluids in a homogeneous stable state for more that 24 hours [2].

To prevent oxidation of metallic particles, a one-step technique is preferable for synthesizing nanofluids containing metal particles. The one-step *physical* method developed in [37, 38] involves nanoparticle source evaporation and direct condensation and dispersion into a flowing base fluid in a vacuum chamber. The method has been successfully used to synthesize nanofluids of Cu particles in ethylene glycol with small copper nanoparticles (about 10nm) and high thermal conductivity enhancement (about 40% at the particle volume concentration of 0.3%) [38]. Another one-step *physical* method (the submerged arc nanoparticle synthesis system; SANSS) has also been used to synthesize nanofluids of TiO_2 particles in deionized water [39], CuO particles in deionized water [40] and Cu particles in the mixture of deionized water and ethylene glycol [41]. With the SANSS, the nanofluids are generated by vaporizing the solid material by the submerged arc and condensing into the base liquid in a vacuum chamber. Although these one-step physical methods are capable of synthesizing nanofluids with different nanostructures, they would be difficult to scale-up mainly because of their high cost and their demand for a vacuum.

In addition to the challenge of how to effectively prevent nanoparticles from agglomerating or aggregating, the key issue in either of these two approaches is the lack of effective means for synthesizing nanofluids with controllable microstructures due to either the limitation of available nanoparticle powers in the two-step method or the limitation of the system used in the one-step physical method. In an attempt to develop more effective techniques, a one-step *chemical* solution method has been recently developed [16, 20, 30, 43-47]. The strength of the solution chemistry for synthesizing nanofluids lies in its ability to manipulate atoms and molecules in the liquid phase, thereby providing a powerful arsenal for synthesis of tailor-designed nanofluids using a bottom-up approach [16].

Figure 1 shows the flow chart of the chemical solution method (CSM) [16]. The reaction between Reactants A (e.g. Cu^{2+}) and B (e.g. OH^-) in the liquid phase yields the solution or colloid containing the precursor C (e.g. $Cu(OH)_2$). The additives (e.g. ammonium citrate or cetyltrimethyl ammonium bromide) are then added into the solution/colloid. Finally the solution/colloid of the precursor C transforms into nanofluid D (e.g. CuO-particles-in-water) under ultrasonic or/and microwave irradiation.

Precursor C normally exists in the form of solution or colloid and is not, in general, the nanoparticle in the nanofluid D. Its solution or colloid can directly transform into the required nanofluids with the help of additives and external

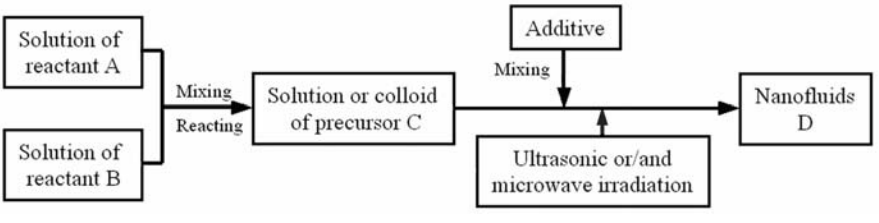

Fig. 1 Chemical solution method (CSM) for synthesis of nanofluids: flow chart

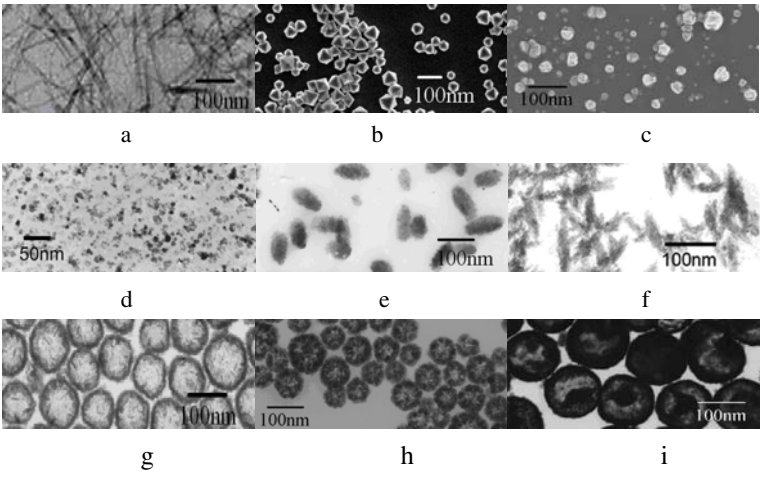

Fig. 2 TEM/SEM images of some nanoparticles from "drying" samples of nanofluids synthesized by the chemical solution method [16, 20, 30, 43-47]: (a) $CePO_4$ nanofibers. (b) octahedral Cu_2O nanoparticles. (c) N-vinylcaprolactam polymer-nanoparticles. (d) spherical Fe_3O_4 nanoparticles. (e) elliptic Cu nanorods. (f) needle-like CuO nanoparticles. (g) hollow CuS nanoparticles. (h) hollow and wrinkled Cu_2O nanoparticles. (i) Cu_2O(core)/CuS(shell) nanoparticles

fields such as ultrasonic and microwave irradiation. Both the additives and the external fields are used to prevent nanoparticles from agglomeration and growth and thus control nanofluid microstructures.

The method has been successfully applied to produce nine kinds of nanofluids in Fig. 2 [16, 20, 30, 43-47]. The nanofluids synthesized by this method have both higher conductivity enhancement and better stability than those produced by the other methods. This method is distinguished from the others also by its controllability. The nanofluid microstructure can be varied and manipulated by adjusting synthesis parameters such as temperature, acidity, ultrasonic and microwave irradiation, types and concentrations of reactants and additives, and the order in which the additives are added to the solution [16].

Problems with the CSM come mainly from the *macroscale batch* reactors where reactions take place:

- The CSM uses a bottom-up approach to generate nanoparticles through chemical reactions in the liquid phase, and thereby it has the potential to manipulate atoms and molecules. However, the difficulty of controlling the microscale while operating at the macroscale is insuperable.
- Mixing in a macroscale batch reactor is usually achieved by stirring. In this case, the fluid entity is broken into fragments by circular motion. The last part of mixing takes place based on molecular diffusion. In the diffusion

process, the mixing time t depends on the diffusion path d in the form of $t \propto d^2/D$, v where D is the diffusion coefficient. Therefore, if the diffusion path becomes smaller, the mixing time becomes shorter. However, it is very difficult to make small-sized fragments by conventional stirring in solution phase. At the macroscale, therefore, mixing time is usually much larger than reaction time. The reaction rate is normally determined by the mixing time and is usually very low (reaction time: min-h). Moreover, the longer mixing time and lack of effective ways to accurately control mixing also lead to poor product selectivity of competitive reactions either in parallel or in consecutive, thereby leading to poor quality of synthesized nanofluids that could contain some undesired side products.

- Generally, the heat generation rate in reaction increases in proportion to the reactor volume. Because the heat of reaction is removed through the wall of the reactor, the wall-surface-area/reactor-volume ratio, which decreases with the increasing reactor size, plays a crucial role. Therefore, heat removal capacity is also a key issue for highly exothermic and extremely fast reactions in macroreactors.
- Because of high labor and work-up demand, a batch-model operation is not commercially economical. The repeatability of nanofluids' structures is also poor with the batch-model operation.

To resolve these critical issues, the batch-based macroreactors in the CSM can be replaced by continuous-flow microfluidic microreactors, for example, those in Fig. 3. This allows a continuous and scaleable (simply by numbering-up) synthesis of high-quality nanofluids with a more accurate and effective control over particle microstructures such as the size, distribution and shape. Microreactors exhibit numerous practical advantages, including safety, easy modulation, and numbering-up for industrial production, when compared with traditional macroreactors. It is also advantageous that the reactions can be controlled more accurately through efficient mixing, enhanced reaction/product selectivity, and effective mass and heat transfer, due to short diffusion paths and high surface-to-volume ratios at the microscale. Running the one-step chemical process in a continuous mode would not only increase its commercial viability, but also improve its repeatability significantly. Growth of nanoparticles directly in the base fluids through chemical reactions enables us to manipulate atoms and molecules in the liquid phase, thereby providing a powerful arsenal for synthesis of tailor-designed nanofluids using a bottom-up approach [16].

Mixing has a decisive influence on the heat transfer, mass transfer, yield and selectivity of a reaction. Shrinking the reactor size to the microscale reduces the diffusion length between the reactant fluids, thus enhancing the mixing by molecular diffusion. The mixing by convection at the microscale is, however,

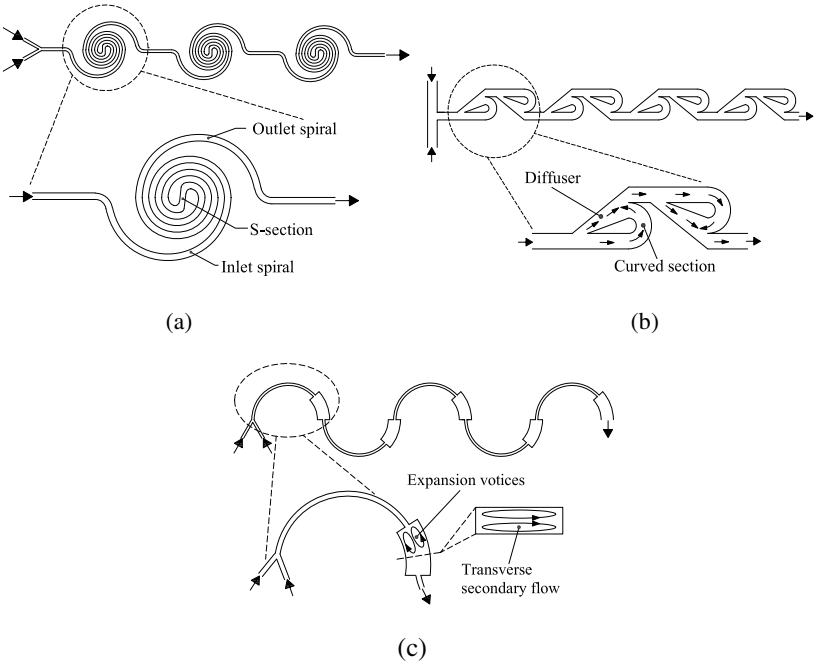

Fig. 3 Three kinds of microfluidic reactors (a: three spiral-microchanel units; b: four modified-Tesla-structure units; c: five semicircular-arc units)

weak because typically, flow in microchannels is laminar with Reynolds numbers well below the threshold for turbulence. Transverse secondary flows--which arise as a result of centrifugal effects experienced by fluids traveling along a curved trajectory and continuously expand interfacial area between reagent streams through stretching, folding and breakup processes--offer an attractive possibility of providing enhanced mixing in an easily-fabricated planar format by simply introducing curvature to the flow path. Expansion vortices or direct collision of slit fluid streams can also be generated by manipulating the geometrical structure of curved channels, and hence further enhance the mixing. Figure 3 shows three types of microreactors that are made of planar and smooth-walled curved microchannels on the one hand, and have a rapid laminar-flow mixing on the other hand.

All three kinds of microreactors consist of several units of curved microchannels connected in series (three, four and five, respectively, in Fig. 3a-c for illustration and example). The unit in Fig. 3a-c is the spiral microchanel having an inlet and outlet spiral connected by a central S-shaped channel, the modified Tesla structure containing two modified Tesla microchannels in opposite directions, and

the semicircular arc involving an abrupt width increase over the last quarter, respectively. These microreactors can have a very rapid mixing between reactant fluids due to both the short diffusion length and the centrifugal-force-driven transverse secondary flow in curved microchannels [48-53]. The mixing is also further enhanced by the direct collision of slit fluid streams in the Tesla structure (Fig. 3b) and by the expansion vortices that arise in the horizontal plane due to an abrupt increase in the channel width (Fig. 3c) [54, 55].

The centrifugal-force-driven transverse secondary flow becomes stronger following increases in the channel curvature ratio σ defined by $\sigma = w / R$ (w and R are the channel width and the curvature radius, respectively) and the Dean number defined by $\mathrm{De} = \mathrm{Re}\sqrt{\sigma}$ (Re is the Reynolds number) [48-50]. The mixing performance thus becomes better as the Re increases for all three microreactors in Fig. 3, with consequently all working well as high-Re (Re>100) reactors. The first two types of microreactors (Fig. 3a, b) also work well as the low-Re (Re<10) and the intermediate-Re (10<Re<100) reactors [51, 52, 55], respectively, due to a very high curvature ratio σ used in the inner region of spiral microchannels in Fig. 3a and the fluid-stream direct collision in Fig. 3b.

In this microfluidic approach for nanofluids synthesis, solutions of the two reagents are injected as steady streams into a microfluidic channel at initial point (s=0) where the reaction between them starts (t=0). Here s and t are the distance and time, respectively. As their mixture flows at a constant velocity v, the reaction time is *linearly* related to the spatial distance by $t=s/v$. Interactions of multiple chemical reactions in time could thus be controlled simply by varying flow velocities and by creating a network of converging and diverging channels for carrying reaction mixtures. Therefore, this approach offers simple means for controlling many chemical reactions, including when each reaction starts, for how long each reaction evolves before it is separated or combined with other reactions, and when each reaction is quenched.

Droplets and slugs formed within microfluidic channels can also serve as microreactors in the CSM for nanofluids synthesis. Figures 4 and 5 illustrate two such microfluidic systems. In the first type (Fig. 4), discrete droplets are formed at the T-junction and are encapsulated by a dispersing liquid that wets the microchannel. These droplets form the dispersed phase in which the reaction between Reactants A (e.g. phosphoric acid H_3PO_4) and B (e.g. cerium nitrate $Ce(NO_3)_3$) occurs in the liquid phase. After separating the dispersing liquid in the separator, we can obtain nanofluids (e.g. suspensions of cerium phosphate ($CePO_4$) nanofibers in water, Fig. 2a). In the second type (Fig. 5), liquid slugs are separated by discrete gas bubbles generated at the T-junction of microfluidic channels. Reactions occur within the slugs that form the continuous phase. The nanofluids are

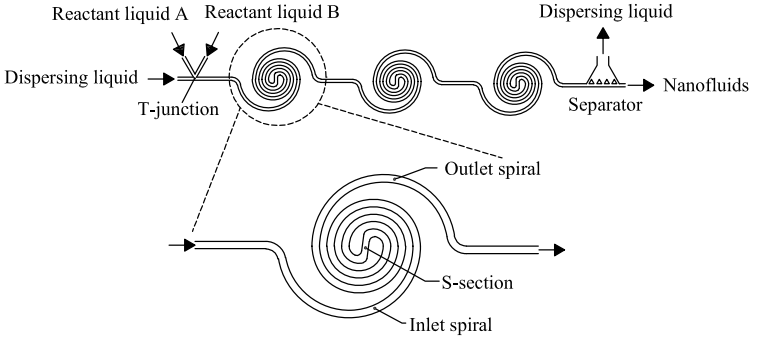

(a)

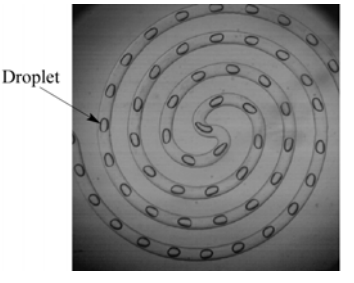

(b)

Fig. 4 Nanofluids synthesis by compartmentalizing chemical reactions in microfluidic droplets: (a) microfluidic system; (b) microfluidic droplets

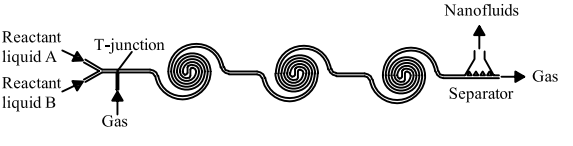

(a)

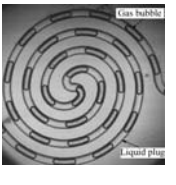

(b)

Fig. 5 Nanofluids synthesis by compartmentalizing chemical reactions in microfluidic slugs mediated by gas bubbles: (a) microfluidic system; (b) microfluidic slugs mediated by gas bubbles

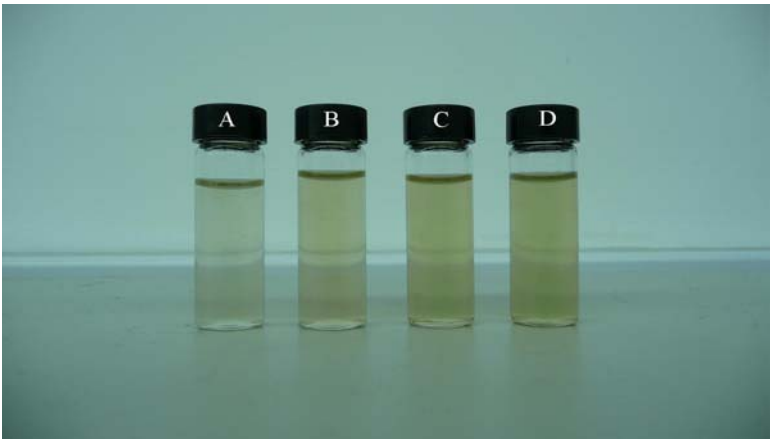

(a)

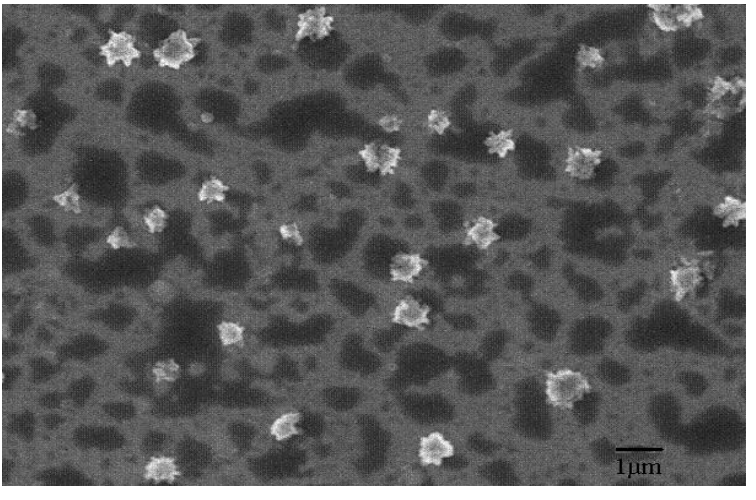

(b)

Fig. 6 Microfluidic Cu_2O-particles-in-water nanofluids 24 hours after their preparation [70]: (a) stable nanofluid samples; (b) SEM images of flower-shaped Cu_2O-particles

collected after separating the gas bubbles in the separator. The first type differs from the second type in that reagents in droplets do not come into contact with the microchannel wall.

The additional advantage of compartmentalizing reactions in droplets or slugs of femoliter to microliter include the enhanced mixing from the internal recirculation within the droplets or slugs [55-66] and enhanced controllability of reactions due to the simplicity and accuracy in manipulating microfluidic droplets, bubbles

and slugs in various ways [67-69]. For example, the ability to split and fuse individual droplets improves simplicity with which the reagent volume and concentrations can be controlled precisely.

Figure 6 (a) shows the photos of some microfluidic Cu_2O nanofluids 24 hours after their preparation [70], with the enhanced stability, highly monodispersed particles and reduced particle size compared with those synthesized by the CSM [47]. The particle shape can also be designed with this type of synthesis method. Figure 6(b) illustrates some flower-shaped Cu_2O-particles that are difficult to form by the other methods [70].

Therefore, microstructures of microfluidic nanofluids (the nanofluids synthesized through liquid-phase chemical reactions in microfluidic systems) can be precisely controlled by reagent fluid properties, system geometrical properties and fluid dynamical parameters such as flow rates. Intensified future effort is required to define the potential of this promising synthesis technique against an important target of controlling reactions accurately with a rapid and precise mixing. Specifically, the research focus should be on the correlations between nanofluids microstructures and controlling parameters of fluid physical/chemical/dynamical properties and microfluidic geometrical features.

3 Macroscale Heat Conduction: Thermal Waves

In the *phenomenological* approach for heat conduction study, the *thermal conductivity* of a material is defined as the *rate of heat transfer through a unit thickness of the material per unit area per unit temperature difference*. The thermal conductivity thus reflects the ability of a material to conduct heat. A high value for thermal conductivity implies that the material is a good heat conductor, and a low value indicates that the material is a poor heat conductor. Typically, the value of liquid thermal conductivity is several orders lower than most of the metals or metal oxides (Table 1). It would thus be logical to boost the conductivity of a fluid by using a suspension of particles of a highly conducting solid in it, the idea that was first suggested more than one century ago. Most of the early studies, however, used suspensions of millimeter- or micrometer-sized particles, which, while they showed some promise, suffered from problems such as poor suspension stability and channel clogging. Nanoparticles are the obvious substitute candidates; and thus studying the thermal conductivity of nanofluids has grabbed the considerable attention of scientists and engineers in the last decade [1-3, 16, 30-34].

A relatively intensified effort has been made on determining nanofluid thermal conductivity from experiments, particularly for the nanofluids with spherical nanoparticles or nanotubes. While the data from these experiments have enabled some trends to be identified, there is still no consensus on the effects of some parameters such as particle size, shape, distribution and additives in the nanofluids [1-3, 14, 30-34]. There also exist wide discrepancies and inconsistencies in the reported conductivity data due to a limited understanding of the precise nature of

Table 1 Thermal conductivity comparison

	Materials	Thermal conductivity (W/mK)
	Carbon nanotube	200-6000
Liquids	Ethylene glycol	0.25
	Mineral oil	0.13
	Water	0.6
Metal oxide solids	Alumina	40
	Copper oxide	70
	Zinc oxide	60
Metallic solids	Aluminum	230
	Copper	385
	Silver	410

heat conduction in nanofluids, the poor microstructure characterization and the unavailability of nanofluids with various microstructures [1-3, 16, 30-34]. In many cases the microstructural parameters were not measured by the experimenters themselves but rather taken from the powder manufacturers' nominal information. To reconcile these discrepancies and inconsistencies and to lay the foundations for better and more efficient designs of nanofluids, it is essential to generate nanofluids of various microstructures, characterize their microstructures by state-of-the-art instrumentation and develop precise heat-conduction model for nanofluids [16].

Suggested *microscopic* reasons for experimental finding of significant conductivity enhancement include the nanoparticle Brownian motion effect [71-76], the liquid layering effect at the liquid-particle interface [77-82], and the nanoparticle cluster/aggregate effect [83, 84]. As generally accepted [1-3, 30-34, 85-88], however, no conclusive explanation is available. Often, the explanation by one research group is confronted by others. The recent examination of available experimental data has even tended to disqualify all these microscopic reasons [89, 90]. There is also a lack of agreement between experimental results and between theoretical models. The fact that the conductivity enhancement comes from the presence of nanoparticles has directed research efforts nearly exclusively towards thermal transport at nanoscale. The classical heat-conduction equation has been *postulated* as the macroscale model but without adequate justification. Thermal conductivity is a *macroscale phenomenological* characterization of heat conduction and the conductivity measurements are not performed at the nanoscale, but rather at the macroscale. Therefore, interest should focus not only on what

happens at the nanoscale but also on how the presence of nanoparticles affects the heat transport at macroscale.

In an attempt to isolate the mechanism responsible for the significant enhancement of thermal conductivity, a macroscale heat-conduction model in nanofluids has been recently developed from first principles [16, 35, 91]. The model was obtained by scaling-up a microscale model for heat conduction in nanoparticles and in base fluids. The approach for scaling-up is the volume averaging with help of multiscale theorems [35, 36, 92]. The microscale model for the heat conduction in the nanoparticles and in the base fluids comes from the first law of thermodynamics and the Fourier law of heat conduction. The result shows that the presence of nanoparticles leads to a dual-phase-lagging heat conduction in nanofluids at macroscale with a potential of higher thermal conductivity. In this section, we first detail the development of this theory for a structured access to its physics, application conditions and the ways of further improvement, then examine the macroscale manifestation of microscale physics, and finally identify the future research needs.

3.1 Macroscale Heat-Conduction Models

The microscale model for heat conduction in nanofluids is well-known. It consists of the field equation and the constitutive equation. The field equation comes from the first law of thermodynamics. The commonly-used constitutive equation is the Fourier law of heat conduction for the relation between the temperature gradient ∇T and the heat flux density vector $\mathbf{q}$ [93].

For transport in nanofluids, the macroscale is a phenomenological scale that is much larger than the microscale and much smaller than the system length scale. Interest in the macroscale rather than the microscale comes from the fact that a prediction at the microscale is complicated due to the complex microscale structure of nanofluids, and also because we are usually more interested in large scales of transport for practical applications. Existence of such a macroscale description equivalent to the microscale behavior requires a good separation of length scales and has been discussed in [35, 94].

To develop a macroscale model of heat conduction in nanofluids, the method of volume averaging starts with a microscale description [36, 92]. Both conservation and constitutive equations are introduced at the microscale. The resulting microscale field equations are then averaged over a representative elementary volume (REV), the smallest differential volume resulting in statistically meaningful local averaging properties, to obtain the macroscale field equations. In the process of averaging, the *multiscale theorems* are used to convert integrals of gradient, divergence, curl, and partial time derivatives of a function into some combination of gradient, divergence, curl, and partial time derivatives of integrals of the function and integrals over the boundary of the REV [35, 36, 92]. The readers are referred to [35, 36, 92] for the details of the method of volume averaging and to [35, 36] for a summary of the other scaling-up methods.

3.1.1 Volume Averaging

Consider heat conduction in nanofluids with the base fluid and the nanoparticle denoted by $\beta-$ and $\sigma-$phases, respectively. By the first law of thermodynamics and the Fourier law of heat conduction, we have the microscale model for heat conduction in nanofluids (Fig. 7) [95]

$$\left(\rho c_p\right)_\beta \frac{\partial T_\beta}{\partial t} = \nabla \cdot \left(k_\beta \nabla T_\beta\right), \qquad \text{in the } \beta\text{-phase} \tag{1}$$

$$\text{B.C.1} \qquad T_\beta = T_\sigma, \text{ at } \quad A_{\beta\sigma} \tag{2}$$

$$\text{B.C.2} \qquad \mathbf{n}_{\beta\sigma} \cdot k_\beta \nabla T_\beta = \mathbf{n}_{\beta\sigma} \cdot k_\sigma \nabla T_\sigma, \qquad \text{at } \quad A_{\beta\sigma} \tag{3}$$

$$\left(\rho c_p\right)_\sigma \frac{\partial T_\sigma}{\partial t} = \nabla \cdot \left(k_\sigma \nabla T_\sigma\right), \quad \text{in the } \sigma\text{-phase} \tag{4}$$

Here T is the temperature. ρ, c and k are the density, specific heat and thermal conductivity, respectively. Subscripts β and σ refer to the β- and σ-phases, respectively. $A_{\beta\sigma}$ represents the area of the β – σ interface contained in the REV (Fig. 7); $\mathbf{n}_{\beta\sigma}$ is the outward-directed surface normal from the β-phase toward the σ-phase, and $\mathbf{n}_{\beta\sigma} = -\mathbf{n}_{\sigma\beta}$. In addition to the interfacial boundary conditions indicated by Eqs. (2) and (3), we also need boundary conditions at the entrances and exists of the macroscopic system shown in Fig. 7. In general, these conditions will not be

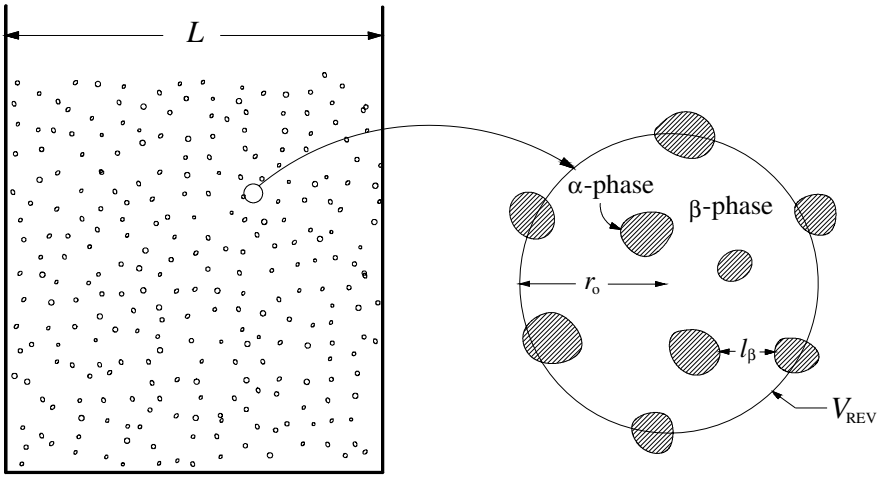

Fig. 7 Nanofluids and representative elementary volume (REV)

available in terms of the point values of the temperature, and we need to construct jump conditions in terms of volume-averaged values of temperature [96, 97].

In order to develop the volume-averaged form of the heat-conduction equation, we associate an average volume V_{REV} with every point in space and define average values in terms of that volume. Such an averaging volume is illustrated in Fig. 7, and can be represented in terms of the volume of the individual phases according to

$$V_{\mathrm{REV}} = V_{\beta}(\mathbf{r}) + V_{\sigma}(\mathbf{r}) \tag{5}$$

where V_{REV}, V_{β} and V_{σ} are the volumes of the REV, β-phase in REV and σ-phase in REV, respectively. In Fig. 8 we have indicated that the centroid of an averaging volume is located by the position vector **r**, and that points in the β-phase are located by the *relative position* vector $\mathbf{y}_{\beta}$.

We will use the averaging volume V_{REV} to define two averages: the *superficial average* and the *intrinsic average*. Each of the two averages is routinely used in the description of multiphase transport processes, and it is important to clearly define them. In terms of the averaging volume, we define the *superficial average* of some function Ψ_{β} by

$$\langle \Psi_{\beta} \rangle|_{\mathbf{r}} = \frac{1}{V_{\mathrm{REV}}} \int_{V_{\beta}(\mathbf{r})} \Psi_{\beta}(\mathbf{r} + \mathbf{y}_{\beta}) \mathrm{d}V_{y} \,. \tag{6}$$

This clearly indicates that $\langle \Psi_{\beta} \rangle$ is associated with the centroid and that integration is carried out with respect to the components of the relative position vector $\mathbf{y}_{\beta}$. The *intrinsic average* is defined by

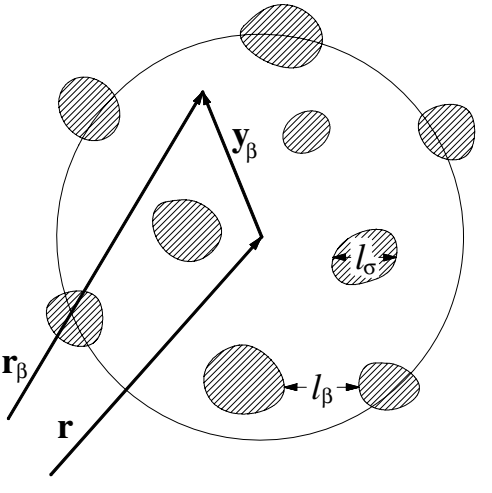

Fig. 8 Position vectors associated with REV

$$\left\langle \Psi_\beta \right\rangle^\beta \Big|_{\mathbf{r}} = \frac{1}{V_\beta(\mathbf{r})} \int_{V_\beta(\mathbf{r})} \Psi_\beta(\mathbf{r}+\mathbf{y}_\beta)\,\mathrm{d}V_y \,. \tag{7}$$

It is important to know the precise notation used in Eqs. (6) and (7); however, in our analysis we will make use of the simpler representations given by

$$\left\langle \Psi_\beta \right\rangle = \frac{1}{V_{\mathrm{REV}}} \int_{V_\beta} \Psi_\beta \mathrm{d}V, \tag{8}$$

$$\left\langle \Psi_\beta \right\rangle^\beta = \frac{1}{V_\beta} \int_{V_\beta} \Psi_\beta \mathrm{d}V. \tag{9}$$

These two averages are related by

$$\left\langle \Psi_\beta \right\rangle = \varepsilon_\beta \left\langle \Psi_\beta \right\rangle^\beta \tag{10}$$

in which ε_β is the volume fraction of the β-phase,

$$\varepsilon_\beta = V_\beta / V_{\mathrm{REV}} \,. \tag{11}$$

In this notation for the volume average, a *Greek subscript* is used to identify the particular phase under consideration and a *Greek superscript* is used to identify an intrinsic average. Since the intrinsic and superficial averages differ by a factor of ε_β, it is essential to make use of a notation that clearly distinguishes between the two.

When we take the volume average of any microscale heat-conduction equation, we are immediately confronted with the average of a gradient or the average of a divergence and it is the gradient or divergence of the average that we are seeking. In order to interchange integration and differentiation, we will make use of the multiscale theorem (Theorem 40 in [35]) [35, 92, 98, 99]:

$$\int_{V_\beta} \nabla \circ F_\beta dV = \nabla \circ \int_{V_\beta} F_\beta dV + \int_{A_{\beta\sigma}} \mathbf{n}_{\beta\sigma} \circ F_\beta \mathrm{d}A \tag{12}$$

where $\nabla \circ F_\beta$ can be any of the three operators: $\nabla f, \nabla \cdot \mathbf{f}$ and $\nabla \times \mathbf{f}$. $f(\mathbf{r},t)$ and $\mathbf{f}(\mathbf{r},t)$ are spatial scalar and vector functions of position vector $\mathbf{r}$ and time t defined in β-phase, respectively. ∇ in the integrand is the microscopic spatial operator. ∇ Operating on the integral is the macroscopic spatial operator. $A_{\beta\sigma}$ represents the interfacial area contained within the averaging volume.

Performing superficial average of Eq. (1) yields

$$\frac{1}{V_{\mathrm{REV}}}\int_{V_\beta}\left(\rho c_p\right)_\beta\frac{\partial T_\beta}{\partial t}\mathrm{d}V=\frac{1}{V_{\mathrm{REV}}}\int_{V_\beta}\nabla\cdot\left(k_\beta\nabla T_\beta\right)\mathrm{d}V\,. \tag{13}$$

It is possible that the physical properties of the β-phase vary significantly over the macroscopic region shown in Fig. 7; however, variations over the averaging volume can normally be neglected [92] and this allows us to reduce Eq. (13) into

$$\left(\rho c_p\right)_\beta\frac{1}{V_{\mathrm{REV}}}\int_{V_\beta}\frac{\partial T_\beta}{\partial T}\mathrm{d}V=\frac{1}{V_{\mathrm{REV}}}\int_{V_\beta}\nabla\cdot\left(k_\beta\nabla T_\beta\right)\mathrm{d}V\,. \tag{14}$$

Consider the system to be rigid so that V_β is time-independent. We can thus interchange integration and differentiation in the left-hand side of Eq. (14) to obtain

$$\left(\rho c_p\right)_\beta\frac{1}{V_{\mathrm{REV}}}\int_{V_\beta}\frac{\partial T_\beta}{\partial t}\mathrm{d}V=\left(\rho c_p\right)_\beta\frac{\partial\left\langle T_\beta\right\rangle}{\partial t}=\varepsilon_\beta\left(\rho c_p\right)_\beta\frac{\partial\left\langle T_\beta\right\rangle^\beta}{\partial t}\,. \tag{15}$$

Here we have chosen to represent the average temperature in terms of the *intrinsic average* because this temperature best represents the heat-conduction process taking place in the β-phase. After applying the multiscale theorem to the conductive transport term in the right-hand side of Eq. (14), we have

$$\varepsilon_\beta\left(\rho c_p\right)_\beta\frac{\partial\left\langle T_\beta\right\rangle^\beta}{\partial t}=\nabla\cdot\left\langle k_\beta\nabla T_\beta\right\rangle+\frac{1}{V_{\mathrm{REV}}}\int_{A_{\beta\sigma}}\mathbf{n}_{\beta o}\cdot k_\beta\nabla T_\beta\mathrm{d}A\,. \tag{16}$$

The last term will *connect* the β-phase equation to the σ-phase equation (4). Once again we ignore the variation of a physical property *within the averaging volume* and apply the multiscale theorem again to reduce the first term on the right–hand side of Eq. (16) into

$$\nabla\cdot\left\langle k_\beta\nabla T_\beta\right\rangle=\nabla\cdot\left[k_\beta\left\langle\nabla T_\beta\right\rangle\right]=\nabla\cdot\left[k_\beta\left(\nabla\left\langle T_\beta\right\rangle+\frac{1}{V_{\mathrm{REV}}}\int_{A_{\beta\sigma}}\mathbf{n}_{\beta\sigma}T_\beta dA\right)\right]. \tag{17}$$

Here we are facing with the two problems: the *superficial average* temperature that we would like to replace with the *intrinsic average* temperature, and the *point* temperature that we are attempting to avoid. The former can be resolved by the use of Eq. (10) in the form

$$\left\langle T_\beta \right\rangle = \varepsilon_\beta \left\langle T_\beta \right\rangle^\beta \tag{18}$$

whereas the latter requires decomposition in terms of the intrinsic average temperature and a spatial deviation temperature:

$$T_\beta = \left\langle T_\beta \right\rangle^\beta + \tilde{T}_\beta . \tag{19}$$

Substituting Eqs. (18) and (19) into Eq. (17) leads to

$$\nabla \cdot \left\langle k_\beta \nabla T_\beta \right\rangle = \nabla \cdot \left[k_\beta \left(\varepsilon_\beta \nabla \left\langle T_\beta \right\rangle^\beta + \left\langle T_\beta \right\rangle^\beta \nabla \varepsilon_\beta + \frac{1}{V_{\mathrm{REV}}} \int_{A_{\beta\sigma}} \mathbf{n}_{\beta\sigma} \left\langle T_\beta \right\rangle^\beta \mathrm{d}A + \frac{1}{V_{\mathrm{REV}}} \int_{A_{\beta\sigma}} \mathrm{n}_{\beta\sigma} \tilde{T}_\beta \mathrm{d}A \right) \right] . \tag{20}$$

This represents a non-local form in terms of the average temperature $\left\langle T_\beta \right\rangle^\beta$ since this quantity is evaluated over the $\beta - \sigma$ interface at points other than the centroid of the averaging volume illustrated in Fig. 8. If we can remove $\left\langle T_\beta \right\rangle^\beta$ from the area integral over $A_{\beta\sigma}$ (see [92, 95] for the length-scale constraints associated with this simplification), the multiscale theorem (12) leads to

$$\frac{1}{V_{\mathrm{REV}}} \int_{A_{\beta\sigma}} \mathbf{n}_{\beta\sigma} \left\langle T_\beta \right\rangle^\beta \mathrm{d}A = \left\langle T_\beta \right\rangle^\beta \left\{ \frac{1}{V_{\mathrm{REV}}} \int_{A_{\beta\sigma}} \mathbf{n}_{\beta\sigma} \mathrm{d}A \right\} = - \left\langle T_\beta \right\rangle^\beta \nabla \varepsilon_\beta . \tag{21}$$

Under these circumstances, Eq. (20) can be simplified to

$$\nabla \cdot \left\langle k_\beta \nabla T_\beta \right\rangle = \nabla \cdot \left[k_\beta \left(\varepsilon_\beta \nabla \left\langle T_\beta \right\rangle^\beta + \frac{1}{V_{\mathrm{REV}}} \int_{A_{\beta\sigma}} \mathbf{n}_{\beta\sigma} \tilde{T}_\beta \mathrm{d}A \right) \right] . \tag{22}$$

Substitution of Eq. (22) into Eq. (16) yields the volume-averaged heat-conduction equation

$$\underbrace{\varepsilon_\beta \left(\rho c_p \right)_\beta \frac{\partial \left\langle T_\beta \right\rangle^\beta}{\partial t}}_{\text{accumulation}} = \underbrace{\nabla \left[k_\beta \left(\varepsilon_\beta \nabla \left\langle T_\beta \right\rangle^\beta + \frac{1}{V_{\mathrm{REV}}} \int_{A_{\beta\sigma}} \mathbf{n}_{\beta\sigma} \tilde{T}_\beta \mathrm{d}A \right) \right]}_{\text{conduction}} + \underbrace{\frac{1}{V_{\mathrm{REV}}} \int_{A_{\beta\sigma}} \mathbf{n}_{\beta\sigma} \cdot k_\beta \nabla T_\beta \mathrm{d}A}_{\text{interfacial flux}} . \tag{23}$$

The analogous result for the σ-phase reads

$$\underbrace{\varepsilon_\beta \left(\rho c_p \right)_\sigma \frac{\partial \left\langle T_\sigma \right\rangle^\sigma}{\partial t}}_{\text{accumulation}} = \underbrace{\nabla \cdot \left[k_\sigma \left(\varepsilon_\sigma \nabla \left\langle T_\sigma \right\rangle^\sigma + \frac{1}{V_{\mathrm{REV}}} \int_{A_{\sigma\beta}} \mathbf{n}_{\sigma\beta} \tilde{T}_\sigma \mathrm{d}A \right) \right]}_{\text{conduction}} + \underbrace{\frac{1}{V_{\mathrm{REV}}} \int_{A_{\sigma\beta}} \mathbf{n}_{\sigma\beta} \cdot k_\sigma \nabla T_\sigma \mathrm{d}A}_{\text{interfacial flux}} . \tag{24}$$

A decomposition of the temperature in the interfacial flux term of Eq. (23) leads to

$$\frac{1}{V_{\mathrm{REV}}}\int_{A_{\beta\sigma}}\mathbf{n}_{\beta\sigma}\cdot k_\beta\nabla T_\beta \mathrm{d}A=\frac{1}{V_{\mathrm{REV}}}\int_{A_{\beta\sigma}}\mathbf{n}_{\beta\sigma}\cdot k_\beta\nabla\left\langle T_\beta\right\rangle^\beta \mathrm{d}A+\frac{1}{V_{\mathrm{REV}}}\int_{A_{\beta\sigma}}\mathbf{n}_{\beta\sigma}\cdot k_\beta\nabla\tilde{T}_\beta \mathrm{d}A\,. \quad (25)$$

When the standard length-scale constraints are valid [100], the gradient of the average temperature can be removed from inside the integral, leading to

$$\frac{1}{V_{\mathrm{REV}}}\int_{A_{\beta\sigma}}\mathbf{n}_{\beta\sigma}\cdot k_\beta\nabla T_\beta \mathrm{d}A=\left\{\frac{1}{V_{\mathrm{REV}}}\int_{A_{\beta\sigma}}\mathbf{n}_{\beta\sigma}\mathrm{d}A\right\}\cdot k_\beta\nabla\left\langle T_\beta\right\rangle^\beta+\frac{1}{V_{\mathrm{REV}}}\int_{A_{\beta\sigma}}\mathbf{n}_{\beta\sigma}\cdot k_\beta\nabla\tilde{T}_\beta \mathrm{d}A\,. \quad (26)$$

From the multiscale theorem we have the geometrical relation [35]

$$\frac{1}{V_{\mathrm{REV}}}\int_{A_{\beta\sigma}}\mathbf{n}_{\beta\sigma}\mathrm{d}A=\nabla\varepsilon_\beta\,. \quad (27)$$

This reduces Eq. (26) into

$$\frac{1}{V_{\mathrm{REV}}}\int_{A_{\beta\sigma}}\mathbf{n}_{\beta\sigma}\cdot k_\beta\nabla T_\beta \mathrm{d}A=-\nabla\varepsilon_\beta\cdot k_\beta\nabla\left\langle T_\beta\right\rangle^\beta+\frac{1}{V_{\mathrm{REV}}}\int_{A_{\beta\sigma}}\mathbf{n}_{\beta\sigma}\cdot k_\beta\nabla\tilde{T}_\beta \mathrm{d}A\,. \quad (28)$$

Substitution of this expression for the interfacial flux into the β-phase heat-conduction equation (23) leads to

$$\varepsilon_\beta\left(\rho c_p\right)_\beta\frac{\partial\left\langle T_\beta\right\rangle^\beta}{\partial t}=\nabla\cdot\left[k_\beta\left(\varepsilon_\beta\nabla\left\langle T_\beta\right\rangle^\beta+\frac{1}{\nu}\int_{A_{\beta\sigma}}\mathbf{n}_{\beta\sigma}\tilde{T}_\beta \mathrm{d}A\right)\right]-\nabla\varepsilon_\beta\cdot k_\beta\nabla\left\langle T_\beta\right\rangle^\beta$$

$$+\frac{1}{V_{\mathrm{REV}}}\int_{A_{\beta\sigma}}\mathbf{n}_{\beta\sigma}\cdot k_\beta\cdot\nabla\tilde{T}_\beta \mathrm{d}A\,. \quad (29)$$

It is interesting to note that part of the interfacial flux is proportional to the gradient of the temperature and thus convective-like. The analogous equation for the σ-phase is

$$\varepsilon_\sigma\left(\rho c_p\right)_\sigma\frac{\partial\left\langle T_\sigma\right\rangle^\sigma}{\partial t}=\nabla\cdot\left[k_\sigma\left(\varepsilon_\sigma\nabla\left\langle T_\sigma\right\rangle^\sigma+\frac{1}{\nu}\int_{A_{\beta\sigma}}\mathbf{n}_{\beta\sigma}\tilde{T}_\sigma \mathrm{d}A\right)\right]-\nabla\varepsilon_\sigma\cdot k_\sigma\nabla\left\langle T_\sigma\right\rangle^\sigma$$

$$+\frac{1}{V_{\mathrm{REV}}}\int_{A_{\beta\sigma}}\mathbf{n}_{\beta\sigma}\cdot k_\sigma\nabla\tilde{T}_\sigma \mathrm{d}A\,. \quad (30)$$

We must then develop the closure problem for $\tilde{T}_\beta$ and $\tilde{T}_\sigma$ to complete the analysis.

3.1.2 Closure Problem

In order to develop a governing differential equation for $\tilde{T}_\beta$, rearrange Eq. (29) into

$$\left(\rho c_p\right)_\beta \frac{\partial \left\langle T_\beta \right\rangle^\beta}{\partial t} = \nabla \cdot \left(k_\beta \nabla \left\langle T_\beta \right\rangle^\beta\right) + \varepsilon_\beta^{-1} \nabla \cdot \left(\frac{k_\beta}{V_{\text{REV}}} \int_{A_{\beta\sigma}} \mathbf{n}_{\beta\sigma} \tilde{T}_\beta \mathrm{d}A\right) + \frac{\varepsilon_\beta^{-1}}{V_{\text{REV}}} \int_{A_{\beta\sigma}} \mathbf{n}_{\beta\sigma} \cdot k_\beta \nabla \tilde{T}_\beta \mathrm{d}A \tag{31}$$

Applying the decomposition in Eq. (19) and subtracting Eq. (31) from Eq. (1) yield a governing differential equation for $\tilde{T}_\beta$

$$\left(\rho c_p\right)_\beta \frac{\partial \tilde{T}_\beta}{\partial t} = \nabla \cdot \left(k_\beta \nabla \tilde{T}_\beta\right) \underbrace{- \varepsilon_\beta^{-1} \nabla \cdot \left(\frac{k_\beta}{V_{\text{REV}}} \int_{A_{\beta\sigma}} \mathbf{n}_{\beta\sigma} \tilde{T}_\beta \mathrm{d}A\right)}_{\text{non-local conduction}} - \frac{\varepsilon_\beta^{-1}}{V_{\text{REV}}} \int_{A_{\beta\sigma}} \mathbf{n}_{\beta\sigma} \cdot k_\beta \nabla \tilde{T}_\beta \mathrm{d}A \,. \tag{32}$$

Here we have used the word *non-local* to describe the term in which $\tilde{T}_\beta$ is evaluated at points different from the centroid of the averaging volume. We can simplify this result on the basis of the restriction

$$\nabla \cdot \left(k_\beta \nabla \tilde{T}_\beta\right) \gg \underbrace{\varepsilon_\beta^{-1} \nabla \cdot \left(\frac{k_\beta}{V_{\text{REV}}} \int_{A_{\beta\sigma}} \mathbf{n}_{\beta\sigma} \tilde{T}_\beta \mathrm{d}A\right)}_{\text{non-local conduction}} . \tag{33}$$

This restriction can be satisfied whenever $\ell_\beta \ll L$ [92, 95]; thus the non-local term will generally be negligible in the *spatial deviation transport equation* and the imposition of this restriction simplifies Eq. (32) significantly. The governing equation for $\tilde{T}_\sigma$ can be derived following the same procedure, and the boundary conditions for the spatial deviation temperatures are obtained directly from Eqs. (2) and (3), leading to the following closure problem

$$\left(\rho c_p\right)_\beta \frac{\partial \tilde{T}_\beta}{\partial t} = \nabla \cdot \left(k_\beta \nabla \tilde{T}_\beta\right) - \frac{\varepsilon_\beta^{-1}}{V_{\text{REV}}} \int_{A_{\beta\sigma}} \mathbf{n}_{\beta\sigma} \cdot k_\beta \nabla \tilde{T}_\beta \mathrm{d}A \tag{34}$$

$$\text{B.C.1} \qquad \tilde{T}_\beta = \tilde{T}_\sigma - \underbrace{\left(\left\langle T_\beta \right\rangle^\beta - \left\langle T_\sigma \right\rangle^\sigma\right)}_{\text{source}}, \qquad \text{at} \quad A_{\beta\sigma} \tag{35}$$

$$\text{B.C.2} \qquad \mathbf{n}_{\beta\sigma} \cdot k_\beta \nabla \tilde{T}_\beta = \mathbf{n}_{\beta\sigma} \cdot k_\sigma \nabla \tilde{T}_\sigma - \underbrace{\mathbf{n}_{\beta\sigma} \cdot k_\beta \nabla \left\langle T_\beta \right\rangle^\beta}_{\text{source}} + \underbrace{\mathbf{n}_{\beta\sigma} \cdot k_\sigma \nabla \left\langle T_\sigma \right\rangle^\sigma}_{\text{source}}, \text{ at } A_{\beta\sigma} \tag{36}$$

$$\left(\rho c_p\right)_\sigma \frac{\partial \tilde{T}_\sigma}{\partial t} = \nabla \cdot \left(k_\sigma \nabla \tilde{T}_\sigma\right) - \frac{\varepsilon_\sigma^{-1}}{V_{\mathrm{REV}}} \int_{A_{\beta\sigma}} \mathbf{n}_{\sigma\beta} \cdot k_\sigma \nabla \tilde{T}_\sigma \mathrm{d}A \,. \tag{37}$$

To simplify the closure problem, impose the quasi-steady condition

$$\frac{\alpha_\beta t^*}{\ell^2_\beta} \gg 1, \qquad \frac{\alpha_\sigma t^*}{\ell^2_\sigma} \gg 1 \tag{38}$$

in which α_β and α_σ are the thermal diffusivities for the β- and σ-phases. The closure problem can now be simplified to

$$0 = \nabla \cdot \left(k_\beta \nabla \tilde{T}_\beta\right) - \frac{\varepsilon_\beta^{-1}}{V_{\mathrm{REV}}} \int_{A_{\beta\sigma}} \mathbf{n}_{\beta\sigma} \cdot k_\beta \nabla \tilde{T}_\beta \mathrm{d}A \tag{39}$$

B.C.1 $$\tilde{T}_\beta = \tilde{T}_\sigma - \underbrace{\left(\left\langle T_\beta \right\rangle^\beta - \left\langle T_\sigma \right\rangle^\sigma\right)}_{\text{source}}, \quad \text{at} \quad A_{\beta\sigma} \tag{40}$$

B.C.2 $$\mathbf{n}_{\beta\sigma} \cdot k_\beta \nabla \tilde{T}_\beta = \mathbf{n}_{\beta\sigma} \cdot k_\sigma \nabla \tilde{T}_\sigma - \underbrace{\mathbf{n}_{\beta\sigma} \cdot k_\beta \nabla \left\langle T_\beta \right\rangle^\beta}_{\text{source}} + \underbrace{\mathbf{n}_{\beta\sigma} \cdot k_\sigma \nabla \left\langle T_\sigma \right\rangle^\sigma}_{\text{source}}, \text{ at } A_{\beta\sigma} \tag{41}$$

$$0 = \nabla \cdot \left(k_\sigma \nabla \tilde{T}_\sigma\right) - \frac{\varepsilon_\sigma^{-1}}{V_{\mathrm{REV}}} \int_{A_{\beta\sigma}} \mathbf{n}_{\sigma\beta} \cdot k_\sigma \nabla \tilde{T}_\sigma \mathrm{d}A \tag{42}$$

Average: $$\left\langle \tilde{T}_\beta \right\rangle^\beta = 0, \qquad \left\langle \tilde{T}_\sigma \right\rangle^\sigma = 0 \tag{43}$$

Periodicity: $\tilde{T}_\beta\left(\mathbf{r} + \ell_i\right) = \tilde{T}_\beta\left(\mathbf{r}\right)$, $\tilde{T}_\sigma\left(\mathbf{r} + \ell_i\right) = \tilde{T}_\sigma\left(\mathbf{r}\right)$, i=1,2,3, (44)

in which ℓ_i (i=1, 2, 3) are the lattice vectors. Here we have imposed a *periodicity condition* on the spatial deviation temperatures with the idea that we only need to solve the closure problem in some *representative region* that can be treated as a unit cell in a spatially periodic model of nanofluids. In addition to the periodicity condition, we also require that the average of the spatial deviation temperatures be zero; this is necessary in order to determine the value of the area integrals in Eqs. (39) and (42). We can make use of the flux boundary condition (3) to show that

$$\frac{1}{V_{\mathrm{REV}}} \int_{A_{\beta\sigma}} \mathbf{n}_{\beta\sigma} \cdot k_\beta \nabla \tilde{T}_\beta \mathrm{d}A = \frac{1}{V_{\mathrm{REV}}} \int_{A_{\beta\sigma}} \mathbf{n}_{\beta\sigma} \cdot k_\sigma \nabla \tilde{T}_\sigma \mathrm{d}A \,. \tag{45}$$

The evaluation of these integrals is available in [95, 101].

Given the three sources in the closure problem, we can follow [95, 100, 102] to express the spatial deviation temperatures by

$$\tilde{T}_\beta = \mathbf{b}_{\beta\beta} \cdot \nabla \left\langle T_\beta \right\rangle^\beta + \mathbf{b}_{\beta\sigma} \cdot \nabla \left\langle T_\sigma \right\rangle^\sigma - s_\beta \left(\left\langle T_\beta \right\rangle^\beta - \left\langle T_\sigma \right\rangle^\sigma \right) \tag{46a}$$

$$\tilde{T}_\sigma = \mathbf{b}_{\sigma\beta} \cdot \nabla \left\langle T_\beta \right\rangle^\beta + \mathbf{b}_{\sigma\sigma} \cdot \nabla \left\langle T_\sigma \right\rangle^\sigma - s_\sigma \left(\left\langle T_\sigma \right\rangle^\sigma - \left\langle T_\beta \right\rangle^\beta \right). \tag{46b}$$

The new variables, $\mathbf{b}_{\beta\beta}$, $\mathbf{b}_{\beta\sigma}$, s_β, $\mathbf{b}_{\sigma\beta}$, $\mathbf{b}_{\sigma\sigma}$ and s_σ, are the *closure variables* or the *mapping variables*, and we only need to determine these variables in some *representative region* in order to evaluate the terms in Eqs. (29) and (30) that contain the spatial deviation variables. The first closure problem is associated with $\nabla \left\langle T_\beta \right\rangle^\beta$ and takes the form

Problem I

$$0 = k_\beta \nabla^2 \mathbf{b}_{\beta\beta} - \varepsilon_\beta^{-1} \mathbf{c}_{\beta\beta}, \quad \text{in the } \beta\text{-phase} \tag{47a}$$

B.C.1 $$\mathbf{b}_{\beta\beta} = \mathbf{b}_{\sigma\beta}, \quad \text{at } A_{\beta\sigma} \tag{47b}$$

B.C.2 $$\mathbf{n}_{\beta\sigma} \cdot k_\beta \nabla \mathbf{b}_{\beta\beta} = \mathbf{n}_{\beta\sigma} \cdot k_\sigma \nabla \mathbf{b}_{\sigma\beta} - \mathbf{n}_{\beta\sigma} k_\beta, \quad \text{at } A_{\beta\sigma} \tag{47c}$$

$$0 = k_\sigma \nabla^2 \mathbf{b}_{\sigma\beta} + \varepsilon_\sigma^{-1} \mathbf{c}_{\beta\beta}, \quad \text{in the } \sigma\text{-phase} \tag{47d}$$

Periodicity: $\mathbf{b}_{\beta\beta}(\mathbf{r} + \ell_i) = \mathbf{b}_{\beta\beta}(\mathbf{r})$, $\mathbf{b}_{\sigma\beta}(\mathbf{r} + \ell_i) = \mathbf{b}_{\sigma\beta}(\mathbf{r})$, i=1,2,3 (47e)

Average: $$\left\langle \mathbf{b}_{\beta\beta} \right\rangle^\beta = 0, \quad \left\langle \mathbf{b}_{\sigma\beta} \right\rangle^\sigma = 0. \tag{47f}$$

Here $\mathbf{c}_{\beta\beta}$ is unknown integral represented by

$$\mathbf{c}_{\beta\beta} = \frac{1}{V_{\text{REV}}} \int_{A_{\beta\sigma}} \mathbf{n}_{\beta\sigma} \cdot k_\beta \nabla \mathbf{b}_{\beta\beta} \mathrm{d}A \tag{47g}$$

and it is the constraints on the averages of $\mathbf{b}_{\beta\beta}$ and $\mathbf{b}_{\sigma\beta}$ that allows us to determine the constant vector $\mathbf{c}_{\beta\beta}$. A detailed description of the evaluation of this unknown integral is available in [92, 95, 101].

The term $\nabla \left\langle T_\sigma \right\rangle^\sigma$ is also a source in the closure problem for $\tilde{T}_\beta$ and $\tilde{T}_\sigma$. The boundary value problem associated with the mapping variable for $\nabla \left\langle T_\sigma \right\rangle^\sigma$ is given by

Problem II

$$0 = k_\beta \nabla^2 \mathbf{b}_{\beta\sigma} - \varepsilon_\beta^{-1} \mathbf{c}_{\beta\sigma}, \quad \text{in the } \beta\text{-phase} \tag{48a}$$

B.C.1 $$\mathbf{b}_{\beta\sigma} = \mathbf{b}_{\sigma\sigma}, \quad \text{at } A_{\beta\sigma} \tag{48b}$$

B.C.2 $$\mathbf{n}_{\beta\sigma} \cdot k_\beta \nabla \mathbf{b}_{\beta\sigma} = \mathbf{n}_{\beta\sigma} \cdot k_\sigma \nabla \mathbf{b}_{\sigma\sigma} - \mathbf{n}_{\beta\sigma} k_\sigma, \quad \text{at } A_{\beta\sigma} \tag{48c}$$

$$0 = k_\sigma \nabla^2 \mathbf{b}_{\sigma\sigma} + \varepsilon_\sigma^{-1} \mathbf{c}_{\beta\sigma}, \quad \text{in the } \sigma\text{-phase} \tag{48d}$$

Periodicity: $\mathbf{b}_{\beta\sigma}(\mathbf{r} + \ell_i) = \mathbf{b}_{\beta\sigma}(\mathbf{r})$, $\mathbf{b}_{\sigma\sigma}(\mathbf{r} + \ell_i) = \mathbf{b}_{\sigma\sigma}(\mathbf{r})$, i=1,2,3 (48e)

Average: $$\langle \mathbf{b}_{\beta\sigma} \rangle^\beta = 0, \quad \langle \mathbf{b}_{\sigma\sigma} \rangle^\sigma = 0 \cdot \tag{48f}$$

Here the single undetermined constant is given by

$$\mathbf{c}_{\beta\sigma} = \frac{1}{V_{\text{REV}}} \int_{A_{\beta\sigma}} \mathbf{n}_{\beta\sigma} \cdot k_\beta \nabla \mathbf{b}_{\beta\sigma} \mathrm{d}A \tag{48g}$$

and can be evaluated by means of Eq. (48f).

The boundary value problem associated with the *mapping scalars* s_β and s_σ for $\langle T_\beta \rangle^\beta - \langle T_\sigma \rangle^\sigma$ is given by

Problem III

$$0 = k_\beta \nabla^2 s_\beta - \varepsilon_\beta^{-1} (a_v h), \quad \text{in the } \beta\text{-phase} \tag{49a}$$

B.C.1 $$\mathbf{n}_{\beta\sigma} \cdot k_\beta \nabla s_\beta = \mathbf{n}_{\beta\sigma} \cdot k_\sigma \nabla s_\sigma, \quad \text{at } A_{\beta\sigma} \tag{49b}$$

B.C.2 $$s_\beta = s_\sigma + 1, \quad \text{at } A_{\beta\sigma} \tag{49c}$$

$$0 = k_\sigma \nabla^2 s_\sigma + \varepsilon_\sigma^{-1} (a_v h), \quad \text{in the } \sigma\text{-phase} \tag{49d}$$

Periodicity: $s_\beta(\mathbf{r} + \ell_i) = s_\beta(\mathbf{r})$, $s_\sigma(\mathbf{r} + \ell_i) = s_\sigma(\mathbf{r})$, i=1,2,3 (49e)

Average: $\left\langle s_\beta \right\rangle^\beta = 0$, $\left\langle s_\sigma \right\rangle^\sigma = 0 \cdot$ (49f)

In this closure problem, the undetermined constant is

$$a_v h = \frac{1}{V_{\mathrm{REV}}} \int_{A_{\beta\sigma}} \mathbf{n}_{\beta\sigma} \cdot k_\beta \nabla s_\beta \mathrm{d}A \tag{49g}$$

and can be determined by means of Eq. (49f) [95, 101, 103].

3.1.3 Closed Forms

The closed forms of the β- and σ-phase heat-conduction equations can be obtained by applying the spatial deviation temperatures given by Eq. (46) into Eqs. (29) and (30). For the β-phase,

$$\varepsilon_\beta \left(\rho c_p\right)_\beta \frac{\partial \left\langle T_\beta \right\rangle^\beta}{\partial t} - \mathbf{u}_{\beta\beta} \cdot \nabla \left\langle T_\beta \right\rangle^\beta - \mathbf{u}_{\beta\sigma} \cdot \nabla \left\langle T_\sigma \right\rangle^\sigma$$

$$= \nabla \cdot \left(\mathbf{K}_{\beta\beta} \cdot \nabla \left\langle T_\beta \right\rangle^\beta + \mathbf{K}_{\beta\sigma} \cdot \nabla \left\langle T_\sigma \right\rangle^\sigma \right) - a_v h \left(\left\langle T_\beta \right\rangle^\beta - \left\langle T_\sigma \right\rangle^\sigma \right) \tag{50}$$

in which the *effective* thermal conductivity tensor $\mathbf{K}_{\beta\beta}$ and the *coupling* thermal conductivity tensor $\mathbf{K}_{\beta\sigma}$ are defined by

$$\mathbf{K}_{\beta\beta} = \varepsilon_\beta k_\beta \mathbf{I} + \frac{k_\beta}{V_{\mathrm{REV}}} \int_{A_{\beta\sigma}} \mathbf{n}_{\beta\sigma} \mathbf{b}_{\beta\beta} \mathrm{d}A \,, \tag{51}$$

$$\mathbf{K}_{\beta\sigma} = \frac{k_\beta}{V_{\mathrm{REV}}} \int_{A_{\beta\sigma}} \mathbf{n}_{\beta\sigma} \mathbf{b}_{\beta\sigma} \mathrm{d}A \,. \tag{52}$$

The heat transfer coefficient is determined by the solution of Problem Ⅲ, and the result is given by

$$a_v h = \frac{1}{V_{\mathrm{REV}}} \int_{A_{\beta\sigma}} \mathbf{n}_{\beta\sigma} \cdot k_\beta \nabla s_\beta \mathrm{d}A \,. \tag{53}$$

The two non-traditional convective transport terms in Eq. (50) depend on the coefficients $\mathbf{u}_{\beta\beta}$ and $\mathbf{u}_{\beta\sigma}$,

$$\mathbf{u}_{\beta\beta} = \frac{1}{V_{\mathrm{REV}}} \int_{A_{\beta\sigma}} \mathbf{n}_{\beta\sigma} \cdot k_\beta \nabla \mathbf{b}_{\beta\beta} \mathrm{d}A - \frac{k_\beta}{V_{\mathrm{REV}}} \int_{A_{\beta\sigma}} \mathbf{n}_{\beta\sigma} \cdot s_\beta \mathrm{d}A \,, \tag{54}$$

$$\mathbf{u}_{\beta\sigma} = \frac{1}{V_{\mathrm{REV}}} \int_{A_{\beta\sigma}} \mathbf{n}_{\beta\sigma} \cdot k_\beta \nabla \mathbf{b}_{\beta\sigma} \mathrm{d}A + \frac{k_\beta}{V_{\mathrm{REV}}} \int_{A_{\beta\sigma}} \mathbf{n}_{\beta\sigma} \cdot s_\beta \mathrm{d}A \,. \tag{55}$$

It is interesting to note that in the closed form of the β-phase heat-conduction equation we have discarded the term $k_\beta \nabla \varepsilon_\beta \cdot \nabla \left\langle T_\beta \right\rangle^\beta$ which appear in Eq. (29) as part of the interfacial flux. For a process in which this term is *not negligible*, it is likely that the errors occurring in the three closure problems are also *non-negligible* [102].

The closed form of the σ-phase transport equation is

$$\varepsilon_\sigma \left(\rho c_p\right)_\sigma \frac{\partial \left\langle T_\alpha \right\rangle^\sigma}{\partial t} - \mathbf{u}_{\sigma\beta} \cdot \nabla \left\langle T_\beta \right\rangle^\beta - \mathbf{u}_{\sigma\sigma} \nabla \left\langle T_\alpha \right\rangle^\sigma = \nabla \cdot \left(\mathbf{K}_{\sigma\beta} \cdot \nabla \left\langle T_\beta \right\rangle^\beta + \mathbf{K}_{\sigma\sigma} \cdot \nabla \left\langle T_\sigma \right\rangle^\sigma \right)$$

$$- a_v h \left(\left\langle T_\sigma \right\rangle^\sigma - \left\langle T_\beta \right\rangle^\beta \right) \tag{56}$$

in which the *coupling* thermal conductivity tensor $\mathbf{K}_{\sigma\beta}$ and the *effective* thermal conductivity tensor $\mathbf{K}_{\sigma\sigma}$ are defined by [95]

$$\mathbf{K}_{\sigma\beta} = \mathbf{K}_{\beta\sigma} = \frac{k_\sigma}{V_{\mathrm{REV}}} \int_{A_{\beta\sigma}} \mathbf{n}_{\sigma\beta} \mathbf{b}_{\sigma\beta} \mathrm{d}A \,, \tag{57}$$

$$\mathbf{K}_{\sigma\sigma} = \varepsilon_\sigma k_\sigma \mathbf{I} + \frac{k_\sigma}{V_{\mathrm{REV}}} \int_{A_{\beta\sigma}} \mathbf{n}_{\sigma\beta} \mathbf{b}_{\sigma\sigma} \mathrm{d}A \,. \tag{58}$$

The velocity-like coefficients are given by

$$\mathbf{u}_{\sigma\beta} = \frac{1}{V_{\mathrm{REV}}} \int_{A_{\sigma\beta}} \mathbf{n}_{\sigma\beta} \cdot k_\sigma \nabla \mathbf{b}_{\sigma\beta} \mathrm{d}A - \frac{k_\sigma}{V_{\mathrm{REV}}} \int_{A_{\sigma\beta}} \mathbf{n}_{\sigma\beta} s_\sigma \mathrm{d}A \,, \tag{59}$$

$$\mathbf{u}_{\sigma\sigma} = \frac{1}{V_{\mathrm{REV}}} \int_{A_{\sigma\beta}} \mathbf{n}_{\sigma\beta} \cdot k_\sigma \nabla \mathbf{b}_{\sigma\sigma} \mathrm{d}A + \frac{k_\sigma}{V_{\mathrm{REV}}} \int_{A_{\sigma\beta}} \mathbf{n}_{\sigma\beta} s_\sigma \mathrm{d}A \,. \tag{60}$$

It can also been shown that [95]

$$\mathbf{K}_{\sigma\beta} = \mathbf{K}_{\beta\sigma} \,, \tag{61}$$

$$\mathbf{u}_{\beta\beta} + \mathbf{u}_{\beta\sigma} + \mathbf{u}_{\sigma\beta} + \mathbf{u}_{\sigma\sigma} = 0 \,. \tag{62}$$

3.2 Thermal Waves

Rewrite Eqs. (50) and (56) in their operator form [16, 35, 91]

$$\begin{bmatrix} \gamma_\beta \dfrac{\partial}{\partial t} - \mathbf{u}_{\beta\beta} \cdot \nabla - \nabla \cdot (\mathbf{K}_{\beta\beta} \cdot \nabla) + a_v h & -\mathbf{u}_{\beta\sigma} \cdot \nabla - \nabla \cdot (\mathbf{K}_{\beta\sigma} \cdot \nabla) - a_v h \\ -\mathbf{u}_{\sigma\beta} \cdot \nabla - \nabla \cdot (\mathbf{K}_{\sigma\beta} \cdot \nabla) - a_v h & \gamma_\sigma \dfrac{\partial}{\partial t} - \mathbf{u}_{\sigma\sigma} \cdot \nabla - \nabla \cdot (\mathbf{K}_{\sigma\sigma} \cdot \nabla) \end{bmatrix} \begin{bmatrix} \left\langle T_\beta \right\rangle^\beta \\ \left\langle T_\sigma \right\rangle^\sigma \end{bmatrix} = 0 \cdot \tag{63}$$

We then obtain a uncoupled form by evaluating the operator determinant such that

$$\left[\left(\gamma_\beta \frac{\partial}{\partial t} - \mathbf{u}_{\beta\beta}\cdot\nabla - \nabla\cdot(\mathbf{K}_{\beta\beta}\cdot\nabla) + a_v h\right)\left(\gamma_\sigma \frac{\partial}{\partial t} - \mathbf{u}_{\sigma\sigma}\cdot\nabla - \nabla\cdot(\mathbf{K}_{\sigma\sigma}\cdot\nabla)\right)\right.$$

$$\left. -\left(\mathbf{u}_{\beta\sigma}\cdot\nabla + \nabla\cdot(\mathbf{K}_{\beta\sigma}\cdot\nabla) + a_v h\right)\left(\mathbf{u}_{\sigma\beta}\cdot\nabla + \nabla\cdot(\mathbf{K}_{\sigma\beta}\cdot\nabla) + a_v h\right)\right]\langle T_i\rangle^i = 0, \tag{64}$$

where the index i can take β or σ. $\gamma_\beta = \varepsilon_\beta(\rho c)_\beta$ and $\gamma_\sigma = \varepsilon_\sigma(\rho c)_\sigma$ are the β-phase and σ-phase effective thermal capacities, respectively. Its explicit form reads, after dividing by $a_v h(\gamma_\beta + \gamma_\sigma)$ [16, 35, 91]

$$\frac{\partial\langle T_i\rangle^i}{\partial t} + \frac{\gamma_\beta\gamma_\sigma}{a_v h(\gamma_\beta+\gamma_\sigma)}\frac{\partial^2\langle T_i\rangle^i}{\partial t^2} = \frac{1}{\gamma_\beta+\gamma_\sigma}\left[\nabla\cdot(\mathbf{K}_{\beta\beta}\cdot\nabla) + 2\nabla\cdot(\mathbf{K}_{\beta\sigma}\cdot\nabla) + \nabla\cdot(\mathbf{K}_{\sigma\sigma}\cdot\nabla)\right]\langle T_i\rangle^i$$

$$+\frac{1}{a_v h(\gamma_\beta+\gamma_\sigma)}\left\{\gamma_\beta\frac{\partial}{\partial t}\left[\nabla\cdot(\mathbf{K}_{\sigma\sigma}\cdot\nabla)\right] + \gamma_\sigma\frac{\partial}{\partial t}\left[\nabla\cdot(\mathbf{K}_{\beta\beta}\cdot\nabla)\right]\right\}\langle T_i\rangle^i$$

$$+\frac{1}{a_v h(\gamma_\beta+\gamma_\sigma)}\left\{\left\{\left[\nabla\cdot(\mathbf{K}_{\beta\sigma}\cdot\nabla)\right]\left[\nabla\cdot(\mathbf{K}_{\sigma\beta}\cdot\nabla)\right] - \left[\nabla\cdot(\mathbf{K}_{\beta\beta}\cdot\nabla)\right]\left[\nabla\cdot(\mathbf{K}_{\sigma\sigma}\cdot\nabla)\right]\right\}\langle T_i\rangle^i\right.$$

$$+\left[\gamma_\beta\frac{\partial}{\partial t}\left(\mathbf{u}_{\sigma\sigma}\cdot\nabla\langle T_i\rangle^i\right) + \gamma_\sigma\frac{\partial}{\partial t}\left(\mathbf{u}_{\beta\beta}\cdot\nabla\langle T_i\rangle^i\right)\right]$$

$$-\left\{\left(\mathbf{u}_{\beta\beta}\cdot\nabla\right)\left[\nabla\cdot(\mathbf{K}_{\sigma\sigma}\cdot\nabla)\right] + \left(\mathbf{u}_{\sigma\sigma}\cdot\nabla\right)\left[\nabla\cdot(\mathbf{K}_{\beta\beta}\cdot\nabla)\right] - \left(\mathbf{u}_{\beta\sigma}\cdot\nabla\right)\left[\nabla\cdot(\mathbf{K}_{\sigma\beta}\cdot\nabla)\right]\right.$$

$$\left.\left.-\left(\mathbf{u}_{\sigma\beta}\cdot\nabla\right)\left[\nabla\cdot(\mathbf{K}_{\beta\sigma}\cdot\nabla)\right]\right\}\langle T_i\rangle^i - \left[\left(\mathbf{u}_{\beta\beta}\cdot\nabla\right)\left(\mathbf{u}_{\sigma\sigma}\cdot\nabla\right) - \left(\mathbf{u}_{\beta\sigma}\cdot\nabla\right)\left(\mathbf{u}_{\sigma\beta}\cdot\nabla\right)\right]\langle T_i\rangle^i\right\}\cdot \tag{65}$$

When the system is isotropic and the physical properties of the two phases are constant, it reduces to

$$\frac{\partial\langle T_i\rangle^i}{\partial t} + \tau_q\frac{\partial^2\langle T_i\rangle^i}{\partial t^2} = \alpha\,\Delta\langle T_i\rangle^i + \alpha\tau_T\frac{\partial}{\partial t}\left(\Delta\langle T_i\rangle^i\right) + \frac{\alpha}{k}\left[F(\mathbf{r},t) + \tau_q\frac{\partial F(\mathbf{r},t)}{\partial t}\right], \tag{66}$$

where

$$\tau_q = \frac{\gamma_\beta\gamma_\sigma}{h a_\upsilon(\gamma_\beta+\gamma_\sigma)}, \tag{67}$$

$$\tau_T = \frac{\gamma_\beta k_{\sigma\sigma} + \gamma_\sigma k_{\beta\beta}}{h a_\upsilon(k_{\beta\beta}+k_{\sigma\sigma}+2k_{\beta\sigma})}, \tag{68}$$

$$k = k_{\beta\beta} + k_{\sigma\sigma} + 2k_{\beta\sigma}, \tag{69}$$

$$\alpha = \frac{k_{\beta\beta} + k_{\sigma\sigma} + 2k_{\beta\sigma}}{\gamma_\beta + \gamma_\sigma}, \tag{70}$$

$$F(\mathbf{r},\, t) + \tau_q \frac{\partial F(\mathbf{r},\, t)}{\partial t} = \frac{1}{a_v h}\left\{\left(k_{\beta\sigma}^2 - k_{\beta\beta}k_{\sigma\sigma}\right)\Delta^2 \left\langle T_i \right\rangle^i + \left[\gamma_\beta \frac{\partial}{\partial t}\left(\mathbf{u}_{\sigma\sigma}\cdot\nabla\left\langle T_i\right\rangle^i\right) + \gamma_\sigma \frac{\partial}{\partial t}\left(\mathbf{u}_{\beta\beta}\cdot\nabla\left\langle T_i\right\rangle^i\right)\right]\right.$$

$$-\left\{k_{\sigma\sigma}\Delta\left(\mathbf{u}_{\beta\beta}\cdot\nabla\right) + k_{\beta\beta}\Delta\left(\mathbf{u}_{\sigma\sigma}\cdot\nabla\right) - k_{\sigma\beta}\Delta\left(\mathbf{u}_{\beta\sigma}\cdot\nabla\right) - k_{\beta\sigma}\Delta\left(\mathbf{u}_{\sigma\beta}\cdot\nabla\right)\right\}\left\langle T_i\right\rangle^i$$

$$\left.-\left[\left(\mathbf{u}_{\beta\beta}\cdot\nabla\right)\left(\mathbf{u}_{\sigma\sigma}\cdot\nabla\right) - \left(\mathbf{u}_{\beta\sigma}\cdot\nabla\right)\left(\mathbf{u}_{\sigma\beta}\cdot\nabla\right)\right]\left\langle T_i\right\rangle^i\right\}. \tag{71}$$

This is a dual-phase-lagging heat-conduction equation with τ_q and τ_T as the phase lags of the heat flux and the temperature gradient, respectively [16, 35, 91, 104, 105]. Here, $F(\boldsymbol{r},t)$ is the volumetric heat source. k, ρc and α are the effective thermal conductivity, capacity and diffusivity of nanofluids, respectively. Therefore, the presence of nanoparticles shifts the Fourier heat conduction in the base fluid into the dual-phase-lagging heat conduction in nanofluids at the macroscale. This is significant because all results regarding dual-phase-lagging heat conduction can thus be applied to study heat conduction in nanofluids [91, 104-107].

It is interesting to note that there are non-traditional convective terms $-\mathbf{u}_{\beta\beta}\cdot\nabla\left\langle T_\beta\right\rangle^\beta - \mathbf{u}_{\beta\sigma}\cdot\nabla\left\langle T_\sigma\right\rangle^\sigma$ and $-\mathbf{u}_{\sigma\beta}\cdot\nabla\left\langle T_\beta\right\rangle^\beta - \mathbf{u}_{\sigma\sigma}\nabla\left\langle T_\alpha\right\rangle^\sigma$ in Eqs. (50) and (56), respectively. In Eq. (66), however, such terms disappear because of the constraint in Eq. (62). Therefore, the microscale physics does not manifest itself as the macroscale convection. The velocity-like terms appear only in the source term in Eq. (66).

The dual-phase-lagging heat conduction equation originates from the first law of thermodynamics and the dual-phase-lagging constitutive relation of heat flux density [91, 104, 106]. It was developed in examining energy transport involving the high-rate heating in which the non-equilibrium thermodynamic transition and the microstructural effect become important associated with shortening of the response time. In addition to its application in the ultrafast pulse-laser heating, the dual-phase-lagging heat conduction equation also arises in describing and predicting phenomena such as propagating of temperature pulses in superfluid liquid helium, nonhomogeneous lagging response in porous media, thermal lagging in amorphous materials, and effects of material defects and thermomechanical coupling [104]. Furthermore, the dual-phase-lagging heat conduction equation forms a generalized, unified equation with the classical parabolic heat-conduction equation, the hyperbolic heat-conduction equation, the energy

equation in the phonon scattering model, and the energy equation in the phonon-electron interaction model as its special cases [91, 104]. This, with the rapid growth of microscale heat conduction of high-rate heat flux, has attracted the recent research effort on dual-phase-lagging heat conduction: its physical basis and experimental verification, well-posedness, solution structure, analytical and numerical solutions, methods of measuring thermal relaxation times, thermal oscillation and resonance, and equivalence with and application in two-phase-system heat conduction [91, 104].

The dual-phase-lagging heat conduction has been shown to be admissible by the second law of the extended irreversible thermodynamics and by the Boltzmann transport equation [91, 104]. It is also proven to be well-posed in a finite region of n-dimension ($n \geq 1$) under any linear boundary conditions including Dirichlet, Neumann and Robin types [91, 106-108]. The solution structure theorems have been developed as well for both mixed and Cauchy problems of dual-phase-lagging heat-conduction equations [91, 106-108]. These theorems inter-relate contributions (to the temperature field) of the initial temperature distribution, the source term and the initial time-rate change of the temperature, uncover the structure of temperature field and considerably simplify the development of solutions. The thermal oscillation and resonance in the dual-phase-lagging heat conduction have also been examined in [91, 109, 110]. Conditions and features of underdamped, critically-damped and overdamped oscillations have been obtained and compared with those in the classical parabolic heat conduction and the hyperbolic heat conduction [91]. The condition for the thermal resonance is also available in [91, 109].

The presence of nanoparticles gives rise to variations of thermal capacity, conductivity and diffusivity, which are given by, in terms of ratios over those of the base fluid,

$$\frac{\rho c}{(\rho c)_\beta} = (1-\varepsilon_\sigma) + \varepsilon_\sigma \frac{(\rho c)_\sigma}{(\rho c)_\beta}, \tag{72}$$

$$\frac{k}{k_\beta} = \frac{k_{\beta\beta} + k_{\sigma\sigma} + 2k_{\beta\sigma}}{k_\beta}, \tag{73}$$

$$\frac{\alpha}{\alpha_\beta} = \frac{k}{k_\beta}\frac{(\rho c)_\beta}{\rho c}. \tag{74}$$

Therefore, $\rho c/(\rho c)_\beta$ depends *only* on the volume fraction of nanoparticles and the nanoparticle-fluid capacity ratio. However, both k/k_β and α/α_β are affected by the geometry, property and dynamic process of nanoparticle-fluid interfaces. This dependency causes the most difficulty because it is the least precisely known feature of a nanofluid. The future research effort should thus focus on

$(k_{\beta\beta} + k_{\sigma\sigma} + 2k_{\beta\sigma})/k_{\beta}$ to develop predicting models of thermal conductivity for nanofluids.

Consider

$$\frac{\tau_T}{\tau_q} = 1 + \frac{\gamma_\beta^2 k_{\sigma\sigma} + \gamma_\sigma^2 k_{\beta\beta} - 2\gamma_\beta\gamma_\sigma k_{\beta\sigma}}{\gamma_\beta\gamma_\sigma(k_{\beta\beta} + k_{\sigma\sigma} + 2k_{\beta\sigma})}. \tag{75}$$

It can be large, equal or smaller than 1 depending on the sign of $\gamma_\beta^2 k_{\sigma\sigma} + \gamma_\sigma^2 k_{\beta\beta} - 2\gamma_\beta\gamma_\sigma k_{\beta\sigma}$. Therefore, by the condition for the existence of thermal waves that requires $\tau_T/\tau_q < 1$ [91, 109], we may have thermal waves in nanofluid heat conduction when

$$\gamma_\beta^2 k_{\sigma\sigma} + \gamma_\sigma^2 k_{\beta\beta} - 2\gamma_\beta\gamma_\sigma k_{\beta\sigma} = \left(\gamma_\beta\sqrt{k_{\sigma\sigma}} - \gamma_\sigma\sqrt{k_{\beta\beta}}\right)^2 + 2\gamma_\beta\gamma_\sigma(\sqrt{k_{\beta\beta}k_{\sigma\sigma}} - k_{\beta\sigma}) < 0. \tag{76}$$

A necessary (but not sufficient) condition for Eq. (76) is $k_{\beta\sigma} > \sqrt{k_{\beta\beta}k_{\sigma\sigma}}$. Note also that for heat conduction in nanofluids there is a time-dependent source term $F(\boldsymbol{r},t)$ in the dual-phase-lagging heat conduction [Eqs. (66) and (71)]. Therefore, the resonance can also occur. These thermal waves and possibly resonance are believed to be the driving force for the conductivity enhancement. When $k_{\beta\sigma}$=0 so that τ_T/τ_q is always larger than 1, thermal waves and resonance would not appear. The coupled conductive terms in Eqs. (50) and (56) are thus responsible for thermal waves and resonance in nanofluid heat conduction. It is also interesting to note that although each τ_q and τ_T is ha_v-dependent, the ratio τ_T/τ_q is not. Therefore the evaluation of τ_T/τ_q will be much simpler than τ_q or τ_T.

Addition of 4% of Al_2O_3 particles was reported to increase thermal conductivity by a factor of 8% [19], while CuO particles at the same volume fraction enhance the conductivity by about 12% [32]. This is interesting because conductivity of CuO is less than that of Al_2O_3. The thermal wave theory can explain this since the conductivity enhancement k/k_β equals to $(k_{\beta\beta} + k_{\sigma\sigma} + 2k_{\beta\sigma})/k_\beta$ [Eq. (73)], which are strongly affected by nanofluids microstructures and interfacial properties/ processes of nanoparticle-fluid interfaces.

Therefore, the molecular physics and the microscale physics (interactions between nanoparticles and base fluids at the microscale in particular) manifest themselves as heat diffusion and thermal waves at the macroscale, respectively. Their overall macroscopic manifestation shifts the Fourier heat conduction in the base fluid into the dual-phase-lagging heat conduction in nanofluids. When $\tau_T/\tau_q < 1$, thermal waves dominant and Eq. (66) is of a hyperbolic type [91, 106, 107, 110]. When $\tau_T/\tau_q \geq 1$, however, heat diffusion dominants and Eq. (66) is parabolic [91,

Table 2 Measured conductivity ratio k/k_r of some nanofluids (k: nanofluid thermal conductivity; k_r: water thermal conductivity for $CePO_4$ nanofluids and residual fluid thermal conductivity for the others)

Nanofluids	$CePO_4$ nanofibers in water [16, 20]	Cu_2O spherical particles in water [47]	Cu_2O octahedral particles in water [47]	CuS/Cu_2S hollow spherical particles in water [46]	CuS/Cu_2S core-shell spherical particles in water [46]	Olive oil droplets in water [16]
k/k_r	0.67~1.54	0.83~1.24	0.89~1.24	0.85~1.18	0.82~1.21	0.636~2.533

106, 107, 110]. Depending on factors like material properties of nanoparticles and base fluids, nanoparticles' geometrical structure and their distribution in the base fluids, and interfacial properties and dynamic processes on particle-fluid interfaces, the heat diffusion and thermal waves may either enhance or counteract each other. Consequently, the heat conduction may be enhanced or weakened by the presence of nanoparticles. Table 2 lists the conductivity ratio k/k_r measured by the standard transient hot-wire method (also called transient line-source method; KD2, Decagon Devices, USA). Here k and k_r are the thermal conductivity of the nanofluid and the residual fluid (the left fluid after removing the nanoparticles by strongly centrifugation), respectively. It shows that: (i) the interaction between the heat diffusion and the thermal waves can either upgrade or downgrade fluid conductivity by the presence of higher-conductivity nanoparticles, and (ii) extraordinary water conductivity enhancement (up to 153%) can be achievable by the presence of lower-conductivity oil droplets due to strong thermal waves.

The immediate and intensive efforts should thus focus on: (i) solving the three closure problems analytically and numerically for unit cells with various microscale physics to find the correlation between the microscale physics and the nanofluid macroscale properties (effective thermal conductivity, effective thermal diffusivity, phase lag of the heat flux τ_q, and phase lag of the temperature gradient τ_T); (ii) studying the dual-phase-lagging heat conduction equation Eq. (66) analytically and numerically for various nanofluids systems to find properties of thermal waves and how they interact with the heat diffusion. Focused experiments in these areas are also in great demand for experimentally confirming the analytical/numerical findings. Such studies, together with the development of microfluidic nanofluids should lead to methodologies of controlling nanofluids macroscale properties through manipulating their microscale physics, a significant step forward towards creating nanofluids by design. The first of Type-(i) work has recently been made in [111] with three two-dimensional unit cells in Fig. 9, showing that the model developed

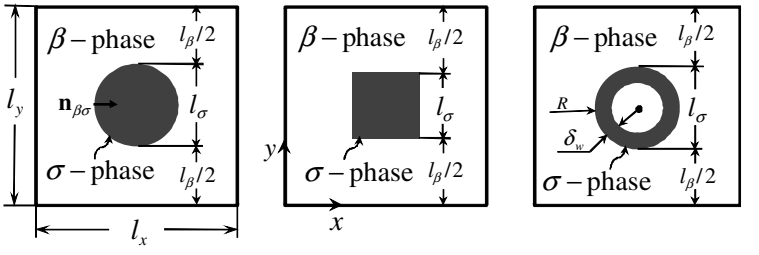

Fig. 9 Three types of unit cells of in-line arrays of cylinders used in [111]: (a) circular cylinders; (b) square cylinders; (c) hollow cylinders

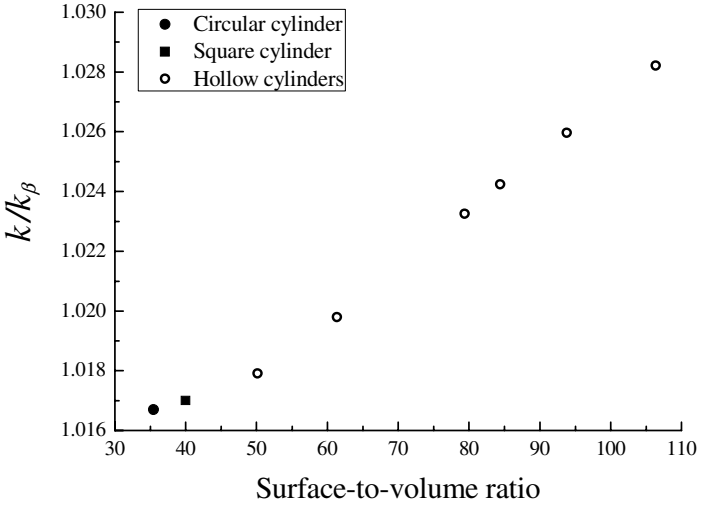

Fig. 10 Variation of thermal conductivity ratio k/k_β with particle surface-to-volume ratio at $\phi = 0.01$ and $k_\sigma/k_\beta = 10$ [111]

here works very well and uncovering some important features regarding the model itself and the microstructure-conductivity correlation. For example, the effective thermal conductivity obtained by using spatially periodic unit cells in the three closure problems is essentially identical to that without imposing such a periodic boundary condition [111]. The effective thermal conductivity also depends on the particle surface-to-volume ratio sensitively (Fig. 10).

4 Megascale Optimization: Constructal Nanofluids

In the field of nanofluid heat conduction, efforts have been nearly exclusively on correlating thermal conductivity of nanofluids with their microscale physics, as a fundamental step of searching for optimal thermal conductivity [1-3, 16, 30-34]. The attention to system megascale properties has been very limited. However, practical applications of nanofluids as the heat-conduction fluids have often with a different ultimate aim such as minimization of system highest temperature and minimization of system overall thermal resistance. Therefore, interest should focus not only on optimizing nanofluid macroscale properties but also on designing nanofluids for the best system performance at megascale.

By its very nature, the optimization of microscale physics for the best system performance at megascale fits well into the design with constructal theory [112-114]. First developed in the late 1990s, the constructal theory holds that flow architecture arises from the natural evolutionary tendency to generate greater flow access in time and in flow configurations that are free to morph [112]. The constructal theory unites nature with engineering and helps us generate novel designs across the board [112]. It also complements the march toward micro and nano scales with the sobering reminder that useful devices must always be macroscopic, and that larger and larger numbers of small-scale components must be assembled and connected by flows that keep them alive. The real challenge is *to construct*, to assemble and optimize while assembling, and to generate complex multi-scale flow architectures [112-114].

A flow system studied in the constructal theory distinguishes it from a static system by following properties [112]: (i) global external size *L*, (ii) global internal size, (iii) at least one global objective or performance at megascale, (iv) configuration, drawing, architecture, and (v) freedom to morph (freedom to change the configuration). All nanofluid systems are endowed with these five properties. The external and internal sizes are the length scale of the body bathed by the nanofluids and the total volume of the nanoparticles inside nanofluids, respectively. For any application of nanofluids, we do have at least one global objective, for example, minimizing the global heat-flow resistance in the systems that apply nanofluids as the heat transfer fluids. The nanoparticles' structure and distribution in base fluids form configuration, drawing, or architecture of nanofluid systems. Nanofluids are endowed with the freedom to change microscale structures as well for the best megascale performance. Here, we present the constructal design of nanofluids through optimizing the distribution of particle volume fraction and particle microstructure in some simple megascale systems to illustrate the fundamental principles.

4.1 Constructal Design of Particle Volume Fraction

Consider nanofluid heat conduction in four systems [115]: a circular domain of radius R_o (System 1, Fig. 11(a)), a sphere of radius R_o (System 2, Fig. 11(b)), a

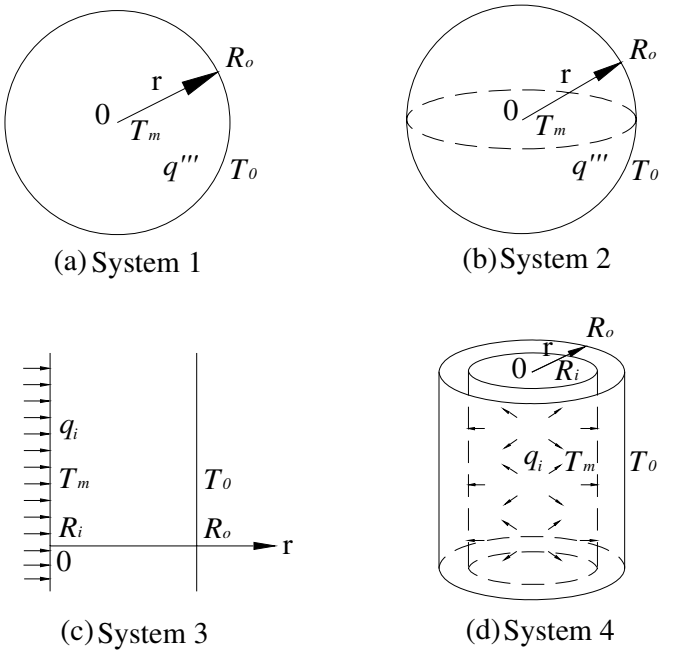

Fig. 11 Heat conduction in four systems of nanofluids: (a) a circular disc of radius R_o and unit thickness (System 1); (b) a sphere of radius R_o (System 2); (c) a plane slab of thickness $R_o - R_i$ (System 3); (d) a circular annulus of inner radius R_i and outer radius R_o (System 4) [115]

plane slab of thickness $R_o - R_i$ (System 3, Fig. 11(c)), and a circular annulus of inner radius R_i and outer radius R_o (System 4, Fig. 11(d)). The temperature at $r = R_o$ is maintained at a fixed value T_0 for all four systems. The volumetric heat generation rate q''' is constant in Systems 1 and 2, where the disc thickness in System 1 is unit. In Systems 3 and 4, a constant heat flux input q_i occurs at $r = R_i$. For the coordinates shown in Fig. 11, the one-dimensional (along *r*-direction) steady heat conduction equation is:

$$\frac{1}{r^m}\frac{d}{dr}[kr^m\frac{dT}{dr}] = -pq''', \tag{77}$$

Where m and p values are listed in Table 3 for each of the four systems. k is the effective thermal conductivity of nanofluids. Here we consider four types of nanofluids

Table 3 m and p values for four systems [115]

Systems	**System 1 (Fig. 11a)**	**System 2 (Fig. 11b)**	**System 3 (Fig. 11c)**	**System 4 (Fig. 11d)**
***m* and *p* values**	$m=1,\ p=1$	$m=2,\ p=1$	$m=0,\ p=0$	$m=1,\ p=0$

whose effective thermal conductivity satisfies Birchak, Laudau & Lifshitz, Lichtenecker and Maxwell formulas, respectively [3]. The first three can be written as:

$$k = k_f\{1+v[(\frac{k_p}{k_f})^{1/n}-1]\}^n, \tag{78}$$

where n values are listed in Table 4 for each of the three types of nanofluids. k_p and k_f are the thermal conductivities of particles and base fluids, respectively, and are assumed to be material constants. v is the particle volume fraction. For the Maxwell nanofluids,

$$k = k_f + 3k_f \frac{k_p - k_f}{2k_f + k_p - (k_p - k_f)v(r)}v. \tag{79}$$

The composition of the nanoparticles and the base fluid is fixed, and is accounted for by the particle volume fraction

$$\phi = \frac{\text{volume of } k_p \text{ material}}{\text{total volume}}. \tag{80}$$

Our goal is to search for the constructal $v(r)$ to minimize the system highest temperature T_m that appears at $r=0$ for Systems 1 and 2 and at $r=R_i$ for Systems 3 and 4. We detail the process of finding the constructal $v(r)$ by using Eq. (78)

Table 4 n values for the three types of nanofluids [115]

Nanofluids	**Value of n**
Birchak	$n=2$
Laudau & Lifshitz	$n=3$
Lichtenecker	$n\to\infty$

for the effective thermal conductivity. The results for the Maxwell nanofluids can be readily obtained by using a similar approach and are listed directly in Tables.

4.1.1 Case of $p=1$

By integrating Eq. (77) with respect to *r* from 0 to r, we obtain

$$\frac{dT}{dr}=\frac{-q'''r}{(m+1)k}. \tag{81}$$

Substituting Eq. (78) and integrating again with respect to *r* from 0 to R_o yield

$$T_m-T_0=\int_0^{R_o}\frac{q'''r}{(m+1)k_f\{1+v(r)[(\frac{k_p}{k_f})^{1/n}-1]\}^n}dr. \tag{82}$$

The fixed composition constraint for the case *p*=1 can be written as

$$\int_0^{R_o}(v(r)-\phi)r^m dr=0. \tag{83}$$

Minimizing (T_m-T_0) under the constraint (83) is the same as minimizing [116]

$$J=\int_0^{R_o}F(r)dr, \tag{84}$$

where

$$F(r)=\frac{q'''r}{(m+1)k_f\{1+v(r)[(\frac{k_p}{k_f})^{1/n}-1]\}^n}+\lambda r^m[v(r)-\phi], \tag{85}$$

and λ is the Lagrangian multiplier.

Minimizing *J* by applying Euler-Lagrange equation [116]

$$F_{v(r)}-\frac{d}{dr}F_{v'(r)}=-\frac{nq'''r[(\frac{k_p}{k_f})^{1/n}-1]}{(m+1)k_f\{1+v(r)[(\frac{k_p}{k_f})^{1/n}-1]\}^{n+1}}+\lambda r^m=0 \tag{86}$$

yields,

$$v(r)=\{\frac{nq'''}{(m+1)\lambda k_f[(\frac{k_p}{k_f})^{1/n}-1]^n r^{m-1}}\}^{1/(n+1)}-\frac{1}{[(\frac{k_p}{k_f})^{1/n}-1]}. \tag{87}$$

Substituting Eq. (87) into Eq. (83) leads to

$$\lambda = \frac{nq'''}{(m+1)[1+\frac{1-m}{(m+1)(n+1)}]^{n+1} k_f [(\frac{k_p}{k_f})^{1/n}-1]^n \{\phi + \frac{1}{[(\frac{k_p}{k_f})^{1/n}-1]}\}^{n+1} R_o^{m-1}}. \tag{88}$$

Therefore, we obtain the constructal $v(r)$

$$v_{\text{con}}(r) = [1+\frac{1-m}{(m+1)(n+1)}]\{\phi + \frac{1}{[(\frac{k_p}{k_f})^{1/n}-1]}\}(\frac{R_o}{r})^{\frac{m-1}{n+1}} - \frac{1}{[(\frac{k_p}{k_f})^{1/n}-1]}. \tag{89}$$

Since

$$F_{v(r)v(r)} - \frac{d}{dr}(F_{v(r)v'(r)}) = \frac{n(n+1)q'''r[(\frac{k_p}{k_f})^{1/n}-1]^2}{(m+1)k_f\{1+v(r)[(\frac{k_p}{k_f})^{1/n}-1]\}^{n+2}} > 0 \tag{90}$$

and

$$F_{v'(r)v'(r)} = 0, \tag{91}$$

the $v_{\text{con}}(r)$ in Eq. (89) is indeed the constructal distribution of particle volume fraction that minimizes the system highest temperature T_m (Table 5).

Substituting Eq. (89) into Eq. (82) yields the constructal overall temperature difference $(T_m - T_0)_{\text{con}}$ that is the minimal $(T_m - T_0)$,

$$(T_m - T_0)_{\text{con}} = \frac{q''' R_0^2}{\frac{(mn+n+2)^{n+1}}{(m+1)^{n-1}(n+1)^{n+1}} k_f \{1+\phi[(\frac{k_p}{k_f})^{1/n}-1]\}^n} \tag{92}$$

which is listed in Table 6 for different combinations of *m* and *n*. Table 7 lists the corresponding constructal overall thermal resistance $R_{\text{th,con}}$ (normalized by using $1/k_f$) that is the minimal overall thermal resistance.

4.1.2 Case of $p = 0$

By integrating Eq. (77) with respect to r from R_i to r, we obtain

$$(kr^m \frac{dT}{dr})_{r=r} - (kr^m \frac{dT}{dr})_{r=R_i} = 0. \tag{93}$$

Table 5 Constructal volume fraction distributions [115]

Systems / Nanofluids	System 1 (Fig. 11a)	System 2 (Fig. 11b)	System 3 (Fig. 11c)	System 4 (Fig. 11d)
Birchak	$v_{con}(r)=\phi$	$v_{con}(r)=\frac{8}{9}\{\phi+\frac{1}{[(\frac{k_p}{k_f})^{1/2}-1]}\}(\frac{r}{R_o})^{-1/3}-\frac{1}{[(\frac{k_p}{k_f})^{1/2}-1]}$	$v_{con}(r)=\phi$	$v_{con}(r)=\frac{2[1-(\frac{R_i}{R_o})^2]}{3[1-(\frac{R_i}{R_o})^{4/3}]}\{\phi+\frac{1}{[(\frac{k_p}{k_f})^{1/2}-1]}\}(\frac{r}{R_o})^{-2/3}-\frac{1}{[(\frac{k_p}{k_f})^{1/2}-1]}$
Laudau & Lifshitz	$v_{con}(r)=\phi$	$v_{con}(r)=\frac{11}{12}[\phi+\frac{1}{(\frac{k_p}{k_f})^{1/3}-1}](\frac{r}{R_o})^{-1/4}-\frac{1}{[(\frac{k_p}{k_f})^{1/3}-1]}$	$v_{con}(r)=\phi$	$v_{con}(r)=\frac{3[1-(\frac{R_i}{R_o})^2]}{4[1-(\frac{R_i}{R_o})^{3/2}]}\{\phi+\frac{1}{[(\frac{k_p}{k_f})^{1/3}-1]}\}(\frac{r}{R_o})^{-1/2}-\frac{1}{[(\frac{k_p}{k_f})^{1/3}-1]}$
Lichtenecker	$v_{con}(r)=\phi$	$v_{con}(r)=-\frac{\ln(r/R_o)}{\ln(k_p/k_f)}+\phi-\frac{1}{3\ln(k_p/k_f)}$	$v_{con}(r)=\phi$	$v_{con}(r)=\frac{1}{\ln(k_p/k_f)}[-2\ln\frac{r}{R_o}-\frac{2(\frac{R_i}{R_o})^2}{1-(\frac{R_i}{R_o})^2}\ln\frac{R_i}{R_o}+\phi\ln\frac{k_p}{k_f}-1]$
Maxwell	$v_{con}(r)=\phi$	$v_{con}(r)=\frac{5}{6}[\phi+\frac{2+k_p/k_f}{2(k_p/k_f-1)}](\frac{r}{R_o})^{-1/2}-\frac{2+k_p/k_f}{2(k_p/k_f-1)}$	$v_{con}(r)=\phi$	$v_{con}(r)=\frac{1}{2}(1+\frac{R_i}{R_o})[\phi+\frac{2+k_p/k_f}{2(k_p/k_f-1)}](\frac{r}{R_o})^{-1}-\frac{2+k_p/k_f}{2(k_p/k_f-1)}$

Table 6 Constructal overall temperature difference [115]

Systems / Nanofluids	System 1 (Fig. 11a)	System 2 (Fig. 11b)	System 3 (Fig. 11c)	System 4 (Fig. 11d)
Birchak	$(T_m-T_0)_{\text{con}}=\frac{q'''R_o^2}{4}\frac{1}{k_\phi}$; $k_\phi=k_f\{1+\phi[(\frac{k_p}{k_f})^{1/2}-1]\}^2$	$(T_m-T_0)_{\text{con}}=\frac{81q'''R_o^2}{512}\frac{1}{k_\phi}$; $k_\phi=k_f\{1+\phi[(\frac{k_p}{k_f})^{1/2}-1]\}^2$	$(T_m-T_0)_{\text{con}}=q_i(R_o-R_i)\frac{1}{k_\phi}$; $k_\phi=k_f\{1+\phi[(\frac{k_p}{k_f})^{1/2}-1]\}^2$	$(T_m-T_0)_{\text{con}}=\frac{27(R_o^{4/3}-R_i^{4/3})^3q_iR_i}{16(R_o^2-R_i^2)^2}\frac{1}{k_\phi}$; $k_\phi=k_f\{1+\phi[(\frac{k_p}{k_f})^{1/2}-1]\}^2$
Laudau & Lifshitz	$(T_m-T_0)_{\text{con}}=\frac{q'''R_o^2}{4}\frac{1}{k_\phi}$; $k_\phi=k_f\{1+\phi[(\frac{k_p}{k_f})^{1/3}-1]\}^3$	$(T_m-T_0)_{\text{con}}=\frac{2304q'''R_o^2}{14641}\frac{1}{k_\phi}$; $k_\phi=k_f\{1+\phi[(\frac{k_p}{k_f})^{1/3}-1]\}^3$	$(T_m-T_0)_{\text{con}}=q_i(R_o-R_i)\frac{1}{k_\phi}$; $k_\phi=k_f\{1+\phi[(\frac{k_p}{k_f})^{1/3}-1]\}^3$	$(T_m-T_0)_{\text{con}}=\frac{128(R_o^{3/2}-R_i^{3/2})^4q_iR_i}{81(R_o^2-R_i^2)^3}\frac{1}{k_\phi}$; $k_\phi=k_f\{1+\phi[(\frac{k_p}{k_f})^{1/3}-1]\}^3$
Lichtenecker	$(T_m-T_0)_{\text{con}}=\frac{q'''R_o^2}{4}\frac{1}{k_\phi}$; $k_\phi=k_f\left(k_p/k_f\right)^\phi$	$(T_m-T_0)_{\text{con}}=\frac{e^{1/3}q'''R_o^2}{9}\frac{1}{k_\phi}$; $k_\phi=k_f\left(k_p/k_f\right)^\phi$	$(T_m-T_0)_{\text{con}}=q_i(R_o-R_i)\frac{1}{k_\phi}$; $k_\phi=k_f\left(k_p/k_f\right)^\phi$	$(T_m-T_0)_{\text{con}}=\frac{(R_o^2-R_i^2)eq_iR_i}{2R_o^{\frac{2R_o^2}{R_o^2-R_i^2}}R_i^{1-\frac{R_o^2+R_i^2}{R_o^2-R_i^2}}}\frac{1}{k_\phi}$; $k_\phi=k_f\left(k_p/k_f\right)^\phi$
Maxwell	$(T_m-T_0)_{\text{con}}=\frac{q'''R_o^2}{4}\frac{1}{k_\phi}$; $k_\phi=k_f[1+\frac{3(k_p-k_f)\phi}{2k_f+k_p-(k_p-k_f)\phi}]$	$(T_m-T_0)_{\text{con}}=\frac{3q'''R_o^2(2k_f+k_p)}{25k_f(k_p-k_f)[\phi+\frac{2k_f+k_p}{2(k_p-k_f)}]}$ $-\frac{q'''R_o^2}{12k_f}\approx\frac{47}{300}q'''R_o^2\frac{1}{k_\phi}$ (approximation for the case of $\phi\ll1$); $k_\phi=k_f[1+\frac{3(k_p-k_f)\phi}{2k_f+k_p-(k_p-k_f)\phi}]$	$(T_m-T_0)_{\text{con}}=q_i(R_o-R_i)\frac{1}{k_\phi}$; $k_\phi=k_f[1+\frac{3(k_p-k_f)\phi}{2k_f+k_p-(k_p-k_f)\phi}]$	$(T_m-T_0)_{\text{con}}=\frac{6q_iR_i(R_o-R_i)(2k_f+k_p)}{2(R_o+R_i)k_f[2(k_p-k_f)\phi+2k_f+k_p]}$ $-\frac{q_iR_i\ln\frac{R_o}{R_i}(R_o+R_i)[2k_f+k_p+2(k_p-k_f)\phi]}{2(R_o+R_i)k_f[2(k_p-k_f)\phi+2k_f+k_p]}$ $\approx\ln\frac{R_o}{R_i}q_iR_i\frac{1}{k_\phi}$ (approximation for the case of $\frac{R_i}{R_o}$ from 0.5 to 1); $k_\phi=k_f[1+\frac{3(k_p-k_f)\phi}{2k_f+k_p-(k_p-k_f)\phi}]$

Since

$$(-k\frac{dT}{dr})_{r=R_i} = q_i\,, \tag{94}$$

Eq. (93) becomes

$$\frac{dT}{dr} = \frac{-q_i R_i^m}{kr^m}\,. \tag{95}$$

Substituting Eq. (78) and integrating again with respect to *r* from R_i to R_o yield

$$T_m - T_0 = \int_{R_i}^{R_o} \frac{q_i R_i^m}{r^m k_f \{1+v(r)[(\frac{k_p}{k_f})^{1/n}-1]\}^n}\,dr\,. \tag{96}$$

The fixed composition constraint for the case $p=0$ can be written as

$$\int_{R_i}^{R_o} (v(r)-\phi)r^m dr = 0\,. \tag{97}$$

Minimizing $(T_m - T_0)$ under the constraint (97) is the same as minimizing [116]

$$J = \int_0^{R_o} F(r)dr\,, \tag{98}$$

where

$$F(r) = \frac{q_i R_i^m}{r^m k_f \{1+v(r)[(\frac{k_p}{k_f})^{1/n}-1]\}^n} + \lambda r^m [v(r)-\phi]\,, \tag{99}$$

and λ is the Lagrangian multiplier.

Minimizing *J* by applying Euler-Lagrange equation [116]

$$F_{v(r)} - \frac{d}{dr}F_{v'(r)} = -\frac{nq_i R_i^m [(\frac{k_p}{k_f})^{1/n}-1]}{k_f r^m \{1+v(r)[(\frac{k_p}{k_f})^{1/n}-1]\}^{n+1}} + \lambda r^m = 0 \tag{100}$$

yields,

$$v(r) = \{\frac{nq_i R_i^m}{\lambda k_f [(\frac{k_p}{k_f})^{1/n}-1]^n r^{2m}}\}^{1/(n+1)} - \frac{1}{[(\frac{k_p}{k_f})^{1/n}-1]}\,. \tag{101}$$

Substituting Eq. (101) into Eq. (97) leads to

$$\lambda = \frac{nq_i R_i^m}{[\frac{mn-m+n+1}{(m+1)(n+1)}]^{n+1} k_f [(\frac{k_p}{k_f})^{1/n}-1]^n \{\phi + \frac{1}{[(\frac{k_p}{k_f})^{1/n}-1]}\}^{n+1} [\frac{R_o^{m+1}-R_i^{m+1}}{R_o^{\frac{mn-m+n+1}{n+1}} - R_i^{\frac{mn-m+n+1}{n+1}}}]^{n+1}}. \quad (102)$$

Therefore, we obtain the constructal $v(r)$

$$v_{\text{con}}(r) = \{\phi + \frac{1}{[(\frac{k_p}{k_f})^{1/n}-1]}\} [\frac{R_o^{m+1}-R_i^{m+1}}{R_o^{\frac{mn-m+n+1}{n+1}} - R_i^{\frac{mn-m+n+1}{n+1}}}] [\frac{mn-m+n+1}{(m+1)(n+1)}] r^{\frac{-2m}{n+1}} - \frac{1}{[(\frac{k_p}{k_f})^{1/n}-1]}. \quad (103)$$

Since

$$F_{v(r)v(r)} - \frac{d}{dr}(F_{v(r)v'(r)}) = \frac{n(n+1)q_i R_i^m [(\frac{k_p}{k_f})^{1/n}-1]^2}{k_f r^m \{1+v(r)[(\frac{k_p}{k_f})^{1/n}-1]\}^{n+2}} > 0 \quad (104)$$

and

$$F_{v'(r)v'(r)} = 0, \quad (105)$$

the $v_{\text{con}}(r)$ in Eq. (103) is indeed the constructal distribution of particle volume fraction that minimizes the system highest temperature T_m (Table 5).

Substituting Eq. (103) into Eq. (96) yields the constructal overall temperature difference $(T_m - T_0)_{\text{con}}$

$$(T_m - T_0)_{\text{con}} = \frac{q_i R_i^m (R_o^{\frac{mn-m+n+1}{n+1}} - R_i^{\frac{mn-m+n+1}{n+1}})^{n+1}}{\frac{(mn-m+n+1)^{n+1}}{(m+1)^n (n+1)^{n+1}} (R_o^{m+1}-R_i^{m+1})^n k_f \{1+\phi[(\frac{k_p}{k_f})^{1/n}-1]\}^n}, \quad (106)$$

which is listed in Table 6 for different combinations of *m* and *n*. The corresponding constructal overall thermal resistance $R_{\text{th,con}}$ (normalized by using $1/k_f$) is listed in Table 7.

4.1.3 Discussion

Both constructal overall temperature difference $(T_m - T_0)_{\text{con}}$ and thermal resistance $R_{\text{th,con}}$ are proportional to k_ϕ^{-1} for all four systems, where k_ϕ is the effective

Table 7 Constructal overall thermal resistance [115]

Systems	**Constructal overall thermal resistance**
System 1 (Fig. 11a)	$R_{\text{th,con}} = \dfrac{(T_m - T_0)_{\text{con}} k_f}{q''' \pi R_o^2 \times 1} = \dfrac{1}{4\pi} \dfrac{k_f}{k_\phi}$
System 2 (Fig. 11b)	**Birchak**: $R_{\text{th,con}} = \dfrac{(T_m - T_0)_{\text{con}} k_f}{q''' \times 4\pi R_o^3 / 3} = \dfrac{243}{2048\pi R_o} \dfrac{k_f}{k_\phi}$; **Laudau & Lifshitz**: $R_{\text{th,con}} = \dfrac{(T_m - T_0)_{\text{con}} k_f}{q''' \times 4\pi R_o^3 / 3} = \dfrac{576}{14641\pi R_o} \dfrac{k_f}{k_\phi}$; **Lichtenecker**: $R_{\text{th,con}} = \dfrac{(T_m - T_0)_{\text{con}} k_f}{q''' \times 4\pi R_o^3 / 3} = \dfrac{e^{1/3}}{12\pi R_o} \dfrac{k_f}{k_\phi}$; **Maxwell**: $R_{\text{th,con}} = \dfrac{(T_m - T_0)_{\text{con}} k_f}{q''' \times 4\pi R_o^3 / 3} == \dfrac{3}{4\pi R_o} \dfrac{(6 - \frac{25}{12})(2k_f + k_p) - \frac{50}{12}(k_p - k_f)\phi}{25[2k_f + k_p + 2(k_p - k_f)\phi]} \approx \dfrac{47}{400\pi R_o} \dfrac{k_f}{k_\phi}$ (approximation for the case of $\phi \ll 1$)
System 3 (Fig. 11c)	$R_{\text{th,con}} = \dfrac{(T_m - T_o)_{\text{con}} k_f}{q_i \times 1 \times 1} = (R_o - R_i) \dfrac{k_f}{k_\phi}$
System 4 (Fig. 11d)	**Birchak**: $R_{\text{th,con}} = \dfrac{(T_m - T_0)_{\text{con}} k_f}{q_i \pi R_i \times 1} = \dfrac{27(R_o^{4/3} - R_i^{4/3})^3}{16\pi (R_o^2 - R_i^2)^2} \dfrac{k_f}{k_\phi}$; **Laudau & Lifshitz**: $R_{\text{th,con}} = \dfrac{(T_m - T_o)_{\text{con}} k_f}{q_i \pi R_i \times 1} = \dfrac{128(R_o^{3/2} - R_i^{3/2})^4}{81\pi (R_o^2 - R_i^2)^3} \dfrac{k_f}{k_\phi}$; **Lichtenecker**: $R_{\text{th,con}} = \dfrac{(T_m - T_o)_{\text{con}} k_f}{q_i \pi R_i \times 1} = \dfrac{e(R_o^2 - R_i^2)}{2\pi R_o^{\frac{2R_o^2}{R_o^2 - R_i^2}} R_i^{1 - \frac{R_o^2 + R_i^2}{R_o^2 - R_i^2}}} \dfrac{k_f}{k_\phi}$; **Maxwell**: $R_{\text{th,con}} = \dfrac{(T_m - T_0)_{\text{con}} k_f}{q_i \pi R_i \times 1} =$ $\dfrac{6(R_o - R_i) - (R_o + R_i) \ln \frac{R_o}{R_i}}{2\pi (R_o + R_i)}](2k_f + k_p) - \dfrac{1}{\pi} \ln \dfrac{R_o}{R_i} (k_p - k_f)\phi}{[2(k_p - k_f)\phi + 2k_f + k_p]} \approx \dfrac{1}{\pi} \ln \dfrac{R_o}{R_i} \dfrac{k_f}{k_\phi}$ (approximation for the case of R_i / R_o from 0.5 to 1)

thermal conductivity evaluated at the overall (average) particle volume fraction ϕ (Tables 6 and 7). The proportional coefficients for $R_{\text{th,con}}$ are either invariant for Systems 1-3 or nearly invariant for System 4 with respect to types of nanofluids (Table 7). Therefore, the constructal thermal resistance $R_{\text{th,con}}$ is indeed an

overall property fixed only by the system global geometry and the average thermal conductivity of nanofluids used in the system. Efforts in upgrading thermal conductivity of nanofluids at macroscale also do lead to reduction of constructal overall thermal resistance at megascale.

However, the constructal particle volume fraction v_{con} (the way by which to realize the constructal thermal resistance) is either a global property invariant with the types and the details of nanofluids for Systems 1 and 3, or a property depending on the types and the details of nanofluids for Systems 2 and 4 (Table 5, Figs. 12 and 13). The march toward synthesizing uniformly-dispersed nanofluids [1-3, 16, 30-34] not necessarily leads to the constructal nanofluids that maximize system overall performance. For example, the constructal nanofluids used in Systems 2 and 4 are with a decreasing particle volume fraction from $r = 0$ or $r = R_i$ where the heat flux is high to $r = R_o$ where the heat flux is lower (Figs. 12 and 13); they depend not only on system global geometry (R_i / R_0) and nanofluid global property (ϕ) but also on the types and the details (k_p / k_f) of nanofluids.

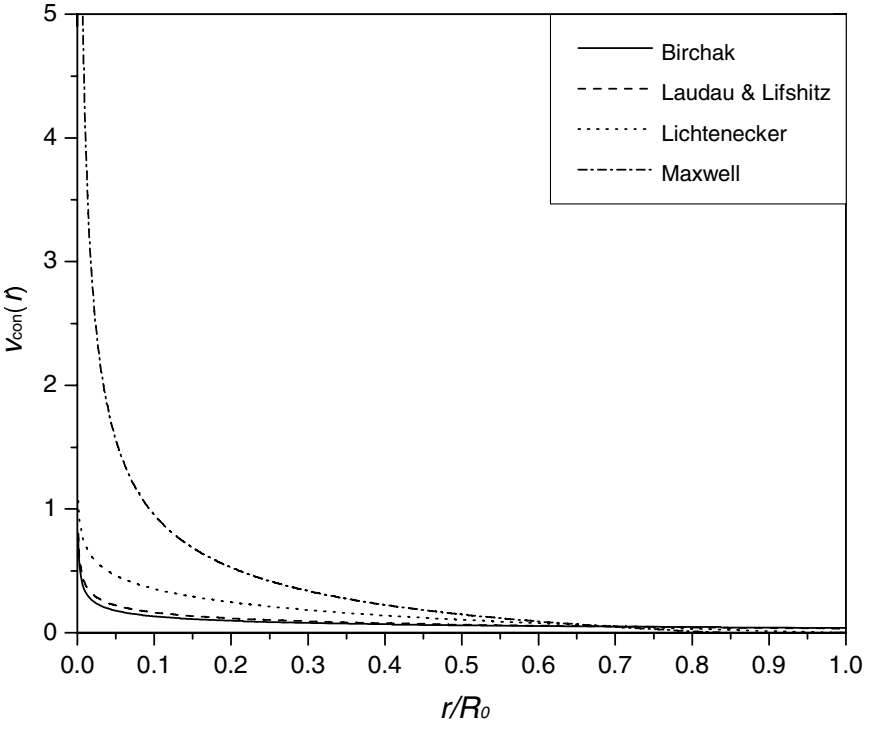

Fig. 12 Distribution of constructal particle volume fraction for System 2 at $\phi = 0.05$ and $k_p / k_f = 385 / 0.6$ (thermal conductivity ratio of copper and water) (after [115])

A uniform distribution of particle volume fraction distribution as the constructal volume fraction is expected for System 3 because the heat flux is uniform everywhere in the system. It comes as a surprise, however, for System 1 in which the heat flux decreases from the center to the periphery. This could represent some kind of new phenomena that demand the further study in the future.

In summary, the constructal overall thermal resistance $R_{\text{th,con}}$ is inversely proportional to the effective thermal conductivity evaluated at the global (average) particle volume fraction ϕ for all four systems. The proportional coefficients are invariant or nearly invariant with respect to types of nanofluids. The constructal particle volume fraction of nanofluids to materialize this $R_{\text{th,con}}$ is a uniform distribution for Systems 1 and 3 (circular disc and plane slab), and a non-uniform distribution with a higher particle volume fraction in the higher heat-flux region for Systems 2 and 4 (sphere and circular annulus). Therefore, the constructal overall thermal resistance can be reduced through enhancing the thermal conductivity of nanofluids at macroscale. The constructal nanofluids that maximize the system

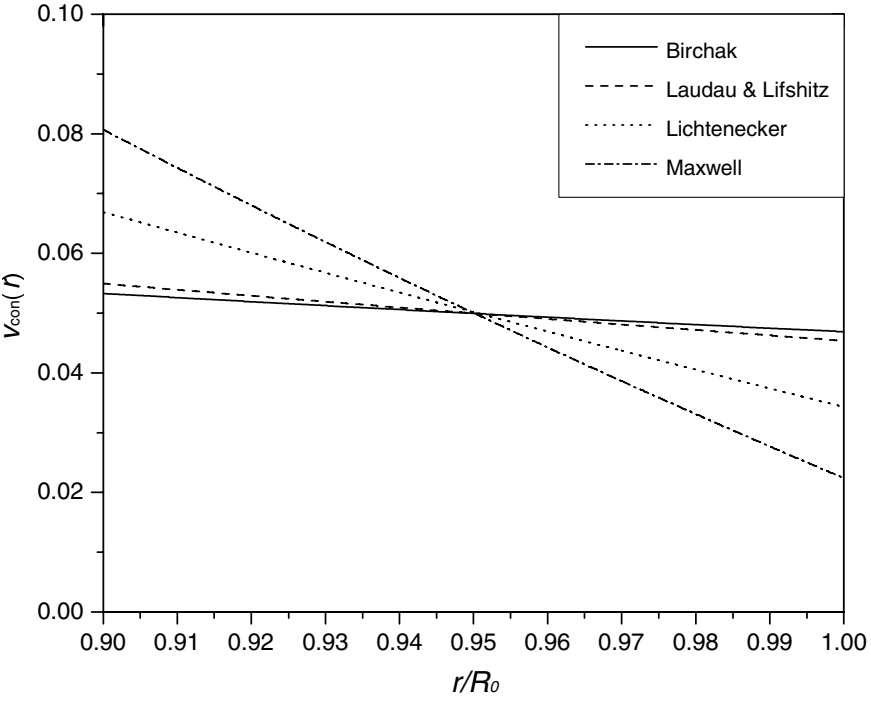

Fig. 13 Distribution of constructal particle volume fraction for System 4 at $R_i/R_o = 0.9$, $\phi = 0.05$ and $k_p/k_f = 385/0.6$ (thermal conductivity ratio of copper and water) (after [115])

megascale performance are not necessarily the ones with uniformly-dispersed particles in base fluids. Our focus of nanofluids research and development should thus be not only on nanofluids themselves but also on their systems and ultimate megascale goals.

4.2 Constructal Microstructure

Consider nanofluid heat conduction in a circular disk of radius R and unit thickness, with uniform distribution of volumetric heat generation rate q''' and one central heat sink (T_0) (Fig. 14) [117]. Nanoparticles are assumed to be thin slab of the width D of high thermal conductivity. The composition of the nanoparticles and the base fluid is fixed, and is accounted for by the particle volume fraction

$$\phi = \frac{\text{volume of } k_p \text{ material}}{\text{total volume}}. \tag{107}$$

Our goal is to optimize the geometry of the heat-conduction paths for minimizing the overall thermal resistance, that is, the hot-spot temperature $T_{\rm m}$, which is likely to occur on the rim.

4.2.1 Zero Branching Architecture

The simplest architecture is the one with no slab branching and the slabs arranged radially and equidistantly with one end touching the heat sink and the other touching the rim (Fig. 14) [112, 117]. A circular sector with adiabatic radial sides (dashed lines in Fig. 14) is associated with each k_p slab. We assume that there are many radial k_p slabs so that one sector is sufficiently slender and can be approximated by an isosceles triangle of base $2H$ and height R (Fig. 15). The area of the elemental sector is fixed,

$$A_s = HR \tag{108}$$

while both H and R may vary. The second constraint is the volume fraction of k_p material

$$\phi = \frac{D\,R}{H\,R} = \frac{D}{H}. \tag{109}$$

For the sake of simplicity in analysis, we assume that: (i) the width D is constant; (ii) the k_p volume fraction is fixed and small, $\phi \ll 1$, and (iii) the ratio of thermal conductivities is fixed and large.

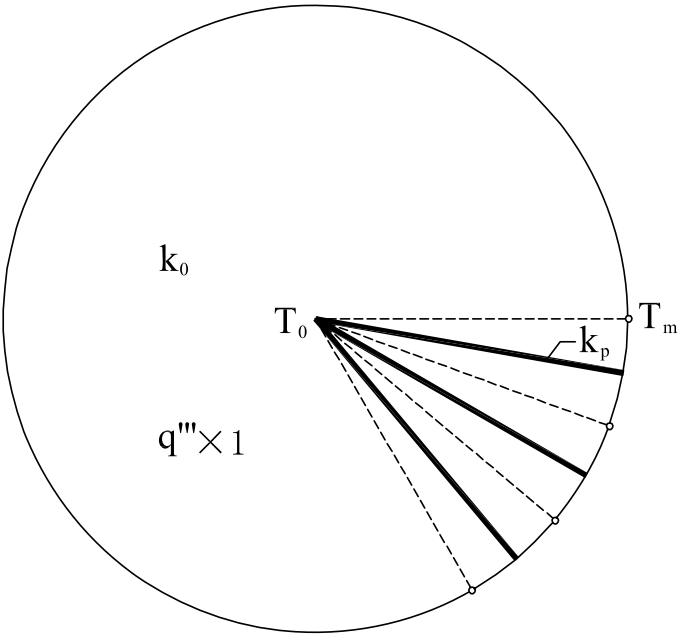

Fig. 14 Nanofluid heat conduction in a circular disk of radius R: zero branching architecture (after [117])

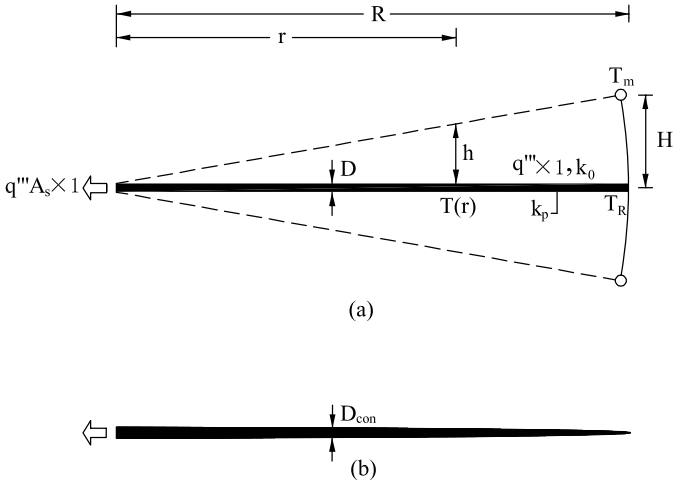

Fig. 15 Constructal sector: (a) circular sector with high-conductivity slab on its center line; (b) constructal slab shape (after [117])

$$\tilde{k} = \frac{k_p}{k_f} \gg 1 \tag{110}$$

Assumption (iii) means that the k_p slab is sufficiently thin and can be represented by the axis of symmetry in Fig. 15 (the $T_R - T_0$ line).

The main unknown of the architecture (freedom) is the aspect ratio of the element, H/R. The objective in constructing H/R is to minimize the overall thermal resistance of the sector,

$$R_{\text{sth}} = \frac{T_{\text{m}} - T_0}{q''' A_s} \tag{111}$$

where $q''' A_s$ is the heat current generated over the entire sector. This can be evaluated by a two-part analysis: calculating $(T_{\text{m}} - T_R)$ and $(T_R - T_0)$. This decoupling is possible because under assumptions (ii) and (iii) the heat conduction through the k_f material is perpendicular to the k_p slab, and the conduction through the k_p material is oriented along the slab [118].

For the vertical k_f heat conduction along the line $T_{\text{m}} - T_R$, the heat-conduction equation is

$$\frac{d^2T}{dy^2} + \frac{q'''}{k_f} = 0 \tag{112}$$

where y is oriented in vertical direction in Fig. 15. The two boundary conditions are:

$$T = T_R \quad \text{at} \quad y = 0 \tag{113}$$

$$\frac{dT}{dy} = 0 \qquad \text{at} \quad y = H \cdot \tag{114}$$

The solution of Eq. (112) under Eqs. (113) and (114) is [112]

$$T = \frac{q'''}{k_f}\left(Hy - \frac{y^2}{2}\right) + T_R \cdot \tag{115}$$

By applying Eq. (115) to the top end of the H-tall line we obtain

$$T_{\text{m}} - T_R = \frac{q''' H^2}{2k_0} \cdot \tag{116}$$

For the heat conduction along the k_p slab, the increase in heat flux q at position r is

$$-dq = 2hq''' \times 1 \, dr \tag{117}$$

where $hq''' \times 1$ is the heat current collected over the vertical surface $h \times 1$, where $h = (H/R)r$. The heat current is proportional to the local temperature gradient:

$$q = k_p \, D \times 1 \frac{dT}{dr}. \tag{118}$$

$(T_R - T_0)$ can be determined by eliminating q from Eqs. (117) and (118), integrating twice with respect to r, and invoking the boundary conditions $dT/dr = 0$ at $r = R$, and $T = T_0$ at $r = 0$. The result is [117]

$$T_R - T_0 = \frac{2q''' R^2}{3k_p \phi}. \tag{119}$$

The overall resistance of the elemental sector is obtained by adding Eqs. (116) and (119), and normalizing R_{sth} by using $1/k_f$,

$$\tilde{R}_{sth} = \frac{T_m - T_0}{q''' A_s / k_f} = \frac{1}{2}\frac{H}{R} + \frac{2}{3\tilde{k}\varphi}\frac{R}{H}. \tag{120}$$

This expression can be minimized with respect to H/R, and the results are [117]

$$\left(\frac{H}{R}\right)_{con} = \frac{2}{(3\tilde{k}\varphi)^{1/2}} \ll 1 \tag{121}$$

$$\frac{(T_m - T_0)_{con}}{q''' A_s / k_f} = \frac{2}{(3\tilde{k}\varphi)^{1/2}}. \tag{122}$$

Equation (121) shows that the assumed slenderness of the optimized sector is consistent with assumption (iii): the ratio of conductivities $\tilde{k}$ must exceed $1/\phi$ in an order of magnitude sense [112].

The constructal aspect ratio (121) fixes the constructal tip angle of the sector. It also fixes the constructal number of such sectors that fit in a complete disc arrangement, $N = 2\pi R/(2H)$, namely,

$$N_{con} = \frac{\pi}{2}(3\tilde{k}\varphi)^{1/2} \gg 1. \tag{123}$$

The constructal size of the disc is thus,

$$\pi R_{\text{con}}{}^2 = N_{\text{con}} A_s = \frac{\pi}{2}(3\tilde{k}\varphi)^{1/2}\ A_s. \tag{124}$$

Larger discs (R) emerge when $\tilde{k}\phi$ increases. The corresponding constructal thermal resistance of the entire disc is obtained by using $N_{\text{con}} A_s$ instead of A_s in Eq. (122):

$$R_{0\text{th,con}} = \frac{(T_{\text{m}} - T_0)_{\text{con}}}{q''' N_{\text{con}}\ A_s / k_f} = \frac{4}{3\pi\tilde{k}\varphi}. \tag{125}$$

The radius of the disc-shaped construct is, from Eq. (124):

$$R_{\text{con}} = (A_s/2)^{1/2}\ (3\tilde{k}\varphi)^{1/4}. \tag{126}$$

The size of the construct (R) is not known in priori. It is the result of construction, that is, the assembly and the constraints that govern the smallest-scale element (A_s,ϕ, $\tilde{k}$). Aggregation, organization, growth and complexity are the result of geometric constraints – trying to fit together a number of smaller optimized parts [112]. A key role is played by the product $\tilde{k}\phi$: larger values of this parameter mean more high-conductivity slabs, more slender slabs, and a disc-shaped construct with larger radius R [112].

For $R_{0\text{th,con}}$ to be smaller than the constructal overall thermal resistance $R_{\text{th,con}}$ in Section 4.1 (Table 7, System 1), we requires

$$\frac{R_{0th,\text{con}}}{R_{\text{th,con}}} = \frac{16}{3}\frac{k_\phi}{\phi k_p} < 1, \tag{127}$$

or

$$\frac{k_\phi}{\phi k_p} < \frac{3}{16}. \tag{128}$$

It is the condition for the recommended transition from a uniform distribution of particle volume fraction to a radial pattern.

Further improvements in the performance of the construct can be made by relaxing some of the simplifying assumptions, increasing the number of degrees of freedom of the design, and optimizing the design with respect to the new degrees of freedom. Instead a constant-D, for example, consider the general function $D(r)$ that is subjected to the same volume fraction constraint:

$$\phi = \frac{1}{HR} \int_0^R D \, dr \cdot \tag{129}$$

The choice of k_p slab profile $D(r)$ affects the global resistance through the part $T_R - T_0$. This relationship is obtained by eliminating q from Eqs. (117) and (118), integrating the resulting equation once with respect to r, invoking $dT/dr = 0$ at $r = R$, and finally integrating from $r = 0$ to $r = R$:

$$T_R - T_0 = \frac{q''' H}{k_p R} \int_0^R \frac{R^2 - r^2}{D} dr \, . \tag{130}$$

By applying the same variational approach as in Section 4.1, we obtain the constructal shape [117]

$$D_{\text{con}} = \frac{4}{\pi} \phi \, H \left[1 - \left(\frac{r}{R} \right)^2 \right]^{1/2} \cdot \tag{131}$$

The optimal shape of the high-conductivity slab is such that the root is thicker and the tip is blunt (note $dD/dr = -\infty$ at $r = R$), as shown in Fig. 15 (b). With $D_{\text{con}}(r)$ in Eq. (131), we have

$$\left(\frac{H}{R} \right)_{\text{con}} = \frac{\pi/2}{(2\tilde{k}\varphi)^{1/2}} \tag{132}$$

$$\frac{(T_{\text{m}} - T_0)_{\text{con}}}{q''' A_s / k_0} = \frac{\pi/2}{(2\tilde{k}\varphi)^{1/2}} \tag{133}$$

$$N_{\text{con}} = 2(2\tilde{k}\varphi)^{1/2} \gg 1 \tag{134}$$

$$\frac{(T_{\text{m}} - T_0)_{\text{con}}}{q''' N_{\text{con}} A_s / k_0} = \frac{\pi}{8\tilde{k}\varphi} \tag{135}$$

$$R_{\text{con}} = (2 A_s / \pi)^{1/2} \, (2\tilde{k}\varphi)^{1/4} \cdot \tag{136}$$

The decrease in the thermal resistance of the sector is evaluated by dividing Eq. (133) by Eq. (122): the result is $(\pi/4)(3/2)^{1/2} = 0.96$, or a 4 percent decrease [112]. The resistance decrease for the entire disc assembly is computed by dividing Eq. (135) by Eq. (125): the result is $3\pi^2/32 = 0.925$ so that a 7.5 percent reduction in global resistance can be achieved.

4.2.2 One Branching Architecture

One branching architecture consists of k_p slabs that stretch radially to the distance L_0 away from the central heat sink, and continue with a number (n) of branches (tributaries) that reach the rim [112, 117]. Its elemental sector contains one stem of aspect ratio H_0/L_0 and n tributaries of aspect ratio H_1/L_1 shown in Fig. 16. The length L_1 is the distance from the hot spot (T_m) to the point of confluence (T_c). The goal is to assemble with minimum thermal resistance a number (N) of branched sectors into a complete disc, as shown in Fig. 17.

Each peripheral sector of radius L_1 is slender enough and is with an optimized shape described by Eq. (121):

$$A_1 = H_1 L_{1,} \tag{137}$$

$$\left(\frac{H_1}{L_1}\right)_{con} = \frac{2}{(3\tilde{k}\varphi_1)^{1/2}}, \tag{138}$$

where

$$\phi_1 = \frac{D_1}{H_1}. \tag{139}$$

The same is not true for the central sector of radius L_0, because, unlike in Section 4.2.1, the T_c end of its high-conductivity slab is not insulated [117]. For

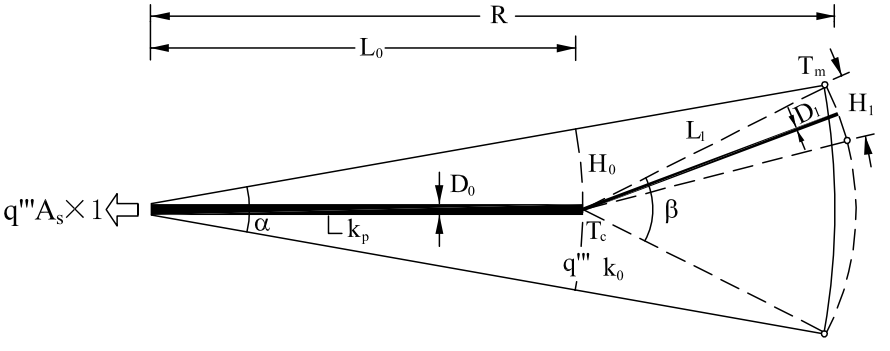

Fig. 16 One-level branching architecture: one central high-conductivity path (L_0, D_0) with n_1 smaller paths (L_1, D_1) as tributaries (after [117])

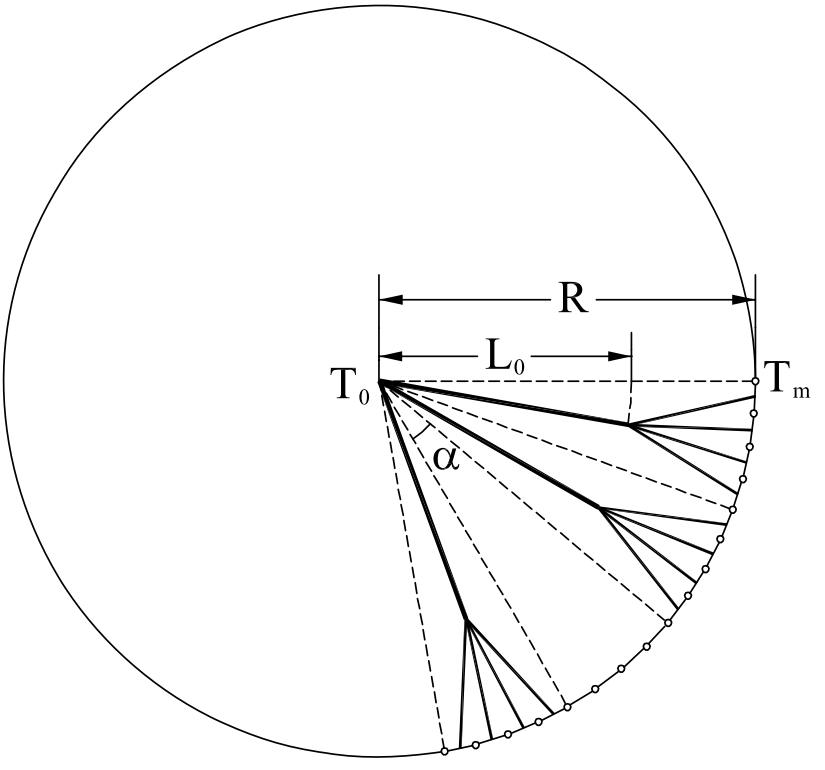

Fig. 17 Constructal structure consisting of several branched sectors in Fig. 16 (after [117])

this reason the aspect ratio of the (H_0, L_0) sector is free to vary, and so is the aspect ratio of the entire sector (radius R) of Fig. 16. For the (H_0, L_0) sector we have

$$\frac{H_0}{L_0} \cong \frac{\alpha}{2} \qquad A_0 = H_0 L_0 \tag{140}$$

where the tip angle α is a function of the assumed n and R values. The number of A_1 elements that fit along the perimeter of the R disc is $N = 2\pi R/(2H_1)$. The number of branched sectors of angle α is N/n. The angle α is then

$$\alpha = \frac{2\pi n}{N} = \frac{2^{3/2} n}{\widetilde{R}(3\widetilde{k}\phi_1)^{1/4}} \tag{141}$$

where the dimensionless radius $\widetilde{R}$ is defined by

$$\widetilde{R} = \frac{R}{A_1^{1/2}}. \tag{142}$$

The area A_0 that is allocated to the stem (L_0, D_0) is $(\alpha/2)\,L_0^2$, where $L_0 \cong R - L_1$. After some algebra, we obtain [117]

$$A_0 \cong \frac{2^{1/2} n\, \tilde{R}\, A_1}{(3\tilde{k}\phi_1)^{1/4}} \left[1 - \frac{(3\tilde{k}\phi_1)^{1/4}}{2^{1/2}\tilde{R}} \right]^2 . \tag{143}$$

Note that Eq. (143) is approximate because not all the A_1 elements have the length L_1. This approximation becomes more accurate as the angles β and α decrease.

By Eq. (122), we have the overall temperature difference over the peripheral sector of radius L_1

$$T_{\mathrm{m}} - T_c = \frac{2q''' A_1}{k_f (3\tilde{k}\varphi_1)^{1/2}} . \tag{144}$$

Note that the T_c tip of the D_0 slab receives the heat current collected by the n peripheral sectors of size A_1. Therefore,

$$q''' \times 1 \times n\, A_1 = k_p D_0 \times 1 \left(\frac{dT}{dt} \right)_{r=L_0} . \tag{145}$$

As in Fig. 15, the radial position in the central sector of Fig. 16 is measured from the center ($r = 0$) to the T_c junction ($r = L_0$). The governing equation for the temperature distribution along the D_0 slab is

$$-dq = 2 \left(\frac{H_0}{L_0} r \right) q''' \times 1\, dr \tag{146}$$

where

$$q = k_p\, D_0 \times 1 \times \frac{dT}{dr} . \tag{147}$$

Eliminating q, integrating twice with respect to r, and invoking the tip condition (145) and $T = T_0$ at $r = 0$ will lead to temperature distribution $T(r)$. In the resulting $T(r)$ expression we set $T(L_0) = T_c$ to obtain

$$T_c - T_0 = \frac{q''' L_0}{k_p\, D_0} \left(\frac{2}{3} A_0 + n\, A_1 \right) . \tag{148}$$

Adding Eqs. (144) and (148), and noting again that $L_0 \cong R - L_1$, we obtain the temperature difference

$$T_{\mathrm{m}} - T_0 \cong \frac{2q'''A_1}{k_f(3\tilde{k}\varphi_1)^{1/2}} + \frac{q'''(R-L_1)}{k_p\, D_0}\left(\frac{2}{3}A_0 + n\,A_1\right). \tag{149}$$

This quantity can be nondimensionalized as

$$\tilde{T} = \frac{T_{\mathrm{m}} - T_0}{q'''A_1/k_0} = \frac{2}{(3\tilde{k}\varphi_1)^{1/2}} + \frac{(3\tilde{k}\varphi_1)^{1/4}}{2^{1/2}\tilde{k}\varphi_1\tilde{D}}$$
$$\times\left[\tilde{R} - \frac{(3\tilde{k}\varphi_1)^{1/4}}{2^{1/2}}\right]\times\left\{\frac{2^{3/2}n\,\tilde{R}}{3(3\tilde{k}\varphi_1)^{1/4}}\left[1 - \frac{(3\tilde{k}\varphi_1)^{1/4}}{2^{1/2}\tilde{R}}\right]^2 + n\right\} \tag{150}$$

where $\tilde{D}$ is the k_p slab width ratio,

$$\tilde{D} = \frac{D_0}{D_1}. \tag{151}$$

The temperature difference $\tilde{T}$ depends on geometry $(n, \tilde{D}, \tilde{R})$, and also on the presence of k_p material $(\tilde{k}, \phi_1)$. The total amount of k_p material in the R disc is represented by the cross-sectional area

$$A_p = ND_1L_1 + \frac{N}{n}D_0L_0 \tag{152}$$

or by the fraction that A_p occupies in the entire disc (πR^2):

$$\phi = \frac{A_p}{\pi R^2} = \frac{(3\tilde{k}\phi_1)^{1/4}\phi_1}{2^{1/2}\tilde{R}} + \frac{\tilde{D}\,\phi_1}{n\tilde{R}}\left[\tilde{R} - \frac{(3\tilde{k}\phi_1)^{1/4}}{2^{1/2}}\right]. \tag{153}$$

The ϕ fraction is fixed (e.g. ϕ = 0.05). Thus Eq. (153) provides a relation among $\tilde{k}, \phi_1, \tilde{D}, n$ and $\tilde{R}$. The $\tilde{k}$ ratio is fixed by the choice of materials (e.g., $\tilde{k}$ = 385/0.6 for copper-nanoparticles-in-water nanofluids). We expect a tradeoff between ϕ_1 and $\tilde{D}$, which will represent the optimal allocation of k_p material to the D_0 and D_1 slabs [117].

For example, set n = 2 and $\tilde{R}$ = 4, and minimize $\tilde{T}$ by varying ϕ_1 and $\tilde{D}$, where ϕ_1 and $\tilde{D}$ are related by Eq. (153). Figure 19 confirms that $\tilde{T}$ has a minimum with respect to how the k_p material is allocated. The resulting features of the optimal configuration ($\phi_{1,\mathrm{con}}$, $\tilde{D}_{\mathrm{con}}, \tilde{T}_{\mathrm{con}}$) are shown in Fig. 19. This figure also shows how the optimum responds to construct's size changes, $\tilde{R}$. The optimal allocation of high-conductivity material is almost insensitive to changes in $\tilde{R}$. The temperature difference $\tilde{T}_{\mathrm{con}}$ is almost proportional to $\tilde{R}$.

The numerical work summarized in Fig. 19 was repeated for other numbers of elemental branches, $n = 4, 6, \ldots$ in [117]. The key feature of these results is that the $\phi_{1,con}$ and $\tilde{T}_{con}$ curves, which were plotted for $n = 2$ in Fig. 19, do not shift as n increases [117]. Figure 20 shows that the $\tilde{D}_{con}$ curve raises as n increases. A larger $\tilde{D}_{con}$ means an elemental insert (D_1) that is thinner relative to the stem (D_0). The numerical values shown in Fig. 20 indicate that $\tilde{D}_{con} / n$ is almost constant. Therefore, the optimum is characterized by $D_0 \approx nD_1$ [117]. This approximation is more exact when $\tilde{R}$ is smaller. In that limit the cross-sectional area of the k_p slabs is conserved at the junction between the stem and the branches. When $\tilde{R}$ is larger, the stem cross-section is larger than the combined cross-section of the branches, $D_0 > nD_1$.

Figure 19 also shows the required number of peripheral elements,

$$N_{con} = 2^{-1/2} \pi \tilde{R} (3\tilde{k}\phi_{1,con})^{1/4}. \tag{154}$$

This number increases as $\tilde{R}$ increase, and is independent of n. The corresponding central length scale of the optimized branched pattern, $\tilde{L}_{con} = L_{0,con} \big/ A_1^{1/2}$, is obtained by $L_0 = R - L_1$ and Eq. (138):

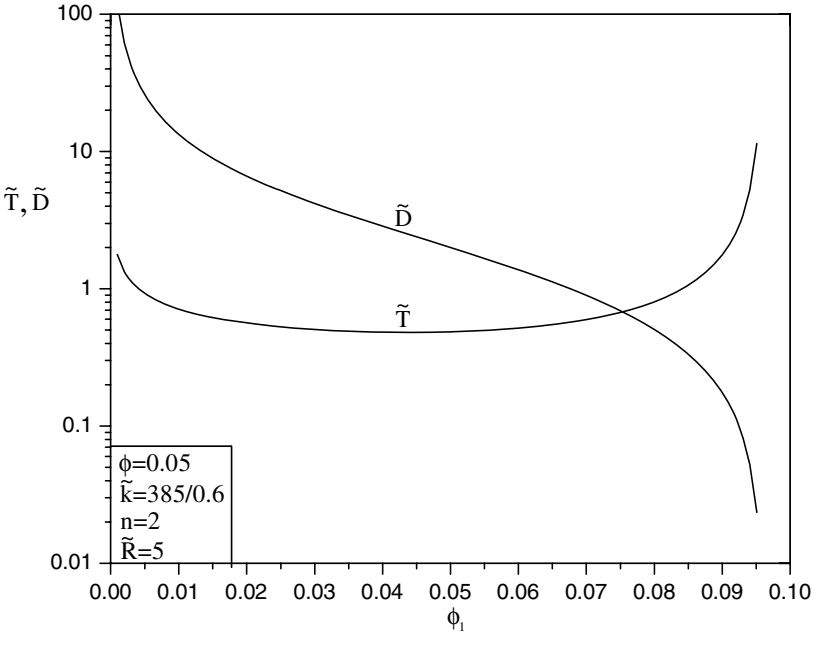

Fig. 18 The minimization of the overall (megascale) temperature difference in the construct of Fig. 17 (after [117])

$$\tilde{L}_{\text{con}} = \tilde{R} - 2^{-1/2}(3\tilde{k}\phi_{1,\text{con}})^{1/4}. \tag{155}$$

This length increases with $\tilde{R}$, and is independent of n (Fig. 19). Note that L_0 shrinks to zero (hence $\phi_{1,\text{con}} = \phi$) when $\tilde{R}$ drops to 2.2148. This critical $\tilde{R}$ value corresponds to the optimized radial pattern without branches (Fig. 14) [117]. The disappearance of the branched pattern at $\tilde{R} = 2.2148$ is responsible for the vanishing of all the curves in Fig. 21 under $\tilde{R} = 2.2148$.

In each of the cases optimized in Figs. 18 through 20 the elemental area A_1 and the disc size R were fixed. This means that the minimization of $\tilde{T}$ is equivalent to the minimization of the thermal resistance of the entire disc:

$$R_{1\text{th,con}} = \frac{(T_{\text{m}} - T_0)_{\text{con}}}{q''' \pi R^2 / k_f} = \frac{\tilde{T}_{\text{con}}}{\pi \tilde{R}^2}. \tag{156}$$

Because $\tilde{T}_{\text{con}}$ is almost proportional to $\tilde{R}$, the minimized resistance [$R_{1\text{th,con}} = \tilde{T}_{\text{con}} / (\pi \tilde{R}^2)$] decreases almost as $\tilde{R}^{-1}$ as $\tilde{R}$ increases [117].

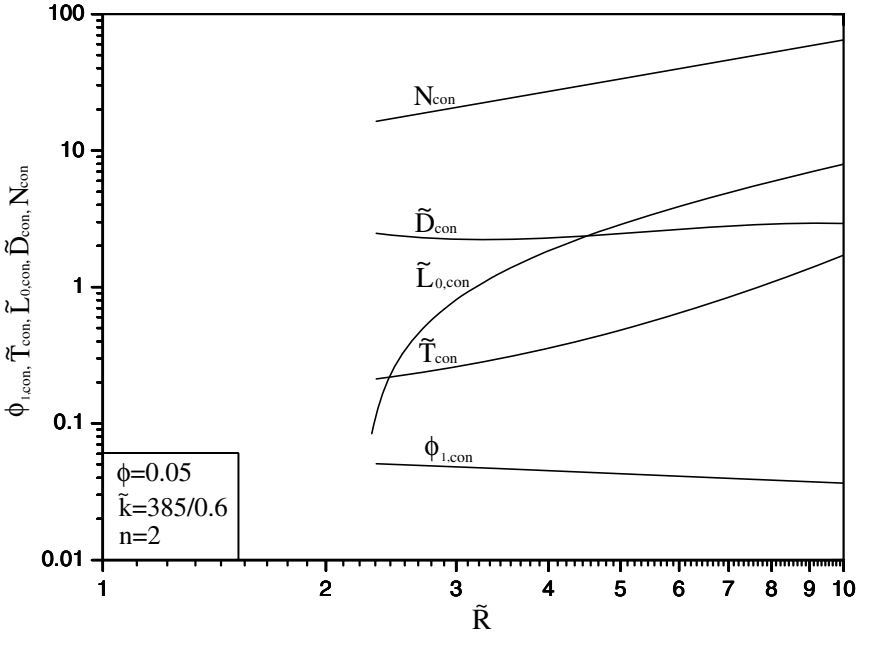

Fig. 19 The disc-size effect on the constructal configuration determined in Fig. 18 (after [117])

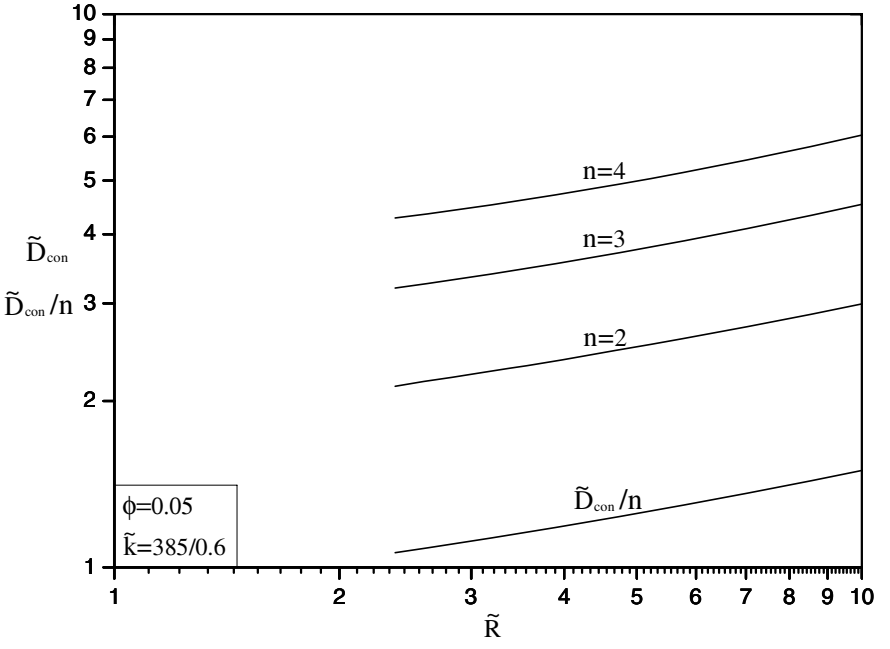

Fig. 20 The effect of the number of elemental branches on the constructal slab width ratio (after [117])

The minimized resistance $R_{1th,con}$ depends on $\tilde{R}, \tilde{k}$ and ϕ. It does not depend on n because $\tilde{T}_{con}$ is n-independent. By comparing the resistance $R_{1th,con}$ with the corresponding resistance $R_{0th,con}$ of the disc with zero branching architecture (Fig. 13), we can determine the recommended transition from radial patterns to branched patterns. We make this comparison based on the same elemental size ($A_s = A_1$) and the same amounts and properties of conducting materials $(\tilde{k}, \phi)$. The dimensionless radius of the radial design of Section 4.2.1 is [Eq. (126)],

$$\tilde{R} = 2^{-1/2}(3\tilde{k}\phi)^{1/4}. \tag{157}$$

In Fig. 14 this radius is fixed when $\tilde{k}$ and ϕ are fixed. In the branched design $\tilde{R}$ can be increased freely. This is why in Fig. 21 one case $(\tilde{k}, \phi)$ is represented by one radial-design point $R_{0th}(\tilde{R})$ and one branched-design curve $R_{1th,con}(\tilde{R})$. The figure shows that when $\tilde{R}$ exceeds 2.2148 (in the case $\phi = 0.05$, $\tilde{k} = 385/0.6$), the global resistance is smaller when the high-conductivity material is distributed according to the optimized branched pattern.

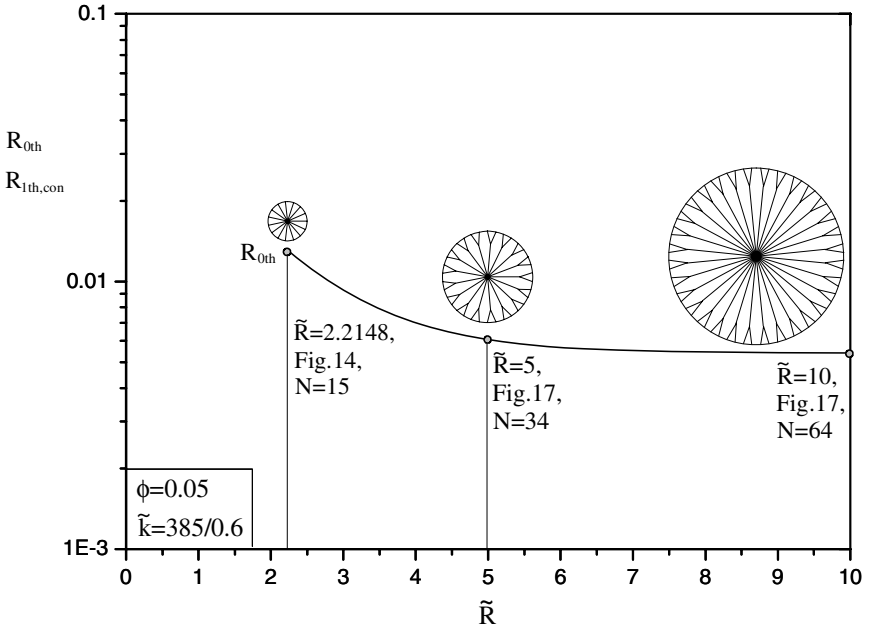

Fig. 21 The constructal overall thermal resistance of constructal zero branching architecture and one-level branching architecture (after [117])

The calculations in Fig. 21 have been repeated in [117] for other values of $\tilde{k}$ and ϕ, in the range $30 \le \tilde{k} \le 1000$ and $0.01 \le \phi \le 0.1$. The same qualitative behavior as in Fig. 21 has been identified. Also founded was the additional feature that the effect of $\tilde{k}$ and ϕ on $R_{1th,con}$ is through the product $\tilde{k}\phi$ [117]. Figure 22 is a condensation of all these results. Lower global resistances are achieved by decreasing $\tilde{k}\phi$, and by switching from the constructal radial pattern (Fig. 14) to the constructal branched pattern (Fig. 17) when $\tilde{R}$ can be made greater than the $\tilde{R}$ value of the constructal radial pattern. Figure 21 illustrates this transition in the case of $\tilde{k} = 385/0.6$ and $\phi = 0.05$, for which the radial pattern has $\tilde{R} = 2.2148$ and 15 elemental sectors, and the branched pattern has 34 peripheral elements for $\tilde{R} = 5$ and 64 peripheral elements for $\tilde{R} = 10$.

Therefore, the constructal design in constructal nanofluids employs a hierarchical strategy for developing the constructal (optimal) heat-flow structure for the constructal (optimal) megascale performance within the limit of available freedom The strategy consists of optimization of heat-flow performance at every scale,

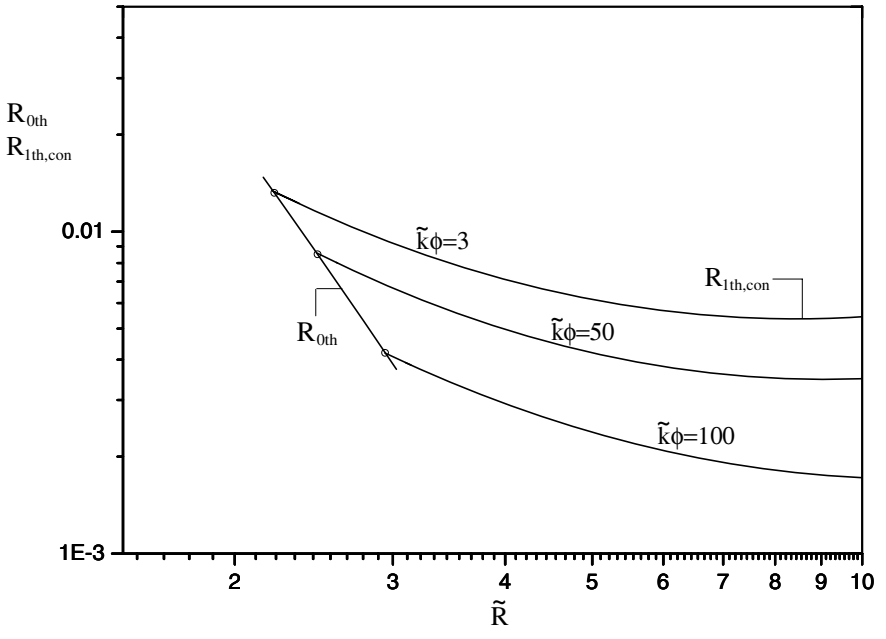

Fig. 22 The effect of $\tilde{k}$ and ϕ on the constructal overall thermal resistance of constructal zero branching architecture and one-level branching architecture (after [117])

followed by the assembly of optimized systems into larger systems. Every geometric detail of the heat-flow structure is derived from principle. The flow structure is the construction (configuration) of the two-material (base fluid and nanostructure) conductive body [112]. As the technology develops, new freedom arises, the optimization with respect to the new freedom yields new and better constructal nanofluids. The focus on megascale serves well the true and ultimate goal of using nanofluids. The focus on optimization, on finding the constructal nanofluids which yield optimal megascale performance, introduces powerful optimization and variation theory to the process of nanofluids research and development [112, 116]. This changes the attitude of nanofluids research and development from observing/describing systems to controlling/optimizing the systems [116].

Therefore, the future effort is in great demand to construct nanofluids with respect to available freedoms for various systems of practical applications. Such studies will inspire the development of microfluidic nanofluids through constantly providing information regarding new nanofluids required.

5 Concluding Remarks

Nanofluids are a very important area of emerging technology and are playing an increasingly important role in the continuing advances of nanotechnology and biotechnology worldwide. They have enormously exciting potential applications, and may revolutionize the field of heat transfer. With powerful microfluidic technology, scaling-up techniques, thermal-wave theory and constructal theory, research and engineering practice in nanofluids is entering a new era. On one side is great opportunity because these technologies empower us to address the central questions of nanofluid research and development such as effective means of microscale manipulation, interplays among physics at different scales and optimization of microscale physics for the optimal megascale properties. On the other side is greater challenge than ever before due to the difficulty related to scales and scaling.

Conventional synthesis approaches have not been satisfactory because of their inadequacies in engineering microstructures of nanofluids. Recently-developed one-step chemical solution method (CSM) takes advantage of the ability of manipulating atoms and molecules through chemical reactions in the liquid phase. However, the difficulty of controlling the microscale while operating at the macroscale is insuperable. By replacing batch-based macroreactors in the CSM by continuous-flow microfluidic microreactors of microchannels, droplets and slugs, a novel microfluidic one-step CSM is proposed for effective synthesis of high-quality nanofluids with controllable microstructures. Future research is in great demand to define the potential of this promising synthesis technique against an important target of controlling reactions accurately with a rapid and precise mixing. The success of this technology may change the way nanofluids are synthesized and applied and should also lead to progress both in creating nanofluids by design and in producing nanofluids economically at a commercial scale.

In an attempt to determine how the presence of nanoparticles affects the heat conduction at the macroscale and isolate the mechanism responsible for the reported significant enhancement of thermal conductivity, a macroscale heat-conduction model in nanofluids is rigorously developed. The model is obtained by scaling-up the microscale model for the heat conduction in the nanoparticles and in the base fluids. The approach for scaling-up is the volume averaging with help of multiscale theorems. The result shows that the presence of nanoparticles leads to a dual-phase-lagging heat conduction in nanofluids at the macroscale. Therefore, the molecular physics and the microscale physics manifest themselves as heat diffusion and thermal waves at the macroscale, respectively. Depending on factors like material properties of nanoparticles and base fluids, nanoparticles' geometrical structure and their distribution in the base fluids, and interfacial properties and dynamic processes on particle-fluid interfaces, the heat diffusion and thermal waves may either enhance or counteract

each other. Consequently, the heat conduction may be enhanced or weakened by the presence of nanoparticles. Focused efforts are required to find the correlation between the microscale physics and macroscale properties based on the three closures and to detail properties of thermal waves and how they interact with the heat diffusion.

Practical applications of nanofluids are always with an ultimate megascale goal to which nanofluid research must pay attention. The constructal design employs a hierarchical strategy to construct nanofluids for the optimal megascale performance and thus serves this very well. Such a study shows, for example, that the march towards uniformly-dispersed particles in base fluids not necessarily leads to an optimal megascale performance depending on systems that use nanofluids. Our focus of future research and development should thus be not only on nanofluids themselves but also on their systems and ultimate goals. The march toward micro and nano scales must also be with the sobering reminder that useful devices are always be macroscopic, and that larger and larger numbers of small-scale components must be assembled and connected by flows that keep them alive. Clearly, an intensive effort is in great demand to *construct* nanofluids with respect to available freedoms for various systems of practical applications.

Acknowledgement. LQW acknowledges the support of the Research Grants Council of Hong Kong (GRF718009, GRF717508 and GRF704906), and of the CRCG of the University of Hong Kong (200811159161, 200707176111 and 200607176138). LQW also acknowledges the interactions with Professors A. Bejan, D. Y. Tzou, P. Vadasz, D. A. Weitz and H. T. Zhu, and the work done by several students, as referenced here, that made it possible to carry out this work and thus present this review.

References

1. Choi, S.U.S., Zhang, Z.G., Keblinski, P.: Nanofluids. In: Nalwa, H.S. (ed.) Encyclopedia of Nanoscience and Nanotechnology, vol. 6, pp. 757–773. American Scientific Publishers (2004)
2. Peterson, G.P., Li, C.H.: Heat and mass transfer in fluids with nanoparticle suspensions. Adv. Heat Transfer 39, 257–376 (2006)
3. Das, S.K., Choi, S.U.S., Yu, W.H., Pradeep, T.: Nanofluids: Science and Technology. John Wiley & Sons, Chichester (2008)
4. Wen, D.S., Ding, Y.L., Williams, R.: Nanofluids turn up the heat. TCE 771, 32–34 (2005)
5. Pileni, M.P.: Magnetic fluids: fabrication, magnetic properties, and organization of nanocrystals. Adv. Funct. Mater. 11, 323–336 (2001)
6. Wasan, D.T., Nikolov, A.D.: Spreading of nanofluids on solids. Nature 423, 156–159 (2003)
7. Gorman, J.: Nanofluid flow: detergents may benefit from new insight. Sci. News 163, 292–293 (2003)

8. Chen, H.S., Ding, Y.L., He, Y.R., Tan, C.Q.: Rheological behaviour of ethylene glycol based titania nanofluids. Chemical Physics Letters 444, 333–337 (2007)
9. Zhang, L.L., Jiang, Y.H., Ding, Y.L., Povey, M., York, D.: Investigation into the antibacterial behaviour of suspensions of ZnO nanoparticles (ZnO nanofluids). Journal of Nanoparticle Research 9, 479–489 (2007)
10. Pomogailo, A.D., Kestelman, V.N.: Metallopolymer Nanocomposites. Springer, Heidelberg (2005)
11. Dice, G.D., Mujumdar, S., Elezzabi, A.Y.: Plasmonically enhanced diffusive and subdiffusive metal nanoparticle-dye random laser. Appl. Phys. Lett. 86, 131105 (2005)
12. Duan, X., Huang, Y., Cui, Y., Wang, J., Lieber, C.M.: Indium phosphide nanowires as building blocks for nanoscale electronic and optoelectronic devices. Nature 409, 241–245 (2001)
13. Duan, X., Huang, Y., Agarwal, R., Lieber, C.M.: Single-nanowire electrically driven lasers. Nature 421, 66–69 (2003)
14. Singh, A.K.: Thermal conductivity of nanofluids. Defence Science Journal 58, 600–607 (2008)
15. Li, C.H., Williams, W., Buongiorno, J., Hu, L.W., Peterson, G.P.: Transient and Steady-State Experimental Comparison Study of Effective Thermal Conductivity of Al_2O_3/Water Nanofluids. J. Heat Transfer 130, 040301/1–044503/4 (2008)
16. Wang, L.Q., Wei, X.H.: Nanofluids: Synthesis, Heat Conduction, and Extension. J. Heat Transfer 131, 033102/1–033102/7 (2009)
17. Jang, S.P., Choi, S.U.S.: Effects of Various Parameters on Nanofluid Thermal Conductivity. J. Heat Transfer 129, 617–623 (2007)
18. Vadasz, P.: Heat Conduction in Nanofluid Suspensions. J. Heat Transfer 128, 465–477 (2006)
19. Lee, S., Choi, S.U.S., Li, S., Eastman, J.A.: Measuring Thermal Conductivity of Fluids Containing Oxide Nanoparticles. J. Heat Transfer 121, 280–289 (1999)
20. Wei, X.H., Zhu, H.T., Wang, L.Q.: $CePO_4$ Nanofluids: Synthesis and Thermal Conductivity. J. Thermophysics Heat Transfer 23, 219–222 (2009)
21. Das, S.K., Putra, N., Thiesen, P., Roetzel, W.: Temperature Dependence of Thermal Conductivity Enhancement for Nanofluids. J. Heat Transfer 125, 567–574 (2003)
22. He, Y.R., Men, Y.B., Liu, X., Lu, H.L., Chen, H.S., Ding, Y.L.: Study on forced convective heat transfer of non-Newtonian nanofluids. J. Thermal Sci. 18, 20–26 (2009)
23. Tzou, D.Y.: Thermal Instability of Nanofluids in Natural Convection. Int. J. Heat Mass Transfer 51, 2967–2979 (2008)
24. Buongiorno, J.: Convection Transport in Nanofluids. J. Heat Transfer 128, 240–250 (2006)
25. Xuan, Y.M., Li, Q.: Investigation on Convective Heat Transfer and Flow Features of Nanofluids. J. Heat Transfer 125, 151–155 (2003)
26. Milanova, D., Kumar, R.: Heat Transfer Behavior of Silica Nanoparticles Experiment in Pool Boiling. J. Heat Transfer 130, 042401/–042401/6 (2009)
27. Kim, S.J., McKrell, T., Buongiorno, J., Hu, L.W.: Alumina Nanoparticles Enhance the Flow Boiling Critical Heat Flux of Water at Low Pressure. J. Heat Transfer 130, 044501/1–044501/3 (2008)
28. Kim, S.J., McKrell, T., Buongiorno, J., Hu, L.W.: Experimental Study of Flow Critical Heat Flux in Alumina-Water, Zinc-Oxide-Water, and Diamond-Water Nanofluids. J. Heat Transfer 131, 043204/1–043204/7 (2009)

29. Kedzierski, M.A.: Effect of CuO Nanoparticle Concentration on R134a/Lubricant Pool-Boiling Heat Transfer. J. Heat Transfer 131, 043205/1–043205/7 (2009)
30. Wu, D.X., Zhu, H.T., Wang, L.Q., Liu, L.M.: Critical Issues in Nanofluids Preparation, Characterization and Thermal Conductivity. Current Nanoscience 5, 103–112 (2009)
31. Choi, S.U.S.: Nanofluids: From Vision to Reality Through Research. J. Heat Transfer 131, 033106/1–033106/9 (2009)
32. Eastman, J.A., Phillpot, S.R., Choi, S.U.S., Keblinski, P.: Thermal transport in nanofluids. Annu. Rev. Mater. Res. 34, 219–246 (2004)
33. Phelan, P.E., Bhattacharya, P., Prasher, R.S.: Nanofluids for heat transfer applications. Annu. Rev. Heat Transfer 14, 255–275 (2005)
34. Sobhan, C.B., Peterson, G.P.: Microscale and Nanoscale Heat Transfer: Fundamentals and Engineering Applications. CRC Press, Boca Raton (2008)
35. Wang, L.Q., Xu, M.T., Wei, X.H.: Multiscale theorems. Adv. Chemical Engineering 34, 175–468 (2008)
36. Wang, L.Q.: Flows through porous media: a theoretical development at macroscale. Transport in Porous Media 39, 1–24 (2000)
37. Choi, S.U.S., Eastman, J.A.: Enhanced heat transfer using nanofluids. United States Patent, US 6221275 B1 (2001)
38. Eastman, J.A., Choi, S.U.S., Li, S., Yu, W., Thompson, L.J.: Anomalously increased effective thermal conductivities of ethylene glycol-based nanofluids containing copper nanoparticles. Appl. Phys. Lett. 78, 718–720 (2001)
39. Chang, H., Tsung, T.T., Chen, L.C., Yang, Y.C., Lin, H.M., Lin, C.K., Jwo, C.S.: Nanoparticle suspension preparation using the arc spray nanoparticle synthesis system combined with ultrasonic vibration and rotating electrode. Int. J. Adv. Manufacturing Tech. 26, 552–558 (2005)
40. Lo, C.H., Tsung, T.T., Chen, L.C., Su, C.H., Lin, H.M.: Fabrication of copper oxide nanofluid using submerged arc nanoparticle synthesis system (SANSS). J. Nanoparticle Research 7, 313–320 (2005)
41. Lo, C.H., Tsung, T.T., Chen, L.C.: Shaped-controlled synthesis of Cu-based nanofluid using submerged arc nanoparticle synthesis system (SANSS). J. Crystal Growth 277, 636–642 (2005)
42. Romano, J.M., Parker, J.C., Ford, Q.B.: Application opportunities for nanoparticles made from condensation of physical vapors. Adv. Powder Metallurgy Particulate Materials 2, 12–13 (1997)
43. Zhu, H.T., Lin, Y.S., Yin, Y.S.: A novel one-step chemical method for preparation of copper nanofluids. J. Colloid Interface Sci. 277, 100–103 (2004)
44. Zhu, H.T., Zhang, C.Y., Liu, S.Q., Tang, Y.M., Yin, Y.S.: Effects of nanoparticle clustering and alignment on thermal conductivities of Fe_3O_4 aqueous nanofluids. Appl. Phys. Lett. 89, 023123 (2006)
45. Zhu, H.T., Zhang, C.Y., Tang, Y.M.: Novel synthesis and thermal conductivity of CuO nanofluids. J. Phys. Chem. C 111, 1646–1650 (2007)
46. Wei, X.H., Kong, T.T., Zhu, H.T., Wang, L.Q.: CuS/Cu_2S nanofluids: synthesis and thermal conductivity. Int. J. Heat Mass Transfer (in press, 2009)
47. Wei, X.H., Zhu, H.T., Kong, T.T., Wang, L.Q.: Synthesis and Thermal Conductivity of Cu_2O Nanofluids. Int. J. Heat Mass Transfer 52, 4371–4374 (2009)
48. Wang, L.Q., Liu, F.: Forced convection in slightly curved microchannels. Int. J. Heat Mass Transfer 50, 881–896 (2007)

49. Wang, L.Q., Yang, T.L.: Multiplicity and stability of convection in curved ducts: review and progress. Adv. Heat Transfer 38, 203–255 (2004)
50. Wang, L.Q., Cheng, K.C.: Flow transitions and combined free and forced convective heat transfer in rotating curved channels: the case of positive rotation. Phys. Fluids 8, 1553–1573 (1996)
51. Sudarsan, A.P., Ugaz, V.M.: Fluid mixing in planar spiral microchannels. Lab on a Chip 6, 74–82 (2006)
52. Hong, C.C., Choi, J.W., Ahn, C.H.: A novel in-plane passive microfluidic mixer with modified Tesla structures. Lab on a Chip 4, 109–113 (2004)
53. Sudarsan, A.P., Ugaz, V.M.: Multivortex micromixing. Proceedings of the National Academy of Sciences of the United States of America 103, 7228–7233 (2006)
54. Alleborn, N., Nandakumar, K., Raszillier, H., Durst, F.: Further contributions on the two-dimensional flow in a sudden expansion. J. Fluid Mech. 330, 169–188 (1997)
55. Nguyen, N.T.: Micromixers: Fundamentals, Design and Fabrication. William-Andrew (2008)
56. Tice, J.D., Song, H., Lyon, A.D., Ismagilov, R.F.: Formation of droplets and mixing in multiphase microfluidics at low values of the reynolds and the capillary numbers. Langmuir 19, 9127–9133 (2003)
57. Günther, A., Jhunjhunwala, M., Thalmann, M., Schmidt, M.A., Jensen, K.F.: Micromixing of miscible liquids in segmented gas–liquid flow. Langmuir 21, 1547–1555 (2005)
58. Hosokawa, K., Fujii, T., Endo, I.: Handling of picoliter liquid samples in a poly (dimethylsiloxane)-based microfluidic device. Anal. Chem. 71, 4781–4785 (1999)
59. Handique, K., Burns, M.A.: Mathematical modeling of drop mixing in a slit-type microchannel. J. Micromech. Microeng. 11, 548–554 (2001)
60. Kashid, M.N., Gerlach, I., Goetz, S., Franzke, J., Acker, J.F., Platte, F., Agar, D.W., Turek, S.: Internal circulation within the liquid slugs of a liquid-liquid slug-flow capillary microreactor. Ind. Eng. Chem. Res. 44, 5003–5010 (2005)
61. Grigoriev, R.O.: Chaotic mixing in thermocapillary-driven microdroplets. Phys. Fluids 17, 033601 (2005)
62. Muradoglu, M., Stone, H.A.: Mixing in a drop moving through a serpentine channel: A computational study. Phys. Fluids 17, 073305 (2005)
63. Garstecki, P., Fischbach, M.A., Whitesides, G.M.: Design for mixing using bubbles in branched microfluidic channels. Appl. Phys. Lett. 86, 244108 (2005)
64. Salman, W., Angeli, P., Gavriilidis, A.: Sample pulse broadening in Taylor flow microchannels for screening applications. Chem. Eng. Technol. 28, 509–514 (2005)
65. Garstecki, P., Fuerstman, M.J., Fischbach, M.A., Sia, S.K., Whitesides, G.M.: Mixing with bubbles: a practical technology for use with portable microfluidic devices. Lab Chip 6, 207–212 (2006)
66. Fan, J., Zhang, Y.X., Wang, L.Q.: Bubble formation in microfluidic T-junctions (submitted, 2009)
67. Tan, Y.C., Lee, A.: Micro/naodroplets in microfluidic devices. In: Bhushan, B. (ed.) Springer Handbook of Nanotechnology, pp. 571–587. Springer, Heidelberg (2007)
68. Wang, L.Q., Zhang, Y.X., Cheng, L.: Magic microfluidic T-junctions: valving and bubbling. Chaos, Solitons & Fractals 39, 1530–1537 (2009)
69. Shah, R.K., Shum, H.C., Rowat, A.C., Lee, D.Y., Agresti, J.J., Utada, A.S., Chu, L.Y., Kim, J.W., Fernandez-Nieves, A., Martinez, C.J., Weitz, D.A.: Designer emulsions using microfluidics. Materials Today 11, 18–27 (2008)
70. Wei, X.H., Wang, L.Q.: Microfluidic Cu_2O nanofluids (submitted, 2009)

71. Xuan, Y.M., Li, Q., Zhang, X., Hu, W.: Aggregation structure and thermal conductivity of nanofluids. AICHE Journal 49, 1038–1043 (2003)
72. Koo, J., Kleinstreuer, C.: A new thermal conductivity model for nanofluids. J. Nanoparticle Research 6, 577–588 (2004)
73. Jang, S.P., Choi, S.U.S.: Role of Brownian motion in the enhanced thermal conductivity of nanofluids. Appl. Phys. Lett. 84, 4316–4318 (2004)
74. Bhattacharya, P., Saha, S.K., Yadav, A., Phelan, P.E., Prasher, R.S.: Brownian dynamics simulation to determine the effect thermal conductivity of nanofluids. J. Appl. Phys. 95, 6492–6494 (2004)
75. Prasher, R., Bhattacharya, P., Phelan, P.E.: Thermal conductivity of nanoscale colloidal solutions (nanofluids). Phys. Rev. Lett. 94, 025901 (2005)
76. Prasher, R., Bhattacharya, P., Phelan, P.E.: Brownian-motion-based convective-conductive model for the effective thermal conductivity of nanofluids. J. Heat Transfer 128, 588–595 (2006)
77. Yu, W., Choi, S.U.S.: The role of interfacial layers in the enhanced thermal conductivity of nanofluids: a renovated Maxwell model. J. Nanoparticle Research 5, 167–171 (2003)
78. Yu, W., Choi, S.U.S.: The role of interfacial layers in the enhanced thermal conductivity of nanofluids: a renovated Hamilton-Crosser model. J. Nanoparticle Research 6, 355–361 (2004)
79. Xue, L., Keblinski, P., Phillpot, S.R., Choi, S.U.S., Eastman, J.A.: Effect of liquid layering at the liquid-solid interface on thermal transport. Int. J. Heat Mass Transfer 47, 4277–4284 (2004)
80. Xie, H., Fujii, M., Zhang, X.: Effect of interfacial nanolayer on the effective thermal conductivity of nanoparticle-fluid mixture. Int. J. Heat Mass Transfer 48, 2926–2932 (2005)
81. Ren, Y., Xie, H., Cai, A.: Effective thermal conductivity of nanofluids containing spherical nanoparticles. J. Phys. D 38, 3958–3961 (2005)
82. Leong, K.C., Yang, C., Murshed, S.M.S.: A model for the thermal conductivity of nanofluids: the effect of interfacial layer. J. Nanopart. Res. 8, 245–254 (2006)
83. Wang, B.X., Zhou, L.P., Peng, X.F.: A fractal model for predicting the effective thermal conductivity of liquid with suspension of nanoparticles. Int. J. Heat Mass Transfer 46, 2665–2672 (2003)
84. Prasher, R., Phelan, P.E., Bhattacharya, P.: Effect of aggregation kinetics on the thermal conductivity of nanoscale colloidal solutions (nanofluid). Nano Letters 6, 1529–1534 (2006)
85. Rusconi, R., Rodari, E., Piazza, R.: Optical measurements of the thermal properties of nanofluids. Appl. Phys. Lett. 89, 261916 (2006)
86. Putnam, S.A., Cahill, D.G., Braun, P.V., Ge, Z.B., Shimmin, R.G.: Thermal conductivity of nanoparticle suspensions. J. Appl. Phys. 99, 084308
87. Eapen, J., Williams, W.C., Buongiorno, J., Hu, L.W., Yip, S.: Mean-field versus microconvection effects in nanofluid thermal conduction. Phys. Rev. Lett. 99, 095901 (2007)
88. Das, S.K., Choi, S.U.S., Patel, H.E.: Heat transfer in nanofluids: a review. Heat Transfer Engng. 27, 3–19 (2006)
89. Keblinski, P., Prasher, R., Eapen, J.: Thermal conductance of nanofluids: is the controversy over? J. Nanopart. Res. 10, 1089–1097 (2008)
90. Murshed, S.M.S.: Correction and comment on thermal conductance of nanofluids: is the controversy over? J. Nanopart. Res. 11, 511–512 (2009)

91. Wang, L.Q., Zhou, X.S., Wei, X.H.: Heat Conduction: Mathematical Models and Analytical Solutions. Springer, Heidelberg (2008)
92. Whitaker, S.: The Method of Volume Averaging. Kluwer Academic, Dordrecht (1999)
93. Wang, L.Q.: Generalized Fourier law. Int. J. Heat Mass Transfer 37, 2627–2634 (1994)
94. Auriault, J.L.: Heterogeneous medium: is an equivalent macroscopic description possible? Int. J. Engng. Sci. 29, 785–795 (1991)
95. Quintard, M., Whitaker, S.: One- and two-equation models for transient diffusion processes in two-phase systems. Adv. in Heat Transfer 23, 369–464 (1993)
96. Ochoa-Tapia, J.A., Whitaker, S.: Heat transfer at the boundary between a porous medium and a homogeneous fluid. Int. J. Heat Mass Transfer 40, 2691–27076 (1997)
97. Ochoa-Tapia, J.A., Whitaker, S.: Heat transfer at the boundary between a porous medium and a homogeneous fluid: The one-equation model. J. Porous Media 1, 31–46 (1998)
98. Howes, F.A., Whitaker, S.: The spatial averaging theorem revisited. Chem. Eng. Sci. 40, 1387–1392 (1985)
99. Gray, W.G., Leijnse, A., Kolar, R.L., Blain, C.A.: Mathematical Tolls for Changing Spatial Scales in the Analysis of Physical Systems. CRC Press, Boca Raton (1993)
100. Carbonell, R.G., Whitaker, S.: Heat and mass transfer in porous media. In: Bear, J., Corapcioglu, M.Y. (eds.) Fundamentals of Transport Phenomena in Porous Media, pp. 123–198. Martinus Nijhoff (1984)
101. Quintard, M., Kaviany, M., Whitaker, S.: Two-medium treatment of heat transfer in porous media: numerical results for effective parameters. Adv. Water Resour. 20, 77–94 (1997)
102. Quintard, M., Whitaker, S.: Theoretical Analysis of Transport in Porous Media. In: Vafai, K. (ed.) Handbook of Heat Transfer in Porous Media, pp. 1–52. Marcel Dekker, New York (2000)
103. Quintard, M., Whitaker, S.: Local thermal equilibrium for transient heat conduction: Theory and comparison with numerical experiments. Int. J. Heat Mass Transfer 38, 2779–2796 (1995)
104. Tzou, D.Y.: Macro-to Microscale Heat Transfer: The Lagging Behavior. Taylor & Francis, Abington (1997)
105. Wang, L.Q., Wei, X.H.: Equivalence between dual-phase-lagging and two-phase-system heat conduction processes. Int. J. Heat Mass Transfer 51, 1751–1756 (2008)
106. Wang, L.Q., Zhou, X.S.: Dual-phase-lagging Heat-Conduction Equations. Shandong University Press (2000)
107. Wang, L.Q., Zhou, X.S.: Dual-phase-lagging Heat-Conduction Equations: Problems and Solutions. Shandong University Press (2001)
108. Wang, L.Q., Xu, M.T., Zhou, X.S.: Well-posedness and solution structure of dual-phase-lagging heat conduction. Int. J. Heat Mass Transfer 44, 1659–1669 (2001)
109. Xu, M.T., Wang, L.Q.: Thermal oscillation and resonance in dual-phase-lagging heat conduction. Int. J. Heat Mass Transfer 45, 1055–1061 (2002)
110. Wang, L.Q., Xu, M.T., Wei, X.H.: Dual-phase-lagging and porous-medium heat conduction processes. In: Vadasz, P. (ed.) Emerging Topics in Heat and Mass Transfer in Porous Media - from Bioengineering and Microelectronics to Nanotechnology, pp. 1–37. Springer, Heidelberg (2008)
111. Fan, J., Wang, L.Q.: Microstructural effects on macroscale thermal properties in nanofluids (submitted, 2009)

112. Bejan, A., Lorente, S.: Design with Constructal Theory. Wiley, Chichester (2008)
113. Reis, A.H.: Constructal theory: from engineering to physics, and how flow systems develop shape and structure. App. Mech. Rev. 59, 269–282 (2006)
114. Bejan, A., Lorente, S.: Constructal theory of configuration generation in nature and engineering. J. App. Phys. 100, 041301/1–041301/27 (2006)
115. Bai, C., Wang, L.Q.: Constructal design of particle volume fraction in nanofluids. J. Heat Transfer 131, 112402/1-112402/7 (2009)
116. Wang, L.Q.: An approach for thermodynamic reasoning. Int. J. Modern Phys. B 10, 2531–2551 (1996)
117. Rocha, L.A., Lorente, S., Bejan, A.: Constructal design for cooling a disc-shaped area by conduction. Int. J. Heat Mass Transfer 45, 1643–1652 (2002)
118. Bejan, A.: Constructal-theory network of conducting paths for cooling a heat generating volume. Int. J. Heat Mass Transfer 40, 799–816 (1997)

Author Index